CO_2 photoreduction with rhenium based porphyrin sensitized homogeneous two–component systems

Alvaro Martinez Ceballos

A thesis submitted for the degree of MSc (by research)

The University of York
Department of Chemistry

December 2012

Abstract

Rhenium diimine tricarbonyl complexes bearing bromide, acetonitrile, 3–picoline or triethylphosphite have been synthesized and employed for selective photocatalytic CO_2 conversion into carbon monoxide. To avoid employing high–energy radiation, multicomponent visible light sensitized systems have been developed combining zinc(II) *meso*–tetrasubstituted porphyrins with the rhenium catalysts. Electron transfer from the sensitizer to the metal complexes was suspected to be a major controlling element and chemical variability was exploited by inclusion of electron donating groups on the sensitizer, employing porphyrins with phenyl, tolyl, *tert*–butyl or methoxyphenyl groups and electron withdrawing substituents on the metal complexes, using 2,2'–bipyridine and 4,4'–bis(methoxycarbonyl)–2,2'–bipyridine (BMCbpy), spanning a wide range of electron transfer driving force values aiming to favor this step. This project was focused on the study of the performance of the different combinations and the understanding of the underlying chemical and thermodynamic factors which control it.

Mixtures with BMCbpy derivatives were found to be essentially non–active, whereas bipyridine complexes with picoline or acetonitrile formed the most active combinations with all porphyrins. These multicomponent systems have proved to be as efficient as similar supramolecular dyads, even better in some cases. We have gained an insight into their catalytic behavior, showing that the chemical nature of the catalyst and not the sensitizer or the electron transfer driving force controls the life span and the catalytic ability of the two component mixtures. Mechanistic information has also been obtained, indicating that chlorin, a reduced species of the parent porphyrin, needs to be present in order to achieve efficient catalysis. Porphyrin decomposition and chlorin formation seems to be strongly correlated with the structure of the catalyst employed. In addition, porphyrin decomposition only occurs when chlorin is present and its kinetics depends on the photoinduced electron transfer driving force.

Table of Contents

List of Figures ..... **vii**

List of Tables ..... **xiii**

List of Schemes ..... **xiv**

List of Equations ..... **xiv**

Chapter 1. Introduction **1**

1.1 General considerations **1**

1.2 CO_2 Reduction mechanism **9**

1.3 Rhenium–based sensitized systems **11**

1.4 Previous work in our group **15**

1.5 Electron transfer reactions **17**

1.6 Aim of this work **22**

Chapter 2. Synthesis **24**

2.1 Synthesis of Free–Base and Metallated Porphyrins **24**

Pyrrole–aldehyde condensation 24

Metallation 24

2.2 Synthesis of Rhenium Complexes **25**

General considerations 25

Substituted bipyridine preparation 26

Bipyridine coordination 26

Bromide substitution 26

Acetonitrile displacement 27

2.3 Structural Characterization **28**

NMR spectroscopy 28

Infrared spectroscopy 54

X–ray crystallography 63

Chapter 3. Electrochemistry 67

3.1 Porphyrins 67

3.2 Rhenium complexes 71

Chapter 4. Photophysics and PET Driving Force 77

4.1 UV–Visible absorption 77

4.2 Room temperature fluorescence 79

4.3 PET driving force 81

Chapter 5. Photocatalytic CO_2 Reduction 83

5.1 Intersystem comparisons 83

5.2 Influence of PET driving force on CO formation 87

5.3 Chlorin influence on CO production 94

5.4 Porphyrin decay reaction kinetics 101

5.5 Conclusions and further work 103

Chapter 6. Experimental 107

6.1 Solvents, Reagents and General Procedures 107

6.2 Physical Measurements 107

6.3 X–ray Crystallography 108

6.4 Photocatalytic CO_2 Reduction 109

6.5 Gas Chromatography 109

6.6 Synthesis 110

5,10,15,20–tetrakis[4–(*tert*–butyl)phenyl]–21*H*,23*H*–porphine: H_2TTBPP (FB–P3) 110

5,10,15,20–tetraphenyl–21*H*,23*H*–porphine zinc(II): ZnTPP (P1) 111

5,10,15,20–tetrakis(4–tolyl)–21*H*,23*H*–porphine zinc(II): ZnTTP (P2) 111

5,10,15,20–tetrakis[4–(*tert*–butyl)–phenyl]–21*H*,23*H*–porphine zinc(II): ZnTTBPP (P3) 112

5,10,15,20–tetrakis(4–methoxyphenyl)–21*H*,23*H*–porphine zinc(II): ZnTMPP (P4) 112

4,4'–bis(methoxycarbonyl)–2,2'–bipyridine: BMCbpy 113

bromopentacarbonylrhenium(I): $[Re(CO)_5Br]$ 113

fac–(2,2'–bipyridine)bromotricarbonylrhenium(I): $[Re(bpy)(CO)_3Br]$ (R1–a) 113

fac–acetonitrile(2,2'–bipyridine)tricarbonylrhenium(I) hexafluorophosphate: $[Re(bpy)(CO)_3(CH_3CN)][PF_6]$ (R2–a) 114

fac–(2,2'–bipyridine)tricarbonyl(3–picoline)rhenium(I) hexafluorophosphate: *fac*–$[Re(bpy)(CO)_3(3–Pic)][PF_6]$ (R3–a) 115

fac–(2,2'–bipyridine)tricarbonyl(triethylphosphite)rhenium(I) hexafluorophosphate: *fac*–$[Re(bpy)(CO)_3\{P(OEt)_3\}][PF_6]$ (R4–a) 115

fac–[4,4'–bis(methoxycarbonyl)–2,2'–bipyridine]bromotricarbonyl rhenium(I): *fac*–$[Re(BMCbpy)(CO)_3Br]$ (R1–b) 116

fac–acetonitrile[4,4'–bis(methoxycarbonyl)–2,2'–bipyridine]tricarbonyl rhenium(I) hexafluorophosphate: $[Re(BMCbpy)(CO)_3(CH_3CN)][PF_6]$ (R2–b) 117

fac–[4,4'–bis(methoxycarbonyl)–2,2'–bipyridine]tricarbonyl(3–picoline) rhenium(I) hexafluorophosphate: $[Re(BMCbpy)(CO)_3(3–Pic)][PF_6]$ (R3–b) 118

fac–[4,4'–bis(methoxycarbonyl)–2,2'–bipyridine]tricarbonyl (triethylphosphite)rhenium(I) hexafluorophosphate: $[Re(BMCbpy)(CO)_3\{P(OEt)_3\}][PF_6]$ (R4–b) 119

fac–[4,4'–bis(methoxycarbonyl)–2,2'–bipyridine](difluorophosphate–1κ*O*) tricarbonylrhenium(I): *fac*–$[Re(BMCbpy)(CO)_3(OPOF_2)][PF_6]$ (R5) 120

Appendices 122

Appendix I. NMR and IR spectra 122

Appendix II. X–ray crystallography data 125

Appendix III. Cyclic voltammograms 126

Appendix IV. UV–Visible absorption and emission spectra of metalloporphyrins 129

Appendix V. CO formation comparisons 135

Appendix VI. Absorbance variation profiles 139

Appendix VII. CO formation profiles 154

Definitions and Abbreviations 162

References 165

List of Figures

Figure 1.1 – Commercial chemicals obtainable from CO and hydrogen[4] 2

Figure 1.2 – Chemical structure of the original catalyst by Lehn and coworkers. Different parts of the catalysts modified in further studies are highlighted 4

Figure 1.3 – Representative photocatalysts based on metals different from rhenium 4

Figure 1.4 – Selected structures of some tricarbonyl complexes studied by Ishitani and coworkers. Photoatalytic activity is qualitatively indicated 5

Figure 1.5 – Rhenium dicarbonyl complexes employed for CO_2 reduction. Carbon dioxide photoreduction ability is also indicated 6

Figure 1.6 – Polyoxometalate–Re(I) supramolecular photocatalyst. Structure of the polyoxometalate is shown on the left. Oxygen (red), tungsten (black), phosphorus (green)[19] .. 7

Figure 1.7 – Pictorial illustration of the supramolecular enzyme–based photoreducing system prepared by Biswas and coworkers[21] 8

Figure 1.8 – Binuclear CO_2 intermediate structure and formation proposal[26] 10

Figure 1.9 – Ruthenium–rhenium conjugate photocatalysts with saturated (left) and conjugated (right) bridging ligand[27] 11

Figure 1.10 – Supramolecular photocatalyst based on a photosensitizing ruthenium core with three attached rhenium catalytic centers[28] 12

Figure 1.11 – Oligopeptidic heterofunctionalized nanotube for CO_2 reduction[36] 13

Figure 1.12 – Supramolecular–enzymatic sensitizedsystem for CO_2 reduction[37,38] 14

Figure 1.13 – Palladium porphyrin–rhenium dyad employed for CO_2 reduction. X= Br^-, NCS^-; L= 3–Picoline[45] 15

Figure 1.14 – Structural comparison of a parent porphyrin (left) and a generic monoreduced species (chlorin, right) found to form during irradiation 16

Figure 1.15 – Representation of energy levels modification of reactant (blue) and product (red) with molecular reorganization. Intensity represents progress along the reaction coordinate (electron location). (A) Initial situation, (B) transition state, (C) final products .. 18

Figure 1.16 – Self–exchange reaction profile. Activation energy $E_a = \lambda/4$ 18

Figure 1.17 – General electron transfer reaction energy profile. Notice that the value of λ does not change with ΔG_0. Dashed line represents the potential energy surface of the product when its minimum is set at the same value as that of the reactant. 19

Figure 1.18 – Energy profiles of the extreme situations of zero activation energy (left) and inverse region (right)..... 20

Figure 1.19 – Compounds synthesized and studied in this project. Rhenium complexes possess hexafluorophosphate as counterion..... 22

Figure 2.1 – ^{1}H NMR spectra labeling notation used for the bipyridine (left) and the picoline (right) ligands..... 28

Figure 2.2 – ^{13}C NMR spectra notation employed for bipyridine (left), carbonyls (center) and picoline (right) ligands..... 28

Figure 2.3 – ^{1}H NMR spectrum of H_2TTBP in $CDCl_3$ (400 MHz) at 298 K. Signals marked with an asterisk correspond to residual solvent peaks assigned according to previously reported values[54]..... 29

Figure 2.4 – ^{1}H NMR spectrum of ZnTPP (P1) in $CDCl_3$ (400 MHz) at 298 K..... 30

Figure 2.5 – ^{1}H NMR spectrum of ZnTPP (P2) in acetone–d_6 (400 MHz) at 298 K..... 31

Figure 2.6 – ^{1}H NMR spectrum of ZnTTBPP (P3) in $CDCl_3$ (400 MHz) at 298 K..... 32

Figure 2.7 – ^{1}H NMR spectrum of ZnTMPP (P4) in $CDCl_3$ (400 MHz) at 298 K..... 33

Figure 2.8 – Donating resonance effect of the methoxy group on the phenyl ring..... 34

Figure 2.9 – ^{1}H NMR spectrum of BMCbpy in $CDCl_3$ (400 MHz) at 298 K..... 34

Figure 2.10 – ^{1}H NMR expansion of [Re(bpy)(CO)$_3$Br] (R1–a) in $CDCl_3$ (400 MHz) at 298 K..... 35

Figure 2.11 – ^{1}H NMR spectrum of [Re(bpy)(CO)$_3$(CH$_3$CN)][PF_6] (R2–a) in acetone–d_6 (400 MHz) at 298 K..... 36

Figure 2.12 – ^{1}H NMR spectrum of [Re(bpy)(CO)$_3$(3–Pic)][PF_6] (R3–a) in acetone–d_6 (400 MHz) at 298 K..... 37

Figure 2.13 – ^{1}H NMR spectrum expansion of a [Re(bpy)(CO)$_3$(3–Pic)][PF_6] (R3–a) sample contaminated with free 3–picoline. acetone–d_6 (400 MHz) at 298 K. Signals corresponding to free picoline are highlighted..... 38

Figure 2.14 – ^{19}F (376.4 MHz, left) and ^{31}P (161.9 MHz, right) NMR spectra of [Re(bpy)(CO)$_3$(3–Pic)][PF_6] (R3–a) in acetone–d_6 at 298 K..... 38

Figure 2.15 – ^{1}H NMR spectrum of [Re(bpy)(CO)$_3${P(OEt)$_3$}][PF_6] (R4–a) in $CDCl_3$ (400 MHz) at 298 K..... 39

Figure 2.16 – ^{19}F (376.4 MHz, left) and ^{31}P (161.9 MHz, center and right) NMR spectra of [Re(bpy)(CO)$_3${P(OEt)$_3$}][PF_6] (R4–a) in $CDCl_3$ at 298 K..... 40

Figure 2.17 – ^{1}H NMR spectrum of [Re(BMCbpy)(CO)$_3$Br] (R1–b) in $CDCl_3$ (400 MHz) at 298 K 41

Figure 2.18 – ^{13}C NMR spectrum of [Re(BMCbpy)(CO)$_3$Br] (R1–b) in $CDCl_3$ (100.6 MHz) at 298 K 42

Figure 2.19 – ^{1}H –^{13}C HSQC spectrum of [Re(BMCbpy)(CO)$_3$Br] (R1–b) in $CDCl_3$ (400 MHz) at 298 K 42

Figure 2.20 – ^{13}C spectra of bpy (top) and BMCbpy (bottom) in $CDCl_3$ (100.6 MHz) at 298 K. Reported assignment for 2,2'–bipyridine[57] is indicated 43

Figure 2.21 – ^{1}H NMR spectrum of [Re(BMCbpy)(CO)$_3$(CH$_3$CN)][PF$_6$] (R2–b) in $CDCl_3$ (400 MHz) at 298 K 44

Figure 2.22 – ^{13}C NMR spectrum of [Re(BMCbpy)(CO)$_3$(CH$_3$CN)][PF$_6$] (R2–b) in acetone–d_6 (125.7 MHz) at 298 K 45

Figure 2.23 – ^{13}C NMR spectrum expansion of [Re(BMCbpy)(CO)$_3$(CH$_3$CN)][PF$_6$] (R2–b) in acetone–d_6 (125.7 MHz) at 298 K. Asterisks denote impurity and not solvent peaks in this case 46

Figure 2.24 – ^{1}H –^{13}C HSQC spectrum of [Re(BMCbpy)(CO)$_3$(CH$_3$CN)][PF$_6$] (R2–b) in acetone–d_6 (500 MHz) at 298 K 46

Figure 2.25 – ^{1}H NMR spectrum of [Re(BMCbpy)(CO)$_3$(3–Pic)][PF$_6$] (R3–b) in acetone–d_6 (400 MHz) at 298 K 47

Figure 2.26 – ^{13}C NMR spectrum of [Re(BMCbpy)(CO)$_3$(3–Pic)][PF$_6$] (R3–b) in acetone–d_6 (125.7 MHz) at 298 K 48

Figure 2.27 – ^{1}H –^{13}C HSQC spectrum of [Re(BMCbpy)(CO)$_3$(3–Pic)][PF$_6$] (R3–b) in acetone–d_6 (500 MHz) at 298 K 48

Figure 2.28 – ^{1}H NMR spectrum of [Re(BMCbpy)(CO)$_3${P(OEt)$_3$}][PF$_6$] (R4–b) in acetone–d_6 (500 MHz) at 298 K 49

Figure 2.29 – ^{13}C NMR spectrum of [Re(BMCbpy)(CO)$_3${P(OEt)$_3$}][PF$_6$] (R4–b) in acetone–d_6 (125.7 MHz) at 298 K 50

Figure 2.30 – ^{1}H –^{13}C HSQC spectrum sections of [Re(BMCbpy)(CO)$_3${P(OEt)$_3$}][PF$_6$] (R4–b) in acetone–d_6 (500 MHz) at 298 K 50

Figure 2.31 – ^{1}H NMR spectrum of [Re(BMCbpy)(CO)$_3$(OPOF$_2$)] (R5) in $CDCl_3$ (400 MHz) at 298 K 51

Figure 2.32 – ^{19}F (376.4 MHz, left) and ^{31}P (161.9 MHz, right) NMR spectra of [Re(BMCbpy)(CO)$_3$(OPOF$_2$)] (R5) in $CDCl_3$ at 298 K 52

Figure 2.33 – Representation of resonant forms that illustrate the –R effect of the methoxycarbonyl substituent on the bipyridine ring. Only half molecule is shown for clarity. 53

Figure 2.34 – Representative examples of symmetry elements of generalized formulae of the rhenium complexes prepared in this work 54

Figure 2.35 – IR spectrum of [Re(CO)$_5$Br] in THF 56

Figure 2.36 – IR spectrum of [Re(bpy)(CO)$_3$Br] (R1–a) in THF 57

Figure 2.37 – IR spectrum of the complex [Re(BMCbpy)(CO)$_3$Br] (R1–b) in THF 57

Figure 2.38 – IR spectrum of [Re(bpy)(CO)$_3$(CH$_3$CN)][PF$_6$] (R2–a) in THF 58

Figure 2.39 – IR spectrum of [Re(BMCbpy)(CO)$_3$(CH$_3$CN)][PF$_6$] (R2–b) in THF 59

Figure 2.40 – IR spectrum of [Re(BMCbpy)(CO)$_3$(3–Pic)][PF$_6$] (R3–b) in THF 59

Figure 2.41 – Infrared spectrum of [Re(bpy)(CO)$_3$(3–Pic)][PF$_6$] (R3–a) in THF 60

Figure 2.42 – ORTEP diagrams of [Re(BMCbpy)(CO)$_3$(CH$_3$CN)][PF$_6$] (R2–b) (top left), [Re(bpy)(CO)$_3$(3–Pic)][PF$_6$] (R3–a) (top right) and [Re(BMCbpy)(CO)$_3$(OPOF$_2$)] (R5) (bottom) with thermal ellipsoids shown at 50% probability. Hydrogen atoms are omitted for clarity 63

Figure 2.43 – Crystal unit cell of [Re(BMCbpy)(CO)$_3$(OPOF$_2$)] (R5). View along the *c* axis. Symmetry elements of the P2$_1$/c space group represented as green lines (two–fold screw axes), pink lines (glide planes) and yellow spots (inversion centers). 64

Figure 2.44 – Superimposition of [Re(BMCbpy)(CO)$_3$(CH$_3$CN)][PF$_6$] (R2–b) and [Re(BMCbpy)(CO)$_3$(OPOF$_2$)] (R5) structures. In both cases, rhenium center and oxygen atoms of the carbonyl ligands were fixed at the same positions, to illustrate the differences on the BMCbpy moiety. 66

Figure 3.1 – Cyclic voltammogram of ZnTPP (P1) with added ferrocene. CH$_2$Cl$_2$ 2.5 mM ZnTPP, 0.1 M TBAPF$_6$, 0.8 mM Fc, scan rate 50 mV/s 68

Figure 3.2 – Cyclic voltammogram of ZnTTP (P2) in the presence of ferrocene. CH$_2$Cl$_2$ 2.5 mM ZnTTP, 0.1 M TBAPF$_6$, 0.8 mM Fc, scan rate 50 mV/s 69

Figure 3.3 – Cyclic voltammograms of ZnTTBPP (P3) in the presence of ferrocene. CH$_2$Cl$_2$ 2.5 mM ZnTTP, 0.1 M TBAPF$_6$, 0.8 mM Fc at scan rates from 50 to 200 mV/s 70

Figure 3.4 – Cyclic voltammogram of [Re(bpy)(CO)$_3$(3–Pic)][PF$_6$] (R3–a). CH$_2$Cl$_2$ 2.5 mM Re complex, 0.1 M TBAPF$_6$, 0.8 mM Fc, scan rate 50 mV/s 71

Figure 3.5 – Cyclic voltammograms of [Re(BMCbpy)(CO)$_3$(3–Pic)][PF$_6$] (R3–b) (solid line) and R3–a (Figure 3.4, dashed line). CH$_2$Cl$_2$ 2.5 mM Re complex, 0.1 M TBAPF$_6$, 0.8 mM Fc 72

Figure 3.6 – Cyclic voltammograms of [Re(BMCbpy)(CO)$_3$(CH$_3$CN)][PF$_6$] (R2–b) at different scan rates. CH$_2$Cl$_2$ 2.5 mM Re complex, 0.1 M TBAPF$_6$, 0.8 mM Fc..... 73

Figure 3.7 – Cyclic voltammograms of [Re(bpy)(CO)$_3$(CH$_3$CN)][PF$_6$] (R2–a) at different scan rates. CH$_2$Cl$_2$ 2.5 mM Re complex, 0.1 M TBAPF$_6$, 0.8 mM Fc..... 74

Figure 4.1 – Frontier molecular orbitals of metalloporphyrins (A) and representation of their electronic states (B)[87]..... 77

Figure 4.2 – UV–Visible absorption spectrum of ZnTPP (P1) in CH$_2$Cl$_2$ recorded at room temperature. Left part 0.5 μM, right part 12.5 μM. Numbers in parentheses indicate initial and final vibrational states, corresponding to the ground and excited electronic states respectively. 78

Figure 4.3 – Emission spectrum of ZnTPP (P1) in CH2Cl2 solution at 298 K. Excitation wavelength 548 nm..... 80

Figure 5.1 – Carbon monoxide formation profile for all ZnTPP (P1):Re complex combinations..... 84

Figure 5.2 – CO formation profile with time for the four ZnTTBPP (P3):Re complex mixtures..... 85

Figure 5.3 – CO formation profile with time for the different ZnTMPP (P4):Re complex mixtures..... 85

Figure 5.4 – CO formation profile with time for the combinations between the four porphyrins and [Re(bpy)(CO)$_3$(CH$_3$CN)][PF$_6$] (R2–a) 86

Figure 5.5 – CO formation profile with time for the combinations between the four porphyrins and [Re(bpy)(CO)$_3$(3–Pic)][PF$_6$] (R3–a)..... 87

Figure 5.6 – Typical catalytic CO formation profile. Graphical definition of parameters TON and t_{TON} is indicated..... 88

Figure 5.7 – Carbon monoxide maximum turnover number *vs*. photoinduced electron transfer driving force plot 90

Figure 5.8 – Representation of the time to reach TON_{max} *vs*. PET driving force. Only those mixtures with significant catalytic activity are represented..... 92

Figure 5.9 – Representation of carbon monoxide turnover number *vs*. time to reach TON_{max}. Straight line is shown to illustrate its linear character for most complexes..... 93

Figure 5.10 – CO formation profile for the porphyrin combinations with [Re(bpy)(CO)$_3${P(OEt)$_3$}][PF$_6$] (R4–a). The existence of an induction period can be observed in all four cases. 94

Figure 5.11 – Porphyrin and chlorin absorbance profiles for the ZnTTP (P2):[Re(bpy)(CO)$_3$(3–Pic)][PF$_6$] (R3–a) mixture during irradiation 95

Figure 5.12 – Porphyrin and chlorin absorbance profiles variation for the ZnTTP (P2):[Re(bpy)(CO)$_3${P(OEt)$_3$}][PF$_6$] (R4–a) mixture 95

Figure 5.13 – Porphyrin and chlorin absorbance profiles for the ZnTTP (P2):[Re(bpy)(CO)$_3$(3–Pic)][PF$_6$] (R3–a) mixture during irradiation and CO formation 96

Figure 5.14 – Carbon monoxide formation and porphyrin and chlorin absorbance profiles variation for the ZnTTP (P2):[Re(bpy)(CO)$_3${P(OEt)$_3$}][PF$_6$] (R4–a) mixture 97

Figure 5.15 – CO formation and porphyrin / chlorin absorbance profiles variation for the ZnTTP (P2):[Re(bpy)(CO)$_3$(CH$_3$CN)][PF$_6$] (R2–a) mixture. Initial overproduction of carbon monoxide can be spotted during the first hour 98

Figure 5.16 – Carbon monoxide formation and absorbance profiles of the mixture ZnTTP (P2):[Re(BMCbpy)(CO)$_3$(CH$_3$CN)][PF$_6$] (R2–b) 98

Figure 5.17 – Electron transfer from excited porphyrin (A) or chlorin (B) to the rhenium complexes. (a) electron transfer, (b) charge recombination, (c) sacrificial electron donor "quenching", (d) backelectron transfer (without charge recombination) 100

Figure 5.18 – Representation of the region and the linear regression employed to determine porphyrin absorbance decay rates as the absolute value of the slope of the straight line shown 101

Figure 5.19 – Porphyrin normalized decay rates *vs.* PET driving force plot. Points labeling according to Table 5.2 102

List of Tables

Table 1.1 – CO_2 reduction potential for the preparation of different products[5] 3

Table 2.1 – ^{1}H chemical shifts of the bipyridine rings protons (in ppm) of bpy, BMCbpy and rhenium complexes prepared in this work. Values are shown for $CDCl_3$ (plain text) or acetone–d_6 (values in brackets). *Note the sequence inversion. 52

Table 2.2 – Symmetry and expected IR active modes for the Re complexes prepared in this work. Note that the intensities of the ν_{CO} bands should all be approximately equal for a *fac*—$M(CO)_3$ unit 55

Table 2.3 – Infrared CO stretching frequencies (in cm^{-1}) of the rhenium complexes prepared in this work. Compounds are classified by apparent symmetry around the metal center. †The mean of the two minima observed for R3–a is employed.....61

Table 2.4 – Selected bond lengths (A — B / Å) and angles (A – B – C / deg) for compounds R3–a, R2–b and R5. Values in brackets represent absolute standard deviation and *X* denotes the heteroatom directly bonded to the rhenium center. For carbon atoms notation see Figure 2.2 on page 28. 65

Table 3.1 – Halfwave potentials of first (P^0/P^+) and second (P^+/P^{2+}) oxidations of the porphyrins studied. Experimental conditions: CH_2Cl_2, 2.5 mM Porphyrin, 0.1 M $TBAPF_6$, 0.8 mM Fc 70

Table 3.2 – First reduction potentials of the rhenium complexes employed in this work. Experimental conditions: CH_2Cl_2, 2.5 mM Re complex, 0.1 M $TBAPF_6$, 0.8 mM Fc. †All complexes are cationic with PF_6^- as counterion except R1–a,b, which are neutral. Values corresponding to *3:2 THF:CH_3CN, ‡CH_3CN or §1:3 MeOH:CH_3CN solutions 75

Table 4.1 – UV–Visible absorption data in CH_2Cl_2 solution of the zinc(II)–porphyrins employed in this work. Maximum absorption wavelengths are expressed in nm and molar extinction coefficients are shown between parentheses in 10^4 $dm^3 \cdot mol^{-1} \cdot cm^{-1}$ 79

Table 4.2 – Fluorescent emission data of the Zn(II)–porphyrins used in this work in CH_2Cl_2 at room temperature (298 K). Values of the energy difference between electronic states (E_{00}) are also listed. Maximum wavelengths are shown in nm 80

Table 4.3 – Driving forces for the different porphyrin–rhenium complexes combinations, expressed in eV, corresponding to the electron transfer from the first electronic excited state of the porphyrin to the ground state of the rhenium complex 81

Table 5.1 – Catalytic parameters of the mixtures between zinc(II)–porphyrins and rhenium tricarbonyl complexes. Entries are referred to TON, t_{TON} in h and TOF in h^{-1} from top to bottom respectively 88

Table 5.2 – Labeling scheme employed for the different catalytic mixtures. It should be noticed that R1–b:P3 and P4 mixtures could not be tested because of time limitations 89

List of Schemes

Scheme 1.1 – Carbon dioxide photocatalytic cycle proposed by Ishitani and coworkers[12] 9

Scheme 2.1 – Synthesis of H_2TTBPP using the Adler–Longo method.....24

Scheme 2.2 – Rhenium acetonitrile complex preparation route. R = H, CO_2Me 25

Scheme 2.3 – Acetonitrile ligand substitution reaction scheme. R = H, CO_2Me.....25

List of Equations

Equation 1.1 – Relationship between electron transfer activation energy and reaction parameters 19

Equation 1.2 – Photoinduced electron transfer (PET) driving force calculation[45].....21

Acknowledgements

I would like to thank first my supervisor, Prof. Robin Perutz for giving me the opportunity to work in his group, for his uncountable hours of stimulating planning and discussion, for leaving and even encouraging me to try what I though was best and, over all, for opening my mind in and out of the lab and his endless patience.

Thanks to my independent panel member, Dr. Richard Douthwaite, for his constant availability, interest and helpful discussion and advices.

Special thanks to the responsible of the department facilities, for their dedication and advices, Heather Fish (NMR spectroscopy), Karl Heaton (Mass Spectrometry), Dr. Graeme McAllister (Elemental analysis), and Dr. Adrian Whitwood (X–ray crystallography). Special mention to Steve Hau and Mike Keogh, from the department stores, to the glass and mechanical workshop teams, for their dedication during all the year and especially after the move, and many other services, like graduate office, porters or IT services.

Thanks to all RNP group, past and present, for offering me so many different points of view and constructive criticism, especially during group meetings. Particular thanks to Dr. Barbara Procacci (Barby), for X–ray structure determination and discussion, introducing me in the wonderful world of crystals, and Dr. Naser Jasim, for his basal work in the group, dealing with our constant requests and, as many others, for his patience. I feel obliged to remember those *great* hours fixing the printer and/or the computers on a daily basis.

I cannot avoid dedicating a separated paragraph to Chris Windle, which happened to be my student mentor and complete the CO_2 reduction team (actually the two of us) and I did not mention until here to speak in a more informal way. He just could have never done a better job. Thank you for the initial tours around the department and for repeating me everything a thousand times, with those “Sorry Chris but, I don’t remember where (whatever) is/are” until I adapted myself to the lab. Apart from that, I keep uncountable hours of help, advices and results

discussion, but also music, laughs, Spanish and Italian lessons or English pronunciation sessions. Thank you very much for everything.

There is not enough space to properly thank all the people, chemists or not, which have supported me during these twelve months of adventure, you all are some of the greatest people I will ever meet. Just to mention Olga, who helped me from the very first e–mail and phone call, Javi, Eva, Fuchu, Pedro and Alejandro, which showed me the best places to eat at the beginning of this journey, and then those who came later and shared so many good times, Fran, Patricia, Sara, Blanca and Akihiro. I hope we can keep what we got and made us so unique, you made more for me during this year than what you could really believe.

Thanks to Estela, who I met right at the end but was a vital pillar in the final stretch until the very last day, working in the lab on that Saturday two days before flying back home, with all the bags still to be done and as stressed as I was at that time. Thank you for those great moments and all you support.

And almost at the end, because she deserves it, Jessica, my favorite adoptive Andalucian neighbor. We started working almost at the same time and I still ignore who was more lost by then. We have lived so many things in there that there is nothing else I can tell you right now. Many thanks for being so authentic and especially for shouting at me from time to time, I cannot imagine how sad this year would have been without you.

Finally, thanks to the complete nucleus back in Spain, which made miracles from home through Skype quite a few times, when I needed it more, and also let me fly away to pursue my wish.

I would also like to thank my sponsor Caja Madrid Foundation for funding, giving me the opportunity to live this experience.

Thank you all.

Author's Declaration

With the exceptions cited below, all the research presented in this thesis was carried out by the author and originally designed by either himself or his supervisor.

Electron transfer mechanisms shown on Figure 5.17 were initially co-proposed by the author and Christopher D. Windle.

Elemental analyses were carried out by Dr. Graeme McAllister, mass spectra were measured by Dr. Karl Heaton and X-ray diffraction experiments were performed by Dr. Adrian Whitwood and Dr. Barbara Procacci (measurement and structure solution and refinement). Dr. Procacci also assisted significantly on X-ray structures analysis and discussion.

By the date of the final submission, no part of this thesis was published as a part of a scientific paper of any kind.

Chapter 1. Introduction

1.1 General considerations

During the last years, carbon dioxide emissions from natural and anthropogenic sources, have been above the natural uptake rates, rising to an increase around 40% in the concentration of CO_2 in the atmosphere, from 270 ppm in the pre–industrial era to 380 ppm nowadays.[1] One of the most important sources of carbon dioxide is the combustion of fossil fuels, so the possibility of converting it into high–energy substances suitable for their use as fuels is a double approach to reduce the impact of carbon dioxide in the atmosphere. Recovering CO_2 from waste streams and converting it into fuels would lead to a more balanced situation where the atmospheric carbon dioxide could be extensively used, reducing its concentration, and also decreasing the consumption of natural fossil fuels, substituted by those generated from carbon dioxide. This strategy is especially interesting when sunlight is used as the primary energy source, converting CO_2 using photocatalytic systems.

Although much work has been carried out concerning CO_2 reduction and some goals have been achieved, the global efficiency of the direct solar conversion of carbon dioxide into fuels must be still improved.[2] A slightly different approach is the use of carbon dioxide as a chemical feedstock,[1] so useful carbon–based substances can be prepared from it, without the need of going so far in the chemical process of obtaining fuels. Carbon monoxide is presented as an interesting alternative product, since it can be converted into fuels reacting with hydrogen in the well–known Fischer–Tropsch process or in many other chemicals through different pathways[3,4] as shown in Figure 1.1.

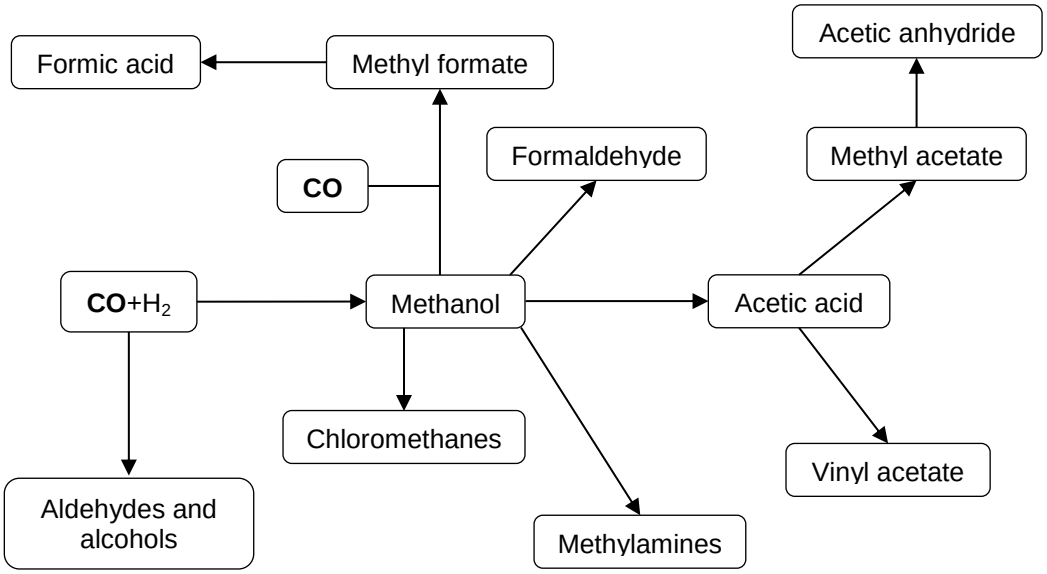

Figure 1.1 – Commercial chemicals obtainable from CO and hydrogen[4]

Direct one–electron reduction of carbon dioxide is extremely unfavored from a thermodynamic point of view, with a reduction potential of –1.9 V (*vs.* Normal Hydrogen Electrode, NHE). Alternatively, multiple reductions coupled with proton incorporation presents more achievable potentials, as shown on Table 1.1. As can be observed, formation of elemental carbon, methane or methanol requires significantly lower reduction potentials, so they could be considered as suitable routes; nevertheless, electron transfer reactions in nature occur in almost all cases one by one, and four, six or eight electrons reductions, coupled with integration of an identical number of protons, always lead to an enormous number of byproducts, impurities and a very low global efficiency, so the direct reduction approach must be essentially abandoned in favor of catalyzed processes.

Reaction	***E*° / V**
$CO_2 + 2\ H^+ + 2\ e^- \rightarrow HCO_2H$	– 0.61
$CO_2 + 2\ H^+ + 2\ e^- \rightarrow CO + H_2O$	– 0.53
$CO_2 + 4\ H^+ + 4\ e^- \rightarrow C + 2\ H_2O$	– 0.20
$CO_2 + 4\ H^+ + 4\ e^- \rightarrow HCHO + H_2O$	– 0.48
$CO_2 + 6\ H^+ + 6\ e^- \rightarrow CH_3OH + H_2O$	– 0.38
$CO_2 + 8\ H^+ + 8\ e^- \rightarrow CH_4 + 2\ H_2O$	– 0.24

Table 1.1 – CO_2 reduction potential for the preparation of different products[5]

Photocatalytic conversion of carbon dioxide into CO with molecular catalysts[6] has been widely investigated since Lehn and coworkers described the ability of the rhenium(I) complex $Re(bpy)(CO)_3Cl$ to perform the transformation of CO_2 into CO and H_2 under UV irradiation in acetonitrile/water/TEA[7] or selectively to carbon monoxide when DMF/TEOA was used, with a quantum yield of 0.14 in the latter case.[8] In both cases, the presence of a sacrificial electron donor like triethylamine (TEA) or triethanolamine (TEOA) was always needed. Small insights into the catalytic mechanism were achieved at that time, showing that addition of an excess of the anionic ligand translated into higher CO production yields, whereas extra amounts of 2,2'–bipyridine did not have any significant effect on the catalytic production. When isotopically labeled $^{13}CO_2$ was employed, the heavier isotopes were found in the carbon monoxide formed, as well as on the formate produced and the carbonyl ligand bonded on the rhenium center. This structure has been modified in further studies and present the standard model of many photocatalysts developed afterwards (Figure 1.2).

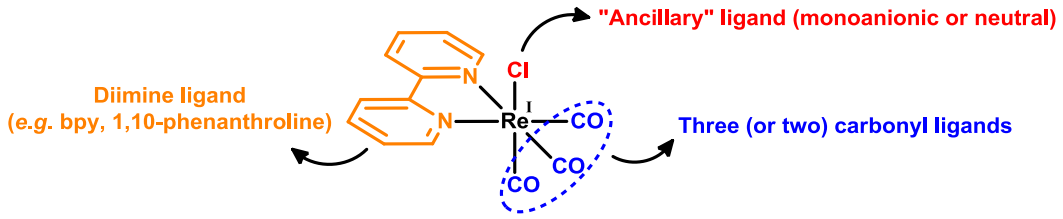

Figure 1.2 – Chemical structure of the original catalyst by Lehn and coworkers. Different parts of the catalysts modified in further studies are highlighted

Many alternative systems with other metals have also been proposed since then, including cobalt or nickel macrocycle complexes and or ruthenium bipyridine carbonyl photocatalysts (Figure 1.3).[5] Due to the extension and unrelated behavior of the rhenium based systems, these different approaches will not be described in detail and only mentioned in some cases.

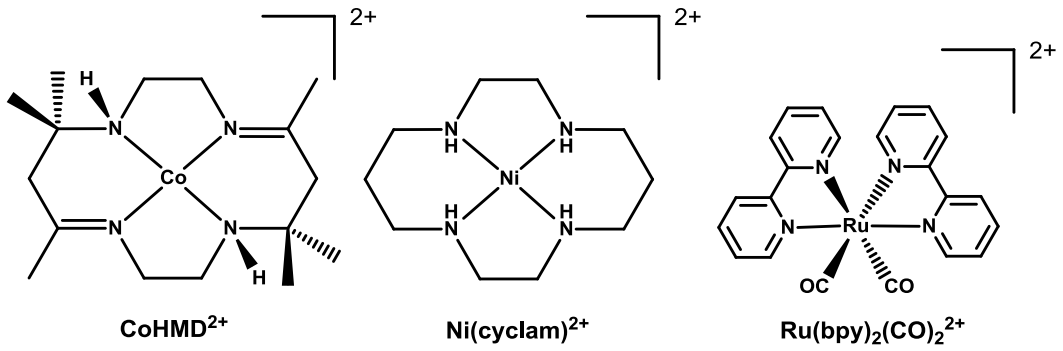

Figure 1.3 – Representative photocatalysts based on metals different from rhenium

Focusing on rhenium(I)–based photocatalytic systems, the field is clearly dominated by rhenium diimine (essentially bipyridine or phenanthroline) tricarbonyl complexes. These structures, which also include the original catalyst employed by Lehn and coworkers, show an extremely high selectivity towards carbon monoxide formation, and no detectable hydrogen or formate, common byproducts for other photocatalysts, have been detected for any derivative when photoreduction was carried out in the standard 5:1 DMF:TEOA solution. In addition, these systems present an enormous chemical variability, being susceptible to substitution on the diimine rings or by including different anionic or neutral ligands on the sixth rhenium coordination position as shown above (Figure 1.2). Some of the most significant advances in this approach have been recently reviewed by Takeda and Ishitani,[9] as well as photochemistry and photocatalysis of

rhenium(I) diimine complexes.[10] The most remarkable advances in mononuclear rhenium complexes are treated next and visible–light sensitized systems are treated separately later, in Section 1.3 (page 11).

As a reference for comparison purposes we reiterate the 0.14 quantum yield of original Lehn's catalyst (in 5:1 DMF:TEOA). The nature of the monodentate ligand drastically changes the catalytic ability of the rhenium complex; in this way, other neutral complexes of formula $Re(bpy)(CO)_3X$ where X is monoanionic, gave very different quantum yields such as 0.05 when X = formate,[11] 0.30 when X = NCS^- or even no catalysis when cyanide was employed.[12] On the other hand, monocationic complexes obtained by using neutral ligands also presented a rich variability, with very low yields (0.03–0.05) for triphenylphosphine, pyridine or acetonitrile derivatives[10] but also better yields, up to 0.38 for the triethylphosphite analogue.[13] Substitution on the bipyridine ring 4 and 4' positions also lead to modification of the catalytic properties. In this way, inclusion of methoxy electron donating groups caused almost no change in the catalytic yield observed, whereas inclusion of electron withdrawing trifluoromethyl substituents decreased it to almost zero.[14] Due to the limited number of compounds studied and the dissimilar results obtained for almost each one of them, no reliable conclusions can be extracted, apart from the obvious influence of both ligands on the catalytic properties. Combining two of these rhenium complexes (a labile acetonitrile compound and the efficient phosphite derivative with electron donating groups) according to the mechanistic findings, (see Section 1.2 on page 9) a very efficient mixture with a quantum yield of 0.59 was developed.[12]

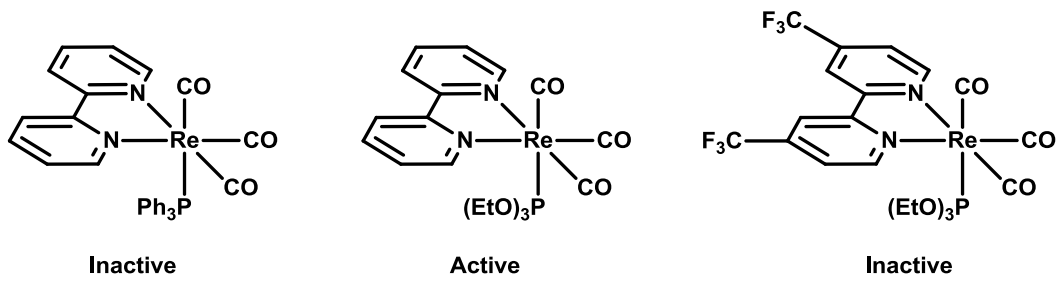

Figure 1.4 – Selected structures of some tricarbonyl complexes studied by Ishitani and coworkers. Photoatalytic activity is qualitatively indicated

Rhenium complexes with two "secondary" phosphorus–based ligands and two carbonyl groups have also been tested, showing completely different results, with the triethylphosphite derivative completely inactive[15] whereas the one with two triphenylphosphine was an extremely good catalyst, working even in the presence of electron withdrawing groups on phenyl rings of the phosphine, showing the high complexity and non–systematic behavior of these systems[16] as cited afterwards.[10]

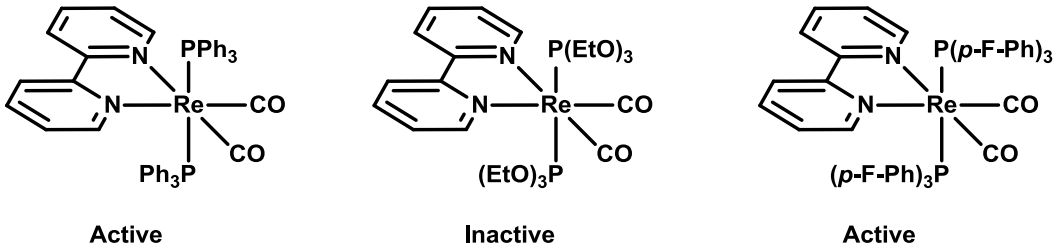

Figure 1.5 – Rhenium dicarbonyl complexes employed for CO_2 reduction. Carbon dioxide photoreduction ability is also indicated

Apart from the rhenium based catalysts cited above and the photosensitized systems that will be described later, many other and more complex alternatives for CO_2 reductions have been made. In order to give a general overview of the current situation, some representative examples from 2000 until now are listed.

Park and coworkers showed activation of Lehn's original catalyst when encapsulated in mesoporous molecular sieves, which acted as supramolecular heterogeneous host, although no quantification of CO was made.[17,18]

Conjugation of a rhenium–phenanthroline complex with a tungsten–based polyoxometalate produced a supramolecular complex capable of reducing carbon dioxide to CO with hydrogen as reducing agent, instead of using sacrificial electron donors like TEOA, producing 22 carbon monoxide turnovers.[19]

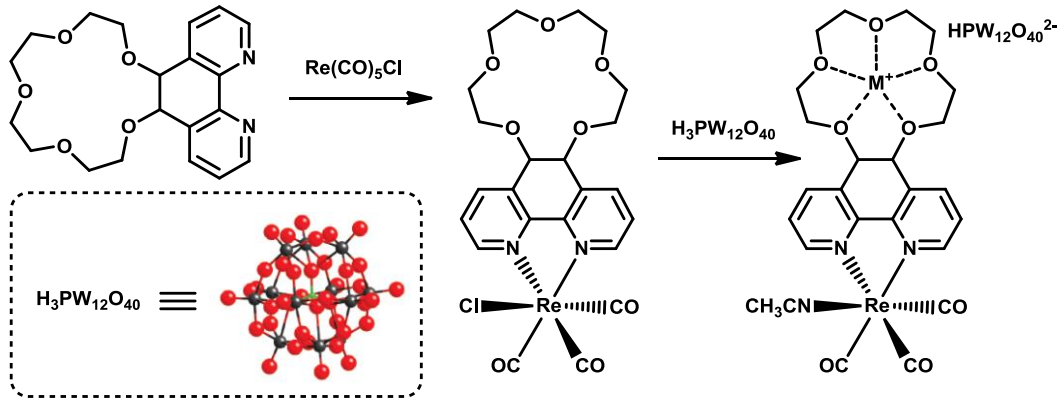

Figure 1.6 – Polyoxometalate–Re(I) supramolecular photocatalyst. Structure of the polyoxometalate is shown on the left. Oxygen (red), tungsten (black), phosphorus (green)[19]

A multicomponent metal–organic framework doped with Re catalysts capable of carrying out CO_2 reduction with low yield (10 turnovers) was developed in 2011. Inclusion of Ir and Ru complexes produced alternative MOFs with water oxidation properties or organophotocatalytic abilities,[20] showing the potential behind this approach by inclusion of more efficient or alternative catalytic centers. Alternatively, simultaneous inclusion of sensitizer and catalyst molecules could lead to an efficient supramolecular system with a rigid and stable backbone.

One of the most recent stages in catalyst development is the formation of hybrid molecular–enzymatic systems, which mimic photosynthesis, like the graphene based supramolecular photocatalyst with formate dehydrogenase, which employed the nucleotide NADH as intermediate redox agent and TEOA as sacrificial electron donor (Figure 1.7). In this case also high catalytic yields were found.[21]

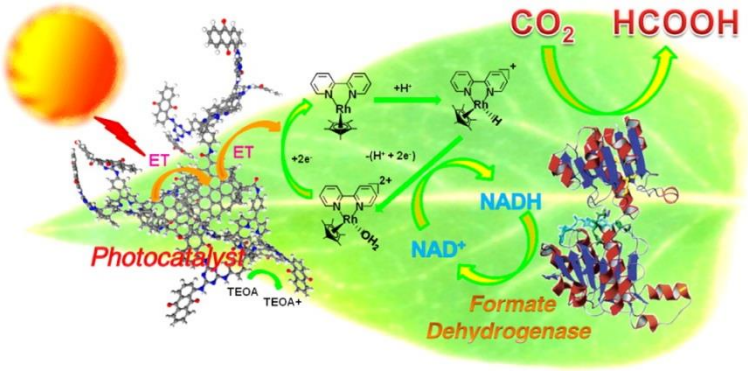

Figure 1.7 – Pictorial illustration of the supramolecular enzyme–based photoreducing system prepared by Biswas and coworkers[21]

As has been shown, research in this field is extremely varied and more and more sophisticated systems are appearing during the last years. However, a deeper understanding of the mechanistic basis of this catalysis, which is discussed in Section 1.2 (page 9), and the relationships between catalyst molecular structure and the obtained yields is necessary to allow the rational design of efficient systems.

Although electrocatalytic methods have also attracted much effort, this field falls out of the scope of this Thesis and will not be covered. Some of the most relevant results have been recently reviewed by Kubiak[22] and the first cell capable to reduce CO_2 to formate, coupled to water oxidation without application of any external bias has been recently reported.[23] This last finding is mentioned since it is the only system capable of working without sacrificial amine or external bias developed so far.

As pointed out in a recent review,[24] the use of these sacrificial electron donors and the poor absorbance of the rhenium complexes in the visible region are two of the main handicaps of these systems. The electrocatalytic coupled system mentioned above described by Sato and coworkers[23] in which water acts as electron donor has been the only significant improvement regarding elimination of the tertiary amine from the reaction mixture. On the other hand, one of the most exploited approaches in order to improve the light harvesting of the process is the use of photosensitizers, capable of absorbing light inside the visible region and promoting an electron transfer to the catalyst (see Section 1.3 on page 11).

1.2 CO_2 Reduction mechanism

Even if many aspects of the mechanism have been clarified, the detailed reaction pathway of this catalytic reaction remains essentially unknown. Although many efforts have been made in this field in the last years, only partial findings have arisen. By means of studying three neutral $Re(bpy)(CO)_3L$ derivatives with L = Cl^-, NCS^- and CN^-, Ishitani and coworkers suggested a plausible partial mechanism, compatible with the data they obtained.[12] According to it, the so–called one–electron–reduced (OER) species plays a vital role in the catalysis, being responsible for both binding carbon dioxide and donating the second electron necessary to carry out its reduction to carbon monoxide. In this sense, high ligand dissociation rates and long OER species lifetimes become necessary in order to obtain effective catalysts. A schematic representation of the mechanistic proposal is shown on Scheme 1.1.

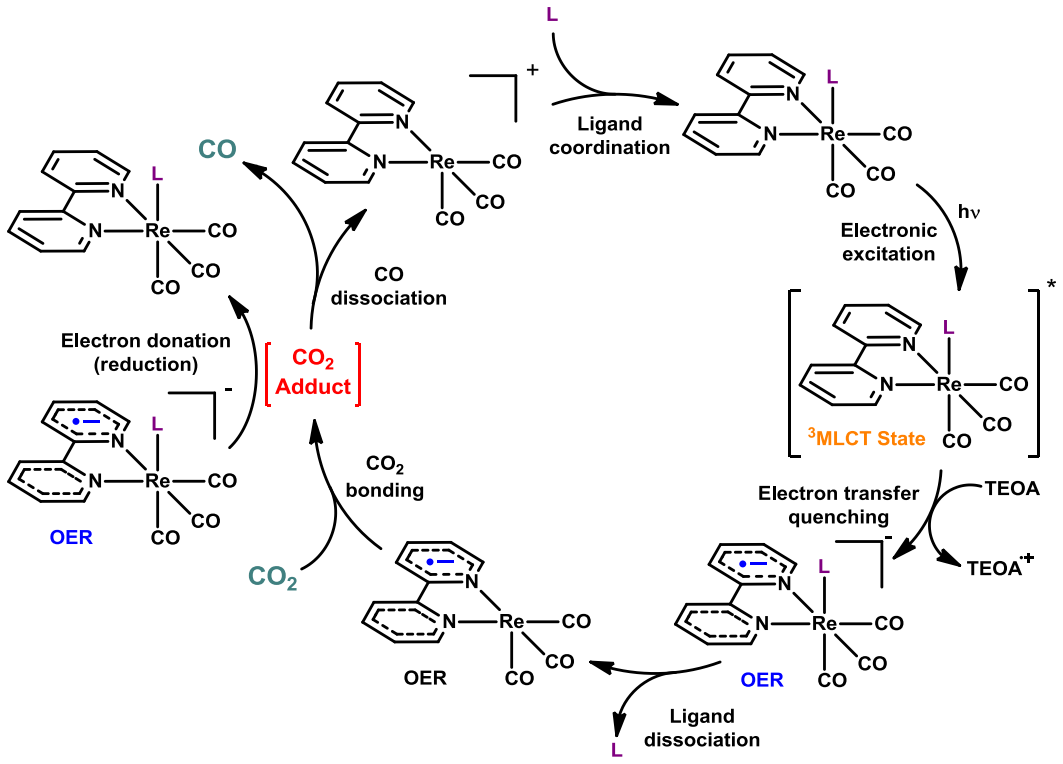

Scheme 1.1 – Carbon dioxide photocatalytic cycle proposed by Ishitani and coworkers[12]

The cycle is initiated with the excitation of a parent rhenium complex with a UV photon to form an excited triplet metal–to–ligand charge transfer state (^{3}MLCT), which is quenched by the sacrificial electron donor forming the OER species. Afterwards, the anionic ligand is dissociated and the unsaturated product somehow binds CO_2 to form an adduct. A second OER species would reduce that complex and one of the four carbon monoxide ligands would dissociate leaving the unsaturated monocationic complex, which would readily coordinate again a ligand completing the catalytic cycle. Despite this proposal, only three different complexes were taken into account during that study, the so–called CO_2 adduct was not detected and no information about it or the missing oxygen atom was given by the authors, so it may be consistent with experimental findings but it is only partial. Later, a theoretical proposal based on DFT calculations suggested the formation and subsequent rearrangement of a bridged carbonate dimer (Figure 1.8).[25] This intermediate and the corresponding pathway agreed with all experimental data obtained so far, including reaction kinetics, isotopic labeling and product identification.[26]

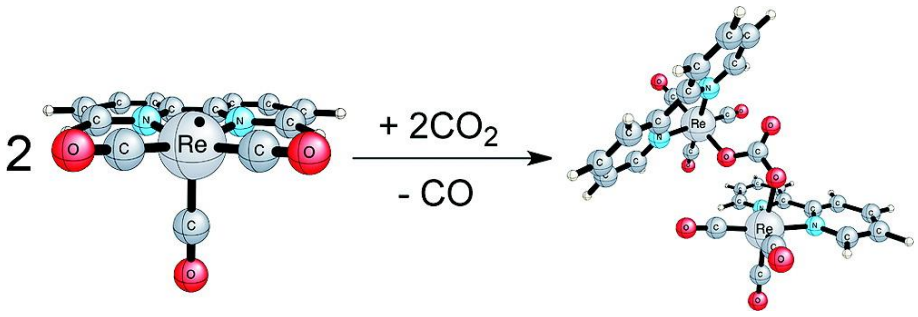

Figure 1.8 – Binuclear CO_2 intermediate structure and formation proposal[26]

1.3 Rhenium–based sensitized systems

In order to avoid the use of ultraviolet light and attempting to produce a more sustainable set of systems from an environmental point of view, different approaches trying to used visible light photosensitizers have been made, so after excitation of the sensitizer with a less energetic (visible) photon, electron transfer to the catalysts yielded the OER species and catalytic cycle is expected to operate as under direct UV irradiation.

One of the most extensively used group of sensitizers are ruthenium bipyridine complexes, covalently attached to the rhenium moiety through different spacers[27–30] or mixed in a two–components solution with an extensive range of catalysts.

Comparison between conjugated and saturated bridges (Figure 1.9) surprisingly showed that higher yields were obtained with the reduced derivative,[27] showing that electron transfer does not takes place through the bridge but through space, preferring the greater flexibility of the saturated system compared with the unsaturated bridge derivative.

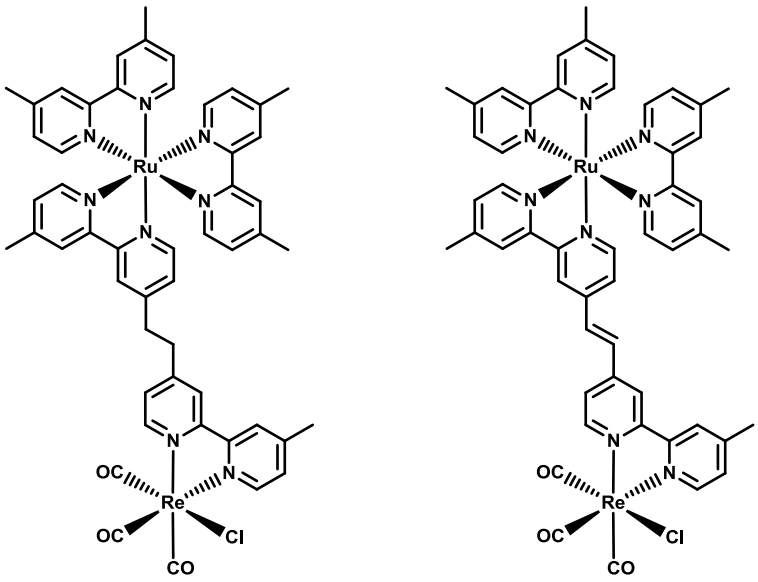

Figure 1.9 – Ruthenium–rhenium conjugate photocatalysts with saturated (left) and conjugated (right) bridging ligand[27]

Alternatively, when saturated spacers with different lengths (2, 4 or 6 carbon atoms) were tried, the most active was the one with only two carbon atoms,[29] although it was found that electronic interaction between the two subunits took place even on the ground state. From the other compounds tested, variation from 4 to 6 atoms did not change the catalytic efficiency and an additional derivative with a 2–hydroxyprop–1,3–diyl bridge (3 C atoms) was slightly more effective than the other two,[30] showing that a minimum level of molecular flexibility is required but no improvement is obtained when increasing the separation between sensitizer and catalyst. Catalytic yields for these systems vary between 100 and 240 turnovers, which can be considered as a moderate–to–high interval of the results typically obtained in these cases.

Studies in which three catalytic centers were attached to one sensitizing units gave better yields than 1:1 dyads with several substituents on the ruthenium photosensitizing unit or phenanthroline modified derivatives.[28] This was attributed to a more effective electron transfer from the OER species of the photosensitizing section to any of the three available catalytic centers. This is the best rhenium–based homogeneous photocatalyst for CO_2 reduction to carbon monoxide reported so far, with a turnover number of 250.

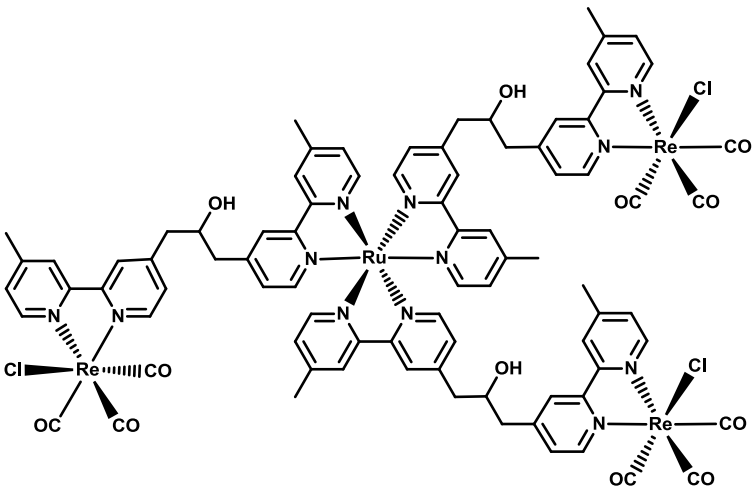

Figure 1.10 – Supramolecular photocatalyst based on a photosensitizing ruthenium core with three attached rhenium catalytic centers[28]

Ruthenium tris–bipyridine complex has been also extensively employed in diverse multicomponent homo and heterogeneous mixtures. For instance, Lehn and coworkers reported low catalytic yields (around 10 TON_{CO}) for sensitized cobalt complexes with this salt,[31,32] or with nickel cyclam catalyst.[33] In a different approach, reduction of CO_2 to methane has been obtained by using *in situ* formed osmium and ruthenium colloids obtained by salt reduction in the presence of the photosensitizer.[34] In all these cases no selectivity towards CO (or CH_4) was found and considerable amounts of molecular hydrogen were formed, common for non–rhenium–based photocatalysts.

Significantly more sophisticated systems have been also reported, coupling viologen photosensitation and NADPH regeneration with formate dehydrogenase, yielding formate from CO_2 under visible irradiation with quantum yields around 1% or the employment of alternative enzymes to incorporate carbon dioxide by carboxylation of different substrates.[35] In a completely novel approach, Ueno and coworkers anchored both sensitizer and catalyst, by selective chemical functionalization, to cysteine or lysine residues on a β–helix peptidic nanotube, achieving higher yields than those obtained when mixing the separate components in solution.[36]

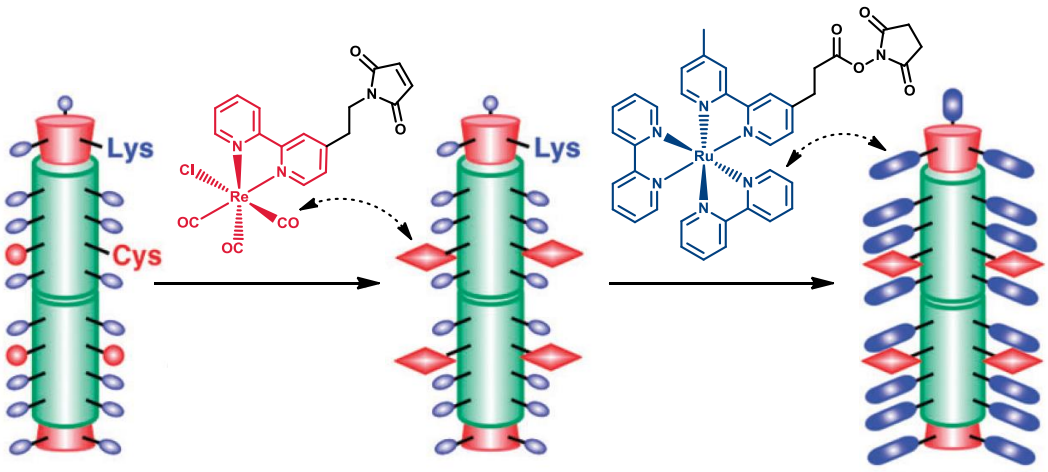

Figure 1.11 – Oligopeptidic heterofunctionalized nanotube for CO_2 reduction[36]

The level of complexity of these systems can be taken even one step further, and a few years ago, Armstrong and coworkers reported a macromolecular multicomponent system which used a modified carbon monoxide dehydrogenase (CODH) supported onto titanium dioxide nanoparticles to effectively produce carbon monoxide when combined with the employment of ruthenium tris–bipyridyl photosensitizer, also attached to the nanoparticle.[37,38]

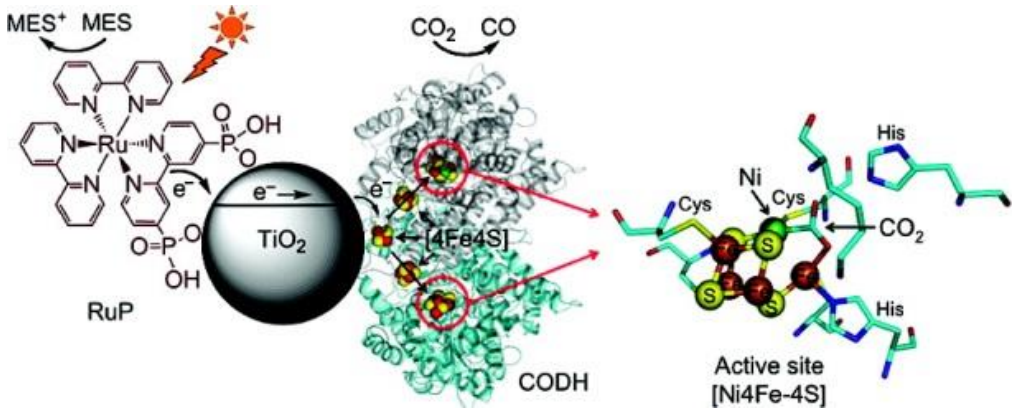

Figure 1.12 – Supramolecular–enzymatic sensitizedsystem for CO_2 reduction[37,38]

The variability of these systems in chemical structure and also physical properties makes this approach more common every year and more complex, fine and effective systems are being reported.

1.4 Previous work in our group

Porphyrins and metalloporphyrins represent another extensively used family of photosensitizers due to their great light absorption capability, and they have been employed in our research group for that purpose for the last years. Photophysics and photochemistry of porphyrins with appended rhenium and tungsten centers have been studied in here.[39,40] Both components of the dyads showed no interaction in the ground state[41] but were able to promote remote–site photosubstitution processes in the presence of an electron donor when irradiated with visible light.[42] That activation was only detected when a metalloporphyrin was used, whereas the free–base did not exhibit photochemical reactivity.[43]

That revealed the importance of the presence of the metal center to probably interact with the electron donor by direct coordination (with TEOA in our case) in the first stage of the reaction. In the absence of the sacrificial donor, charge–separated states with lifetimes in the order of picoseconds could be detected,[41] showing that the electron transfer between the sensitizer and the complex took place but charge recombination was also very fast. All the facts exposed above showed the availability of these systems to act as visible–light sensitized CO_2 photoreduction platforms, with the sensitizing phenomena coming from the metalloporphyrin section of the molecule (*e.g.* dyad on Figure 1.13).[44,45]

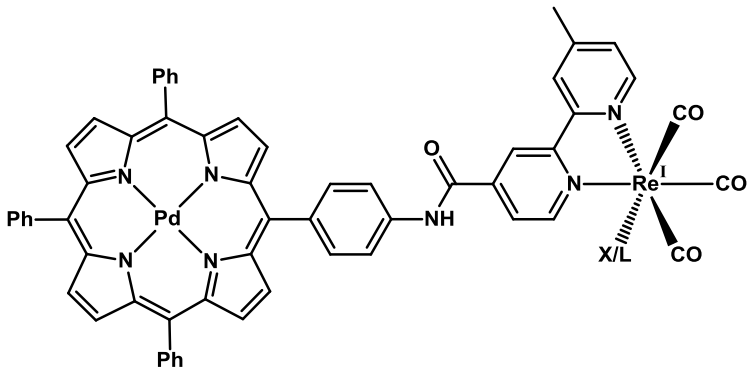

Figure 1.13 – Palladium porphyrin–rhenium dyad employed for CO_2 reduction. X= Br^-, NCS^-; L= 3–Picoline[45]

During the study of the dyad showed in Figure 1.13, the corresponding chlorin, a reduced species of the porphyrin with one of the pyrrolic double bonds saturated, was found to be an intermediate formed during the CO_2 reduction process, with a very characteristic absorption band in the UV–Visible spectrum around 620 nm. As a result of that, the palladium chlorin was prepared and two–component mixtures were studied, yielding comparable results to the dyad in the case of the porphyrin:Re mixture and higher yields when pure chlorin was used. Conversely, when ruthenium tris–bpy was employed, results comparable to the chlorin were obtained.[45]

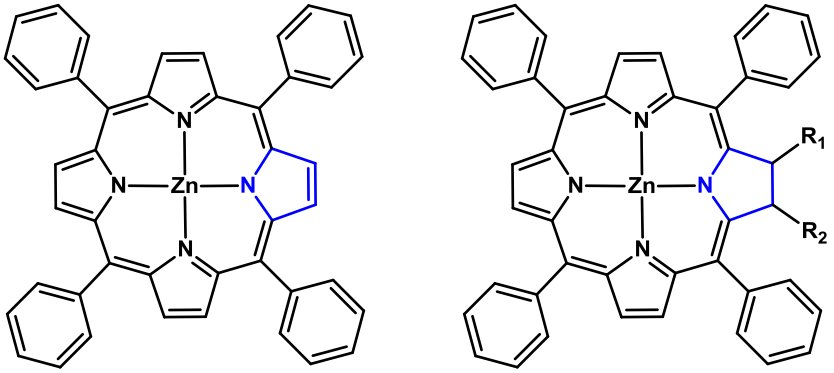

Figure 1.14 – Structural comparison of a parent porphyrin (left) and a generic monoreduced species (chlorin, right) found to form during irradiation

Although the sensitization mechanism is not known, electron transfer from the excited porphyrin, or some derivative product, to the rhenium complex must certainly occur. In the case of the dyads, this electron transfer seems to be intramolecular, whereas bimolecular processes must take place with multicomponent systems. In this way, study of the photophysical and redox properties of electron donor and acceptors in these pairs showed that the highest activity of the chlorin–sensitized mixture could be originated by a higher driving force of the photoinduced electron transfer step, due to the lower oxidation potential of the chlorin compared with the porphyrin. However, recent studies with zinc(II) analogues have shown that this is not true, with chlorin systems being less active than the original one with the parent porphyrin or even the primitive dyad.[46] Bimolecular systems were found to be significantly more effective than supramolecular dyads in that case, with 130 per 30 carbon monoxide turnovers.

1.5 Electron transfer reactions

From the results indicated above, we can say that there are several lines of experimental evidence which suggest that electron transfer from the excited state of the porphyrin to the rhenium complex takes place through the space, as in many other processes. In those cases, Marcus theory of electron transfer reactions may be applied.[47–49] Although there is no room for a complete discussion on electron transfer theory, some useful points of it which allow us to relate driving force and reaction kinetics are shown in this section.

According to his theory, electron transfer reactions consist of five steps, the first and last being the diffusion of the reactants towards or from the original/final complex and the second and third consist of changes in bond lengths, to make the structure more similar to the product, and reorganization of the solvent shell. Finally, the electron transfer step would take place after those two, under suitable conditions.

From all those five steps, only modification of chemical bonds and solvent molecules rearrangement has some energetic cost, so those are the steps to be focused on. These processes are necessary in order to modify the energy surfaces in such a way that isoenergetic electron transfer from reactants to products can take place (Figure 1.15–B), according to the Franck–Condon principle. An schematic example with orbitals corresponding to two generic octahedral d^6 and d^7 metal complexes is shown on Figure 1.15.

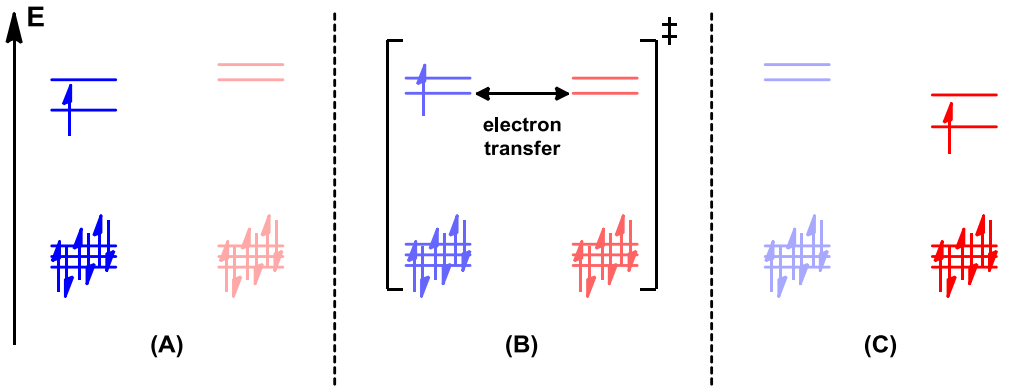

Figure 1.15 – Representation of energy levels modification of reactant (blue) and product (red) with molecular reorganization. Intensity represents progress along the reaction coordinate (electron location). (A) Initial situation, (B) transition state, (C) final products

The reorganization energy (λ) was therefore defined, with contributions from the solvent and the initial complexes. Considering the energy surfaces of the reactant and product along the reaction coordinate (parabolic shapes), it will correspond to the vertical energy difference between the minimum of the first curve (reactant) and the corresponding value of the second curve (product) at that reaction coordinate when both curves are set with their minima at the same value. By using simple geometrical considerations, it was found that the activation energy for going from one curve to the other in self–exchange reactions (both curves at the same height) was one quarter of the value of λ (Figure 1.16).

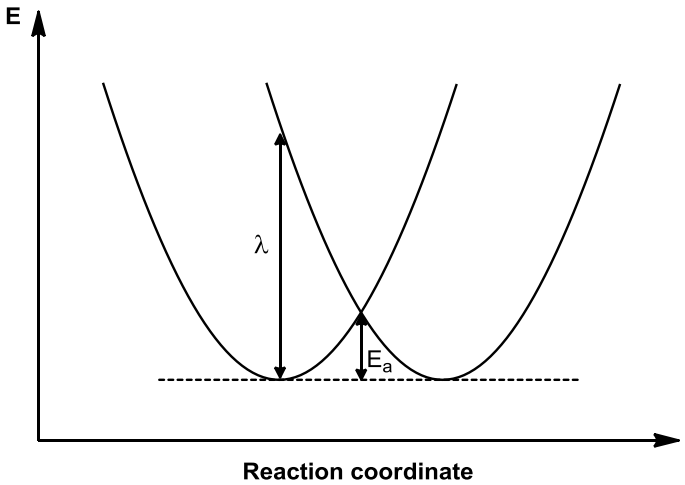

Figure 1.16 – Self–exchange reaction profile. Activation energy $E_a = \lambda/4$

However, the previous treatment and finding are only valid for self–exchange reactions, which are far away from the situations we find with our photocatalytic systems, transferring the electron from the porphyrin to the rhenium complex. Nevertheless, these results can be generalized for the case in which the minima in the potential energy surface of reactants and products are separated by an amount ΔG_0 (Figure 1.17). This amount matches the driving force of the electron transfer step, the free energy difference between reactants and products.

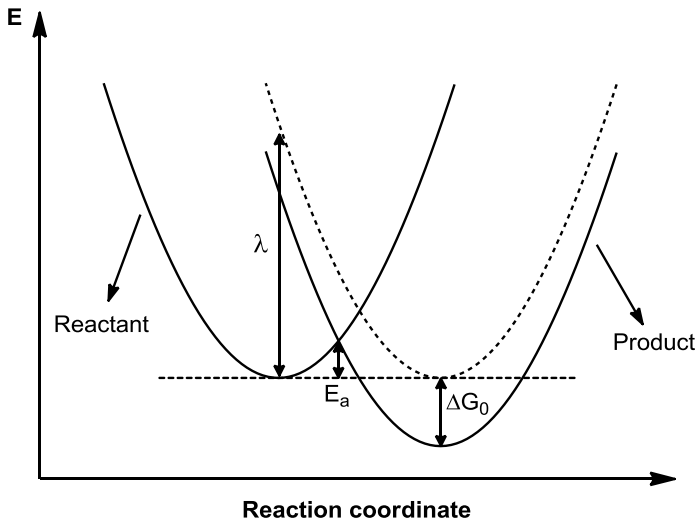

Figure 1.17 – General electron transfer reaction energy profile. Notice that the value of λ does not change with ΔG_0. Dashed line represents the potential energy surface of the product when its minimum is set at the same value as that of the reactant.

In those cases, the value of the activation energy (E_a) depends on both the reorganization energy (λ) and the driving force (ΔG_0), according to Equation 1.1. It can be easily checked that when $\Delta G_0 = 0$ (self–exchange reaction), the right–hand side of Equation 1.1 becomes λ/4 as found before.

$$E_a = \frac{(\Delta G_0 - \lambda)^2}{4\lambda}$$

Equation 1.1 – Relationship between electron transfer activation energy and reaction parameters

With the expression and diagrams showed above, it is possible to discuss the influence of the driving force value on the electron transfer rate, which is related to the activation energy *via* an exponential function of $-E_a/RT$. It can be observed from direct comparison between Figures 1.16 and 1.17 that the activation energy becomes smaller when driving force increases, which agrees with the idea of faster electron transfer for those systems which are more favored from a thermodynamic point of view. However, this situation is only valid when $0 < \Delta G_0 < \lambda$. When $\Delta G_0 = \lambda$, and therefore E_a is very close to zero, electron transfer rate becomes theoretically infinite (actually the process passes to be controlled by diffusion rates of reactants in solution). In addition, when $\Delta G_0 > \lambda$ activation energy increases again, diminishing the kinetics of the reaction; this is known as the Marcus inverted region, in which more thermodynamically favored systems becomes slower when increasing the driving force. These two critical situations are illustrated on Figure 1.18.

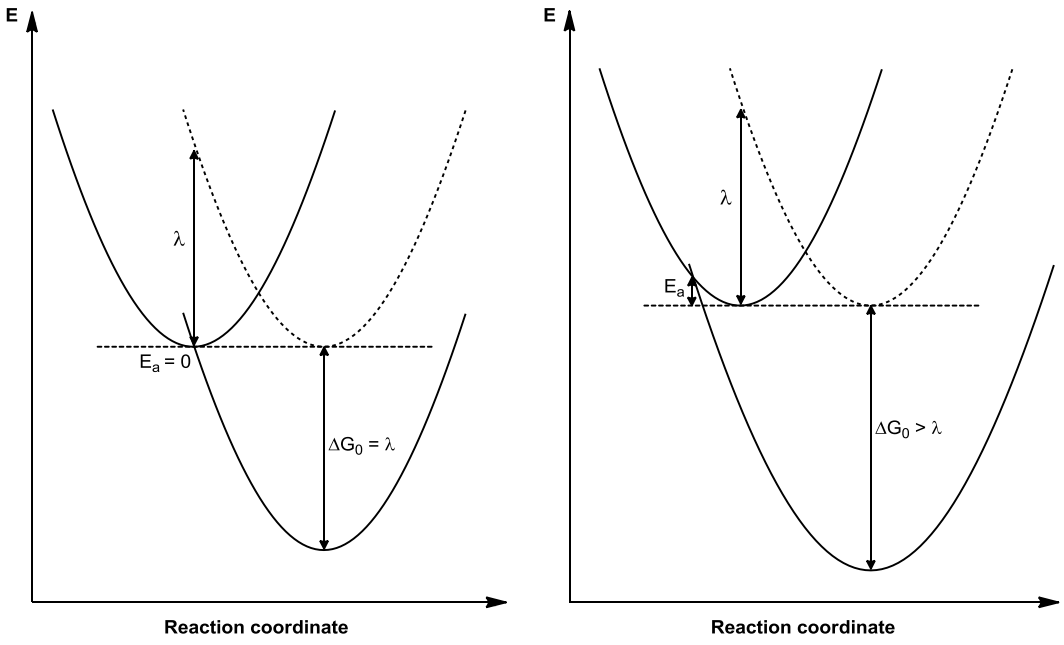

Figure 1.18 – Energy profiles of the extreme situations of zero activation energy (left) and inverse region (right)

We initially assume that our systems fall inside the first region, which behaves in a more intuitive way, since usually very high driving force values are needed to reach any of the other two situations and the trend of the latter systems to generate products on an excited state, which later decays giving rise to chemiluminescence.

The driving force of the photoinduced electron transfer step (ΔG_{PET}, ΔG_0 above) can be estimated from spectroscopic and electrochemical properties of the sensitizer and the catalyst.[45] The calculation requires knowledge of the first reduction potential of the rhenium complex (E_{red}), the first oxidation potential of the porphyrin (E_{ox}) and the energy difference between the lowest vibrational levels of the ground and the first excited electronic states of the porphyrin (E_{00}), usually estimated from the highest energy emission peak in the fluorescence spectrum, preferably measured at low temperature.

$$\Delta G_{PET} = E_{ox} - E_{red} - E_{00}$$

Equation 1.2 – Photoinduced electron transfer (PET) driving force calculation[45]

We will employ the driving force values calculated by means of Equation 1.2 to characterize our porphyrin:rhenium complex mixtures and study their different properties and behavior depending, initially, on the PET driving force.

1.6 Aim of this work

According to the previous work described above, two–component systems are very promising in order to explore new or more efficient CO_2 reduction sensitized platforms, giving even better yields than analogous dyads in some cases.[46]

Due to the long synthetic routes necessary to prepare the dyads and the limited time available, the aim of this project was trying to get some understanding about the energetics of the two–component catalysis. Four zinc–porphyrins and six rhenium complexes (see Figure 1.19), four of them not described before, with different electron donating or withdrawing groups respectively, have been prepared and characterized. The inclusion of electron donating groups on the porphyrin and electron withdrawing groups on the rhenium complexes ligands respond to an attempt to favor the electron transfer step from one component to the other.

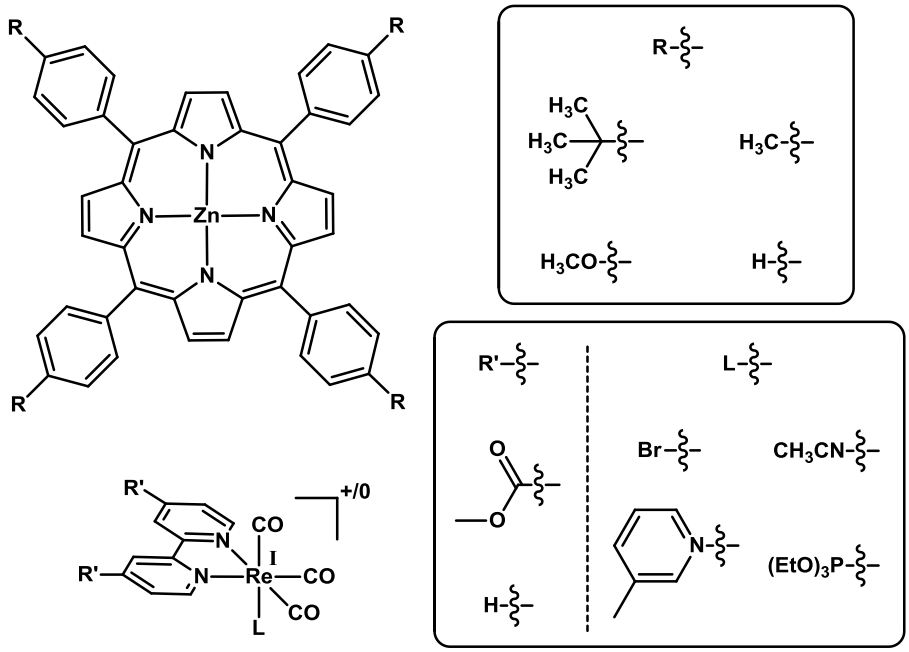

Figure 1.19 – Compounds synthesized and studied in this project. Cationic rhenium complexes possess hexafluorophosphate as counterion

All the possible porphyrin–catalyst mixtures were tested for CO_2 reduction under usual conditions and the results analyzed according to the properties of the different components, trying to get correlations between the nature of the catalytic mixture and the CO formation ability.

Combination of the different components gave us a wide range of chemical structure variation on one, the other or both components and also in PET driving force values, allowing us to study the influence of each variable.

For each mixture, CO formation was followed by gas chromatography and simultaneous monitoring of the UV–Visible spectra allowed us to study the presence of the different components, such as reduced chlorin species, in solution.

Chapter 2. Synthesis

2.1 Synthesis of Free–Base and Metallated Porphyrins

Pyrrole–aldehyde condensation

The Adler–Longo method[50] was employed for the preparation of the *para*–substituted *meso*–tetrakis(*tert*–butylphenyl)porphyrin (H_2TTBPP) **FB–P3**. The general method consists of the condensation of a substituted benzaldehyde with pyrrole refluxing in acetic or propionic acid (Scheme 2.1). In those conditions, the free–base porphyrin is generated and crystallizes in the reaction mixture.

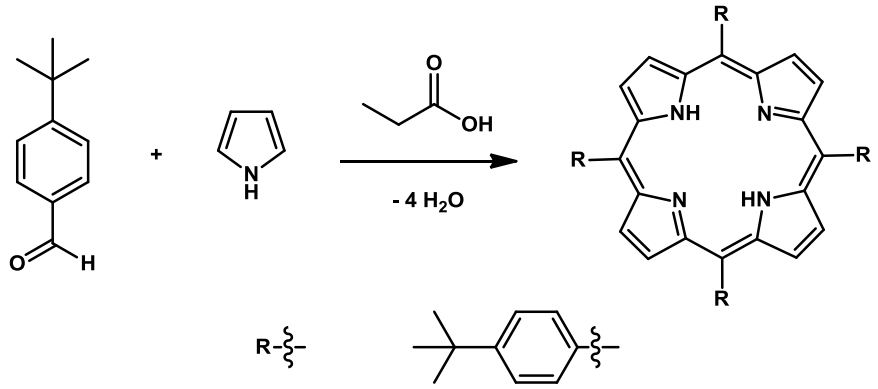

Scheme 2.1 – Synthesis of H_2TTBPP using the Adler–Longo method

The reaction yield is usually around 20 % and the product obtained is pure in most cases if the right solvent is chosen, so no further treatment is needed. The reaction can be carried out in acetic acid but a non–crystalline product is obtained in that case.[50]

Metallation

The typical procedure for inserting zinc into porphyrins involves refluxing the free–base porphyrin with an excess of zinc acetate in a 5:1 chloroform:methanol mixture. The product obtained in this way is not completely pure and column chromatography is the most suitable way to purify it. Due to the high sensitivity of the metallated porphyrins to acid media, silica gel cannot be used and basic alumina was employed to avoid product decomposition. Although previous

reports describe the purification step using dichloromethane or chloroform as eluent and basic alumina as the stationary phase,[51–52] the product was found to decompose in chlorinated solvents when the solution was exposed to light for more than 20 minutes. Because of this, alternative solvent mixtures like ethyl acetate:hexane were used when possible. Despite using non–chlorinated solvents and basic alumina columns, the reaction yield decreased significantly after the purification step.

2.2 Synthesis of Rhenium Complexes

General considerations

Two different sets of rhenium complexes, with the unsubstituted 2,2'–bipyridine (bpy) and its 4,4'–bis(methoxycarbonyl) derivative (BMCbpy) were prepared, labeled as the *a* and *b* series respectively. The synthetic route for both series is mostly similar. In the first part, a labile acetonitrile precursor was prepared according to the reaction sequence shown in Scheme 2.2.

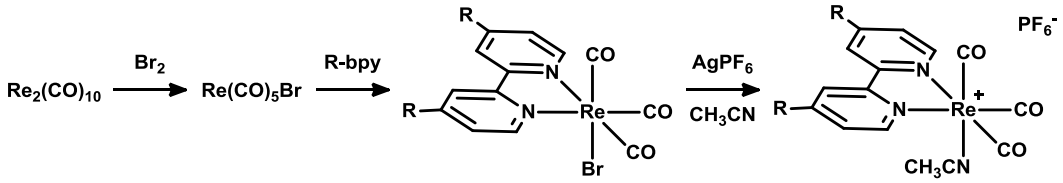

Scheme 2.2 – Rhenium acetonitrile complex preparation route. R = H, CO_2Me

In the second part, the acetonitrile was directly substituted by two different ligands, 3–picoline and triethyl phosphite, as shown in Scheme 2.3.

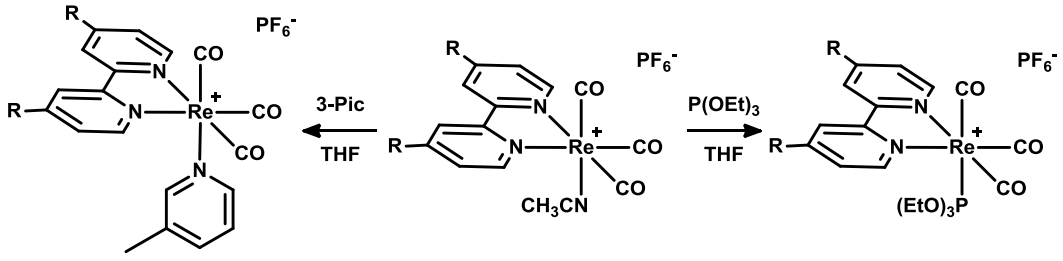

Scheme 2.3 – Acetonitrile ligand substitution reaction scheme. R = H, CO_2Me

A different route was initially tested and [Re(bpy)$(CO)_3$(3–Pic)][PF_6] **R3–a** was prepared directly from the bromide precursor. However, the procedure employed in that case did not work when the triethyl phosphite was employed and was therefore discarded.

Substituted bipyridine preparation

The preparation method used to make the dimethyl ester derivative of the 2,2'–bipyridine–4,4'–dicarboxylic acid was the usual acid–catalyzed esterification of carboxylic acids in the presence of alcohols. Due to the extremely low solubility of the starting material in almost every solvent, the reaction was very clean and the product obtained could be directly used without any purification after extracting it from the reaction mixture.

Bipyridine coordination

The displacement of two carbonyl ligands by a molecule of bipyridine was achieved by using a 1:1 mixture of the rhenium pentacarbonyl precursor and the corresponding bipyridine. The product was observed to precipitate during the reaction time. In this case, the reactions were also very clean because the possible by–products remained in solution. After washing the product with hexane to remove possible rests of toluene, it could be vacuum–dried and used directly in the next steps. In both cases, yields were usually very high and they were found to be higher when increasing the scale of the reaction.

Bromide substitution

Two different halide abstraction reactions were carried out. One of them, in the presence of picoline, yielded directly the picoline–coordinated product **R3–a**, whereas the other one was used to form the acetonitrile intermediates for the later substitution.

In both cases, silver hexafluorophosphate was used to abstract the bromide by precipitation of the silver salt, leaving hexafluorophosphate as the counterion of the rhenium(I) cationic complexes. In previous work done in this group,[41,43,45]

silver triflate was used for this purpose and it was later exchanged for the hexafluorophosphate if necessary. In this project, silver hexafluorophosphate was used in order to avoid the additional step of counterion exchange and because of it is less hygroscopic, allowing storage in a dry and ventilated place for weeks without decomposition, whereas silver triflate must be stored inside a glovebox to avoid its hydrolysis.

It must be noticed that the use of silver hexafluorophosphate is restricted to coordinating solvents, because of the Ag^{+}–catalyzed hydrolysis of the hexafluorophosphate anion in non–coordinating ones like dichloromethane, chloroform or benzene. In our case, the reactions were performed in acetonitrile or THF for the further substitution, in which it has been reported to be stable during several days even in the presence of added water.[53]

The reactions must be carried out in the absence of light to avoid decomposition of either the rhenium complex or the silver salt, which are extremely photosensitive when dissolved. In order to achieve the right light protection, the solid starting materials were placed inside a two–necked round bottomed flask with a condenser and all the system covered with foil. After three pumping–Ar backfilling cycles, the solvent (and the 3–picoline if necessary) was added and the mixture refluxed inside a covered fumehood. Once the product was formed, the foil protection was not necessary and it could be treated under usual conditions.

Acetonitrile displacement

Once the acetonitrile intermediates were formed, they could lead to a vast family of derivatives by refluxing it in THF in the presence of an excess of the ligand that will substitute the coordinated acetonitrile molecule in the final complex. Although the acetonitrile complexes were strong enough to be air–stable, they were readily substituted in solution when a more coordinating ligand was present. Therefore, employing either nitrogen or phosphorus based ligands such as 3–picoline or triethylphosphite, the corresponding compound was formed and the product was essentially pure after removing the solvent and washing the solid obtained. Same considerations about inert conditions and light apply in here.

2.3 Structural Characterization

NMR spectroscopy

For previously reported compounds, ^{1}H NMR spectroscopy was enough in most cases to confirm the presence and purity of the desired product, comparing with literature values or analyzing very characteristic signals. In other cases, high resolution mass spectrometry and elemental analysis were employed together with NMR, IR and UV–Visible absorption spectroscopies to characterize the new compounds synthesized in this work.

Figures 2.1 and 2.2 show the labeling system used for the rhenium complexes ligands. In the case of the BMCbpy complexes, H_4 and $H_{4'}$ are not present. For the carbonyl groups, the subscripts *ct* and *cc* come from the relative *cis–trans* position to the two bipyridine nitrogen atoms. For the porphyrins, the usual notation of aromatic rings was used, considering the carbon atom bonded to the porphyrin core as the reference position.

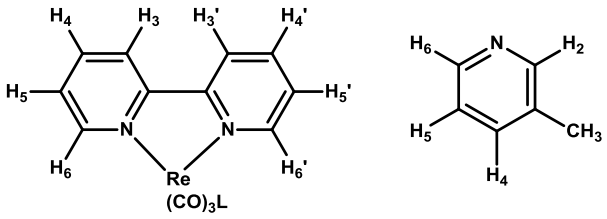

Figure 2.1 – ^{1}H NMR spectra labeling notation used for the bipyridine (left) and the picoline (right) ligands

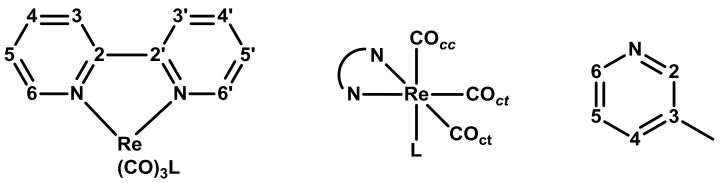

Figure 2.2 – ^{13}C NMR spectra notation employed for bipyridine (left), carbonyls (center) and picoline (right) ligands

- *5,10,15,20–tetrakis[4–(tert–butyl)phenyl]–21H,23H–porphine: H_2TTBPP* ***(FB–P3)***

Due to the symmetry of the molecule, the four phenyl and pyrrole rings are equivalent. This feature is general for all the porphyrins prepared in this work since all of them are equivalently substituted, exhibiting D_{2h} or D_{4h} symmetry for the free–base and the metalloporphyrins respectively. Although only the metallated porphyrins have a four–fold symmetry axis, in the case of the free–base porphyrins there is a fast exchange equilibrium in the NMR timescale between all the porphyrin nitrogen atoms. This equilibrium makes the four porphyrin fragments look equivalent in the NMR spectra, but an averaged situation of a dynamic phenomenon is actually observed.

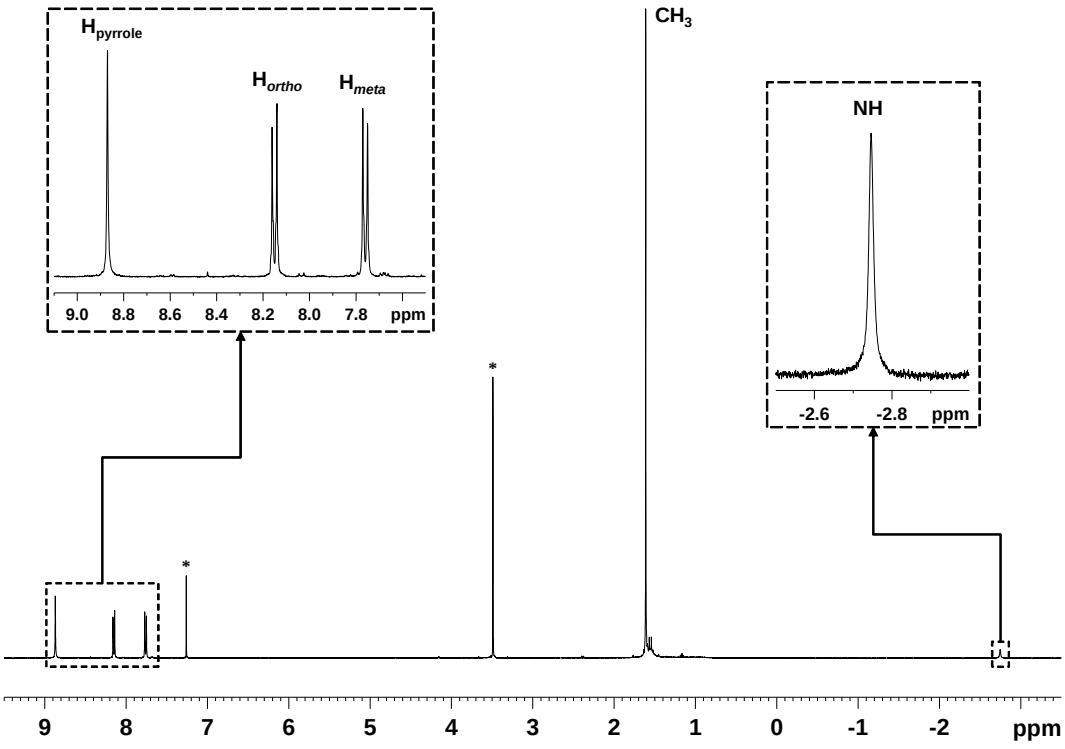

Figure 2.3 – ^{1}H NMR spectrum of H_2TTBP in $CDCl_3$ (400 MHz) at 298 K. Signals marked with an asterisk correspond to residual solvent peaks assigned according to previously reported values[54]

The aromatic signals are in good agreement with the expected ones, showing a singlet for the eight equivalents pyrrole rings protons and two doublets for the typical AB spin system of *para*–substituted benzene rings with small second order effects. However, the most characteristic signal of the free–base porphyrin is the signal of the NH groups, that appears in the negative region due to the ring current effect.[55] The singlet in the aliphatic region corresponds to all the equivalents methyl residues of the *tert*–butyl groups.

- *5,10,15,20–tetraphenyl–21H,23H–porphine zinc(II): ZnTPP (**P1**)*

The spectrum shows a singlet for all the equivalent pyrrolic protons and a poorly resolved spin system corresponding to the phenyl ring protons. Although only the signal corresponding to the protons in the *ortho* position is resolved, integration values are in good agreement with the assignment proposed. Complete metallation of the porphyrin is ensured by the lack of signals in the negative region, which would correspond to the inner NH protons, as shown in the enlargement.

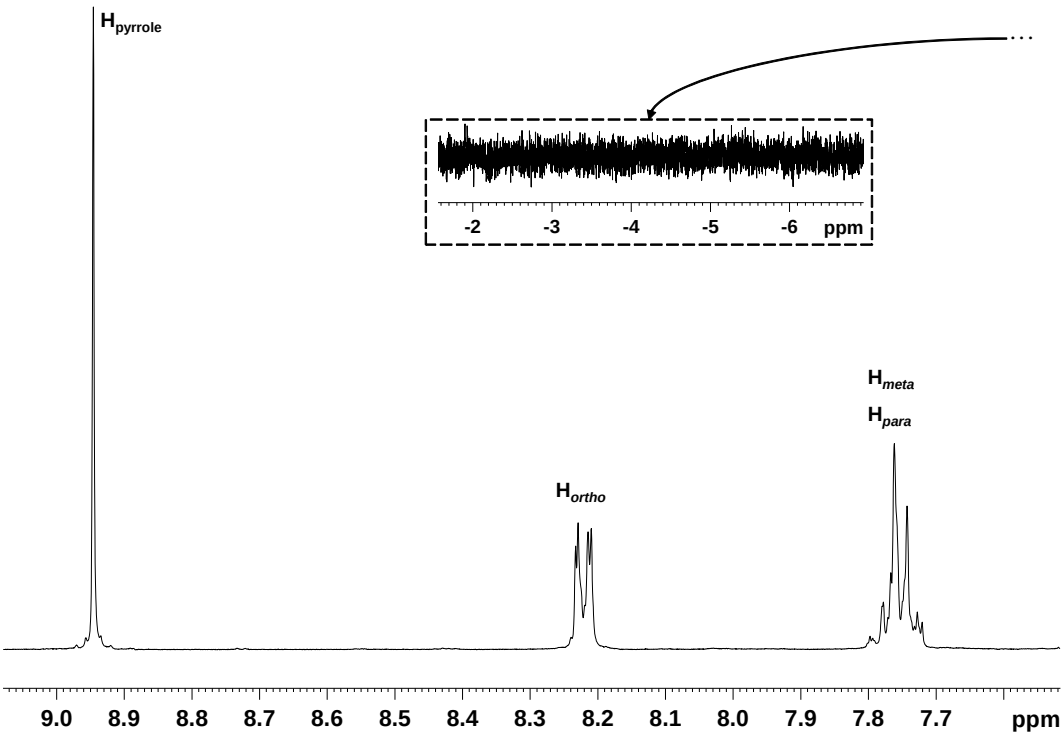

Figure 2.4 – ^{1}H NMR spectrum of ZnTPP (P1) in $CDCl_3$ (400 MHz) at 298 K

- *5,10,15,20–tetrakis(4–tolyl)–21H,23H–porphine zinc(II): ZnTTP (**P2**)*

In the case of the tolyl porphyrin, as discussed before for the *tert*–butyl substituted **FB–P3**, substitution of the phenyl rings leads to a set of two doublets in the aromatic region that appear together with the signal of the protons on the pyrrole rings of the porphyrin. The equivalent methyl groups are found in the aliphatic region and no signal at negative chemical shift could be observed (data not shown), which proves the absence of free–base porphyrin.

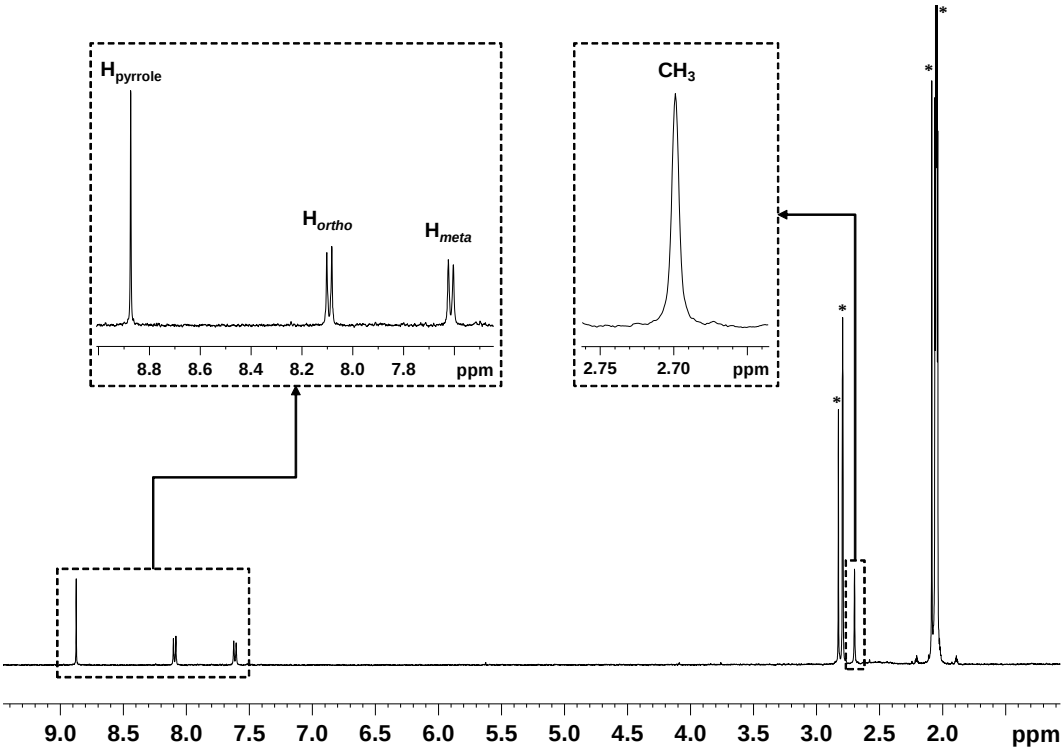

Figure 2.5 – ^{1}H NMR spectrum of ZnTPP (P2) in acetone–d_6 (400 MHz) at 298 K

- *5,10,15,20–tetrakis[4–(tert–butyl)–phenyl]–21H,23H–porphine zinc(II): ZnTTBPP (**P3**)*

Compared with the spectrum of the free–base porphyrin **FB–P3** (Figure 2.3), the metallation has a very small effect on the chemical shift of the aromatic signals. As usual, the absence of signals in the negative region proves the complete metallation of the starting material and the pyrrole protons singlet appears together with the two doublets of the *para*–substituted phenyl ring.

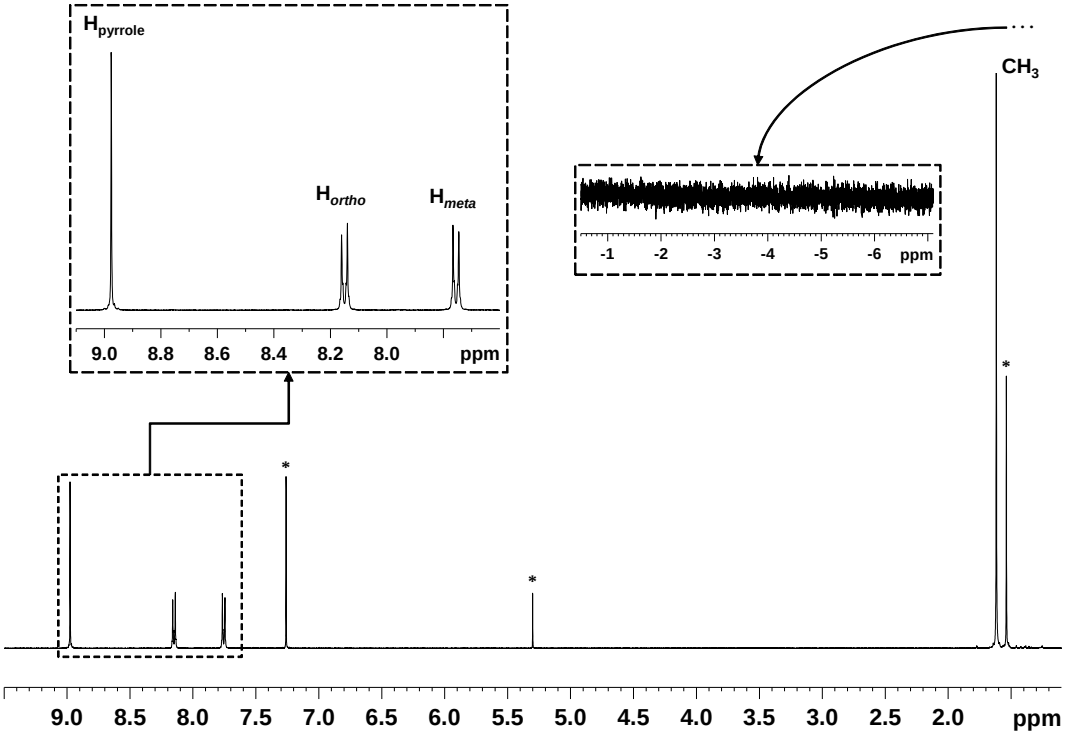

Figure 2.6 – ^{1}H NMR spectrum of ZnTTBPP (P3) in $CDCl_3$ (400 MHz) at 298 K

- *5,10,15,20–tetrakis(4–methoxyphenyl)–21H,23H–porphine zinc(II): ZnTMPP (**P4**)*

In the case of the methoxy substituents, a significant shift was found for the signals of the phenyl ring when compared with **P1–3**; with an upfield shift of the protons in the adjacent position of the substituent to 7.3 ppm, compared with values above 7.5 ppm in all the other cases either in deuterated acetone or chloroform.

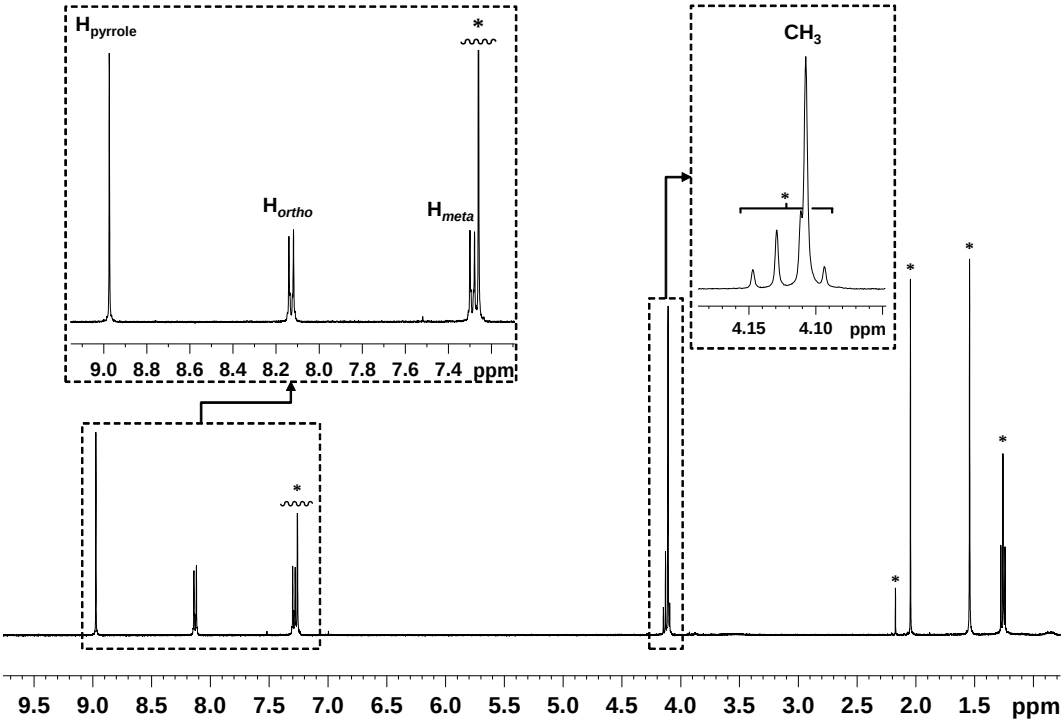

Figure 2.7 – ^{1}H NMR spectrum of ZnTMPP (P4) in $CDCl_3$ (400 MHz) at 298 K

The higher shielding of those protons can be explained in terms of the +R effect of the methoxy substituent, which can donate electron density through resonance to the 2–, 4– and 6–positions relative to it (Figure 2.8); since the *para*–position relative to the methoxy group is occupied by the porphyrin core and no resonance–effect is possible at the 3–position, the effect is only observed for the protons close to the substituent.

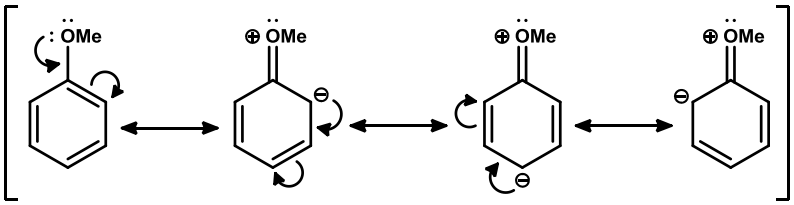

Figure 2.8 – Donating resonance effect of the methoxy group on the phenyl ring.

- *4,4'–bis(methoxycarbonyl)–2,2'–bipyridine: BMCbpy*

In the case of the 4,4'–disubstituted bipyridine derivative, three aromatic signals can be expected. The multiplicities observed, as well as the magnitude of the coupling constants, are in good agreement with the proposed structure, considering long–range coupling through the aromatic ring. The three protons of the methoxycarbonyl group appear around 4 ppm, which is also in good agreement with the strong deshielding effect of the oxygen atom due to its high electronegativity.

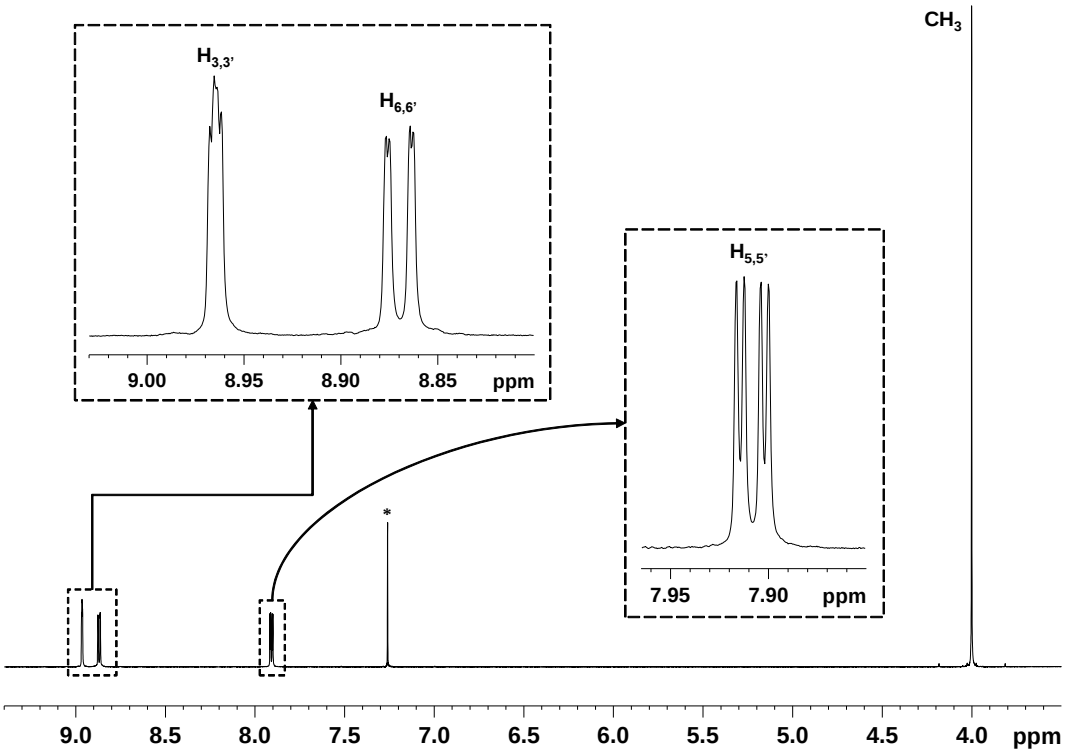

Figure 2.9 – ^{1}H NMR spectrum of BMCbpy in $CDCl_3$ (400 MHz) at 298 K

- *(2,2'–bipyridine)bromotricarbonylrhenium(I): [Re(bpy)(CO)$_3$Br] (**R1**–**a**)*

The only protons present in the molecule are those corresponding to the bipyridine ring. Although the metal coordination produces changes in the chemical shifts, the expected structure of the spectrum is essentially the same as that the one for the free ligand. The most significant change is the downfield shift of the H_6 and $H_{6'}$ protons with the coordination, which will be discussed at the end of this section (see Table 2.1 and discussion on page 52). The results obtained match with those previously reported.[56] Long–range coupling constants can be clearly observed for all the protons except for H_3 and $H_{3'}$ and are of the same magnitude as those for the free 2,2'–bipyridine (data not shown). No significant signals apart from the solvent were present in the rest of the spectrum, omitted in Figure 2.10.

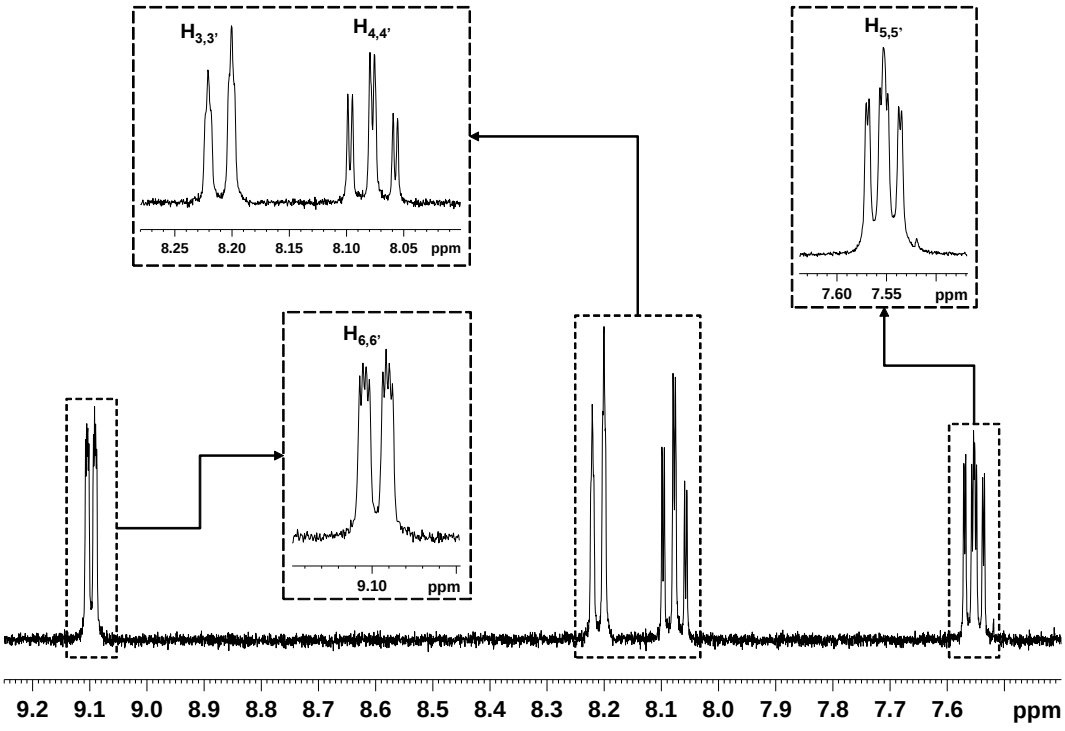

Figure 2.10 – ^{1}H NMR expansion of [Re(bpy)(CO)$_3$Br] (R1–a) in CDCl$_3$ (400 MHz) at 298 K

- *acetonitrile(2,2'–bipyridine)tricarbonylrhenium(I) hexafluorophosphate: [Re(bpy)(CO)$_3$(CH$_3$CN)][PF$_6$]* (***R2–a***)

The spectrum structure is essentially the same as the one reported before for the bromide **R1–a**, with the addition of the methyl group of the coordinated acetonitrile. Relative signal shifts compared with the bromide precursor and following derivatives will be discussed later at the end of this section.

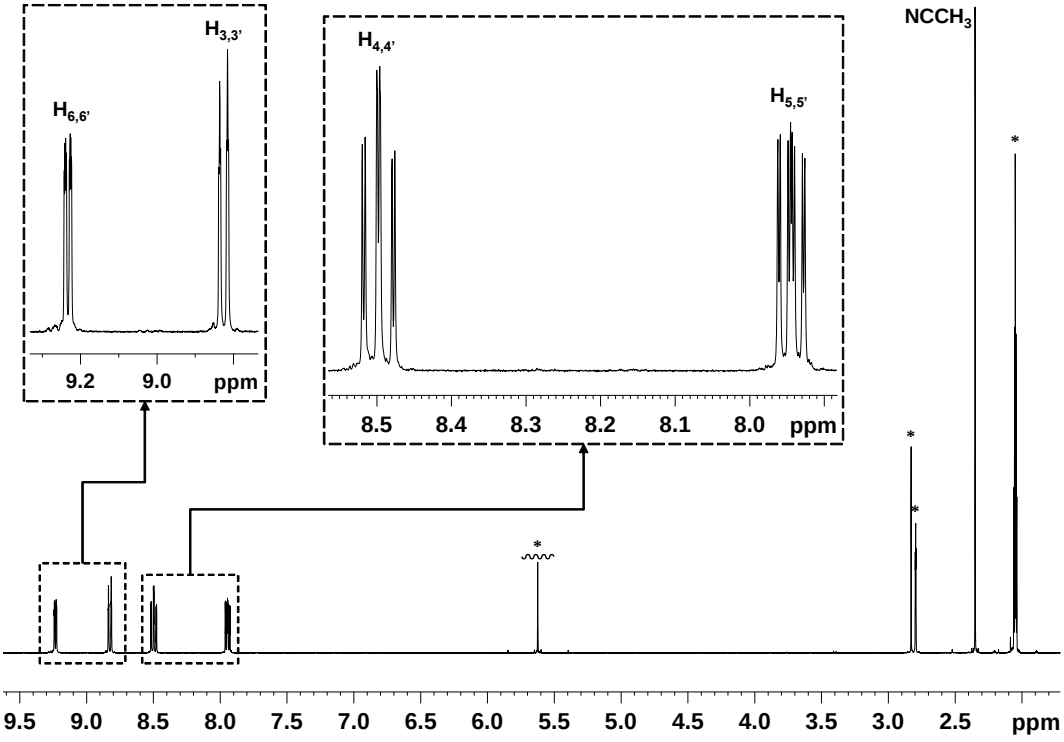

Figure 2.11 – ^{1}H NMR spectrum of [Re(bpy)(CO)$_3$(CH$_3$CN)][PF$_6$] (R2–a) in acetone–d_6 (400 MHz) at 298 K

The presence of coordinated acetonitrile is ensured by the difference in chemical shift compared to the reported value for free acetonitrile in deuterated acetone (2.05 ppm).[54] The signal of the coordinated ligand appears at 2.35 ppm in the case of **R2–a** and the 0.3 ppm difference is big enough to assign it to a coordinated acetonitrile molecule.

- *(2,2'–bipyridine)tricarbonyl(3–picoline)rhenium(I) hexafluorophosphate: [Re(bpy)(CO)$_3$(3–Pic)][PF$_6$] (**R3–a**)*

In this case, due to the presence of the 3–picoline ligand, two sets of signals are expected in the aromatic region. The lack of overlap between the different peaks makes 1D–NMR spectroscopy enough to separate the two different spin systems by simple integration of the signals. The structure of the bipyridine signals is analogous to the ones reported above, showing small changes in the chemical shifts and the coupling constant values.

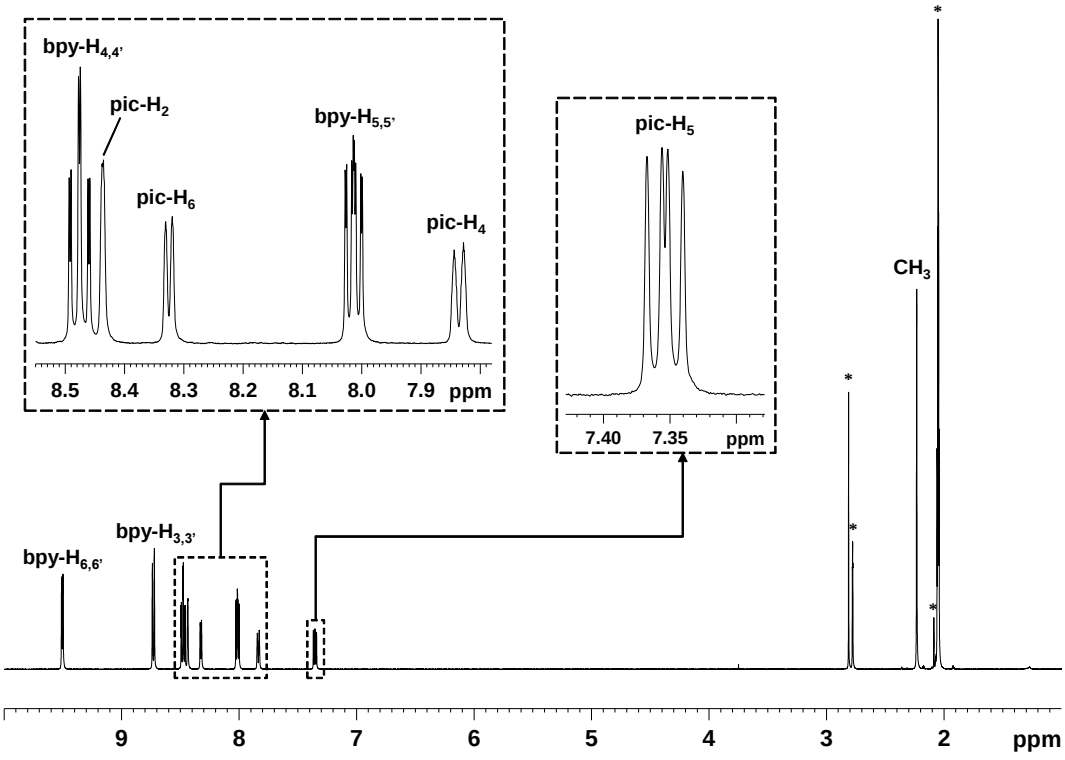

Figure 2.12 – ^{1}H NMR spectrum of [Re(bpy)(CO)$_3$(3–Pic)][PF$_6$] (R3–a) in acetone–d_6 (400 MHz) at 298 K

The picoline signals match with the expected ones in terms of chemical shift and multiplicity and can be completely assigned from the different coupling constant values. Figure 2.13 shows part of the aromatic region of an impure sample that contained some free picoline. The upfield shift of all the signals proved that the signals in Figure 2.12 correspond to coordinated picoline and the product obtained is the one described.

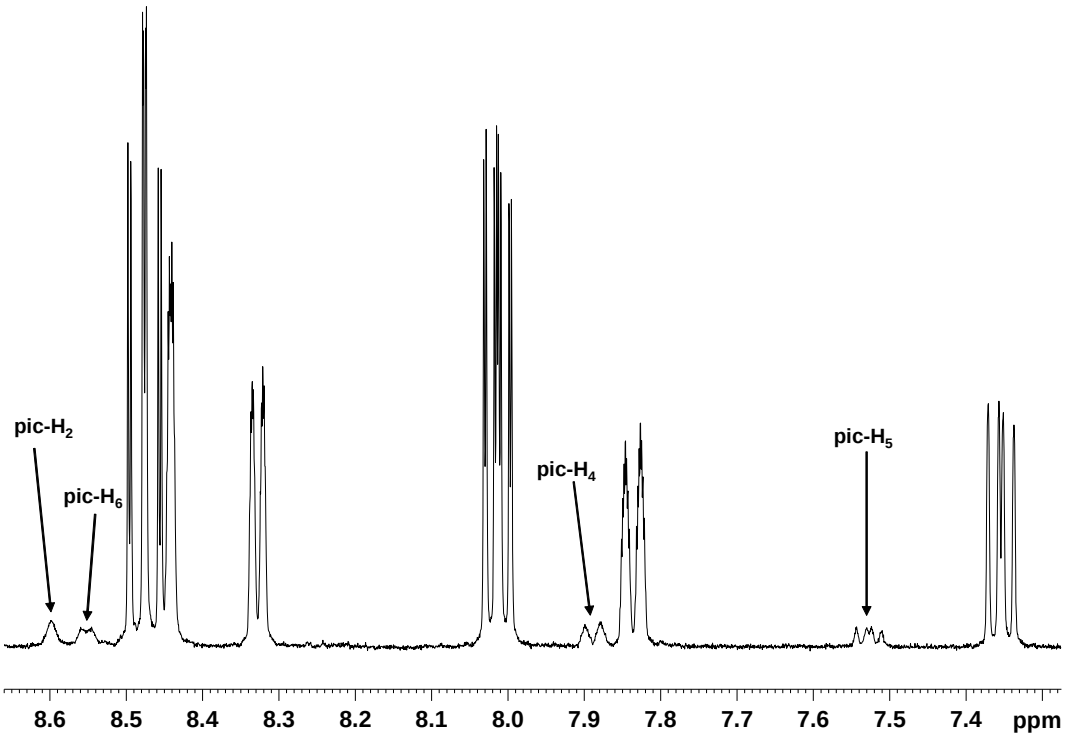

Figure 2.13 – ^{1}H NMR spectrum expansion of a [Re(bpy)(CO)$_3$(3–Pic)][PF$_6$] (R3–a) sample contaminated with free 3–picoline. acetone–d_6 (400 MHz) at 298 K. Signals corresponding to free picoline are highlighted

The presence of the hexafluorophosphate counterion is detected by ^{19}F and ^{31}P NMR spectroscopy as shown in Figure 2.14. Both, chemical shift and multiplicity as well as the P–F coupling constant value fall inside the typical range for this chemical species.

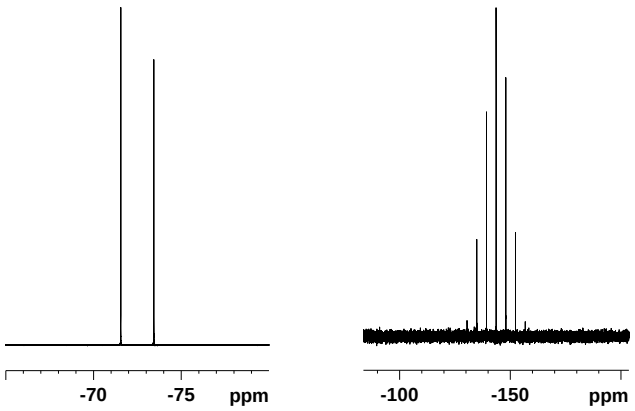

Figure 2.14 – ^{19}F (376.4 MHz, left) and ^{31}P (161.9 MHz, right) NMR spectra of [Re(bpy)(CO)$_3$(3–Pic)][PF$_6$] (R3–a) in acetone–d_6 at 298 K

- *(2,2'–bipyridine)tricarbonyl(triethylphosphite)rhenium(I) hexafluorophosphate: [Re(bpy)(CO)$_3${P(OEt)$_3$}][PF$_6$] (**R4**–**a**)*

Aromatic signals for this complex do not differ from those described above for all the analogous derivatives.

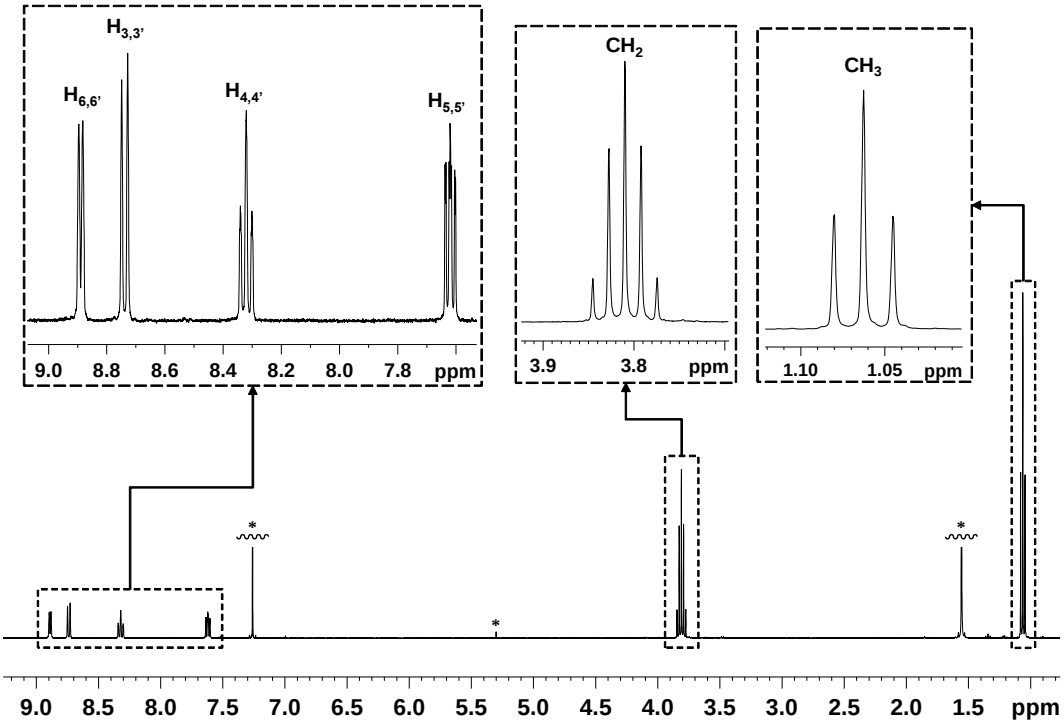

Figure 2.15 – ^{1}H NMR spectrum of [Re(bpy)(CO)$_3${P(OEt)$_3$}][PF$_6$] (R4–a) in CDCl$_3$ (400 MHz) at 298 K

All the equivalent protons of the methylene groups of the phosphite appear as a quintet, due to the coincidence in value of the $^3J_{H,H}$ and $^3J_{P,H}$ coupling constants, around 7 Hz.

The fluorine and phosphorus NMR spectra provide evidence of the presence of the hexafluorophosphate counterion and an additional signal for the phosphorus atom of the phosphite ligand.

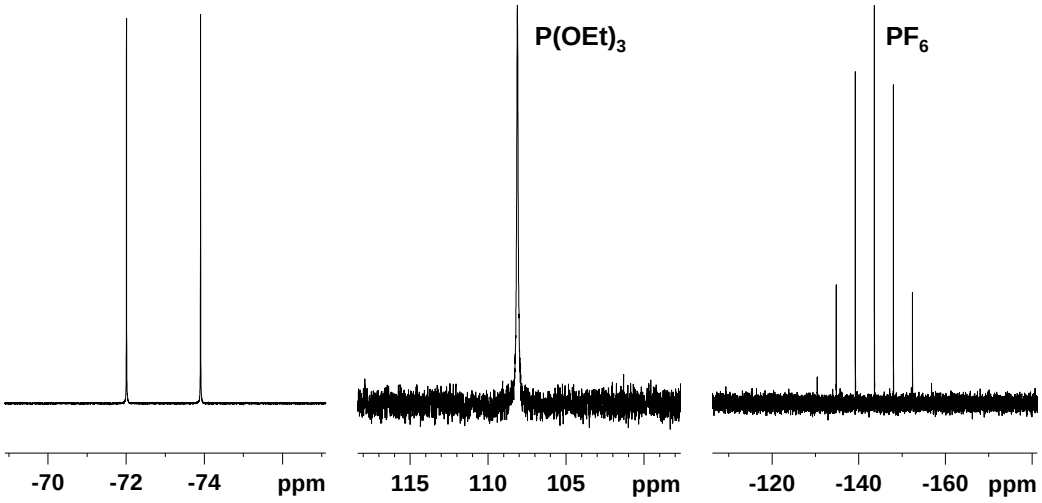

Figure 2.16 – ^{19}F (376.4 MHz, left) and ^{31}P (161.9 MHz, center and right) NMR spectra of $[Re(bpy)(CO)_3\{P(OEt)_3\}][PF_6]$ (R4–a) in $CDCl_3$ at 298 K

- *[4,4'–bis(methoxycarbonyl)–2,2'–bipyridine]bromotricarbonylrhenium(I): [Re(BMCbpy)(CO)$_3$Br] (**R1–b**)*

The proton NMR signals expected for this complex are essentially the same as those for the free BMCbpy shown before in Figure 2.9. The number and multiplicity of the signals is the same but a general downfield shift can be observed. It is especially interesting that the order of the H3,3' and H6,6' signals is inverted, compared to the BMCbpy spectrum. This observation has been found to be the same for all the rhenium complexes of the *b* series and will be discussed later (see Table 2.1 and discussion on page 52)

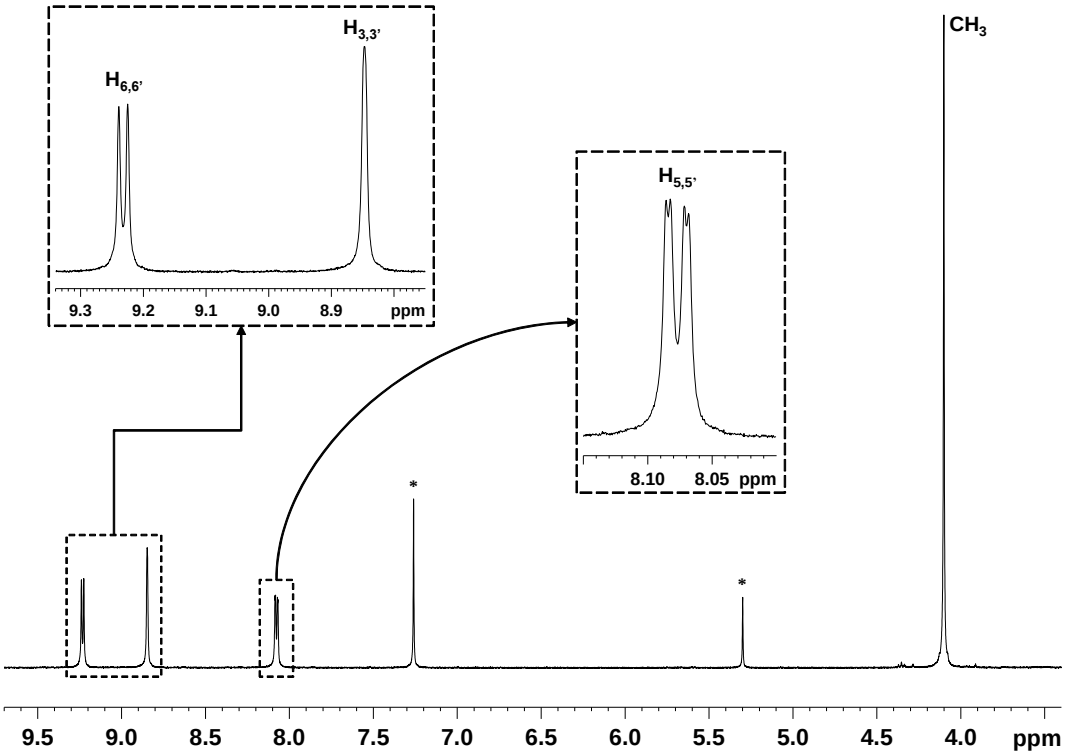

Figure 2.17 – ^{1}H NMR spectrum of [Re(BMCbpy)(CO)$_3$Br] (R1–b) in $CDCl_3$ (400 MHz) at 298 K

The ^{13}C NMR spectrum is also in good agreement with the proposed structure. Most of the signals can be easily assigned by direct analysis or comparing with unsubstituted bipyridine similar compounds previously reported like [Re(bpy)(CO)$_3$Br] (**R1–a**). However, the ^{1}H –^{13}C HSQC spectrum allows us to distinguish between 5,5' and 3,3' positions unambiguously, as shown in Figure 2.19.

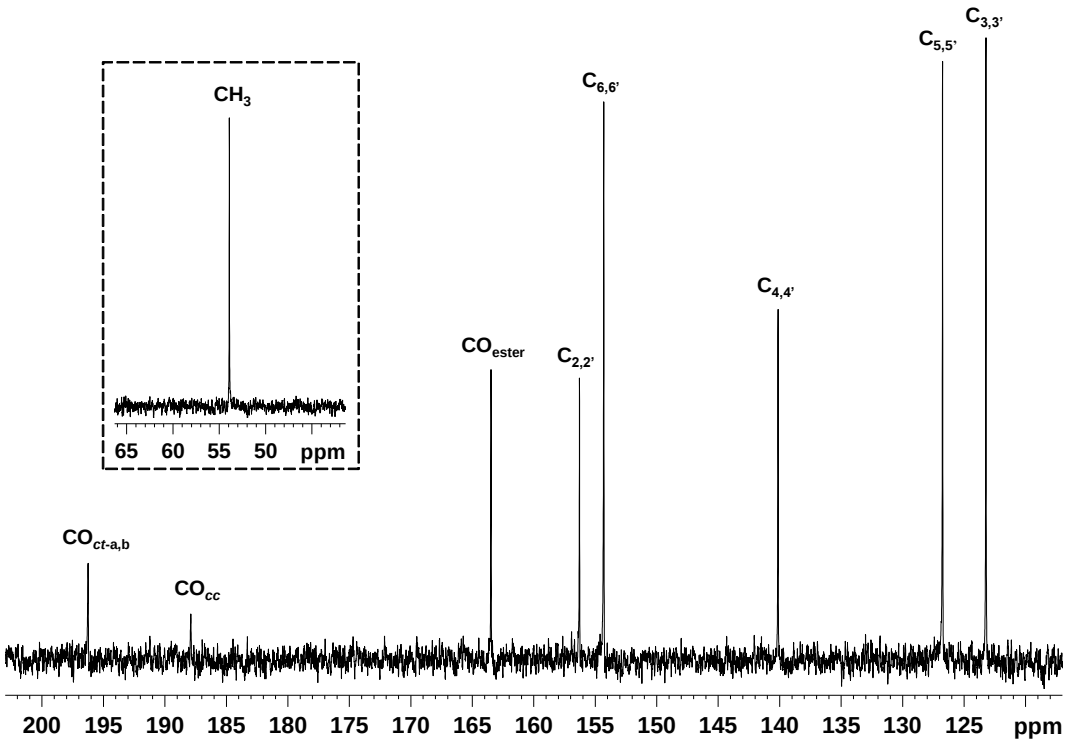

Figure 2.18 – ^{13}C NMR spectrum of [Re(BMCbpy)(CO)$_3$Br] (R1–b) in $CDCl_3$ (100.6 MHz) at 298 K

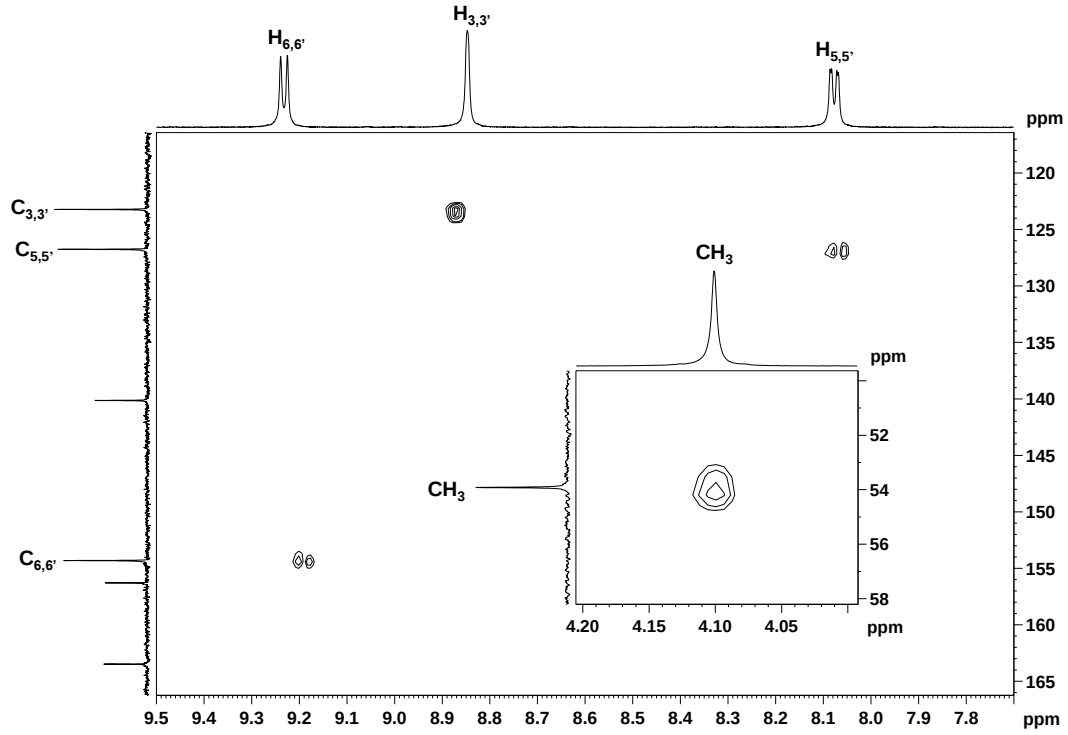

Figure 2.19 – ^{1}H –^{13}C HSQC spectrum of [Re(BMCbpy)(CO)$_3$Br] (R1–b) in $CDCl_3$ (400 MHz) at 298 K

The two carbonyl signals at low field were differentiated according to their different intensity and the existence of two equivalent carbonyl groups. Further arguments supporting this assignment will be shown later (see ^{13}C NMR spectrum discussion of **R4–b** on page 49). Assignment of the ester carbonyl group, $C_{2,2'}$ and $C_{4,4'}$ was based on the comparison of the ^{13}C NMR spectra of bpy and BMCbpy (Figure 2.20) and the reported assignment for the unsubstituted bipyridine.[57]

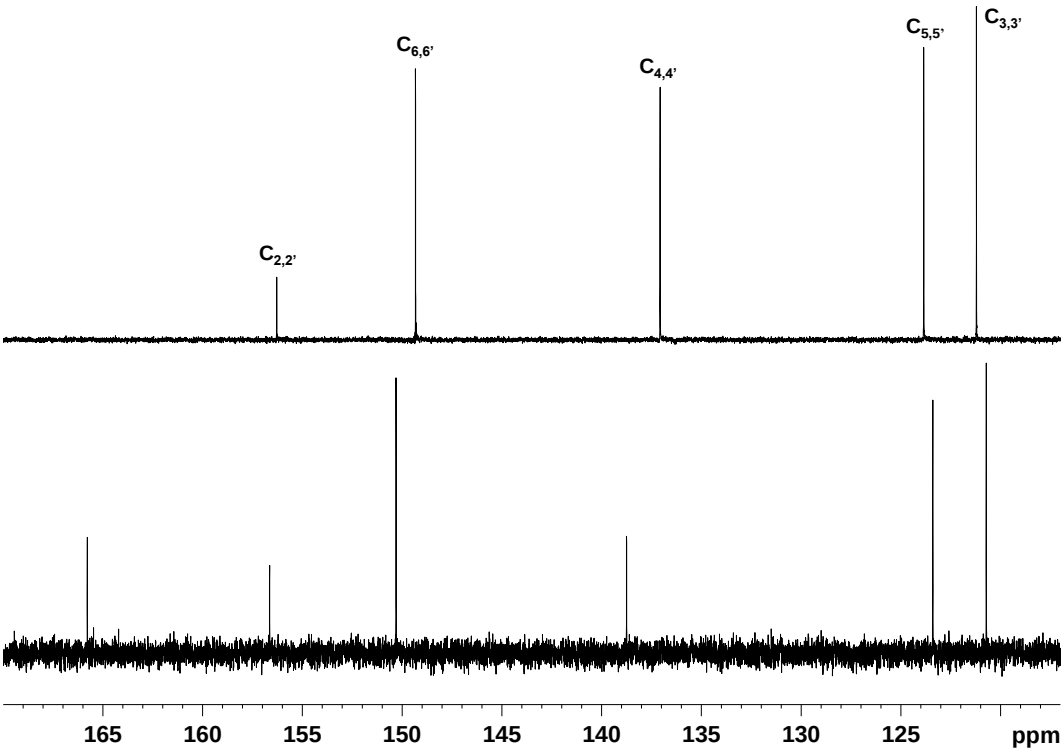

Figure 2.20 – ^{13}C spectra of bpy (top) and BMCbpy (bottom) in $CDCl_3$ (100.6 MHz) at 298 K. Reported assignment for 2,2'–bipyridine[57] is indicated

Substitution of the hydrogen atoms in the 4 and 4' positions by methoxycarbonyl groups leads to the appearance of a new signal above 165 ppm, assigned to the carbonyl carbon atom of the ester. By comparison of the chemical shifts it is possible to assign the remaining two quaternary carbon types (2,2' and 4,4'). It is clear that, with the substitution, the carbons in the 4 and 4' positions experience a bigger shift than the ones in the 2 and 2' ones. In addition, the decrease in the intensity of the signal between 135 and 140 ppm can be explained because of the lack of nuclear Overhauser effect in the BMCbpy due to the substitution of the hydrogen atoms. This analysis can be extended to the following spectra, and the same assignment is reported.

- *acetonitrile[4,4'–bis(methoxycarbonyl)–2,2'–bipyridine]tricarbonyl rhenium(I) hexafluorophosphate: [Re(BMCbpy)(CO)$_3$(CH$_3$CN)][PF$_6$]* ***(R2–b)***

The spectral characteristics of the acetonitrile derivative are essentially the same as those for the bromide complex except for the CH_3CN signals (one in the ^1H and two in the ^{13}C NMR spectrum) and the presence of the hexafluorophosphate ion.

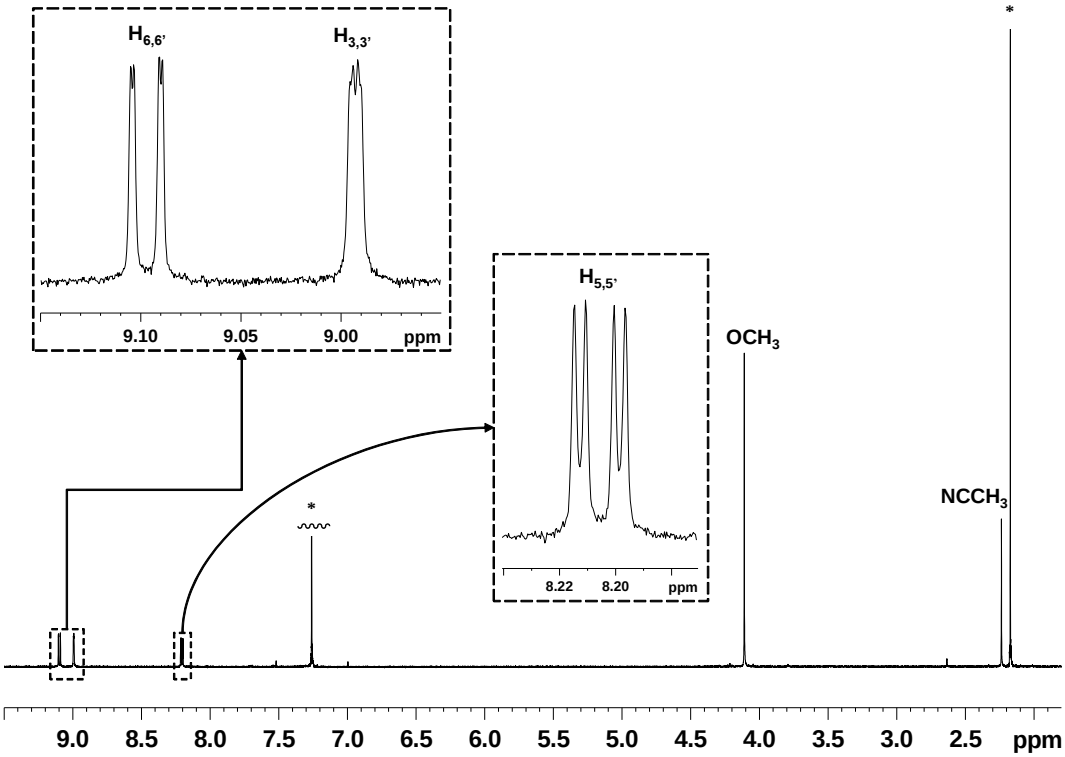

Figure 2.21 – ^{1}H NMR spectrum of [Re(BMCbpy)(CO)$_3$(CH$_3$CN)][PF$_6$] (R2–b) in CDCl$_3$ (400 MHz) at 298 K

The proton NMR spectrum illustrated in Figure 2.21 shows very small shifts for the bipyridine signals, compared to those of the bromide precursor **R1–b**. The signal of the methyl group of the acetonitrile molecule appears at 2.24 ppm, shifted more than 0.1 ppm from the 2.10 ppm value reported for free acetonitrile in deuterated chloroform,[54] proving that it is coordinated to the rhenium center.

Although the ^{1}H NMR spectrum shown above was acquired in deuterated chloroform, the limited solubility of the complex in most common solvents made it necessary to dissolve it in different solvents for the less sensitive experiments. Acceptable spectra were obtained in deuterated acetone.

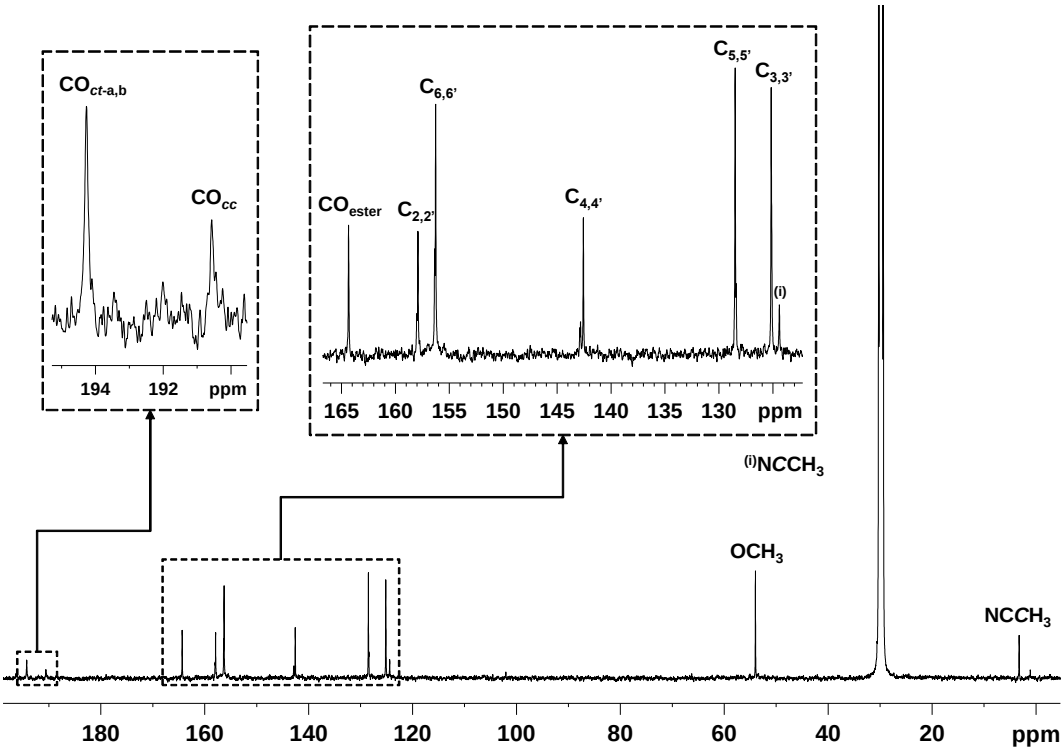

Figure 2.22 – ^{13}C NMR spectrum of [Re(BMCbpy)(CO)$_3$(CH$_3$CN)][PF$_6$] (R2–b) in acetone–d_6 (125.7 MHz) at 298 K

The assignment of all the carbonyl and bipyridine signals is analogous to the one detailed above for the bromide derivative and is also confirmed by two–dimensional heteronuclear experiments (Figure 2.24). The acetonitrile signals observed (124.1 and 3.2 ppm) support the coordinated nature of the ligand when compared with the ones reported for free acetonitrile (117.6 and 1.1 ppm).[54] However, due to the labile nature of the acetonitrile complex, some additional signals were observed (Figure 2.23). These signals were not present when a reduced number of scans was made and can be attributed to decomposition products that appear in solution with time. The purity of the acetonitrile complex has been proven by elemental analysis, ensuring that no other products were present in the original sample.

The presence of the hexafluorophosphate anion was proved by fluorine and phosphorus NMR spectroscopy (data not shown, see Appendix I on page 122).

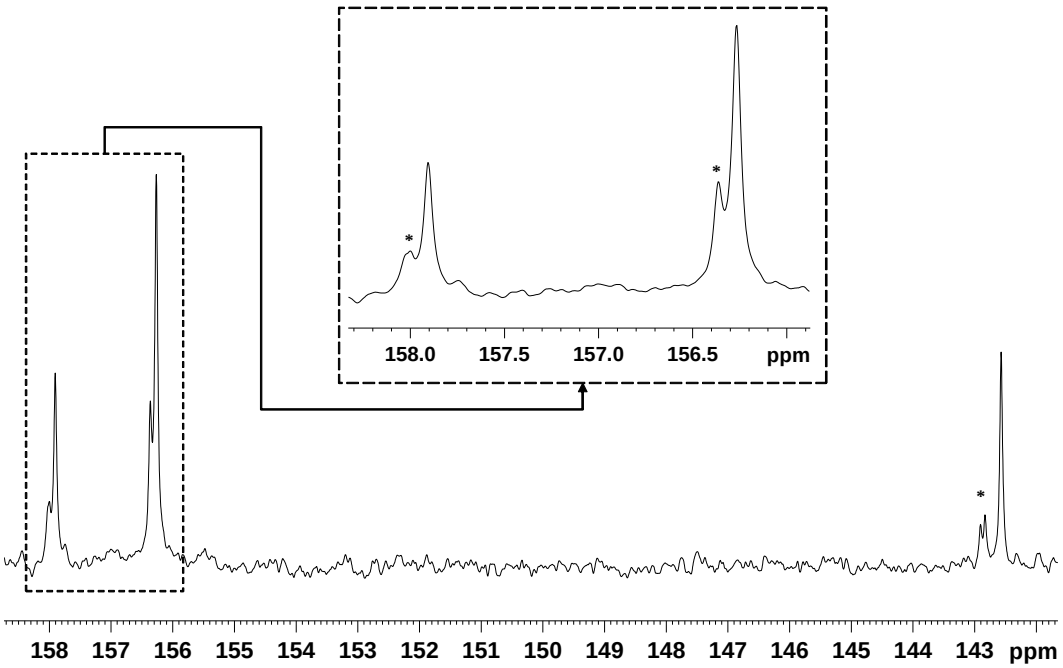

Figure 2.23 – ^{13}C NMR spectrum expansion of [Re(BMCbpy)(CO)$_3$(CH$_3$CN)][PF$_6$] (R2–b) in acetone–d_6 (125.7 MHz) at 298 K. Asterisks denote impurity and not solvent peaks in this case

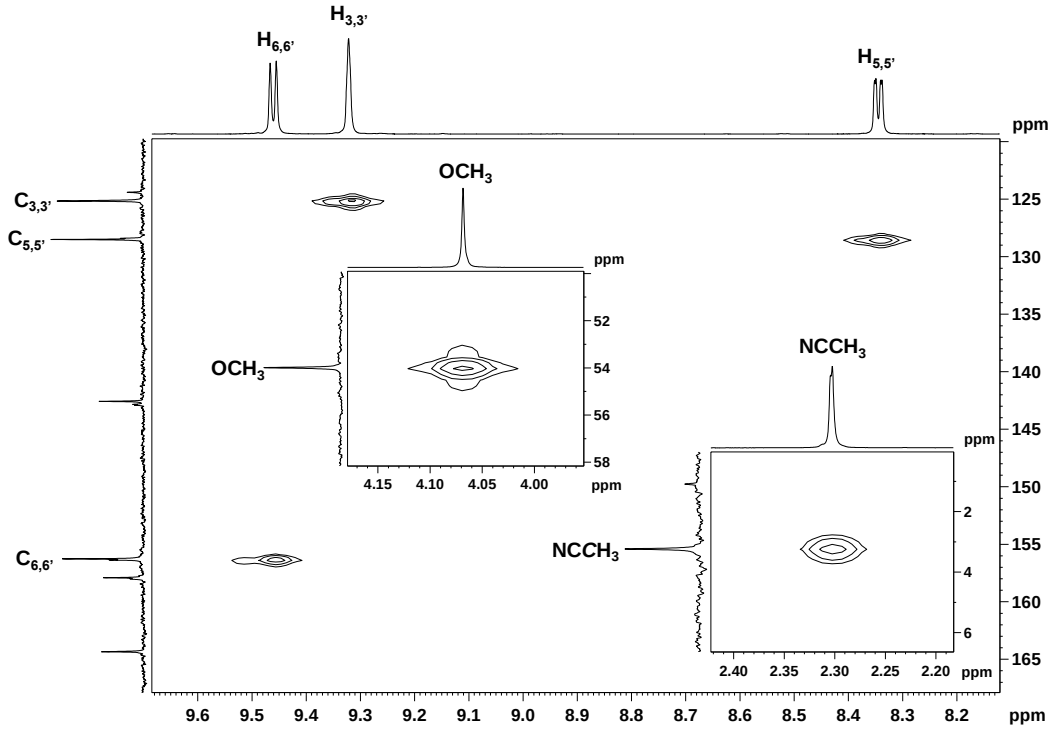

Figure 2.24 – ^{1}H –^{13}C HSQC spectrum of [Re(BMCbpy)(CO)$_3$(CH$_3$CN)][PF$_6$] (R2–b) in acetone–d_6 (500 MHz) at 298 K

- *[4,4'–bis(methoxycarbonyl)–2,2'–bipyridine]tricarbonyl(3–picoline) rhenium(I) hexafluorophosphate: [Re(BMCbpy)(CO)$_3$(3–Pic)][PF$_6$]* ***(R3–b)***

With the exception of the protons in the 4 and 4' positions of the bipyridine ring and the presence of the methoxycarbonyl group protons, the structure of the spectrum should be essentially the same as for **R3–a**.

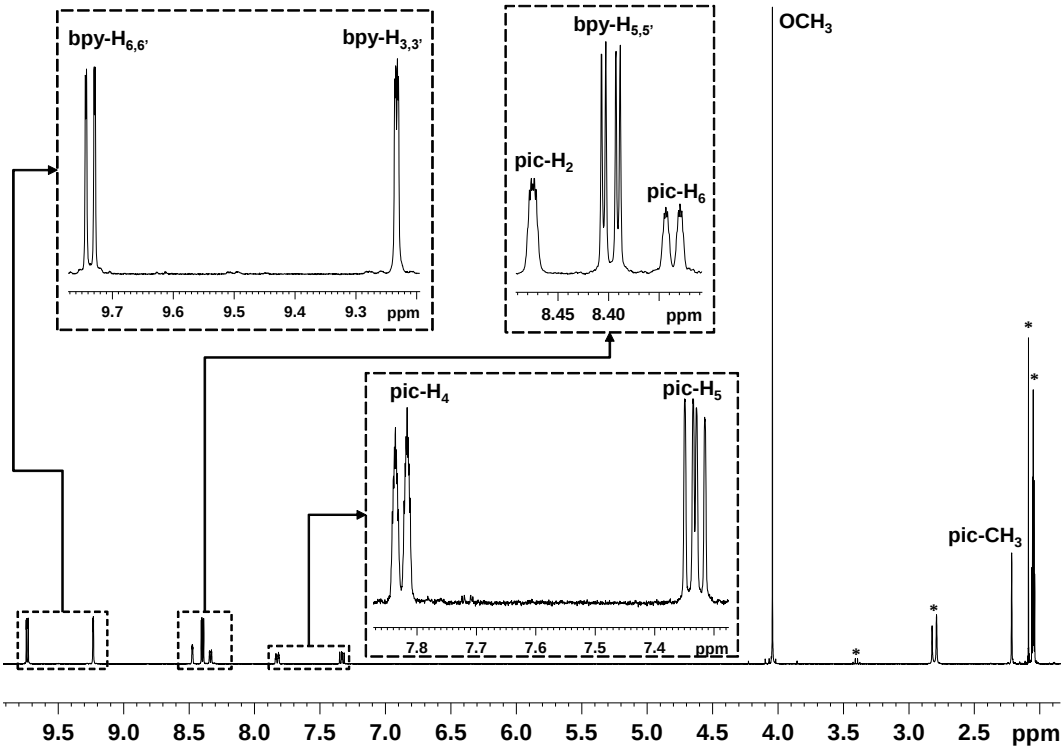

Figure 2.25 – ^{1}H NMR spectrum of [Re(BMCbpy)(CO)$_3$(3–Pic)][PF$_6$] (R3–b) in acetone–d_6 (400 MHz) at 298 K

The aromatic region of the ^{13}C NMR spectrum was slightly complex due to the amount of signals. However, with the assignment of the ^{1}H NMR and the HSQC spectrum (shown in Figure 2.27), all the non–quaternary carbons were unambiguously assigned.

The presence of the hexafluorophosphate counterion was evidenced in phosphorus and fluorine NMR spectra (data not shown, see Appendix I on page 122).

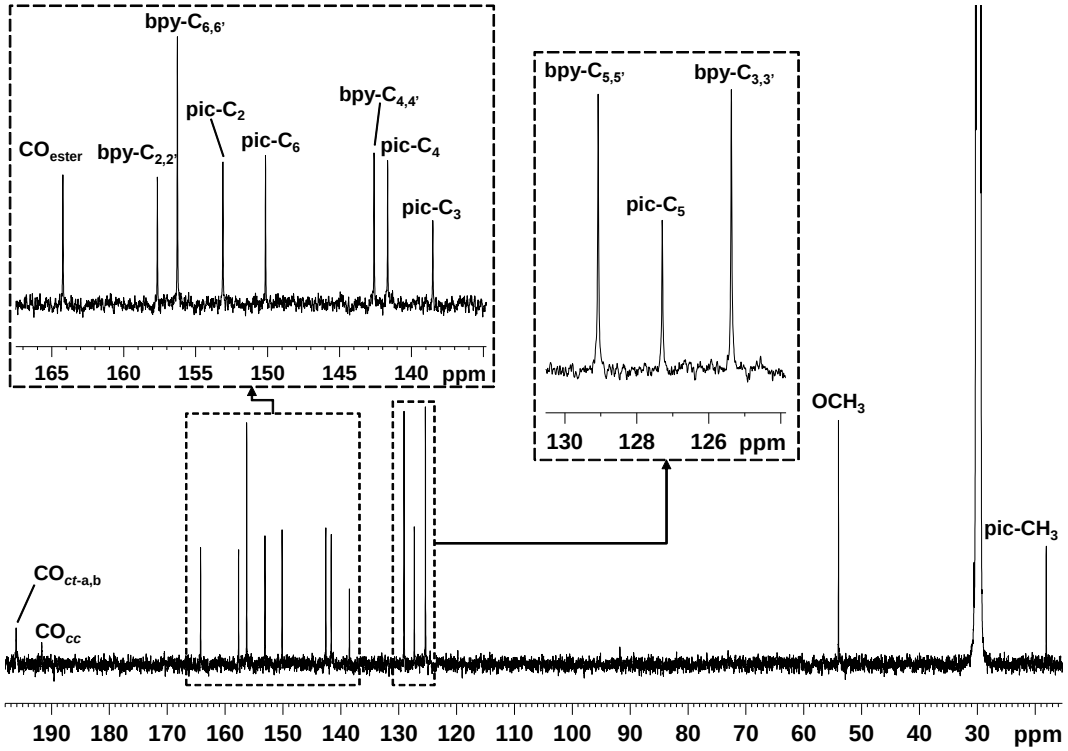

Figure 2.26 – ^{13}C NMR spectrum of [Re(BMCbpy)(CO)$_3$(3–Pic)][PF$_6$] (R3–b) in acetone–d_6 (125.7 MHz) at 298 K

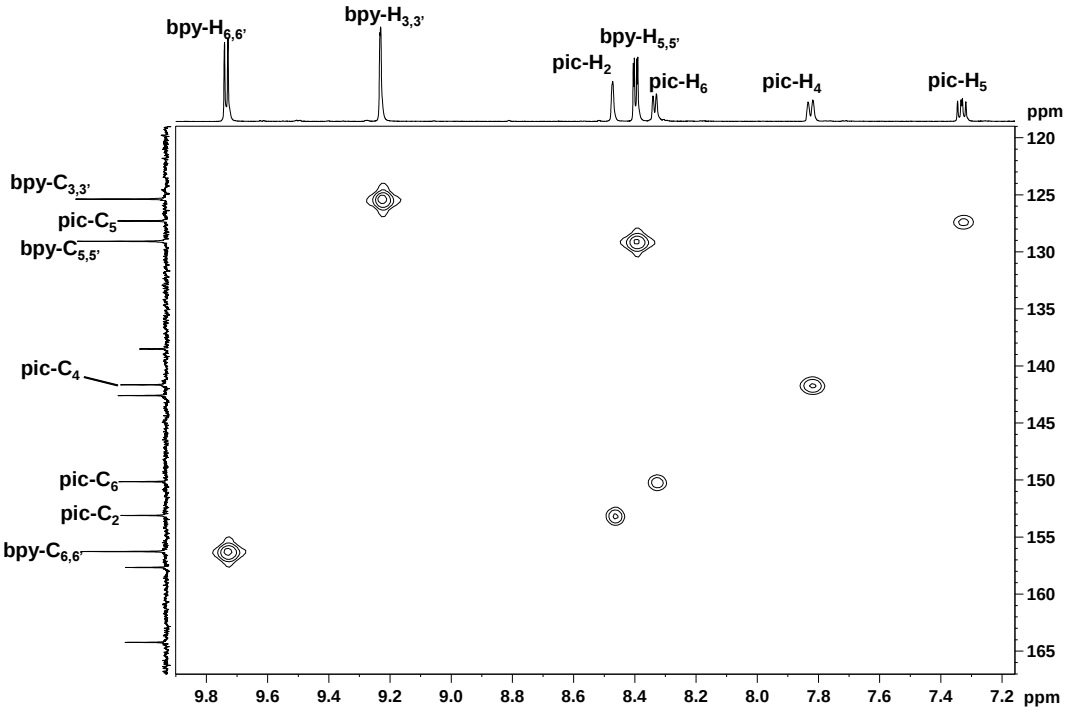

Figure 2.27 – ^{1}H –^{13}C HSQC spectrum of [Re(BMCbpy)(CO)$_3$(3–Pic)][PF$_6$] (R3–b) in acetone–d_6 (500 MHz) at 298 K

- *[4,4'–bis(methoxycarbonyl)–2,2'–bipyridine]tricarbonyl(triethylphosphite) rhenium(I) hexafluorophosphate:*
  *[Re(BMCbpy)(CO)$_3${P(OEt)$_3$}][PF$_6$] (**R4–b**)*

The proton NMR spectrum exhibits the same structure as the one belonging to the *a* series, with the exception of the signal of the methoxycarbonyl protons, that appears around 4 ppm, and the absence of $H_{4,4'}$. In this case, the same quintet as for **R4–a** is observed for the phosphite methylene groups, due to the coincidence of the proton–proton and phosphorus–proton coupling constant values.

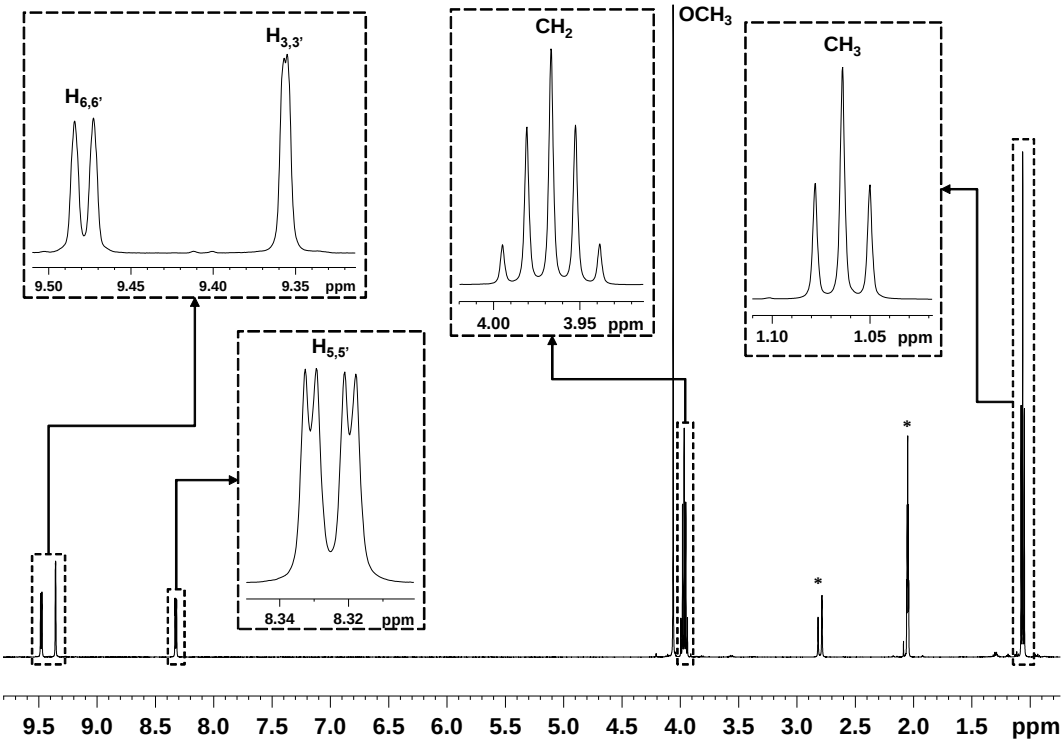

Figure 2.28 – ^{1}H NMR spectrum of [Re(BMCbpy)(CO)$_3${P(OEt)$_3$}][PF$_6$] (R4–b) in acetone–d_6 (500 MHz) at 298 K

The most characteristic feature of the ^{13}C NMR spectrum, is the existence of phosphorus–carbon coupling with the three carbonyls bonded to the rhenium and with the two carbon atoms of the ethyl chains of the phosphite. The different magnitude of the *cis* and *trans* coupling constants, reinforce our initial carbonyl assignment discussed on page 43, which also match with previously reported results for its unsubstituted bipyridine analogue.[58] Two–dimensional experiments (Figure 2.30) were employed to assist the labeling of the remaining carbon atoms.

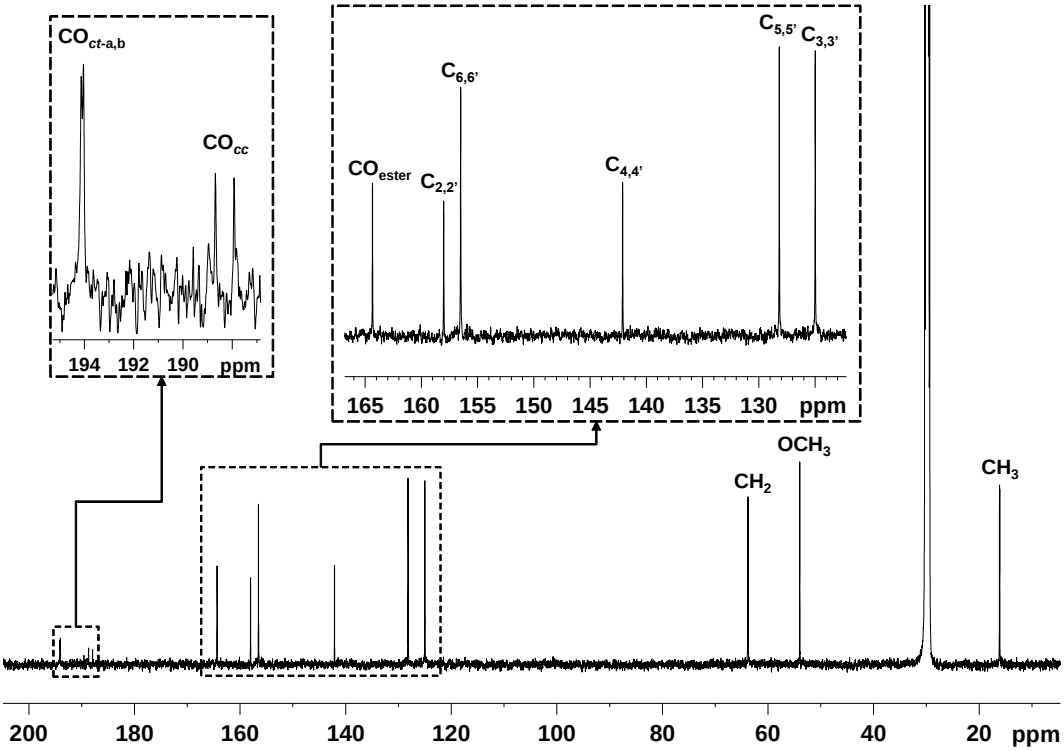

Figure 2.29 – ^{13}C NMR spectrum of [Re(BMCbpy)(CO)$_3${P(OEt)$_3$}][PF$_6$] (R4–b) in acetone–d_6 (125.7 MHz) at 298 K

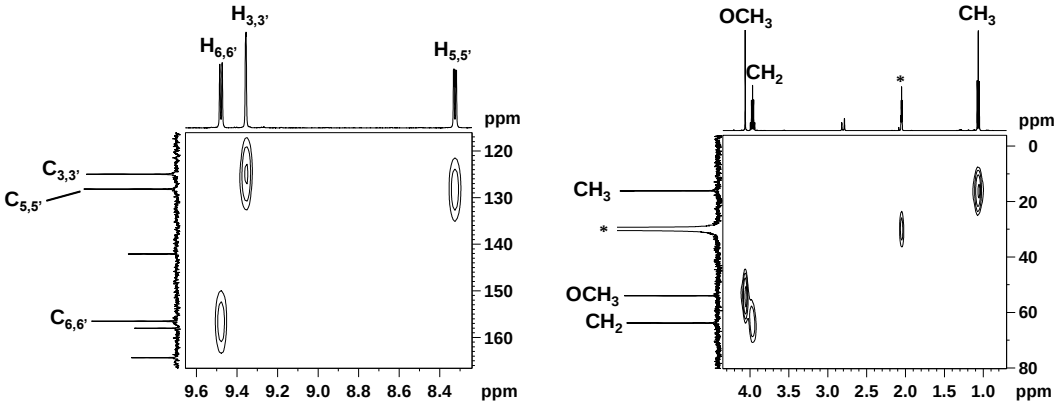

Figure 2.30 – ^{1}H –^{13}C HSQC spectrum sections of [Re(BMCbpy)(CO)$_3${P(OEt)$_3$}][PF$_6$] (R4–b) in acetone–d_6 (500 MHz) at 298 K

The presence of the hexafluorophosphate is detected by fluorine and phosphorus NMR spectroscopy and a singlet corresponding to the coordinated phosphite is also observed slightly above 100 ppm (data not shown, see Appendix I on page 122).

- *[4,4'–bis(methoxycarbonyl)–2,2'–bipyridine]tricarbonyl (difluorophosphate–1κO)rhenium(I) hexafluorophosphate: [Re(BMCbpy)(CO)$_3$(OPOF$_2$)][PF$_6$] (**R5**)*

Due to the absence of protons in the difluorophosphate, the signals expected for this compound are the same than for those of the bromide precursor (Figure 2.17).

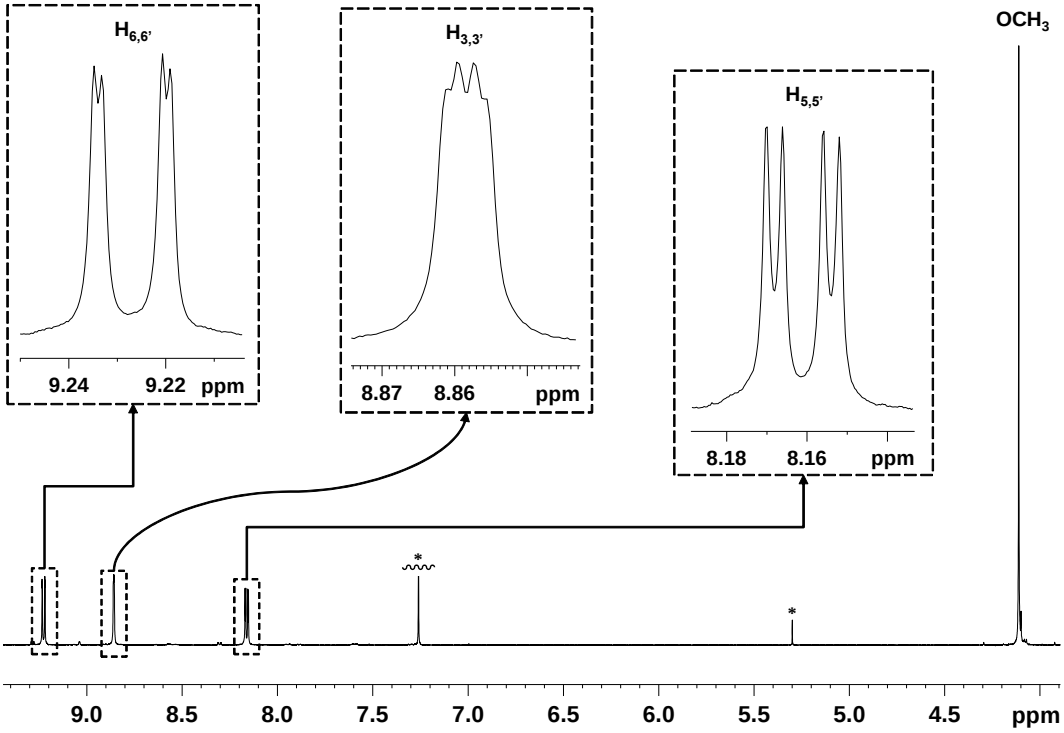

Figure 2.31 – ^{1}H NMR spectrum of [Re(BMCbpy)(CO)$_3$(OPOF$_2$)] (R5) in CDCl$_3$ (400 MHz) at 298 K

Although the ^{19}F NMR spectrum appears to be similar to that of the hexafluorophosphate anions, the presence of a triplet instead of a septet in the ^{31}P NMR spectrum and the higher coupling constant value (970 Hz) than for the hexafluorophosphate (around 700 Hz), indicates the existence of the difluorophosphate species, which was also confirmed by X–ray crystallography and matches with previously reported spectroscopic data for similar compounds.[53]

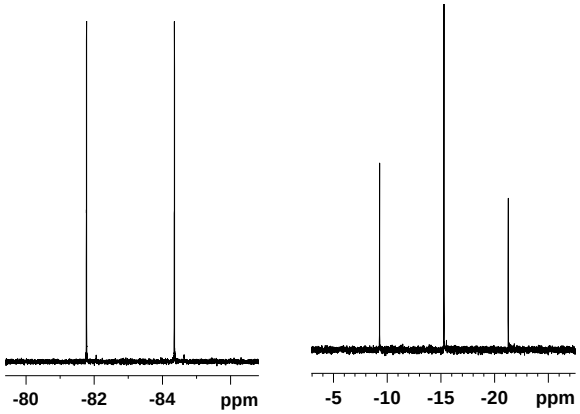

Figure 2.32 – ^{19}F (376.4 MHz, left) and ^{31}P (161.9 MHz, right) NMR spectra of [Re(BMCbpy)(CO)$_3$(OPOF$_2$)] (R5) in $CDCl_3$ at 298 K

The electron distribution of the rhenium complexes can be qualitatively analyzed from the chemical shifts of the bipyridine protons, summarized in Table 2.1.

Bipyridine	Ligand	Compound	$H_{6,6'}$	$H_{3,3'}$	$H_{4,4'}$	$H_{5,5'}$
bpy (*a* series)	—	**bpy**	8.68	8.39	7.81	7.30
	Br^-	**R1–a**	9.10	8.21	8.08	7.55
	CH_3CN	**R2–a**	8.93 (9.23)	8.48 (8.82)	8.25 (8.50)	7.65 (7.94)
	3–Pic	**R3–a**	(9.50)	(8.73)	(8.47)	(8.01)
	$P(OEt)_3$	**R4–a**	8.89	8.74	8.32	7.62
BMCbpy (*b* series)	—	**BMCbpy**	8.87*	8.96*	—	7.91
	Br^-	**R1–b**	9.23	8.85	—	8.08
	CH_3CN	**R2–b**	9.09 (9.46)	8.98 (9.42)	—	8.20 (8.34)
	3–Pic	**R3–b**	(9.74)	(9.23)	—	(8.32)
	$P(OEt)_3$	**R4–b**	(9.47)	(9.35)	—	(8.16)
	$PO_2F_2^-$	**R5**	9.23	8.96	—	8.16

Table 2.1 – ^1H chemical shifts of the bipyridine rings protons (in ppm) of bpy, BMCbpy and rhenium complexes prepared in this work. Values are shown for $CDCl_3$ (plain text) or acetone–d_6 (values in brackets). *Note the sequence inversion.

Due to solubility limitations, it was necessary to employ different solvents to run the NMR experiments, which makes it difficult to compare results. Nevertheless, some conclusions can be extracted from the data shown above if we restrict the discussion to partial subgroups of experiments where the same solvent was employed.

First, comparing the data for **bpy** and **BMCbpy**, the inclusion of the electron withdrawing group induces a general deshielding effect. This effect is more significant for protons in *ortho* positions to the methoxycarbonyl group ($H_{3,3'}$ $H_{5,5'}$), with shifts around 0.6 ppm, compared with the one in the *meta* position ($H_{6,6'}$), being about 0.2 ppm. The difference is big enough to reverse the order of $H_{6,6'}$ and $H_{3,3'}$ signals in the BMCbpy ^{1}H NMR spectrum. This can be explained considering that those positions are affected by the resonant effect of the substituent, whereas the last one is only affected by inductive effects (Figure 2.33).

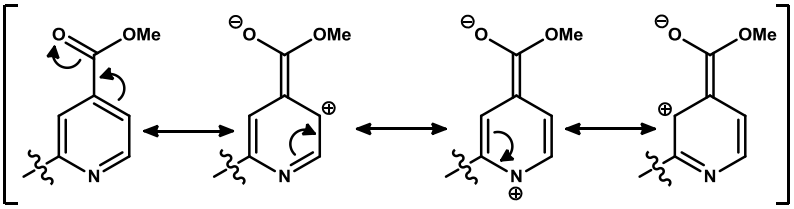

Figure 2.33 – Representation of resonant forms that illustrate the –R effect of the methoxycarbonyl substituent on the bipyridine ring. Only half molecule is shown for clarity.

The coordination to the metal center (**bpy** *vs*. **R1–a** and **BMCbpy** *vs* **R1–b**) results in a downfield shift for $H_{6,6'}$ and $H_{5,5'}$ but a smaller shift toward higher field for $H_{3,3'}$. This new shift is big enough to invert the order of the $H_{6,6'}$ and $H_{3,3'}$ signals again. It can be understood if we consider that the H_6 and $H_{6'}$ protons are located closer to the bipyridine nitrogen coordinated to the metal center and the deshielding effect observed can be due to electron donation from the ligand to the rhenium atom.

When substituting the bromide by acetonitrile, moving from a neutral to a cationic complex, the signal of $H_{6,6'}$ experiences a decrease of around 0.15 ppm whereas $H_{3,3'}$ and $H_{5,5'}$ are deshielded in a magnitude between 0.1 and 0.3 ppm.

If we only analyze the signals of the protons closer to the nitrogen atom (H_6 and $H_{6'}$) of the set of cationic complexes, we can see that the substitution of the acetonitrile by the picoline produces a significant downfield shift, suggesting a higher participation of the bipyridine in the electron donation, whereas only small changes are observed when triethyl phosphite is employed. This may indicate that acetonitrile and $P(OEt)_3$ bind to the rhenium center in a similar fashion.

The two BMCbpy neutral compounds **R1–b** and **R5**, show very similar chemical shift values for all the protons and exactly the same for $H_{6,6'}$.

Infrared spectroscopy

The rhenium carbonyls presented in this work can be divided into three groups according to their molecular symmetry, considering that all of them are geometrically octahedral and, except $Re(CO)_5Br$, *fac* isomers with two adjacent coordination positions occupied by the bipyridine ligand. If we take into account only the atoms directly coordinated to the metal, those complexes with a third nitrogen–based ligand like picoline or acetonitrile will exhibit a higher symmetry than those with a different atom, due to the existence of a *pseudo–*C_{3v} symmetry environment around the metal center. Those without a third nitrogen atom will only possess a symmetry plane (C_s) as shown in Figure 2.34.

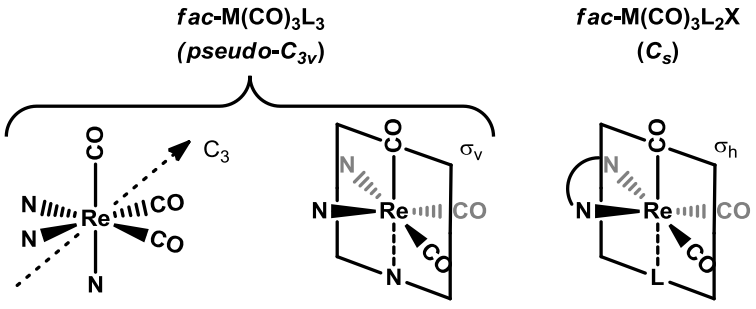

Figure 2.34 – Representative examples of symmetry elements of generalized formulae of the rhenium complexes prepared in this work

Applying simple group theory, considering the symmetry of the different molecules and the CO stretching vectors, it is possible to predict the number of vibrational modes that will be active in IR.

Complexes	Symmetry	IR active modes
[Re(CO)$_5$Br]	C_{4v}	$2\,A_1 + E$
R1–a, **R4–a, R1–b**, **R4–b, R5**	C_s	$2\,A' + A''$
R2–a, **R3–a**†, **R2–b**, **R3–b**	*pseudo*–C_{3v}	$A_1 + E$

Table 2.2 – Symmetry and expected IR active modes for the Re complexes prepared in this work. Note that the intensities of the ν_{CO} bands should all be approximately equal for a *fac*—M(CO)$_3$ unit

†Although both picoline (**R3**) complexes are expected to exhibit *pseudo*–C_{3v} symmetry, this is not entirely observed in the case of **R3–a**, see below for further comments. For those complexes corresponding to the *b* series, with BMCbpy, an additional CO stretching band can be expected due to the presence of the ester carbonyl group in the region between 1650 and 1790 cm^{-1}. All IR spectra have been obtained in the same solvent (THF) in order to establish comparisons.

Previously reported references were employed to assign specific vibrational modes to each band (see Section 6.6, on page 110). For the non pseudosymmetric compounds, some contradictions were found within literature values. In all cases, the symmetric stretching band at higher wavenumber corresponds to one of the *A*' symmetry modes, but different orders for the other two bands (*A*' and *A*'') have been reported for similar compounds with phosphorus and nitrogen based ligands,[59,60] although the ligand nature should not have any influence on this. For the purposes of this project, the assignment reported on the most recent reference is employed.[60] Finally, for the *pseudo*–C_{3v} complexes, the band at lower energy arises from the collapse of the two bands present in the less symmetric compounds and corresponds to the doubly degenerate *E* mode.

- *C_{4v} – Bromopentacarbonylrhenium(I): [$Re(CO)_5Br$]*

The three signals of the pentacarbonyl precursor illustrated in Figure 2.35 match approximately with the previously described ones.[61]

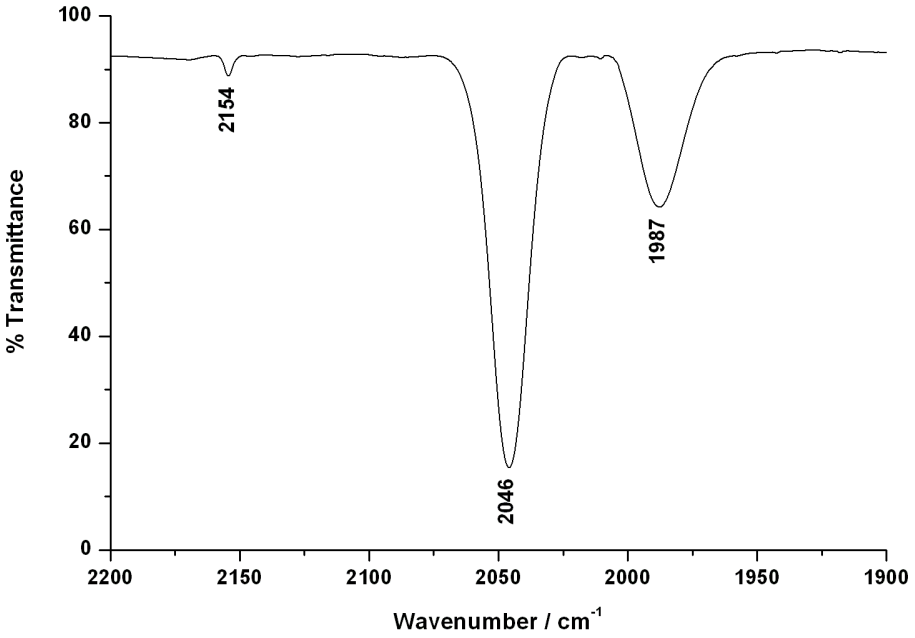

Figure 2.35 – IR spectrum of [$Re(CO)_5Br$] in THF

- C_s – L = Br^- (**R1–a,b**), L = $P(OEt)_3$ (**R4–a,b**), L = $PO_2F_2^-$ (**R5**)

In the representative case of [$Re(bpy)(CO)_3Br$] (**R1–a**), three bands are also expected and all of them can be observed in Figure 2.36.

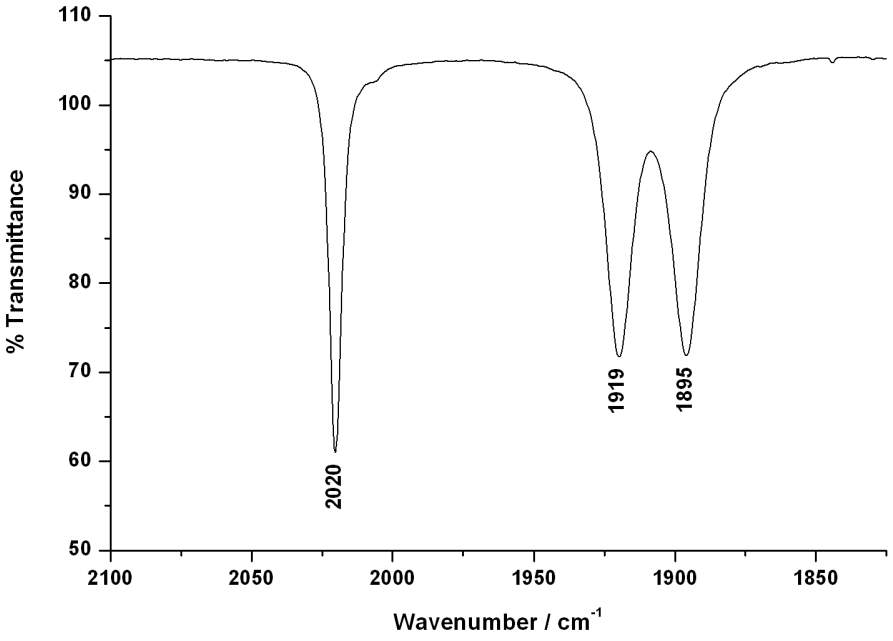

Figure 2.36 – IR spectrum of [Re(bpy)(CO)$_3$Br] (R1–a) in THF

When the BMCbpy derivative **R1–b** was employed, the spectrum observed was analogous to the one for the unsubstituted bipyridine complex (**R1–a**) in Figure 2.36, with the addition of the band corresponding to the ester carbonyl group (Figure 2.37).

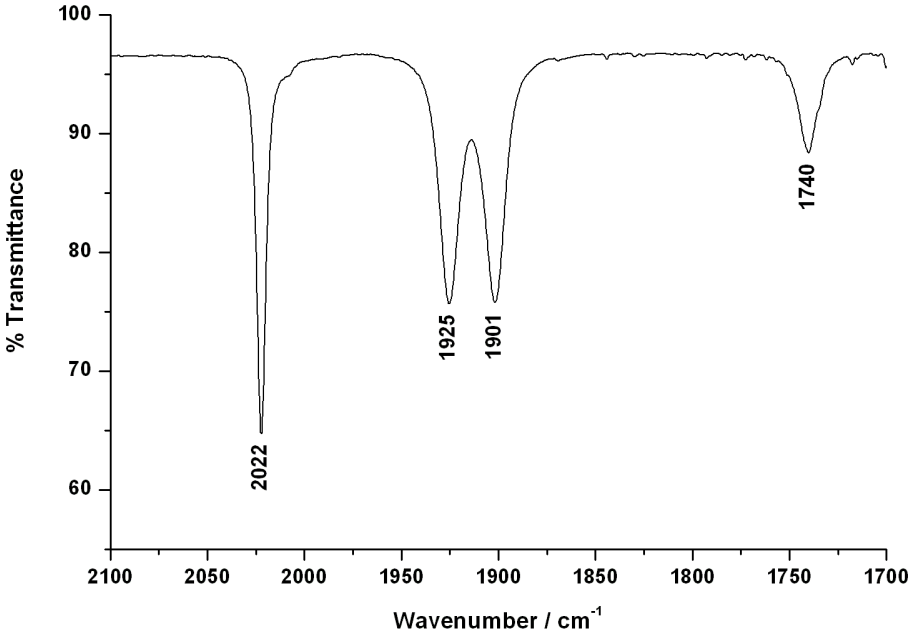

Figure 2.37 – IR spectrum of the complex [Re(BMCbpy)(CO)$_3$Br] (R1–b) in THF

Similar spectra were obtained for the triethylphosphite (**R4–a,b**) and difluorophophate (**R5**) analogues (see Appendix I on page 122).

- *Pseudo–*C_{3v} – L = CH_3CN (**R2–a,b**), L = 3–Pic (**R3–a,b**)

The predicted structure with one sharp peak and a broad band made from the other two peaks collapsing around the same value was observed in the case of $[Re(bpy)(CO)_3(CH_3CN)][PF_6]$ (**R2–a**) (Figure 2.38). The fact that the *E* symmetry band at lower wavenumber is broader that the A_1 one or the bands observed for the bromide precursor **R1–a** is due to the non–entire equivalency of the three nitrogen atoms.[60] This indicates that, in terms of interaction with the rhenium center, no significant differences between the bipyridine and the acetonitrile nitrogen atoms exist.

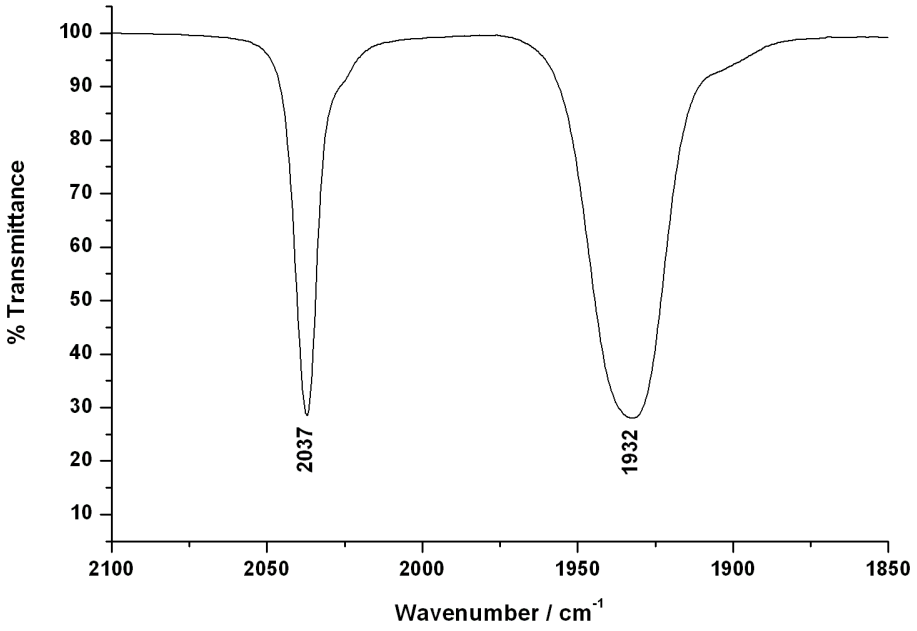

Figure 2.38 – IR spectrum of $[Re(bpy)(CO)_3(CH_3CN)][PF_6]$ (R2–a) in THF

As for the C_s symmetric compounds, the additional ester band is observed for the BMCbpy derivatives, without major changes in the rest of the spectrum, again with the *E* symmetry band significantly broader than the A_1 one.

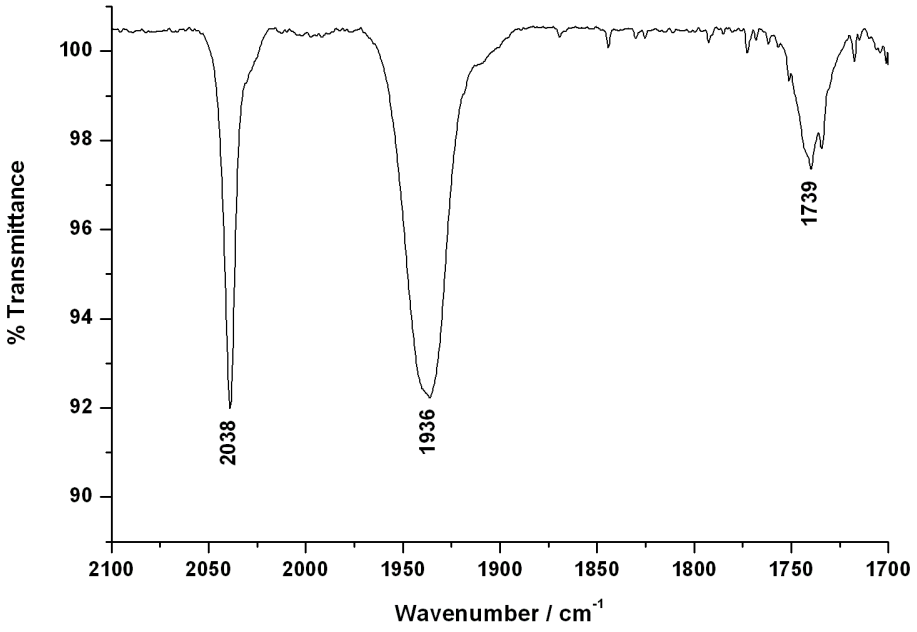

Figure 2.39 – IR spectrum of [Re(BMCbpy)(CO)$_3$(CH$_3$CN)][PF$_6$] (R2–b) in THF

The same results were obtained when acetonitrile was substituted by 3–picoline (Figure 2.40), although some differences were obtained in the case of the unsubstituted bipyridine derivative.

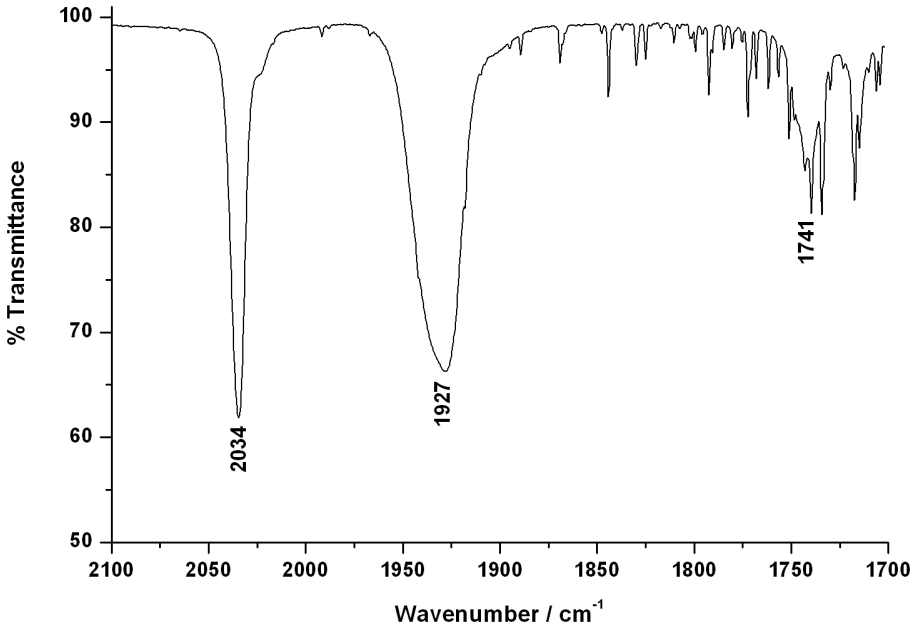

Figure 2.40 – IR spectrum of [Re(BMCbpy)(CO)$_3$(3–Pic)][PF$_6$] (R3–b) in THF

According to the previous discussion, we should also expect two bands for this compound due to its *pseudo–*C_{3v} symmetry around the rhenium, but one clear peak and a two–minimum broad band, are actually observed (Figure 2.41).

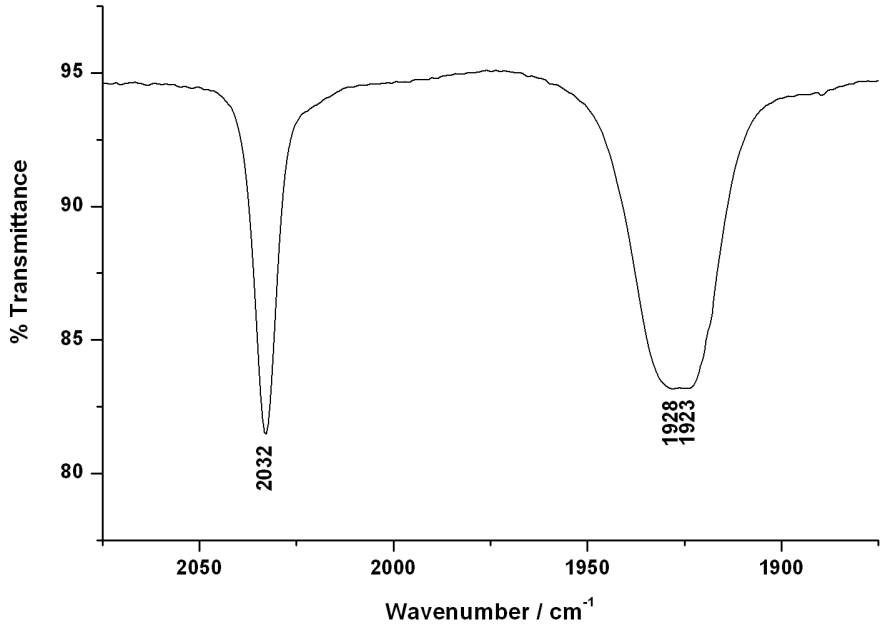

Figure 2.41 – Infrared spectrum of [Re(bpy)(CO)$_3$(3–Pic)][PF$_6$] (R3–a) in THF

This has to be due to the existence of small but noticeable differences between the two types of nitrogen atoms, although all of them are aromatic (sp^2). This evidence surprisingly suggest that these three sp^2 nitrogen atoms interact with the metal in a more different way than in the case of the acetonitrile precursor **R2–a**, with two sp^2 and one *sp*–hybridized nitrogen atoms (Figure 2.38). It should be noticed that this does not depend entirely on the nature of the complex and different results can be expected in different solvents; for instance, in acetonitrile, those two peaks are separated by 35 cm^{-1} for the hexafluroroantimonate derivative.[59]

In the same way that the chemical shift of the bipyridine protons close to the nitrogen atoms have been employed to estimate the involvement of the bipyridine in the metal–ligand bond, the CO stretching frequencies (see Table 2.3) can be used to study the electron density on the rhenium center. Considering what was exposed before about the nature of the Re–CO bond, due to the existence of

backdonation from the metal to a pair of antibonding orbitals of the carbonyl ligand, a higher electron density on the rhenium center will imply higher backbonding. The filling of the CO π–antibonding orbitals weakens the C≡O bonds, shifting the stretching wavenumbers toward smaller values, so the electron density over the rhenium center can be said to be inversely related to the wavenumber of the bands.

Ligand	**Bipyridine**	C_s	**A' (1)**	**A' (2)**	**A''**	**ester**
Br	bpy	**R1–a**	2020	1919	1895	—
	BMCbpy	**R1–b**	2022	1925	1901	1740
$P(OEt)_3$	bpy	**R4–a**	2042	1958	1926	—
	BMCbpy	**R4–b**	2044	1963	1932	1740
$PO_2F_2^-$	BMCbpy	**R5**	2030	1930	1910	1741
Ligand	**Bipyridine**	***pseudo*–C_{3v}**	**A_1**	***E***		***ester***
CH_3CN	bpy	**R2–a**	2037	1932		—
	BMCbpy	**R2–b**	2038	1936		1739
3–Pic	bpy	**R3–a**[†]	2032	1925		—
	BMCbpy	**R3–b**	2034	1927		1741

Table 2.3 – Infrared CO stretching frequencies (in cm^{-1}) of the rhenium complexes prepared in this work. Compounds are classified by apparent symmetry around the metal center. [†]The mean of the two minima observed for R3–a is employed.

First of all, if we analyze the stretching frequency of the ester band, almost no difference is found for any of the *b*–series complexes, which is not surprising considering the big separation between the ester functional group and the rest of the molecule.

If we focus on the CO stretching bands, probably the most interesting fact is that almost no change is observed when moving from the *a* to the *b* series. Despite the high electron withdrawing ability of the methoxycarbonyl groups on the

bipyridine, the electron density around the rhenium center is essentially the same. This implies that electronic environment of the rhenium is not affected by the substitution of the bipyridine, although the same was not true for the electron density around the bipyridine, analyzed by ^{1}H NMR spectroscopy, which suggest that the changes induced by the substitution of the bipyridine are somehow compensated by the remaining ligands.

When the substitution of the ligands is studied, the first obvious classification is dividing all the complexes in neutral (**R1**, **R5**) or cationic (**R2**, **R3**, **R4**). It can be observed that for all the neutral complexes, the bands (*A*'(1) or A_1 depending on the symmetry) appears at lower wavenumber than the analogous for the cationic ones, which implies a higher electron density around the metal, consistent with the charge of the complex.

Comparing the different neutral compounds, the bromides (**R1**) exhibit higher electron density around the rhenium than the difluorophosphate one (**R5**). This bigger interaction between the rhenium atom and the bromide can be understood considering two factors: i) the lower electronegativity of the bromine, compared with the oxygen atom and ii) the soft character of the rhenium (third row transition metal), which will make it interact better with *soft* and polarizable Lewis bases like the bromide anion than with *hard* ones, like the oxygen–bonded difluorophosphate.

If we order the ligands of the cationic complexes according to the electron density over the rhenium, the result is 3–Pic > CH_3CN > $P(OEt)_3$, with differences around 5 cm^{-1} when moving from one ligand to the next one. The phosphite complexes are the ones with less electron density over the rhenium, since it is the only ligand that can also act as π–acceptor. Between the picoline and the acetonitrile ligands, a plausible cause will be that the sp^2 nitrogen atom of the picoline ligand, with a 66% of *p*–character, may be easier to polarize than the *sp* one of the acetonitrile, with only a 50%, and therefore a more effective donation over the rhenium takes place, increasing its electron density.

X–ray crystallography

Some of the new complexes prepared in this work and a previously described complex made in this group[45] have been characterized by X–ray crystallography and the results obtained are briefly discussed. Molecular structures of $[Re(BMCbpy)(CO)_3(CH_3CN)][PF_6]$ (**R2–b**), $[Re(bpy)(CO)_3(3–Pic)][PF_6]$ (**R3–a**) and $[Re(BMCbpy)(CO)_3(OPOF_2)]$ (**R5**) are shown in Figure 2.42.

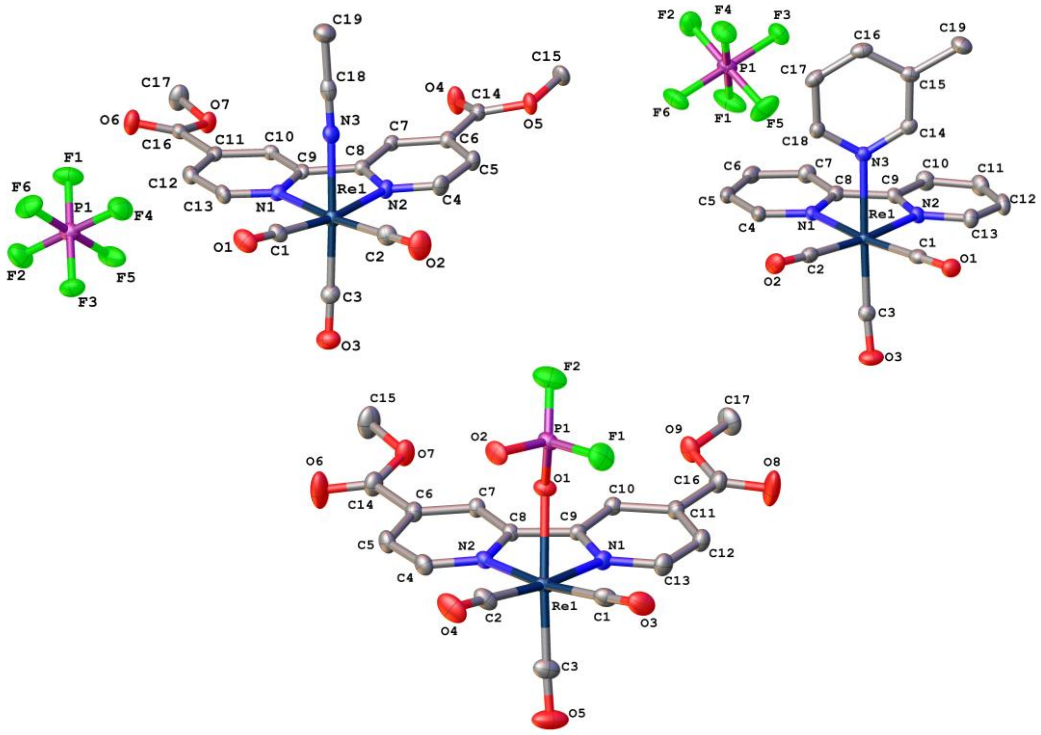

Figure 2.42 – ORTEP diagrams of $[Re(BMCbpy)(CO)_3(CH_3CN)][PF_6]$ (R2–b) (top left), $[Re(bpy)(CO)_3(3–Pic)][PF_6]$ (R3–a) (top right) and $[Re(BMCbpy)(CO)_3(OPOF_2)]$ (R5) (bottom) with thermal ellipsoids shown at 50% probability. Hydrogen atoms are omitted for clarity.

Refinement parameters were good in all cases (see Appendix II on page 125) and no disorder was found for any of the structures.

The space group was found to be $P2_1/c$ in all cases, belonging to the monoclinic crystal system, with a primitive lattice and presenting two–fold screw axes along *b*, c–type glide planes perpendicular to *b* and inversion centers (see Figure 2.43 for an illustrative example), therefore being a centrosymmetric space group.

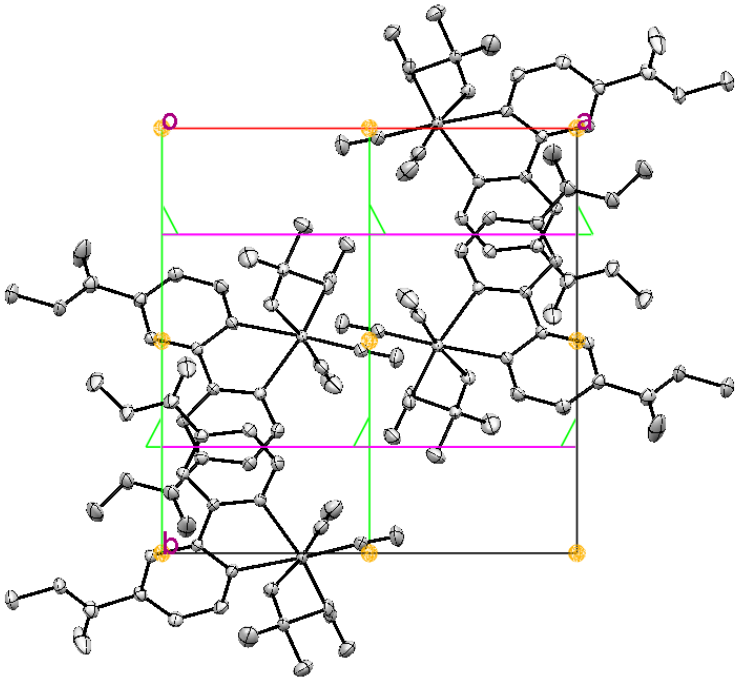

Figure 2.43 – Crystal unit cell of [Re(BMCbpy)(CO)$_3$(OPOF$_2$)] (R5). View along the *c* axis. Symmetry elements of the P2$_1$/c space group represented as green lines (two–fold screw axes), pink lines (glide planes) and yellow spots (inversion centers).

Selected bond distances and angles are shown in Table 2.4. The two cationic complexes **R3–a** and **R2–b** show very similar bond lengths except for the Re–N bond corresponding to the picoline or the acetonitrile molecule, being shorter in the case of the acetonitrile complex. This result is consistent with the *sp* character of the acetonitrile nitrogen bond compared to the sp^2 nitrogen of the picoline ring. When comparing **R5** with **R3–a** and **R2–b**, most distances are similar with the exception of the Re–C of the carbonyl groups. In the neutral complex (**R5**), the carbonyl group in *cis* position to the two bipyridine rings (C_{cc}) is closer to the metal than the other two carbonyl groups ($C_{ct\text{-}a,b}$), whereas in the cationic complexes this order is reversed, with differences bigger than the standard deviation of the bond lengths.

Complex	R3–a (X = N)	R2–b (X = N)	R5 (X = O)
Re—N1	2.1730(17)	2.176(3)	2.172(2)
Re—N2	2.1672(17)	2.168(3)	2.148(2)
Re—C_{cc}	1.933(2)	1.930(4)	1.903(3)
Re—$C_{ct\text{-}a}$	1.918(2)	1.918(4)	1.930(3)
Re—$C_{ct\text{-}b}$	1.917(2)	1.924(4)	1.921(3)
Re—X	2.2081(18)	2.120(4)	2.1541(19)
N1–Re–N2	75.14(7)	75.48(11)	74.76(8)
N1–Re–X	84.15(6)	83.21(12)	78.66(8)
N2–Re–X	85.74(7)	81.64(12)	79.23(8)

Table 2.4 – Selected bond lengths (A — B / Å) and angles (A – B – C / deg) for compounds R3–a, R2–b and R5. Values in brackets represent absolute standard deviation and *X* denotes the heteroatom directly bonded to the rhenium center. For carbon atoms notation see Figure 2.2 on page 28.

The bond angles between the two bipyridine nitrogen atoms and the rhenium center are very similar in all cases, but the angle between one of those and the heteroatom of the additional ligand is significantly smaller for **R5** than for the two cationic complexes, which indicates that in the neutral complex, the ligand is bent towards the bipyridine ring. However, this result was also found in the case of [Re(bpy)(CO_3)($OPOF_2$)], with similar distances and angles.[62] Finally, the orientation of one of the methoxycarbonyl groups of the **R2–b** and **R5** were compared (Figure 2.44). This was found to be due to short interactions between one of the hydrogen atoms on the methyl group with the hexafluorophosphate counterion.

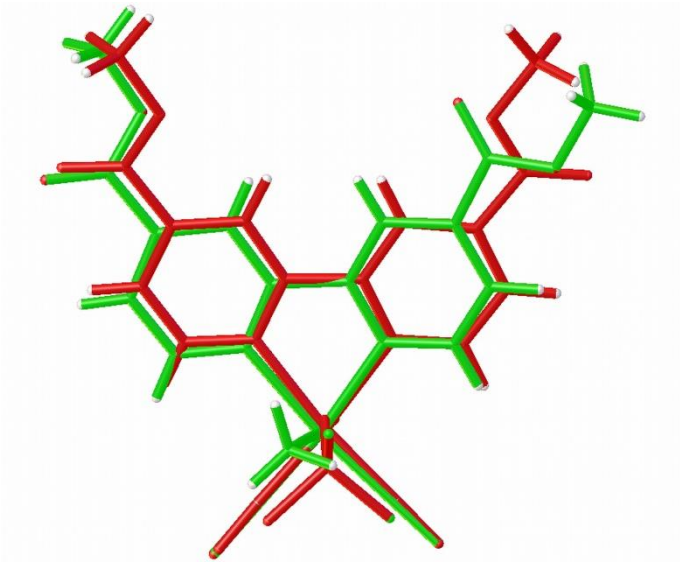

Figure 2.44 – Superimposition of [Re(BMCbpy)(CO)$_3$(CH$_3$CN)][PF$_6$] (R2–b) and [Re(BMCbpy)(CO)$_3$(OPOF$_2$)] (R5) structures. In both cases, rhenium center and oxygen atoms of the carbonyl ligands were fixed at the same positions, to illustrate the differences on the BMCbpy moiety.

Chapter 3. Electrochemistry

Both porphyrins and rhenium complexes exhibit well–known redox activity and have been characterized by cyclic voltammetry in order to measure the first oxidation or reduction potential respectively, although in some particular cases this study was extended beyond the first redox steps.

When comparing with previously reported values, +0.48 V is taken as the halfwave potential of ferrocene/ferrocenium couple (Fc/Fc^+) vs. Ag/AgCl reference electrode.[63] The Fc/Fc^+ oxidation process has been proved to be independent of the polarity of the solvent[64–66] and the nature of the supporting electrolyte employed.[67] However, strong dependence on the supporting electrolyte concentration[68] and influence of the anion of the reference electrode silver salt or its concentration have been recently summarized and serious doubts have raised about establishing comparison when this couple is used as internal reference.[69] Because the aim of our measurements is to compare and employ only the results obtained within this work and not any previously reported data, the method employed is suitable, because all the experiments have been run under the same experimental conditions. Comparisons with previous results are included but should be taken only as illustrative examples. All potentials in the present Chapter are quoted relative to the ferrocene/ferrocenium couple and literature values have been converted when values related to a different reference were reported.

3.1 Porphyrins

Literature values for the different porphyrins in the most similar conditions to those employed in this work were obtained from different sources as cited by Kadish *et. al.*[70] In the case of **ZnTPP** (**P1**), two oxidation and one reduction steps were observed inside the scan window employed. The symmetry of all the peaks in Figure 3.1 proves that all the processes are single–electron steps and the peak–to–peak distances (between 80 and 91 mV) illustrate their reversibility, falling in the range between reversible and quasi–reversible processes.

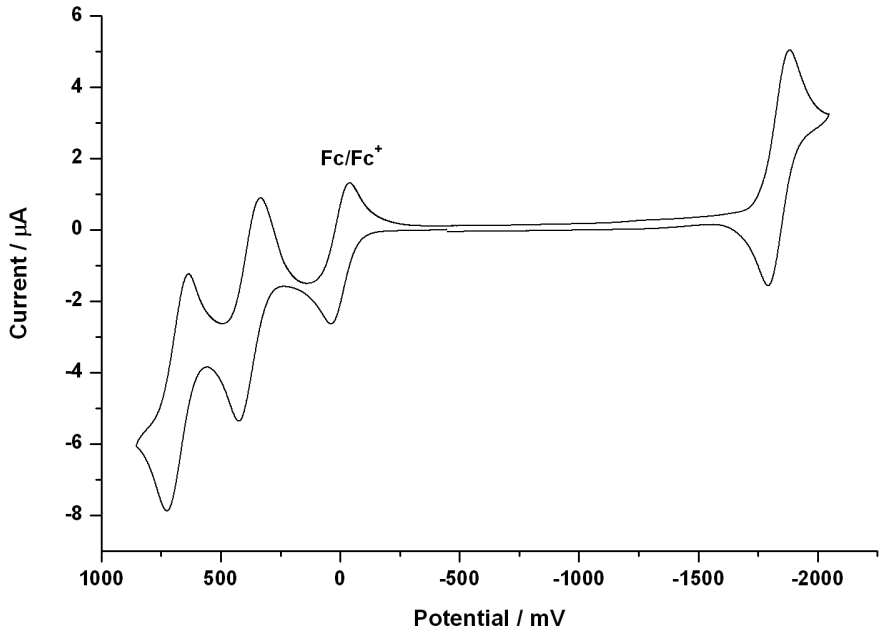

Figure 3.1 – Cyclic voltammogram of ZnTPP (P1) with added ferrocene. CH_2Cl_2 2.5 mM ZnTPP, 0.1 M $TBAPF_6$, 0.8 mM Fc, scan rate 50 mV/s

Oxidation halfwave potential values obtained are listed together later with those of the other porphyrins (see Table 3.1 on page 70), matching significantly well with previously reported data.[63,71–74]

In this case of **ZnTTP** (**P2**), and all the following ones, only the oxidation region was studied. Values obtained were in good agreement with those reported in the literature,[73,75] being also single–electron quasi–reversible processes, as shown by the symmetric shape and the distance between the anodic and cathodic peaks of both processes.

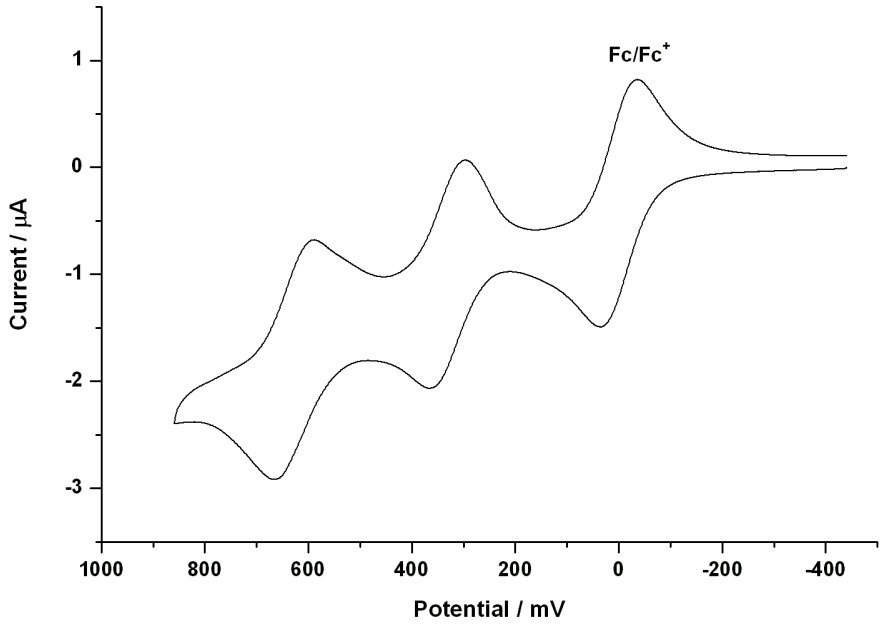

Figure 3.2 – Cyclic voltammogram of ZnTTP (P2) in the presence of ferrocene. CH_2Cl_2 2.5 mM ZnTTP, 0.1 M $TBAPF_6$, 0.8 mM Fc, scan rate 50 mV/s

In the case of **ZnTTBPP** (**P3**), only the first oxidation step could be studied due to the appearance of secondary processes when scanned beyond this point. The reason why this specific porphyrin does not exhibit a clean redox profile remains unknown; we suggest it may be due to the formation of some activated byproducts, such as radicals, which induces subsequent chemical processes. This will be favored due to the high stability conferred by the *tert*–butyl groups, either by hyperconjugation or homodissociation of one of the methyl residues, mechanisms that are not possible for any of the other porphyrins employed in this work. In addition, non–completely reversible waves were obtained at 50 and 100 mV/s scan rates; however, at 200 mV/s the processes became quasi–reversible, suggesting relatively slow kinetics for these secondary processes. This peculiarity is not described in previous work.[76] Nevertheless, the first oxidation halfwave potential reported is consistent with our results. The concentration of porphyrin employed in that case was five times smaller, what induces us to believe that this could be the origin of this different behavior.

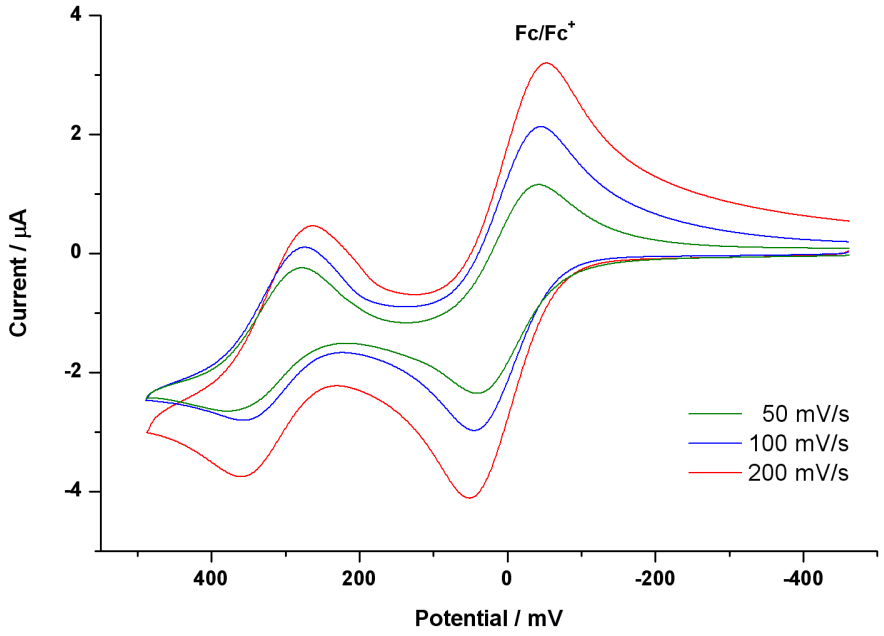

Figure 3.3 – Cyclic voltammograms of ZnTTBPP (P3) in the presence of ferrocene. CH_2Cl_2 2.5 mM ZnTTP, 0.1 M $TBAPF_6$, 0.8 mM Fc at scan rates from 50 to 200 mV/s

The methoxyphenyl derivative **ZnTMPP** (**P4**) exhibited the same oxidation profile as **P2** (see Appendix III on page 126), and the halfwave potential values match previously reported data,[77] as cited by Schmidt and Schuster.[78]

Table 3.1 summarizes the electrochemical data obtained for the different Zn(II)–metallated *meso*–tetrasubstituted porpyrins used in this work (**P1**–**P4**).

Substituent	Porphyrin	$^{1st}E_{1/2}$ / V	$^{2nd}E_{1/2}$ / V	Reported $^{1st}E_{1/2}$ / V
–H	**P1**	+ 0.38	+ 0.68	+ 0.36[73]
$–CH_3$	**P2**	+ 0.33	+ 0.63	+ 0.32[73]
$–C(CH_3)_3$	**P3**	+ 0.32	—	+ 0.35[76]
$–OCH_3$	**P4**	+ 0.28	+ 0.57	+ 0.26[77,78]

Table 3.1 – Halfwave potentials of first (P^0/P^+) and second (P^+/P^{2+}) oxidations of the porphyrins studied. Experimental conditions: CH_2Cl_2, 2.5 mM Porphyrin, 0.1 M $TBAPF_6$, 0.8 mM Fc

We can conclude that substitution of the porphyrin phenyl ring with increasing electron donating groups systematically decreases the value of the oxidation potentials, making the porphyrins more easily oxidized. This is in good agreement with the idea of electron donation coming from the substituent, by either inductive or mesomeric effects, compensating the electron withdrawal during the oxidation process and stabilizing the cationic species formed afterwards.

3.2 Rhenium complexes

In all cases only the first reduction step was studied. Nice single–electron reversible/quasi–reversible waves were obtained for most compounds except for both acetonitrile derivatives (**R2–a**,**b**), which will be separately discussed later.

In the case of the bipyridine picoline complex (**R3–a**), the reduction step was found to occur with a halfwave potential of –1.57 V, as shown in Figure 3.4, presenting the general characteristics mentioned above. This exactly matches with the reported value for this complex, measured under the same conditions in our research group.[45] Figure 3.4 can be taken as the standard example for bromide and phosphite rhenium complexes bearing unsubstituted bipyridine ligands.

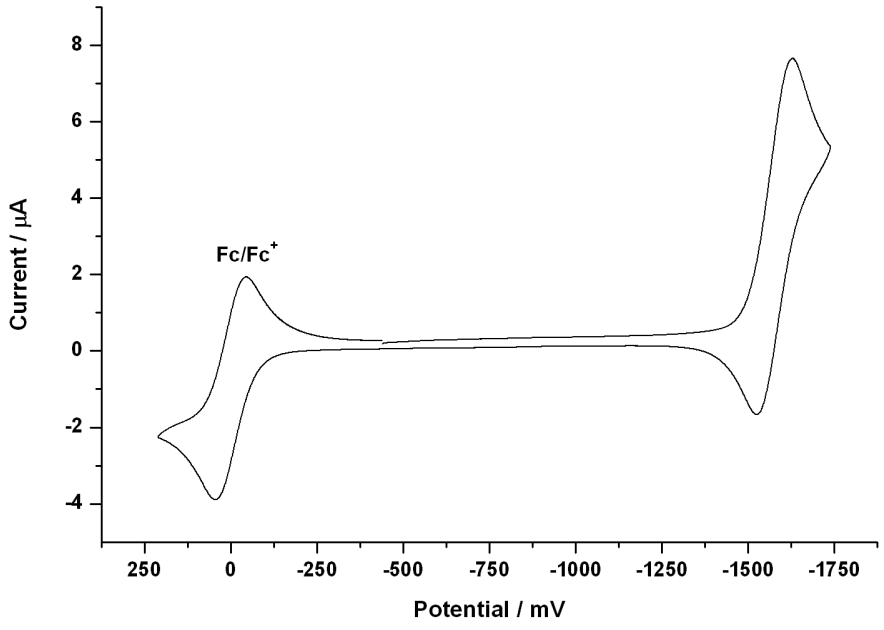

Figure 3.4 – Cyclic voltammogram of [Re(bpy)(CO)$_3$(3–Pic)][PF$_6$] (R3–a). CH$_2$Cl$_2$ 2.5 mM Re complex, 0.1 M TBAPF$_6$, 0.8 mM Fc, scan rate 50 mV/s

Although there are no significant changes in the shape of the band when methoxycarbonyl substituents are anchored to the bipyridine core, the reduction wave was considerably shifted toward less negative values, as can be observed in Figure 3.5. This shows the strong effect which has the substitution on the bipyridine ring has on the electrochemical properties of the rhenium complexes, significantly higher than ligand substitution, which produces much smaller shifts. The relative influence of the different factors will be discussed later on. Similar results are obtained with acetonitrile or triethyl phosphite analogues

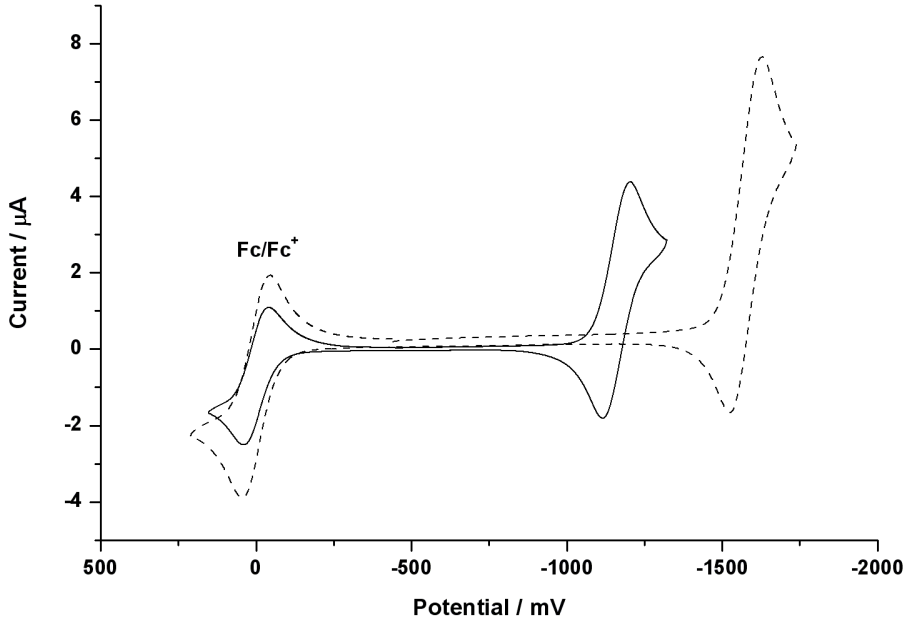

Figure 3.5 – Cyclic voltammograms of [Re(BMCbpy)(CO)$_3$(3–Pic)][PF$_6$] (R3–b) (solid line) and R3–a (Figure 3.4, dashed line). CH$_2$Cl$_2$ 2.5 mM Re complex, 0.1 M TBAPF$_6$, 0.8 mM Fc

In the case of acetonitrile compounds, more complex electrochemistry was found. The case of the substituted bipyridine complex (**R2–b**) will be discussed first because of the simpler appearance of its cyclic voltammograms. In Figure 3.6 it is possible to observe that, at the same scan rate as used in other experiments (50 mV/s, green line), the reduction wave exhibited a typical irreversible profile, but when scan rate was increased, the reversibility of the process became progressively higher. This is compatible with the existence of a chemical process taking place after the electrochemical reduction. Considering the chemical nature of this compound, this is probably caused by a dissociation of the acetonitrile

molecule once the complex has been reduced. The fact that the process became quasi–reversible when the scan rate was further increased suggests that dissociation might become slower than the reoxidation process at those rates, so the reduced species can be reoxidized before dissociation takes place, showing a small but partial stability of the reduced complex of, at least, a few seconds.

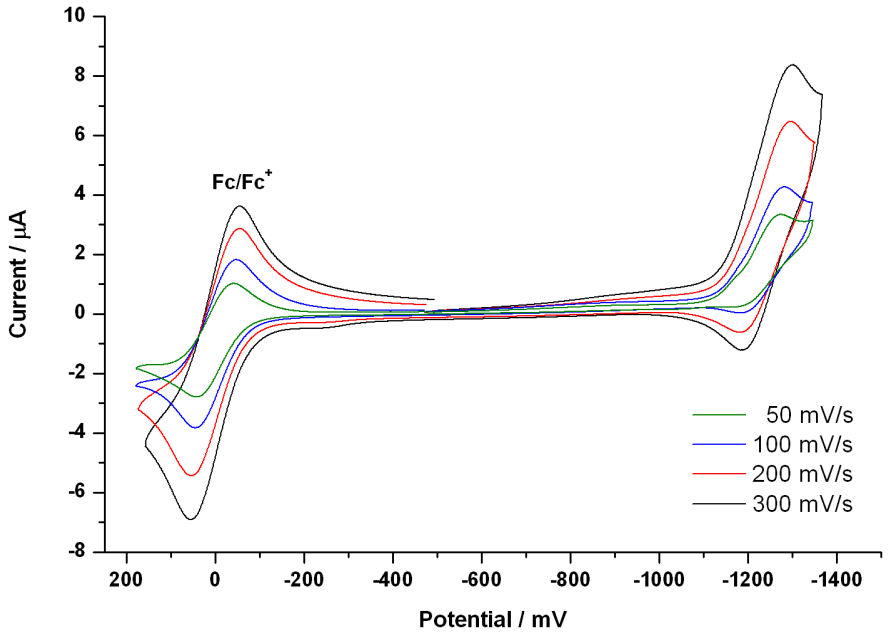

Figure 3.6 – Cyclic voltammograms of [Re(BMCbpy)(CO)$_3$(CH$_3$CN)][PF$_6$] (R2–b) at different scan rates. CH$_2$Cl$_2$ 2.5 mM Re complex, 0.1 M TBAPF$_6$, 0.8 mM Fc.

The case of the analogous complex with parent bipyridine (**R2–a**) is slightly more complex and probably additional secondary reactions take place. In this case, the first reduction step never became reversible at any scan rate employed, and a subsequent quasi–reversible process took place in all cases. Again, it is reasonable to ascribe this to an acetonitrile dissociation process after reduction. However, in this case, results suggest a much faster dissociation and formation of some derivative species which can be further reduced and reoxidized in an apparently reversible manner. In this case, the maximum of the first reduction peak has been taken as the reduction potential for further calculations. The nature of this secondary compound is unknown and no further investigation was carried out in this way. Although many studies have been made on this complex, none of them report experiments when dichloromethane was employed as a solvent.[79–81] Differences between this and the previous case could be

explained in terms of higher stabilization of the reduced complex of by the substituted bipyridine in the case of **R2–b** due to higher delocalization of the additional negative charge, especially if we take into account that several studies support that the first reduction step of these rhenium complexes is specifically located on the bipyridine ring.[59,82–84]

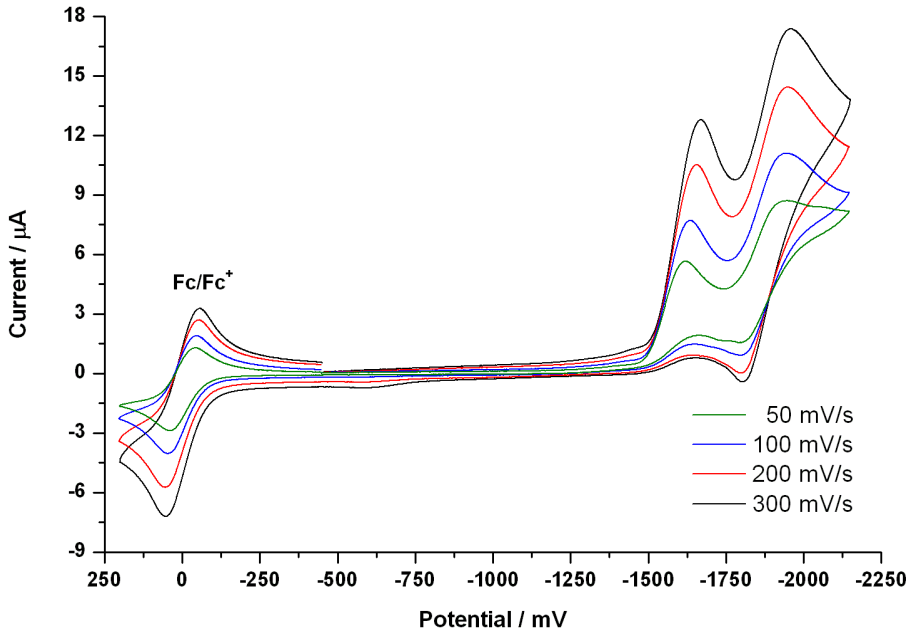

Figure 3.7 – Cyclic voltammograms of $[Re(bpy)(CO)_3(CH_3CN)][PF_6]$ (R2–a) at different scan rates. CH_2Cl_2 2.5 mM Re complex, 0.1 M $TBAPF_6$, 0.8 mM Fc

The first reduction potentials of all rhenium complexes employed in this work are shown in Table 3.2, classified in two series depending on the bipyridine ring and sorted in increasing order of the reduction potential inside each series. In the next discussion, all reduction potentials are negative and magnitude terms such as higher or lower are referred always to its absolute value; in this way, higher reduction potentials correspond to systems that are more difficult to be reduced and *vice versa*. For not shown spectra see Appendix III on page 126.

Bipyridine	Ligand	Compound	$^{1st}E_{1/2}$ / V	Reported $E_{1/2}$ / V
bpy (*a* series)	3–Pic	**R3–a**	– 1.57	– 1.57[45]
	CH_3CN	**R2–a**	– 1.63	– 1.58[*,79]
	$P(OEt)_3$	**R4–a**	– 1.68	– 1.63[‡,79]
	Br^-	**R1–a**[†]	– 1.86	– 1.87[§,85]
BMCbpy (*b* series)	3–Pic	**R3–b**	– 1.16	—
	CH_3CN	**R2–b**	– 1.23	
	$P(OEt)_3$	**R4–b**	– 1.25	
	Br^-	**R1–b**[†]	– 1.44	

Table 3.2 – First reduction potentials of the rhenium complexes employed in this work. Experimental conditions: CH_2Cl_2, 2.5 mM Re complex, 0.1 M $TBAPF_6$, 0.8 mM Fc. [†]All complexes are cationic with PF_6^- as counterion except R1–a,b, which are neutral. Values corresponding to [*]3:2 THF:CH_3CN, [‡]CH_3CN or [§]1:3 MeOH:CH_3CN solutions

The first and biggest effect we can notice is the big impact of the bipyridine substitution on the electrochemical behavior of the system. Inclusion of the strong electron withdrawing group makes all the four complexes (**R1–4**) much more sensitive towards reduction, with halfwave potential downshifts of up to 500 mV when moving from the unsubstituted bipyridine (*a* series) to the 4,4'–methoxycarbonyl–bpy (*b* series). This shift is in good agreement with the fact that the reduction step is located on the bipyridine ring (*vide supra*), so inclusion of electron withdrawing substituents on it can be expected to decrease the reduction halfwave potential values, due to higher electron delocalization on the ligand, stabilizing the anionic product.

Substitution of the additional ligand was also found to have a significant, although smaller, impact on the reduction potential, as previously reported for some similar complexes.[59] However, this result differs from previous data on similar neutral compounds,[86] where the ligand nature does not have a high influence on the reduction potential. When analyzing ligand substitution effects, similar results are obtained in both series. Greater differences between bromide complexes (**R1**) and

the rest (**R2** to **R4**) can be explained in terms of the electric charge of the compounds. Bromide complexes are neutral, whereas acetonitrile, picoline and phosphite ones are all monocationic. During reduction, an electron is gained by the complex and negatively charged or neutral reduced species are formed, respectively. Since neutralizing a positive charge is generally easier than generating an anionic complex from a neutral one, bromide complexes exhibit higher reduction potentials than the others.

When the three neutral ligands are compared, small variations are observed in the order Pic > CH_3CN > $P(OEt)_3$, with slightly larger differences between picoline and the other two ligands. This relative order has been already found in this study when ^{1}H–NMR spectra have been discussed (see Table 2.1 on page 52 and following discussion), which suggested higher electron donation of the bipyridine ligand to the rhenium center in the case of picoline complexes. This would make picoline derivatives (**R3**) better electron acceptors, having lower reduction potentials. Smaller and more similar interaction between the diimine ring and the metal when CH_3CN (**R2**) or $P(OEt)_3$ (**R4**) are used would be translated into slightly higher and closer reduction potentials, as can be found in Table 3.2.

Chapter 4. Photophysics and PET Driving Force

Due to their electronic structure and the extensive π–conjugation, porphyrins and metalloporphyrins exhibit very strong and characteristic absorption spectra in the ultraviolet and visible regions, as well as fluorescent properties even at room temperature. As was argued before when Equation 1.2 was introduced (see page 21), characterization of the emission properties of the porphyrins allows us, in conjunction with previously shown electrochemical data, to estimate the driving force of the photoinduced electron transfer between the excited metalloporphyrin and rhenium complexes in their ground state. In this chapter, both absorption and emission studies on the porphyrins employed are shown, together with the derivative results concerning the electron transfer step.

4.1 UV–Visible absorption

The structures absorption spectra of metalloporphyrins have been well understood since the 1960s and can be satisfactorily explained by using the four–orbital model proposed by Gouterman.[87,88] According to it, absorption bands are generated by electronic transitions between HOMO and LUMO, consisting of two orbitals of *a* symmetry (a_{2u} and a_{1u}) and a pair of degenerate e_g orbitals, respectively. In terms of electronic states, this is translated into three singlet non–degenerate states consisting of an A_{1g} ground state and two E_u excited ones (Figure 4.1).

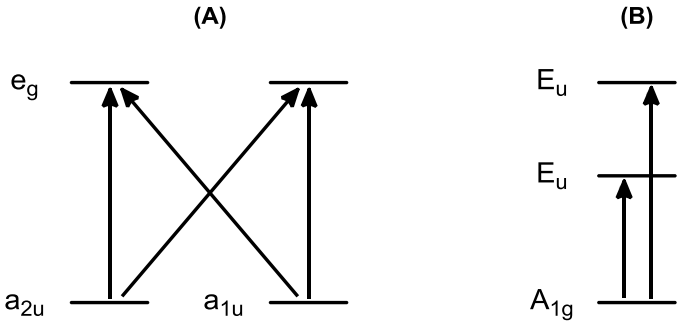

Figure 4.1 – Frontier molecular orbitals of metalloporphyrins (A) and representation of their electronic states (B)[87]

Transitions between them should lead to two main bands, the higher energy absorption (Soret or B–band) and the lower energy absorption (Q–band), always weaker than the first one, which dominates the spectrum. However, more bands are observed due to vibronic coupling, giving rise to transitions between the ground state and different vibrational levels of the excited electronic state. In Figure 3.1 the representative case of **ZnTPP** (**P1**) is illustrated.

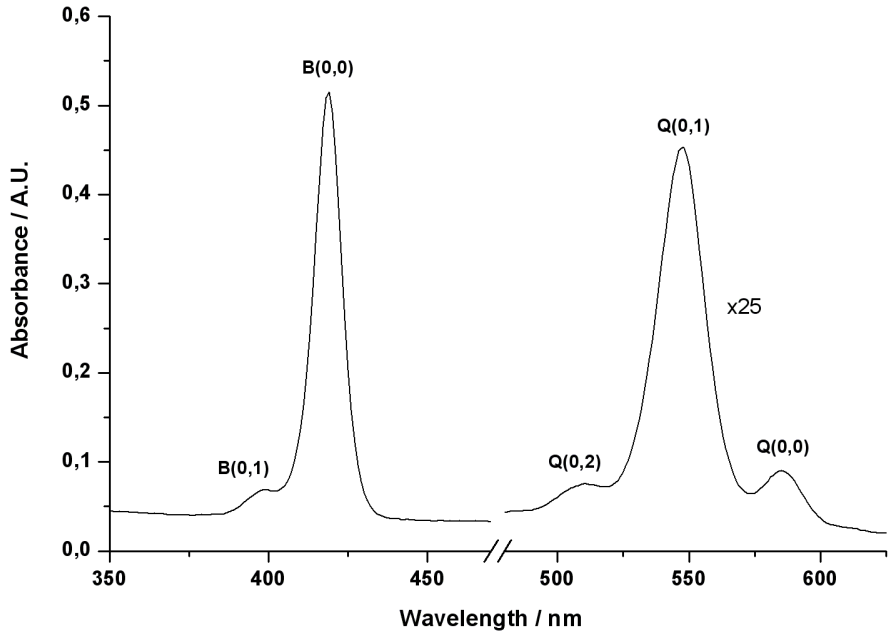

Figure 4.2 – UV–Visible absorption spectrum of ZnTPP (P1) in CH_2Cl_2 recorded at room temperature. Left part 0.5 μM, right part 12.5 μM. Numbers in parentheses indicate initial and final vibrational states, corresponding to the ground and excited electronic states respectively.

Although more bands can be expected for some metalloporphyrins, in the case of zinc(II)–porphyrins the presence of the metal does not generate additional transitions due to its closed–shell electronic configuration. Soret bands appear around 420 nm and Q bands around 550 nm (referred to the most intense one), with small variations depending on the ring substituents. Similar spectra are obtained for the tolyl, *tert*–butylphenyl and methoxyphenyl derivatives (see Appendix IV on page 129), which are omitted in here. Positions and extinction coefficients of the different bands are listed in Table 3.1. Results obtained agree with previously reported data.[76,89–91]

Substituent	Porphyrin	B(0,1)	B(0,0)	Q(0,2)	Q(0,1)	Q(0,0)
–H	**P1**	398 (12.9)	419 (97.0)	510 (0.6)	548 (3.4)	585 (0.7)
$–CH_3$	**P2**	400 (5.8)	421 (56.6)	512 (0.5)	549 (2.2)	587 (0.7)
$–C(CH_3)_3$	**P3**	400 (12.7)	422 (98.2)	512 (0.6)	549 (3.4)	588 (1.0)
$–OCH_3$	**P4**	402 (3.2)	423 (26.1)	514 (0.2)	550 (1.2)	590 (0.4)

Table 4.1 – UV–Visible absorption data in CH_2Cl_2 solution of the zinc(II)–porphyrins employed in this work. Maximum absorption wavelengths are expressed in nm and molar extinction coefficients are shown between parentheses in 10^4 $dm^3 \cdot mol^{-1} \cdot cm^{-1}$

Small shifts towards longer wavelengths can be observed when increasing the electron donating ability of the substituent, which indicates slightly smaller differences between the ground and excited electronic states, whereas differences between vibronic coupling structures remain almost unaffected.

4.2 Room temperature fluorescence

Zinc–metallated porphyrins also exhibit room temperature fluorescence. In all cases two emission bands are observed after excitation of the highest Q–band, which can be assigned to decay processes from the lowest vibrational level of the first excited electronic state to the ground (0,0) or first excited (0,1) vibrational levels of the ground electronic state.

In Figure 4.3 the emission spectrum of **ZnTPP** (**P1**) can be observed as an example. In all other cases the same structure is maintained, with some variations in the intensities. The position of the highest energy band is taken as the energy difference between the two electronic excited states for the photoinduced electron transfer driving force calculations.

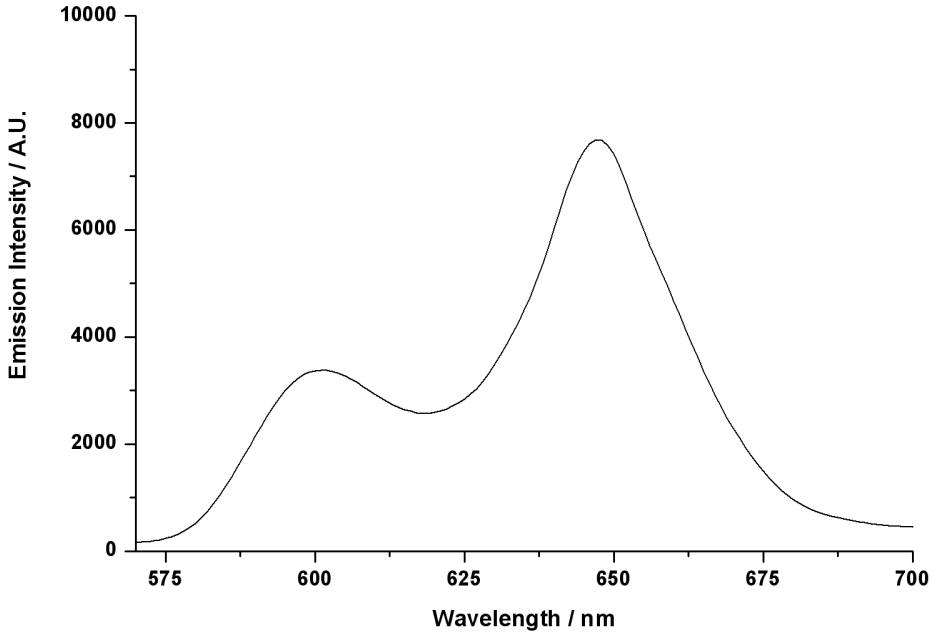

Figure 4.3 – Emission spectrum of ZnTPP (P1) in CH2Cl2 solution at 298 K. Excitation wavelength 548 nm

Emission bands positions of the different metalloporphyrins are shown below in Table 4.2. See Appendix IV on page 129 for all the spectra.

Substituent	Porphyrin	(0,0)	(1,0)	E_{00} / eV
–H	**P1**	601	647	2.062
$–CH_3$	**P2**	603	650	2.056
$–C(CH_3)_3$	**P3**	605	651	2.049
$–OCH_3$	**P4**	607	654	2.042

Table 4.2 – Fluorescent emission data of the Zn(II)–porphyrins used in this work in CH_2Cl_2 at room temperature (298 K). Values of the energy difference between electronic states (E_{00}) are also listed. Maximum wavelengths are shown in nm

Fluorescence data are consistent with the UV–Visible absorptions described above. Inclusion of stronger electron donating groups decreases the gap between the two electronic states and the difference between vibrational levels remains essentially constant, showing stronger influence on the electronic structure. In the only case in which similar experiments were described (**ZnTPP**, **P1**), results match with those previously reported.[92]

4.3 PET driving force

The free energy variation of the electron transfer process between the first excited state of the zinc–porphyrins and the rhenium complexes can be calculated using the photophysical and electrochemical properties shown before as explained in Chapter 1 by using Equation 1.2.

$$\Delta G_{PET} = E_{ox} - E_{red} - E_{00}$$

Equation 1.2 – Photoinduced electron transfer (PET) driving force calculation[45]

Results for the different porphyrin–rhenium complex pairs are presented in Table 4.3, classified by their chemical nature with the same criteria employed for the electrochemical properties of the rhenium complexes (see page 74).

	Substituent		–H	$–CH_3$	$–C(CH_3)_3$	$–OCH_3$
Bipyridine	**Ligand**	**Code**	**P1**	**P2**	**P3**	**P4**
bpy (*a* series)	3–Pic	**R3–a**	– 0.11	– 0.15	– 0.16	– 0.19
	CH_3CN	**R2–a**	– 0.05	– 0.09	– 0.10	– 0.13
	$P(OEt)_3$	**R4–a**	– 0.01	– 0.05	– 0.06	– 0.09
	Br^-	**R1–a**	+ 0.18	+ 0.14	+ 0.13	+ 0.09
BMCbpy (*b* series)	3–Pic	**R3–b**	– 0.52	– 0.56	– 0.57	– 0.61
	CH_3CN	**R2–b**	– 0.45	– 0.49	– 0.50	– 0.53
	$P(OEt)_3$	**R4–b**	– 0.43	– 0.47	– 0.48	– 0.51
	Br^-	**R1–b**	– 0.24	– 0.28	– 0.29	– 0.33

Table 4.3 – Driving forces for the different porphyrin–rhenium complexes combinations, expressed in eV, corresponding to the electron transfer from the first electronic excited state of the porphyrin to the ground state of the rhenium complex

The driving force is higher (more negative values) for those pairs in which the porphyrin is more easily oxidized, the rhenium complex more easily reduced and the energy difference between porphyrin electronic states is as small as possible. We can divide the combinations in three different categories, those with favorable driving forces (negative values), thermodynamically unfavored systems (positive values) and particular cases very close to equilibrium (*e.g.* **P1**:**R4–a**).

These calculated values are just estimates, due to the identification of E_{00} with the highest energy emission band; in addition, they come from properties measured in dichloromethane solution and are therefore valid only in that specific context. However, CO_2 reduction experiments are carried out in 5:1 DMF:TEOA solution. This implies not only a different solvent but also the presence of active species such as the DMF itself, that is believed to participate in many processes[93] or triethanolamine, which could coordinate to the zinc center of the different metalloporphyrins.[46,94,95] We will assume that these differences will affect all the combinations in a similar way, so the relative orders will be preserved and comparisons will be still valid. If CO_2 reduction ability is only or mainly dependent on the electron transfer step, for a given rhenium complex better results should be obtained when a porphyrin with a higher electron donating substituent is employed. For a fixed metalloporphyrin, we could expect significantly better performance for those compounds belonging to the *b* series and different behavior between the bromide derivatives and the rest. In addition to small differences between the different ligands, one of the most important points would be comparing the CO_2 reduction ability of the bromides of the *a* and *b* series, since the first have positive free energies and no CO_2 reduction should be expected in those cases, compared with the reasonably favorable systems of the second case. For some particular cases, intermediate situations with potentially low activity may be found if conditions very close to equilibrium occur.

Chapter 5. Photocatalytic CO_2 Reduction

In this chapter, an exhaustive study on the results of the photocatalytic reduction of carbon dioxide with the different mixtures made of porphyrins and rhenium complexes is reported. In this first incursion into the understanding of the photochemical behavior of these multicomponent systems, only experiments with 1:1 mixtures of porphyrin and rhenium complexes at standard concentrations of 0.05 mM have been performed, which allow us to compare the catalytic efficiency of the complex mixtures under reaction conditions employed previously. Standard conditions consist in solutions of the concentrations indicated above in 5:1 DMF:TEOA, bubbled and left under a CO_2 atmosphere with 5% CH_4 and irradiated with filtered polychromatic radiation with wavelengths greater than 520 nm. Carbon monoxide was quantified by gas chromatography using methane as internal standard.

5.1 Intersystem comparisons

In this section we consider the chemical nature of each sensitizer:catalyst pair and compare results for fixed porphyrins or rhenium complexes, in order to find correlations between subgroups rather than in the complete dataset.
In Figure 5.1, catalytic results are shown as TON against irradiation time, when **ZnTPP** (**P1**) is fixed as common sensitizer.

In all the Figures of this chapter, colors denote the different porphyrins (**P1** ≡ blue, **P2** ≡ orange, **P3** ≡ red and **P4** ≡ green) and shapes and filling the different rhenium complexes (**R1** ≡ tilted squares, **R2** ≡ triangles,**R3** ≡ circles and **R4** ≡ plain squares; filled shapes denote BMCbpy complexes). The complete catalytic mixtures labeling system is illustrated below in Table 5.2 (page 89).

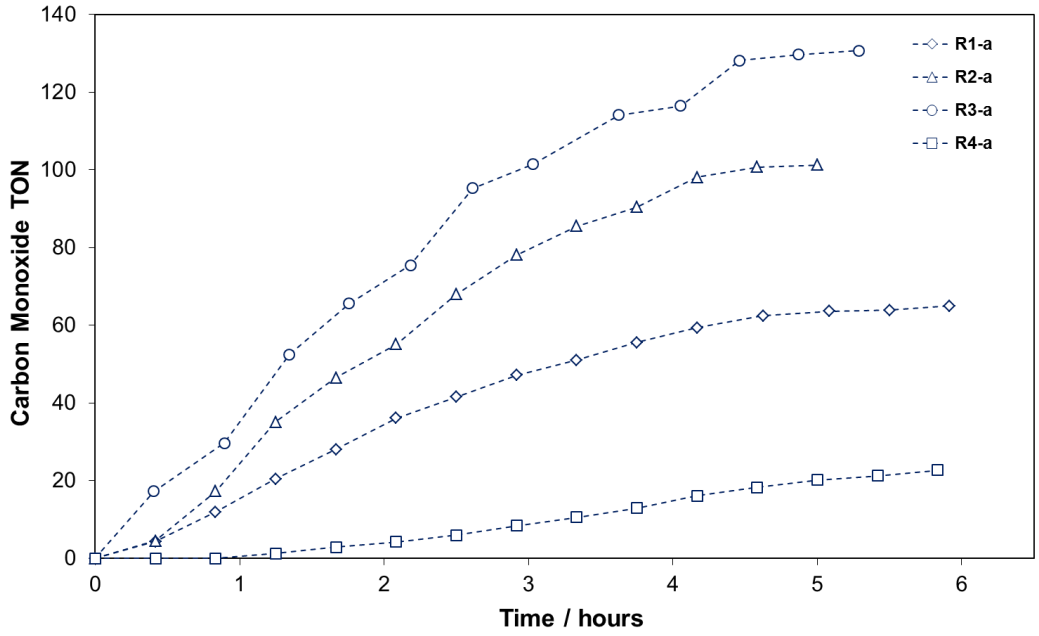

Figure 5.1 – Carbon monoxide formation profile for all ZnTPP (P1):Re complex combinations

It can be seen that better yields are obtained when combined with the picoline complex, followed by the acetonitrile one, the bromide and finally, the triethylphosphite derivative. Excluding the neutral bromide complexes, this trend follow the decreasing driving force order calculated in the previous chapter. When **ZnTTP** (**P2**) was employed (see Appendix V on page 135 for all plots), the same profile is observed; however, with the *tert*–butyl derivative **P3**, with a higher PET driving force, the situation between the first two complexes is reversed and the acetonitrile derivative becomes slightly more active than the picoline one (Figure 5.2). When the porphyrin which generates the highest driving forces is employed (**ZnTMPP**, **P4**), the difference between them becomes even higher, as we can see on Figure 5.3. In all cases, the worst rhenium complex was the triethylphosphite derivative (**R4–a**), followed by the bromide (**R1–a**).

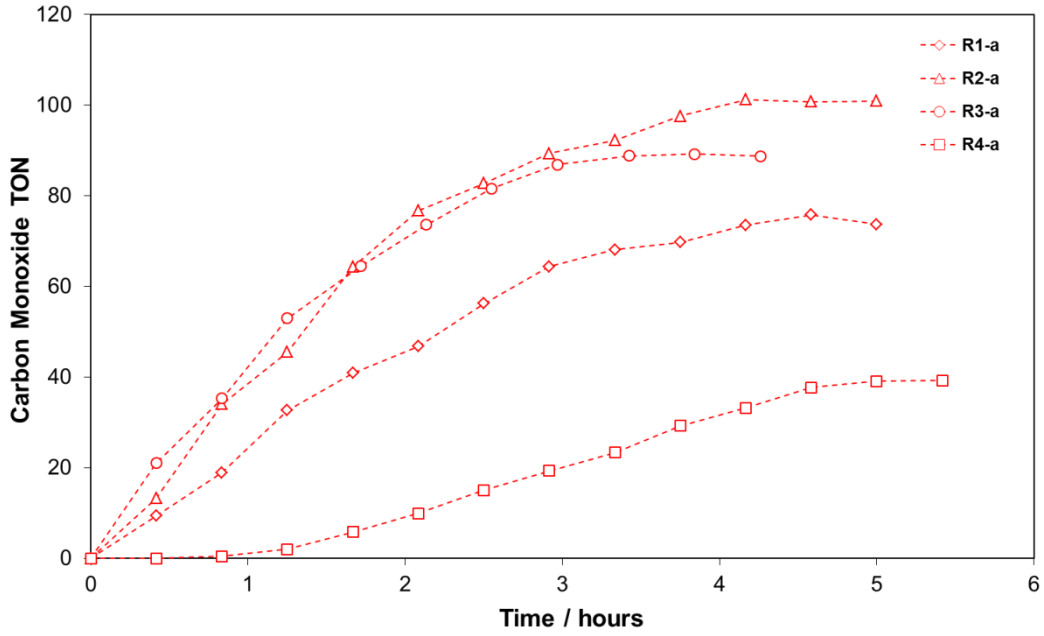

Figure 5.2 – CO formation profile with time for the four ZnTTBPP (P3):Re complex mixtures

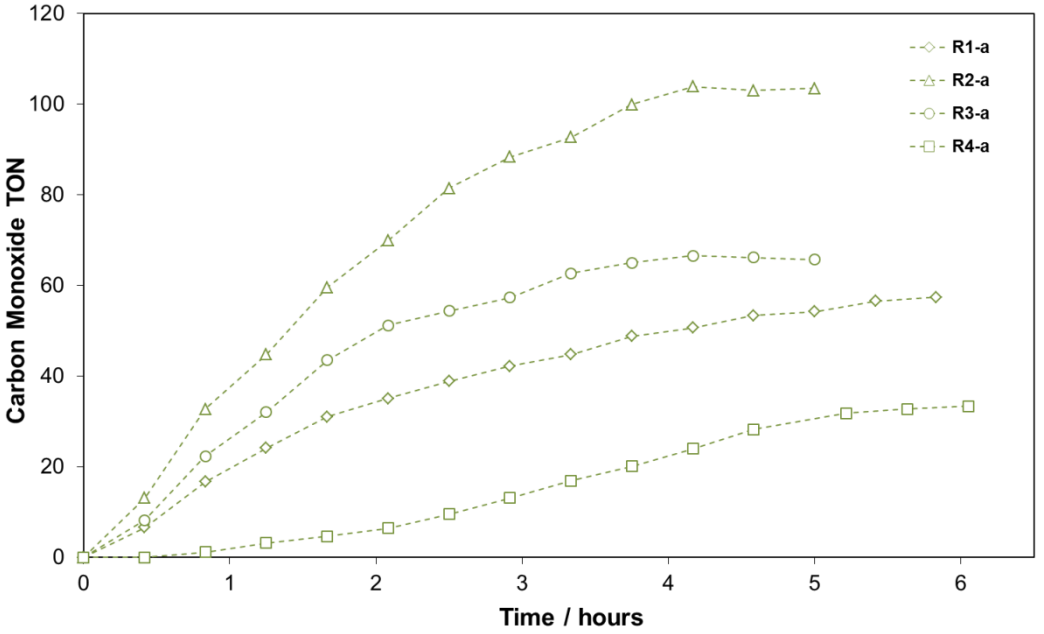

Figure 5.3 – CO formation profile with time for the different ZnTMPP (P4):Re complex mixtures

A detailed analysis of the results shows that the amount of CO produced by the acetonitrile complex (**R2–a**) mixtures is almost constant, around 100 turnovers, for all the four porphyrins, whereas it is the catalytic yield of the picoline complex (**R3–a**) what decreases when increasing the PET driving force by changing the

porphyrin. This can be observed in the analogous plots for a fixed rhenium complex.

In Figure 5.4 we can see that all four combinations give a similar amount of CO when the acetonitrile complex (**R2–a**) is employed, whereas for the picoline or the triethylphosphite compounds, differences between the most and less active systems span 80 and 40 turnovers, respectively.

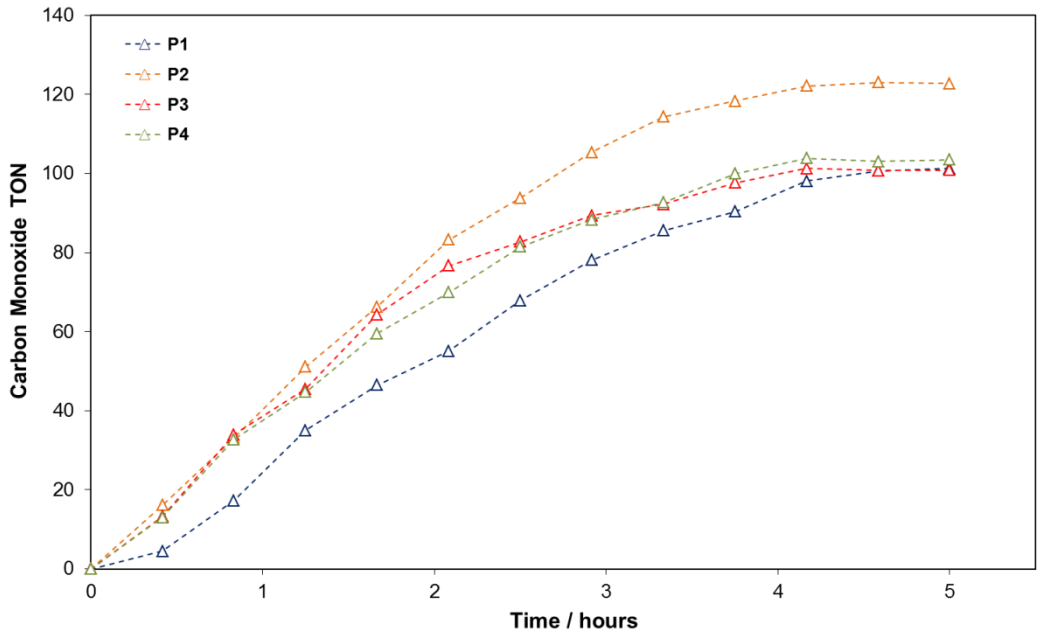

Figure 5.4 – CO formation profile with time for the combinations between the four porphyrins and $[Re(bpy)(CO)_3(CH_3CN)][PF_6]$ (R2–a)

The observation that very similar catalytic yields are obtained only with the acetonitrile complex agrees with the idea that ligand substitution on the rhenium complex plays a very important role in the catalytic mixture. In this case, probably a DMF or TEOA complex is readily formed under irradiation due to the fast dissociation of the acetonitrile molecule, whereas in the other cases, ligand substitution occurs progressively during the experiment at different rates, depending on the metalloporphyrin employed as sensitizer, and therefore, different results are obtained. When results of the other three ligands are compared, no systematic trend is observed, showing that ligand dissociation is not dependent on PET driving force.

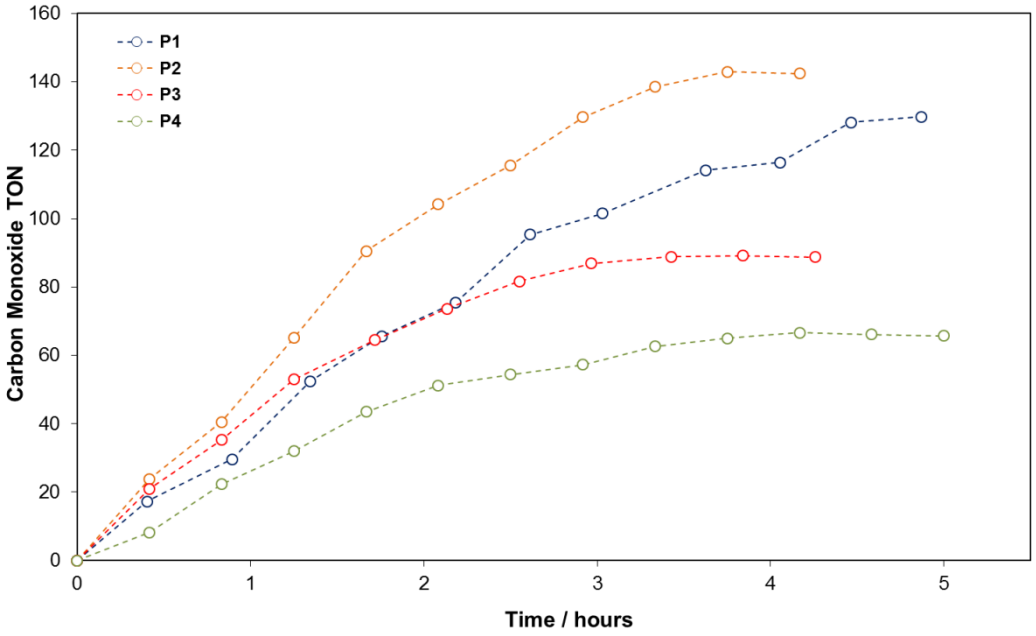

Figure 5.5 – CO formation profile with time for the combinations between the four porphyrins and $[Re(bpy)(CO)_3(3–Pic)][PF_6]$ (R3–a)

5.2 Influence of PET driving force on CO formation

The second important point to check with these systems was whether there was a correlation between the catalytic behavior and the PET step driving force or not. In this way, two parameters were studied, namely the maximum turnover number (TON), and the time to reach this value (t_{TON}). Although it is not explicitly indicated, all parameters are referred to the maximum values obtained after system photobleaching and loss of activity. In Figure 5.6 a graphical representation of both experimental parameters can be observed. The turnover frequency (TOF) has been also included in Table 5.1 and it is simply calculated as the ratio of the other two.

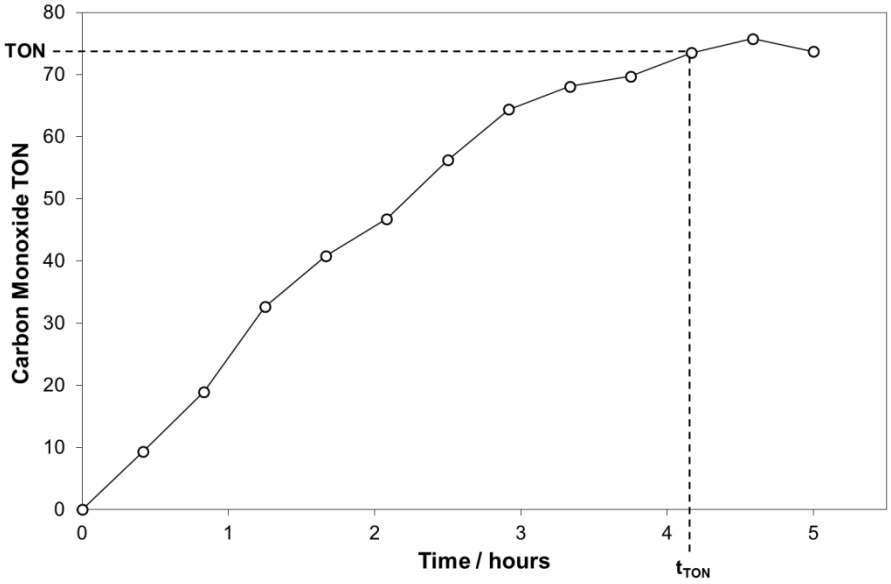

Figure 5.6 – Typical catalytic CO formation profile. Graphical definition of parameters TON and t_{TON} is indicated

Values of the three parameters for the mixtures which presented efficient photocatalysis, only those with unsubstituted bipyridine, are shown in Table 5.1.

	Substituent		–H	$–CH_3$	$–C(CH_3)_3$	$–OCH_3$
Bipyridine	**Ligand**	**Code**	**P1**	**P2**	**P3**	**P4**
bpy (*a* series)	3–Pic	**R3–a**	131 4.5 29	142 3.3 43	89 3.0 30	66 3.3 20
	CH_3CN	**R2–a**	101 4.2 24	123 3.8 33	101 4.2 24	104 4.2 25
	$P(OEt)_3$	**R4–a**	24 5.4 4	59 4.6 13	40 4.6 9	33 5.0 6
	Br^-	**R1–a**	62 4.6 13	71 4.5 16	74 4.2 18	58 5.2 12

Table 5.1 – Catalytic parameters of the mixtures between zinc(II)–porphyrins and rhenium tricarbonyl complexes. Entries are referred to TON, t_{TON} in h and TOF in h^{-1} from top to bottom respectively

Although no BMCbpy derivative (*b* series compounds) have been included, small amounts of CO have been detected in some cases, but always below 5 TON, so they have been considered as non–active systems. Due to the errors in the determination of TON_{max}, small values like those lack statistical significance and no intercomparison will be established.

We can plot these three characteristic parameters against the photoinduced electron transfer driving force to study the possible existence of a correlation. However, TON and TOF present very similar profiles and the second one is omitted. As indicated before, colors and shape/filling are associated with the metalloporphyrin and the rhenium complex present in the catalytic mixture, respectively; the legend is summarized in Table 5.2. The individual identification of each mixture in the representations is critical since it will be used later for discussion and in all plots presented on this chapter.

	Substituent		–H	$–CH_3$	$–C(CH_3)_3$	$–OCH_3$
Bipyridine	**Ligand**	**Code**	**P1**	**P2**	**P3**	**P4**
bpy (*a* series)	3–Pic	**R3–a**	○	○	○	○
	CH_3CN	**R2–a**	△	△	△	△
	$P(OEt)_3$	**R4–a**	□	□	□	□
	Br^-	**R1–a**	◇	◇	◇	◇
BMCbpy (*b* series)	3–Pic	**R3–b**	●	●	●	●
	CH_3CN	**R2–b**	▲	▲	▲	▲
	$P(OEt)_3$	**R4–b**	■	■	■	■
	Br^-	**R1–b**	◆	◆	◆	◆

Table 5.2 – Labeling scheme employed for the different catalytic mixtures. It should be noticed that R1–b:P3 and P4 mixtures could not be tested because of time limitations

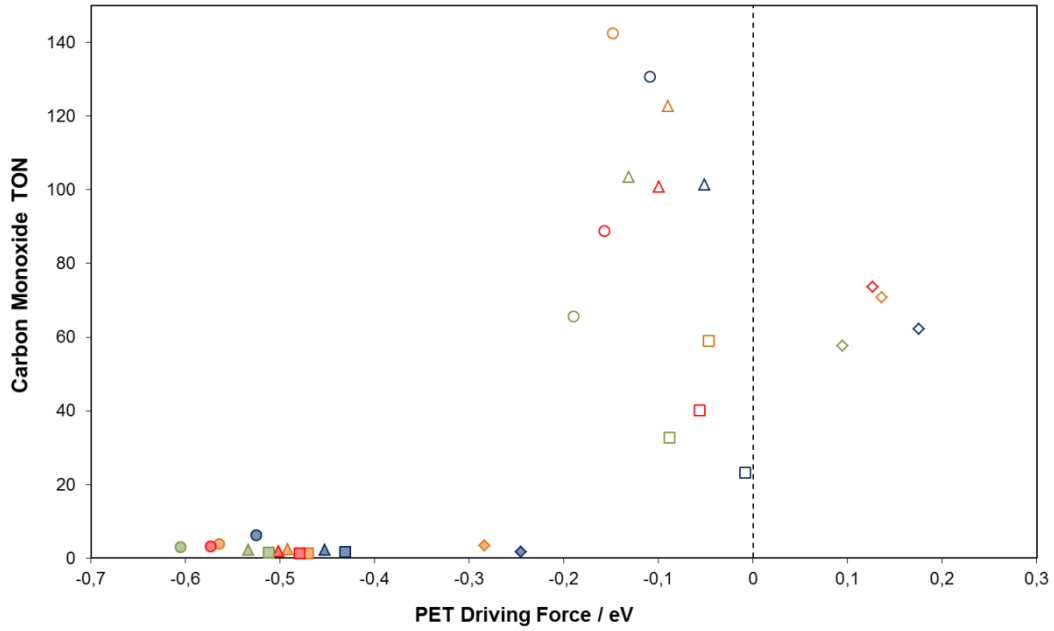

Figure 5.7 – Carbon monoxide maximum turnover number *vs.* photoinduced electron transfer driving force plot

It is not obvious how to analyze these results and it will be done going from general to more restricted observations. Discussion of the relative performance of the neutral bromide derivatives may be illustrative as a starting point. From these results, it is clear that PET driving force, as calculated, cannot be the controlling parameter of our systems, since no catalysis was obtained for those derivatives which form thermodynamic favored combinations but reasonable yields, between 60 and 80 turnovers, were obtained from those with positive driving forces. What is more, none of the compounds bearing BMBbpy exhibited significant catalytic properties, independently of the driving force. In addition, if results are carefully analyzed, it can be seen that in all cases, excluding the picoline derivatives, mixtures which share the same ligand produce very similar amounts of carbon monoxide, whereas bigger differences are observed when this ligand is modified. This can be taken as an indicator of the existence of some specific effects, which depend on the chemical structure of the rhenium complex employed in the catalytic mixture, with only a small influence of the metalloporphyrin used.

Concerning the influence of driving force, there are two additional remarkable features on Figure 5.7. First, the position of the less active bpy system (**P1**:**R4–a**, blue square), which matches with the one which show a PET driving force closer to zero and, secondly, the drastic decrease of the catalytic performance of **R3–a** (circles) mixtures at higher driving forces, when changing the porphyrin, in the region immediately before the first non–active BMCbpy compound, around – 0.2 eV. It may be only a coincidence but since this is the only set of complexes for which that is observed and that no activity is found above those driving force values, it could also indicate the presence of a borderline which impose some limit to the catalytic efficiency, as will be discussed later. However, we cannot either discard the possible existence of specific effects of the BMCbpy ligand on the lack of photocatalysis of those mixtures.

These findings, together with previous results on this field illustrate the great complexity of the problem. In 2011, Perutz and coworkers reported higher catalytic abilities for bimolecular mixtures of palladium tetraphenylchlorin compared with the oxidized porphyrin, using **R3–a** as photocatalyst; the greater efficiency could be initially attributed to a more favorable driving force in the first case, when the chlorin is employed.[45] On the other hand, a recently published study with zinc derivatives and the same rhenium catalyst showed much better performance when the porphyrin was employed, compared with the chlorin, even though it has a significantly lower PET driving force.[46] These apparent contradictions just show again that catalytic ability of these systems cannot be evaluated with one simple parameter, such as PET driving force as was initially assumed. Even if it is a key property and influences the behavior of the catalytic mixture, as will be seen later, the global yield would be determined by a combination of many different factors. It might be noticed that in the case of **P1**:**R3–a**, similar results to those reported by Windle *et al*.[46], in terms of turnover number, were found in this study, which gives us confidence in our data.

Despite the previous discussion, PET driving force seems to have influence on some parameters and phenomena which occurs during the photocatalytic experiments. There is a correlation between the time to reach TON_{max} and the driving force, as shown in Figure 5.8, providing the bromide complexes are excluded.

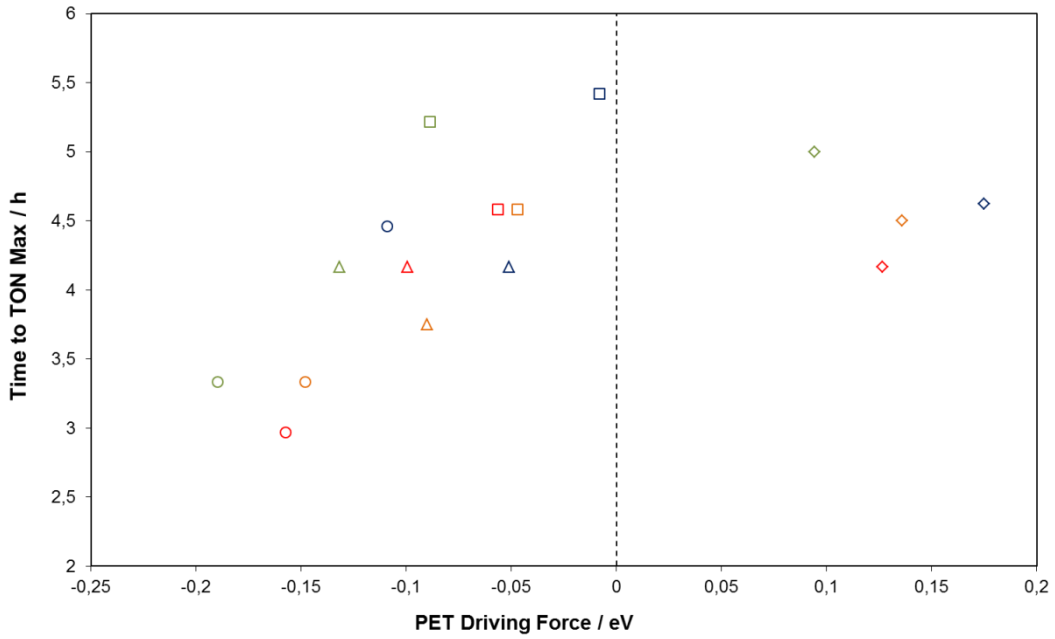

Figure 5.8 – Representation of the time to reach TON_{max} *vs.* PET driving force. Only those mixtures with significant catalytic activity are represented

It can be seen that higher driving forces make the system reach the maximum value of CO production at significantly shorter times. However, if we consider the nature of each mixture, this trend can be decomposed into more accurate terms and the effect is found to be just a consequence of specific chemical differences.

It is generally clear that for a given porphyrin (fixed color), the linear portion of the CO production plot is shorter for those rhenium compounds with higher driving forces. In addition, mixtures in which the rhenium complex contains the same ligand (same shape) have similar "lifespans", independently of the porphyrin that it is combined with (*e.g.* the four acetonitrile compound mixtures, displayed as triangles, are active around 4 hours but driving force varies from – 0,05 to – 0.13 eV), so mixtures with the same *fifth* ligand but different driving forces last very similar times under irradiation.

On the other hand, mixtures with very close driving forces but different ligands such as **P2**:**R2–a** (orange triangle) with **P4**:**R4–a** (green square) or **P1**:**R4–a** (blue square) with **P2**: **R4–a** or **P3**:**R4–a** (red and orange squares) behave in a much more different way. This indicates that chemical nature of the rhenium complex substituent, and not PET driving force, seems to be a much more controlling factor in system stability under irradiation in photocatalytic conditions.

There is a reciprocal relationship between the amount of CO obtained and the time the system is active, which can look counterintuitive at first sight. Systems which produce more carbon monoxide do it in shorter times and die faster. This is fairly clear for all combinations but picoline complex mixtures (Figure 5.9). The reason why only the picoline complexes do not follow that trend remains unknown.

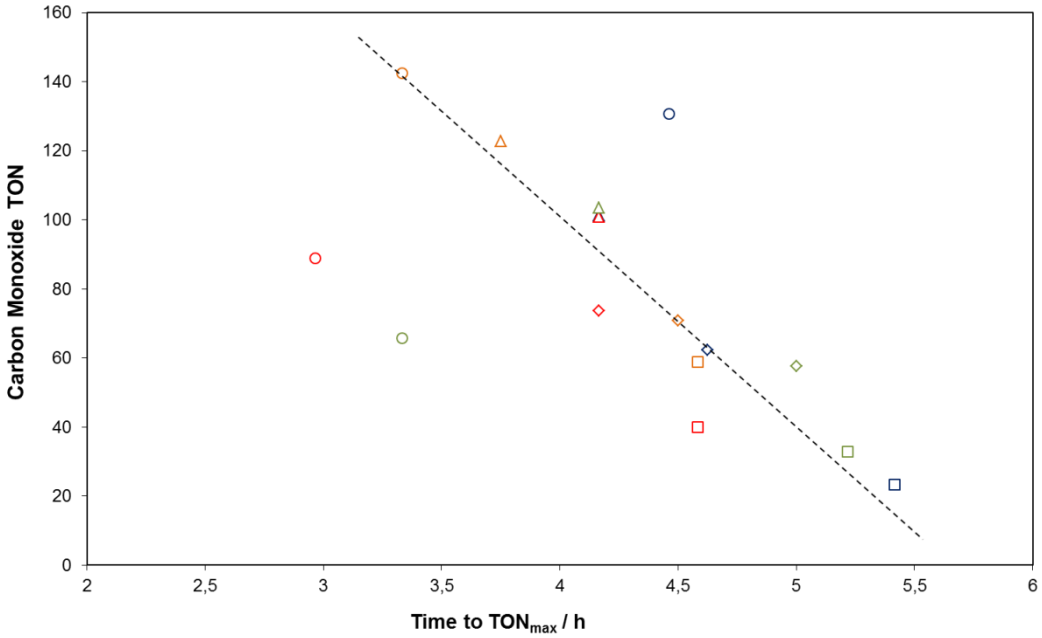

Figure 5.9 – Representation of carbon monoxide turnover number *vs.* time to reach TON_{max}. Straight line is shown to illustrate its linear character for most complexes

5.3 Chlorin influence on CO production

When studying the CO formation profiles of the different mixtures a shape like the one shown in Figure 5.6 was found for almost all systems. The triethylphosphite complex (**R4–a**) was an exception, showing an initial induction period, rather than constant growth and final deactivation (Figure 5.10).

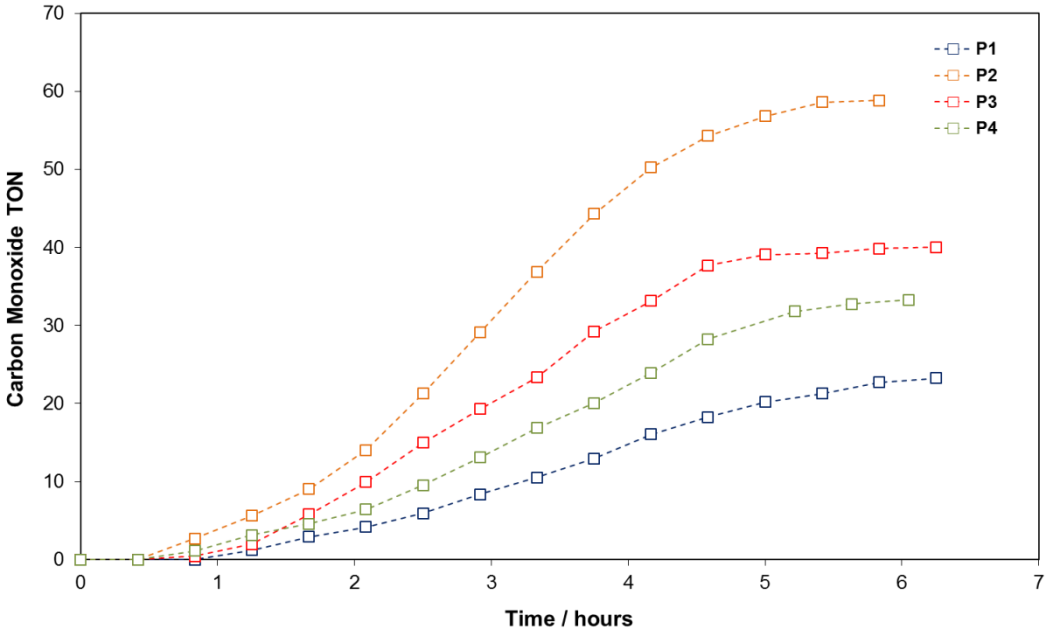

Figure 5.10 – CO formation profile for the porphyrin combinations with $[Re(bpy)(CO)_3\{P(OEt)_3\}][PF_6]$ (R4–a). The existence of an induction period can be observed in all four cases.

In order to find a reason for this, the absorbance profiles corresponding to the two Q bands of the porphyrin (light blue and brown for the Q(0,1) and Q(0,0) respectively) and the reduced chlorin (purple) were studied under irradiation. In all the cases, absorbance values were normalized against porphyrin Q(0,1) band, and are presented as ratios, to make them comparable. In Figure 5.11 we can see that there is a constant decay of the first Q band of the porphyrin, a similar decay of the second one after a short period of almost no variation and initial and fast formation of chlorin followed by a slower decay. This profile is followed, only with small variations, for all combinations between any porphyrin and rhenium complexes bearing picoline, acetonitrile or bromide ligands (see Appendix VI on page 139 for all plots), which also share the same CO formation profile shape.

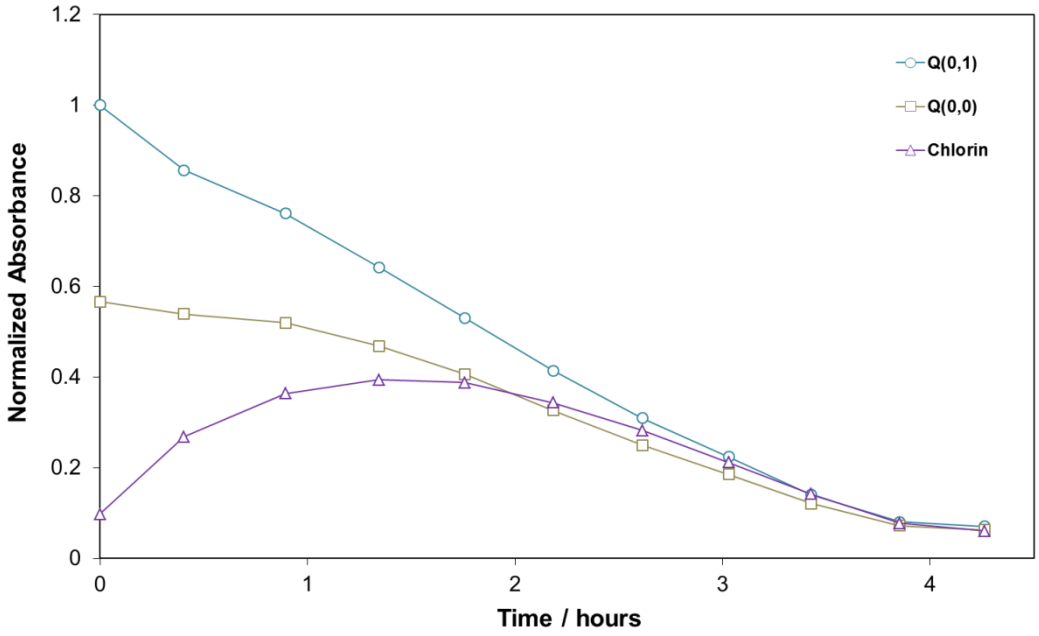

Figure 5.11 – Porphyrin and chlorin absorbance profiles for the ZnTTP (P2):[Re(bpy)(CO)$_3$(3–Pic)][PF$_6$] (R3–a) mixture during irradiation

On the other hand, with the profiles of the mixtures with triethylphosphite complexes a clearly different distribution is observed, with a much slower initial chlorin formation and its maximum shifted to longer times. Porphyrin bands decay in a similar way but at slower rates at the initial stage.

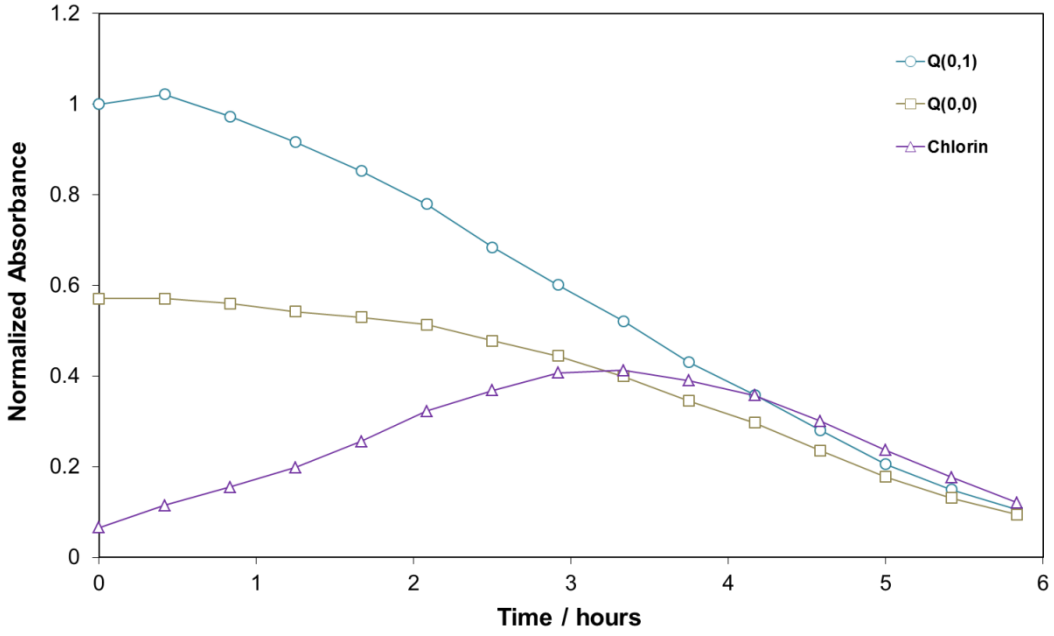

Figure 5.12 – Porphyrin and chlorin absorbance profiles variation for the ZnTTP (P2):[Re(bpy)(CO)$_3${P(OEt)$_3$}][PF$_6$] (R4–a) mixture

The same profile is obtained when any of the four porphyrins is employed so it is reasonable to believe that chlorin formation may be the cause of the distinctive CO formation profiles.

In order to get some deeper understanding on this possible dependence, the amount of CO produced on each step, from sample to sample, was overlaid to the previous plots. As can be seen in Figures 5.13 and 5.14, the presence of the chlorin in the media is closely related to the formation of CO, with both profiles presenting the same shape, showing a relationship between CO formation and the amount of chlorin in the media.

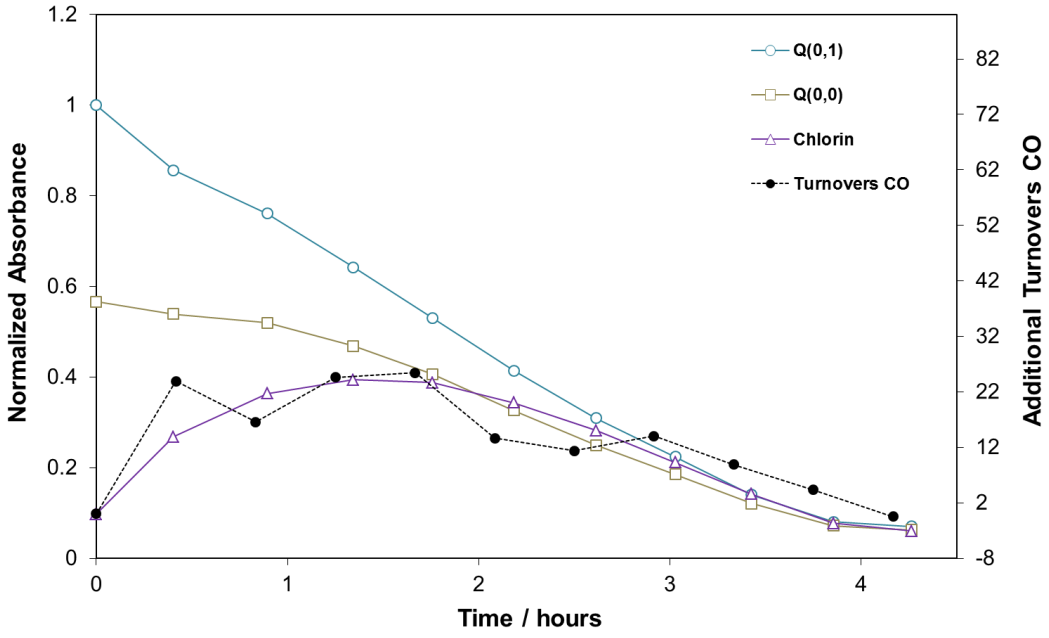

Figure 5.13 – Porphyrin and chlorin absorbance profiles for the ZnTTP (P2):[Re(bpy)(CO)$_3$(3–Pic)][PF$_6$] (R3–a) mixture during irradiation and CO formation

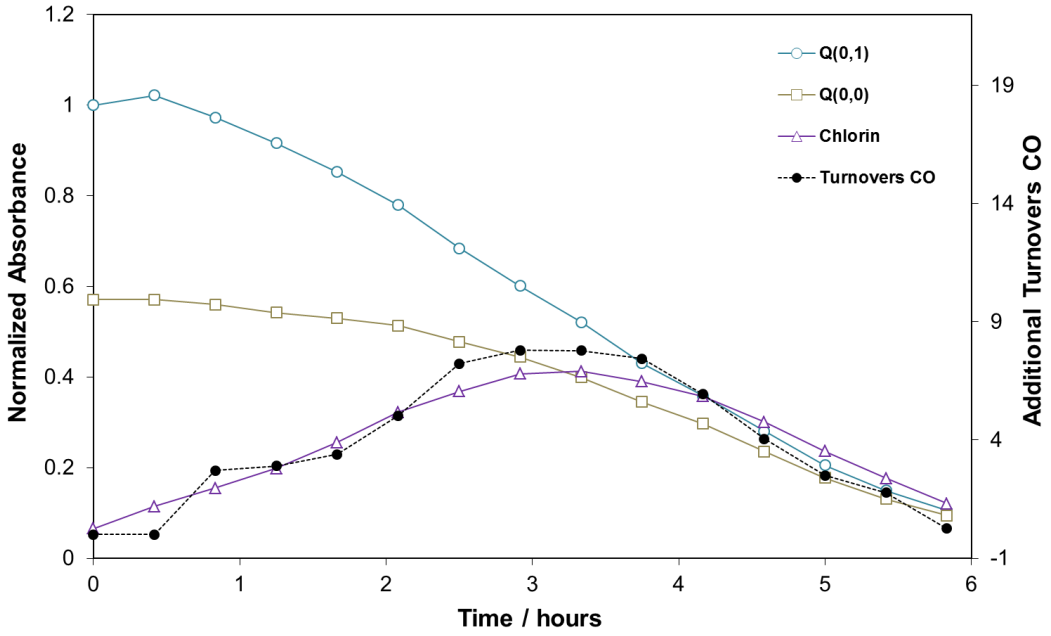

Figure 5.14 – Carbon monoxide formation and porphyrin and chlorin absorbance profiles variation for the ZnTTP (P2):[Re(bpy)(CO)$_3${P(OEt)$_3$}][PF$_6$] (R4–a) mixture

However, in some cases, at the initial stage of the reaction, the amount of CO produced was greater than the expected from the chlorin concentration (Figure 5.15). This could be attributed to the contribution of the native porphyrin to the rhenium sensitizing process, so the combination of both, porphyrin and chlorin would be responsible for the CO formation. After some time, when the porphyrin concentration has decayed significantly and more chlorin is present in solution, the chlorin would play the dominant role and both absorbance values and CO formation decay at the same time. This effect is stressed for **ZnTMPP** (**P4**) mixtures with all but the triethylphosphite bipyridine complexes (**R1–a**, **R2–a** and **R3–a**). However, these differences may not be statistically significant.

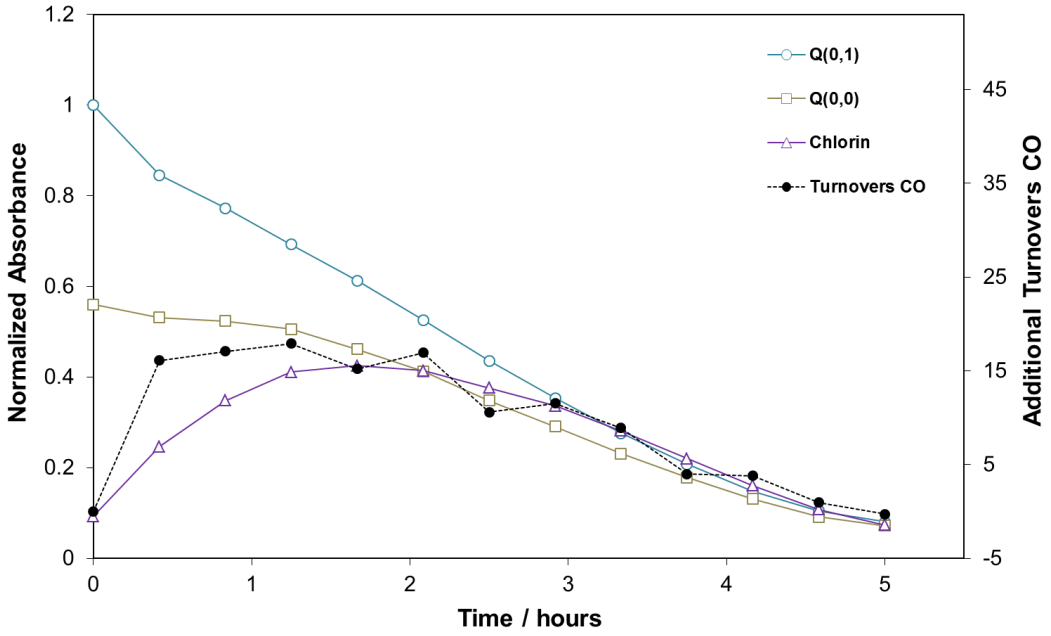

Figure 5.15 – CO formation and porphyrin / chlorin absorbance profiles variation for the ZnTTP (P2):[Re(bpy)(CO)$_3$(CH$_3$CN)][PF$_6$] (R2–a) mixture. Initial overproduction of carbon monoxide can be spotted during the first hour

On the other hand, with the compounds belonging to the *b* series, with very low catalytic ability, chlorin formation was delayed even more and no CO was detected before it was present above a minimum concentration (Figure 5.16).

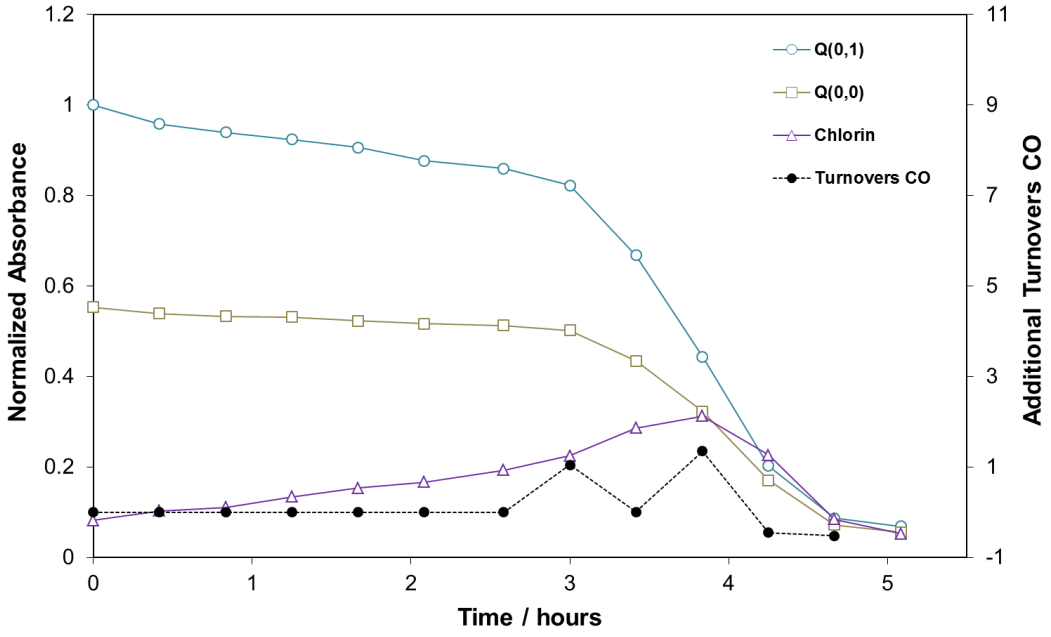

Figure 5.16 – Carbon monoxide formation and absorbance profiles of the mixture ZnTTP (P2):[Re(BMCbpy)(CO)$_3$(CH$_3$CN)][PF$_6$] (R2–b)

When comparing with previous studies on these systems, it has been shown that when pure chlorin is used on its own, with no porphyrin in the media, worse results are obtained.[46] We conclude that although the presence of chlorin is necessary to obtain good catalytic results, it is the simultaneous combination of both porphyrin and chlorin which gives the best results.

The reasons for this cooperation can be understood from two main observations: first, when only the chlorin is present, the global driving force for the electron transfer from the macroheterocycle to the rhenium complex is bigger, which should favor the process, but this also means that it can hinder the reaction if the energy difference is excessive and direct electron transfer from the chlorin to the rhenium center may not be kinetically favored. This could be due to moving the system into the inverted Marcus region, but it seems unlikely if the actual values of driving forces are considered. Alternatively, worse overlap between their energy surfaces, decreasing the electron transfer probability, or higher solvent rearrangement parameters, according to Marcus electron transfer theory, could impede the electron transfer reaction.

On the other hand, although electron transfer from the porphyrin is possible, the thermodynamic PET driving force is smaller, so no significant results are obtained either, maybe due to greater backelectron transfer and fast charge recombination (smaller driving force always mean more favored inverse reaction). When both components are present at the same time, an electron transport chain is formed, in such a way that the excited chlorin could transfer an electron to the rhenium complex through the porphyrin, which acts as a carrier with an intermediate redox potential. It is in those cases that electron transfer is really favored and occurs at appreciable rates, also making charge recombination more difficult due to the inclusion of an intermediate state and multiple charge separated species (Figure 5.17).

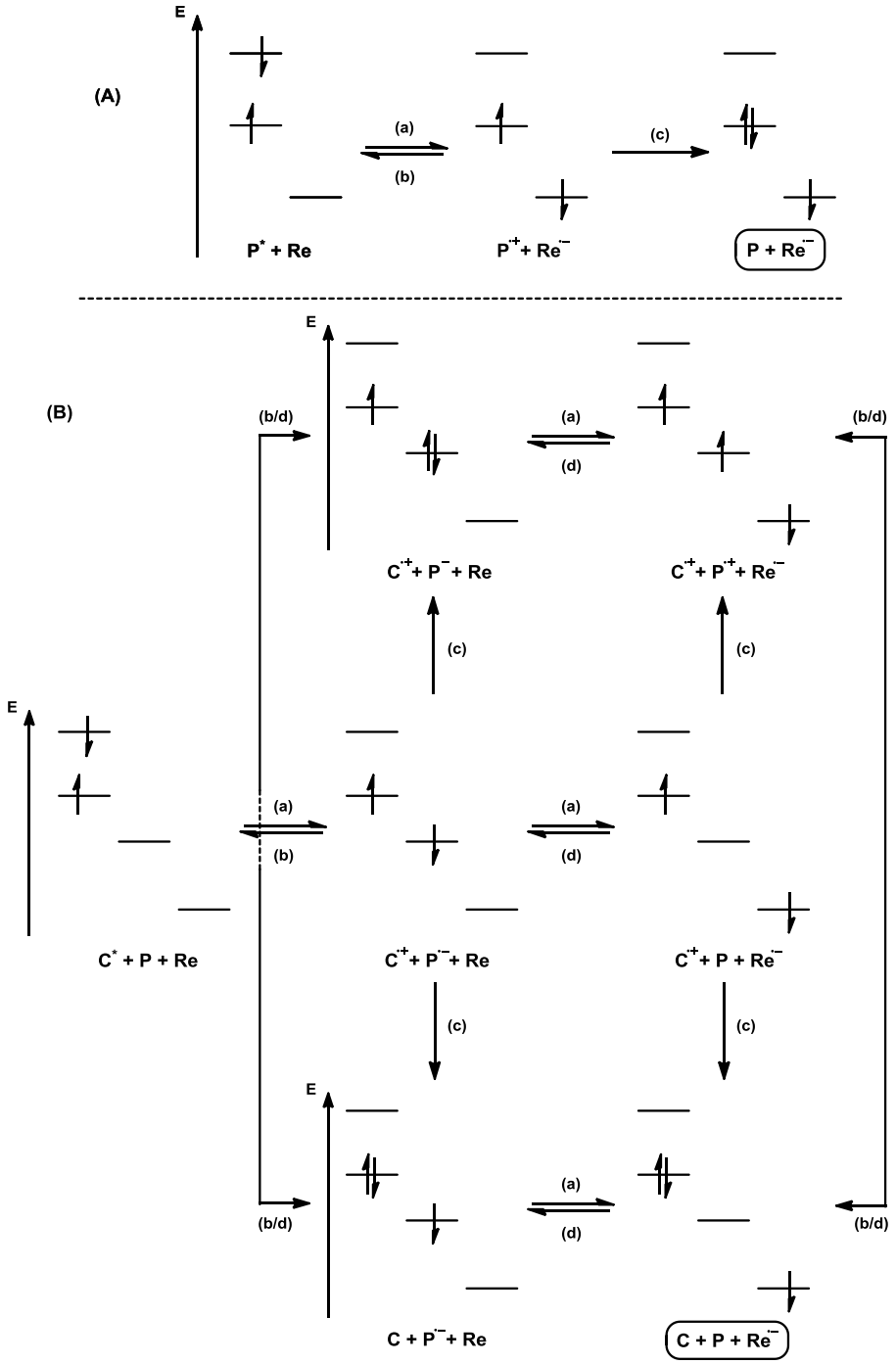

Figure 5.17 – Electron transfer from excited porphyrin (A) or chlorin (B) to the rhenium complexes. (a) electron transfer, (b) charge recombination, (c) sacrificial electron donor "quenching", (d) backelectron transfer (without charge recombination)

The mandatory presence of the chlorin could also explain the activity of the bromide derivatives; although they have been presented with positive PET driving forces, the calculated values have been obtained considering only electron donation from the excited porphyrin. Those values are more positive than the ones obtained when the chlorin is considered, which could shift the global driving force 0.15 – 0.2 eV toward smaller values, maybe entering into the negative region.

5.4 Porphyrin decay reaction kinetics

The strange profiles observed on Figure 5.16 were repeated for all BMCbpy derivatives. It can be observed that porphyrin decomposition and chlorin formation were much smaller at the initial stage of the reaction, with small variations during most of the experiment and sudden porphyrin decomposition and complete photobleaching occurred when a certain amount of chlorin was present. The fact that porphyrin absorbance profile decay was more abrupt only in these cases, with higher PET driving forces, made us believe these two features could be related. We therefore measured the slope of the constant decay region of the normalized absorbance values by least squares linear fitting (Figure 5.18).

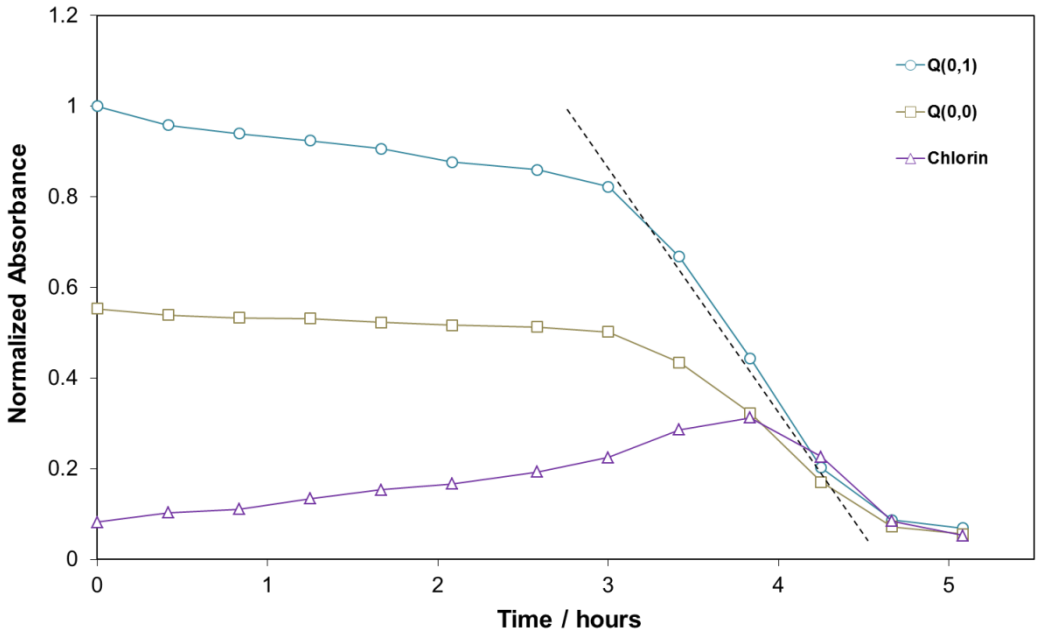

Figure 5.18 – Representation of the region and the linear regression employed to determine porphyrin absorbance decay rates as the absolute value of the slope of the straight line shown

Figure 5.19 shows the values of these slopes represented against PET driving force. From an analytical point of view it is very similar to Figure 5.8, in the sense that it seems to show a correlation between driving force and the decay rate, but being in reality slightly more complex. It is true that increasing driving force implies a faster decay but only if this modification comes from a modification of the rhenium complex ligand or bipyridine substituent. In contrast, when the same rhenium complex is employed and the porphyrin is changed, very similar decay rates are obtained. This is essentially the same conclusion as we found when analyzing the variation of time to reach TON_{max} with the driving force.

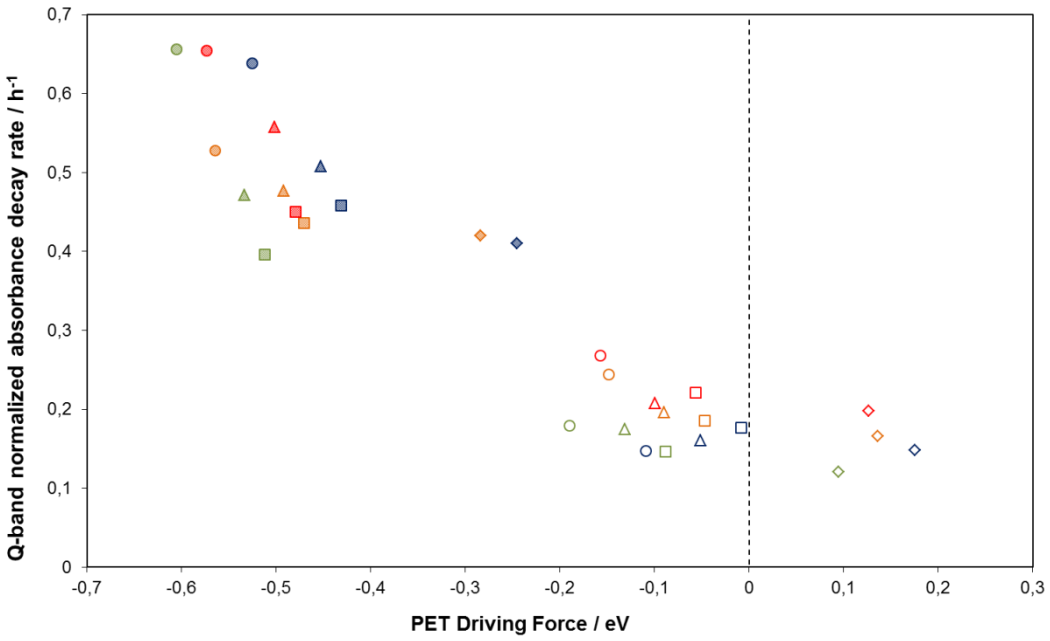

Figure 5.19 – Porphyrin normalized decay rates *vs.* PET driving force plot. Points labeling according to Table 5.2

These findings relate chlorin formation to porphyrin decomposition in a very subtle way. Metalloporphyrin photodecomposition may be dependent on the existence of an effective electron transport chain, which only happens when chlorin concentration is above a certain value, and PET driving force dominates the conversion kinetics under those conditions. In addition, the results clearly suggest that chlorin formation/porphyrin decomposition is highly dependent on the chemical nature of the rhenium complex ligands, rather than on the overall driving force itself, since its effect is only observed when these ligands are modified but not when different porphyrins are employed.

5.5 Conclusions and further work

The set of prepared compounds and experiments carried out allow us to obtain the next main conclusions:

1. Two component mixtures have been shown to be active photocatalytic systems for reduction of CO_2 to CO in many cases, leading to turnover numbers comparable with or better than similar systems with supramolecular dyads. This observation is very promising considering that no optimization of the catalytic conditions has been attempted so far and the easier synthesis of the different components compared with the dyads.

2. The nature of the fifth ligand of the rhenium complex strongly determined the catalytic ability of the system. In general, acetonitrile or picoline complexes were more active than neutral bromides and triethylphosphite compounds were always less active. Carbon monoxide formation seems to be dependent on many different factors, although the chemical nature of the rhenium complex has a strong influence on the properties and behavior of the global mixture.

3. Inclusion of electron withdrawing methoxycarbonyl groups on the bipyridine ring modified the chlorin formation/porphyrin decomposition profiles drastically and catalytic activity was almost completely lost.

4. Inclusion and modification of electron donating groups on the porphyrin substituents modified the amount of CO produced slightly, always with much smaller changes than the rhenium complexes ligands. Data suggest that this influence may arise from modification of rhenium complex ligand substitution rate.

5. No simple correlation between PET driving force and catalytic ability has been obtained, with photoactive systems at non–favored (positive) values and almost inactive systems at the highest driving force range.

6. Carbon dioxide reduction appears to be intimately linked to chlorin formation. Carbon monoxide formation was only observed once chlorin was present in solution over a certain value and the amount of CO produced at each time was proportional to the concentration of chlorin.

In addition, the additional findings showed on the following paragraphs were also found.

A possible borderline at – 0.2 eV could be the reason for the lack of activity of the BMCbpy derivatives. In order to check this possibility, two main experiments should be carried out. First, the BMCbpy compounds should be tested under direct UV irradiation, in order to isolate the nature of the ineffectiveness on the rhenium complexes by themselves or on the sensitation process. If higher catalytic activity was found in that case, an additional rhenium catalyst with unsubstituted bipyridine with driving forces comprised around – 0.2 eV (ideally on both sides of this value) should be tested in the presence of the different porphyrins, to check if the lack of catalysis in the presence of the sensitizing agents is directly related to the driving force or if it is due to specific incompatibilities of the BMCbpy derivatives.

The time during which the system is active, has been shown to have a reciprocal relationship with the maximum turnover number observed. Systems which make bigger amounts of CO also decompose faster.

The way in which components interact in the mixture points to the existence of specific chemical processes and interactions. Acetonitrile complexes behave in a very similar way with all the four zinc porphyrins, which is in good agreement with the well–known lability of the acetonitrile–rhenium bond. However, different trends without simple interpretation are observed in the other cases.

Chlorin formation is strongly influenced by the rhenium complex employed and its presence or, what is more, the coexistence of both porphyrin and chlorin, seems to be required for an effective CO production. Slower chlorin formation explains why an induction period is observed only for the phosphite complex mixtures. It also explains why no carbon monoxide is observed until the very late stage in the case of the less active BMCbpy derivatives, in which the porphyrin reduction is extremely delayed.

Chlorin participation in this process could explain the surprising activity of the neutral bromide complexes, which exhibit driving forces that appear to be positive. If electron transfer occurs from the chlorin to the rhenium complex, the global value of the electron transfer driving force could be shifted enough to fall inside the negative region. In order to test this, even less favored systems with positive driving force values of + 0.3 – 0.4 eV should be tested, employing different ligands, in order to check if the activity is maintained or if it decays. This could be achieved with electron donating groups on the bipyridine.

Results also suggest that porphyrin decomposition only occurs once chlorin is present above a certain value and, under these conditions, the porphyrin Q(0,1) band decay rates are clearly dependent on the rhenium complex ligands. Mixtures with greater driving forces, arising from ligand substitution, lead to faster decomposition rates, independently of the porphyrin employed.

The chemical nature of the rhenium complex plays a vital role because of its intrinsic catalytic ability but also of its interaction with the different porphyrins. An optimum equilibrium between ligand substitution rate, must be found, so a set of compounds with more chemical variability on the fifth ligand should be considered as continuation of this work.

Because of the bimolecular nature of these systems, their flexibility is significantly higher than similar supramolecular dyads, so different concentrations and sensitizer:catalyst ratios should have a big influence on the results obtained. Although in this work standard conditions previously used in our group for

analogous experiments has been employed, it would be interesting to modify both parameters. In this way, a set of five alternative experiment families are proposed: a) modification of the concentration maintaining 1:1 ratio; b1) Mixtures enriched in sensitizer (*n*:1 ratio) in where the metalloporphyrin is maintained at the same concentration and the rhenium complex is diluted; b2) *n*:1 mixtures with the rhenium complex at the standard concentration value and porphyrin present at higher concentration; c1) Mixtures with porphyrin at the same initial concentration and more concentrated in rhenium complex, at 1:*n* ratios and c2) Analogous 1:*n* mixtures in which rhenium catalyst is maintained at the same concentration and the porphyrin is diluted. In addition, only one sacrificial electron donor has been employed (TEOA), so an additional modification pathway would come from modification of its nature.

Time–resolved infrared spectroscopy experiments (TRIR) on active and inactive mixtures would let us know if electron transfer rate or charge recombination are the main causes of these different properties and their variation when modifying ratios and concentrations will be useful in order to rationally design better catalysts.

Due to the possible chemical modifications in the catalytic media and because of the complexity of the results obtained, more precise electrochemical and photophysical analyses on DMF instead of dichloromethane should be carried out. Preliminary studies, not shown in this thesis, have proved the feasibility of making both, electrochemical and fluorescence measurements, in DMF solution. Furthermore, synthesis and characterization of the corresponding chlorins, and not only the porphyrins, could be helpful to clarify, for instance, why the neutral bromides are active with apparently positive driving forces.

This initial first comprehensive study on porphyrin sensitized bimolecular photocatalytic systems has allowed us to gain an insight into the performance and dynamics of these systems, although more questions are presented at this point and a much wider landscape is presented for the future.

Chapter 6. Experimental

6.1 Solvents, Reagents and General Procedures

Chemicals were obtained from the following suppliers: sulfuric acid (BDH); anhydrous magnesium sulfate, MF100 glass microfibre paper, sodium carbonate and sodium hydroxide (Fisher); zinc(II) acetate dihydrate (Fisons); *meso*–tetraphenylporphine (H_2TPP, **FB–P1**), *meso*–tetra(4–tolyl)porphine (H_2TTP, **FB–P2**) and *meso*–tetra(4–methoxyphenyl)porphine (H_2TMPP, **FB–P4**) (Frontier Scientific); ethylenediaminetetraacetic acid (Fluka); silica gel 60 F_{254} TLC plates (Merk); bromine, 2,2'–bipyridine, 2,2'–bipyridine–4,4'–dicarboxylic acid, 4–*tert*–butylbenzaldehyde, Celite 512 medium, dirhenium decacarbonyl, 3–picoline, propionic acid, pyrrole, silver hexafluorophosphate, tetrabutylammonium hexafluorophosphate and triethyl phosphite (Sigma–Aldrich).

Column chromatography of porphyrins was performed on a Combi*Flash* R_f system using 8 g Redi*Sep* R_f basic alumina columns (Teledyne Isco) , loading the samples over neutral alumina (Fluka).

Solvents for general use were obtained from Fisher and used without further purification. Solvents for Schlenk–line work and cyclic voltammetry were dried by refluxing over sodium (THF), P_2O_5 (CH_3CN) or CaH_2 (CH_2Cl_2). After refluxing, they were distilled and stored under argon.

Deuterated solvents for NMR were obtained from Sigma–Aldrich and used as purchased without further purification.

6.2 Physical Measurements

UV–Visible spectra were acquired on an Agilent 8453 diode–array spectrophotometer employing 10 mm path length quartz cuvettes. Fluorescence measurements were performed with 10 mm path length cuvettes on a Hitachi F–4500 fluorimeter exciting the first Q(0,1) band of the porphyrins.

Infrared spectra were recorded in solution on a Unicam RS 10000E FTIR instrument using an Omni Cell system (Specac), averaging 16 scans at 1 cm^{-1} resolution, employing pure solvent was employed as background. EI mass spectra were recorded on a Waters GCT Premier oaTOF mass spectrometer and ESI–MS on a Bruker micrOTOF instrument. NMR spectra were recorded on a Jeol ECX400 or Jeol ECS400 spectrometers. ^{1}H and ^{13}C NMR experiments were calibrated using residual solvent signals; for ^{19}F and ^{31}P calibration, an automatic spectrometer reference was used. Elemental analyses were performed on an Exeter Analytical Inc CE–440 analyser, in combination with a Sartorius S2 analytical balance. Cyclic voltammetry was performed using a BASi C3 Cell Stand potentiostat with platinum working (1.6 mm diameter disc) and auxiliary (wire) electrodes and Ag/AgCl (3M NaCl) reference electrode. Experiments were carried out scanning first to the anodic potential in the case of the porphyrins and to the cathodic one with the rhenium complexes. The working electrode was polished using a water suspension of 0.05 μm size alumina particles before every measurement. Recrystallized and dried[96] tetrabutylammonium hexafluorophosphate ($TBAPF_6$) 0.1 M was used as supporting electrolyte. All the experiments were performed using dry dichloromethane and the solution was purged with nitrogen for 10 minutes prior to measure. Ferrocene/ferrocenium redox couple (Fc/Fc^+) was used as an internal reference and all potentials in this thesis are quoted relative to the Fc/Fc^+ couple.

6.3 X–ray Crystallography

Diffraction data were collected at 110 K on an Agilent SuperNova diffractometer with Mo K_α radiation (λ = 0.71073 Å). Data collection, unit cell determination and frame integration were carried out with "CrysalisPro". Absorption corrections were applied using crystal face–indexing and ABSPACK software within CrysalisPro. Structures were solved and refined using Olex2[97] implementing SHELX algorithms. Structures were solved by either Patterson or direct methods using SHELXS–97 and refined by full–matrix least squares using SHELXL–97.[98] All non–hydrogen atoms were refined anisotropically. Carbon–bound hydrogen atoms were placed at calculated positions and refined using a "riding model".

6.4 Photocatalytic CO_2 Reduction

Photochemical CO_2 reduction experiments were carried out in a custom–designed photolysis kit with a UV–Visible quartz cuvette (10 mm path length). A 3 ml solution of 0.05 mM of both porphyrin and catalyst in 5:1 DMF:TEOA was poured into the UV–Visible cuvette and sealed with a red rubber Suba–seal. The sample was therefore bubbled with 5% CH_4 in CO_2 for 10 minutes to remove air. The solution was irradiated with visible light of $\lambda > 520$ nm (filtered Xenon lamp) and the reaction simultaneously monitored by UV–Visible spectroscopy and GC.

6.5 Gas Chromatography

For GC analysis, a UnicamProGC+ equipment (ThermoONIX) fitted with a thermal conductivity detector (TCD) was used. The gases (air, CO, CH_4 and CO_2) were separated with a Restek ShinCarbonST 100/120 micropacked column (2 m, 1/16'' OD, 1.0 mm ID) fitted with "pigtails" of Restek intermediate–polarity deactivated guard column on either ends (fused silica, 0.53 mm ID, 0.69 ± 0.05 mm OD). Ultra high purity He (N6.0, BOC gases) was used as the carrier gas and was passed through a GC triple carrier gas filter (Focus Technical) to remove trace impurities (oxygen, moisture and hydrocarbons) prior to reaching the column.

The temperature was set up with a constant period of 1 minute at 40 ºC and then a 5 ºC/min slope up to 120 ºC (16 minutes). The injection was made at 220 ºC with a 30 ml/min split flow. The carrier gas (He) was kept at constant pressure of 165 kPa (1.6 atm) and the detector was configured with block and transfer temperatures of 200 and 190 ºC respectively at a constant voltage of 10 V and employing flows of makeup and reference gases of 29 and 30 ml/min respectively.

Gas samples were injected manually (200 μl) using a Hamilton gastight locking syringe (500 μl). The amount of CO produced was quantified using a calibration plot. Known volumes of CO were mixed with a standard volume of CO_2/5% CH_4.

The area of the CO peak was plotted versus the area of the methane peak in the GC chromatogram, considering ideal behavior and turnover numbers (TONs) of CO were calculated based on the moles of catalyst present in the reaction solution.

Elution peaks were manually integrated considering a linear straight baseline between two points selected at both sides of each peak. The smallest (min) and biggest (max) possible values of both carbon monoxide and methane were measured. Combination of CO_{min} area with CH_{4max} and viceversa were taken as the possible extreme values of carbon monoxide in the sample. Arithmetic mean of those two values was taken as the real value and used in further calculations, considering the extremes calculated before as an estimation of its associated error.

6.6 Synthesis

For NMR labeling notation see 0 – NMR spectroscopy on page 28. The IR wavenumber labels correspond to weak (w), medium (m) or strong (s) and the symmetry of the metal carbonyls stretching modes is indicated in brackets for the C_{4v} ([**Re(CO)$_5$Br]**), C_s (**R1–a**, **R3–a**†, **R4–a**, **R1–b** and **R4–b**) or *pseudo*–C_{3v} (**R2–a**, **Re2–b** and **R3–b**) symmetry groups. For symmetry assignment references, see 0 – Infrared spectroscopy on page 54. †Although picoline complexes are expected to exhibit *pseudo*–C_{3v} symmetry, this is not observed in the case of **R3–a**, see Figure 2.41 on page 60 and following discussion.

5,10,15,20–tetrakis[4–(*tert*–butyl)phenyl]–21*H*,23*H*–porphine: H$_2$TTBPP (FB–P3)

The Adler–Longo method[50] was used to synthesize this product. Freshly distilled pyrrole (0.97 ml, 14.06 mmol, 1.0 eq) and 4–*tert*–butylbenzaldehyde (2.35 ml, 14.06 mmol, 1.0 eq) were dissolved in propionic acid (55 ml) and the solution was refluxed for 30 minutes. The mixture experienced progressive colour changes from colourless to dark purple and the appeareance of a dark solid can also be observed. The suspension was allowed to cool and filtered. The purple solid obtained was washed several times with methanol and vacuum dried. Yield: 788 mg (27 %).

R_f (1:5 Ethyl acetate:Hexane): 0.72.

^{1}H NMR (400 MHz, $CDCl_3$): δ_H (ppm): 8.87 (s, 8H, $H_{pyrrole}$), 8.15 (d, 8H, $^3J_{HH}$ = 8.4 Hz, H_{ortho}), 7.76 (d, 8H, H_{meta}), 1.61 (s, 36H, CH_3), –2.74 (s, 2H, NH).

5,10,15,20–tetraphenyl–21*H*,23*H*–porphine zinc(II): ZnTPP (P1)

A previously described porphyrin–metallation procedure was followed.[41] **FB–P1** (300 mg, 0.49 mmol, 1 eq) and zinc(II) acetate dihydrate (484 mg, 2.2 mmol, 4.5 eq) were suspended in 5:1 $CHCl_3$:MeOH (30 ml) and the mixture refluxed for 1 hour. After cooling it down to room temperature, solution was diluted with $CHCl_3$ (100 ml) and washed with an EDTA solution (1 g EDTA per 100 ml of 10% (w/v) Na_2CO_3 aqueous solution) (3 x 200 ml). The organic layers were pooled, dried over $MgSO_4$, filtered and the solvent removed to yield a purple powder (258 mg). The product was purified by column chromatography with 1:20 → 1:1 AcOEt:Hexane as mobile phase. Yield: 179 mg (53 %).

R_f (1:5 Ethyl acetate:Hexane): 0.50.

^{1}H NMR (400 MHz, $CDCl_3$): δ_H (ppm): 8.94 (s, 8H, $H_{pyrrole}$), 8.24–8.20 (m, 8H, H_{ortho}), 7.80–7.71 (m, 12H, H_{meta}, H_{para}).

5,10,15,20–tetrakis(4–tolyl)–21*H*,23*H*–porphine zinc(II): ZnTTP (P2)

The tolyl derivative was prepared in the same way as **P1**. A suspension of **FB–P2** (329 mg, 0.49 mmol, 1 eq) and zinc(II) acetate dihydrate (484 mg, 2.2 mmol, 4.5 eq) in 5:1 $CHCl_3$:MeOH (30 ml) was heated to reflux for 1 hour. After allowing it to cool, the mixture was diluted with chloroform (100 ml) and washed with an EDTA solution (1 g EDTA per 100 ml of 10% (w/v) Na_2CO_3 aqueous solution) (3 x 200 ml). The organic layers were collected, dried over $MgSO_4$, filtered and the solvent removed, to yield a purple powder that required no further purification. Yield: 247 mg (69 %).

R_f (1:5 Ethyl acetate:Hexane): 0.51.

^{1}H NMR (400 MHz, Acetone–d_6): δ_H (ppm): 8.96 (s, 8H, $H_{pyrrole}$), 8.10 (d, 8H, $^3J_{HH}$ = 7.8 Hz, H_{ortho}), 7.55 (d, 8H, H_{meta}), 2.71 (s, 12H, CH_3).

5,10,15,20–tetrakis[4–(*tert*–butyl)–phenyl]–21*H*,23*H*–porphine zinc(II): ZnTTBPP (P3)

The porphyrin was metallated following the same procedure employed to make **P1**. A suspension of **FB–P3** (400 mg, 0.50 mmol, 1 eq) and zinc(II) acetate dihydrate (493 mg, 2.25 mmol, 4.5 eq) in 5:1 $CHCl_3$:MeOH (30 ml) was refluxed for 1 hour. After allowing it to cool, the mixture was diluted with $CHCl_3$ (50 ml) and washed with an EDTA solution (1 g EDTA per 100 ml of 10% (w/v) Na_2CO_3 aqueous solution) (3 x 200 ml). The organic layers were collected, dried over $MgSO_4$, filtered and the solvent removed under vacuum to yield a purple powder (366 mg). A fraction of the product (200 mg) was purified by column chromatography using dichloromethane as eluent. Yield: 90 mg (36 %).

R_f (1:5 Ethyl acetate:Hexane): 0.62.

^{1}H NMR (400 MHz, $CDCl_3$): δ_H (ppm): 8.97 (s, 8H, $H_{pyrrole}$), 8.15 (d, 8H, $^3J_{HH}$ = 8.4 Hz, H_{ortho}), 7.75 (d, 8H, H_{meta}), 1.62 (s, 36H, CH_3).

5,10,15,20–tetrakis(4–methoxyphenyl)–21*H*,23*H*–porphine zinc(II): ZnTMPP (P4)

The same procedure followed for **P1** was employed. In 5:1 $CHCl_3$:MeOH (30 ml), a mixture of **FB–P4** (400 mg, 0.50 mmol, 1 eq) and zinc(II) acetate dihydrate (493 mg, 2.25 mmol, 4.5 eq) was refluxed for 1 hour. After allowing it to cool, $CHCl_3$ (100 ml) was added to dilute the mixture before washing it with an EDTA solution (1 g EDTA per 100 ml of 10% (w/v) Na_2CO_3 aqueous solution) (3 x 200 ml). The organic layers were collected, dried over $MgSO_4$, filtered and the solvent removed *in vacuo* to yield a purple powder (304 mg). A fraction of the product (117 mg) was purified by column chromatography employing 1:9 → 9:1 AcOEt:Hexane as eluent. Yield: 71 mg (17 %).

R_f (1:4 Ethyl acetate:Hexane): 0.19.

^{1}H NMR (400 MHz, $CDCl_3$): δ_H (ppm): 8.97 (s, 8H, $H_{pyrrole}$), 8.13 (d, 8H, $^3J_{HH}$ = 8.6 Hz, H_{ortho}), 7.29 (d, 8H, H_{meta}), 4.11 (s, 12H, CH_3).

4,4'–bis(methoxycarbonyl)–2,2'–bipyridine: BMCbpy

This compound was prepared following a previously described procedure.[99] 2,2'–bipyridine–4,4'–dicarboxylic acid (533 mg, 2.18 mmol) was suspended in methanol (10 ml) and concentrated sulphuric acid (1.1 ml) was added. The reaction mixture was refluxed for 60 hours. After that time, the weakly pink solution was allowed to cool and poured intro 25 ml of water to form a pink slurry. The pH of the solution was adjusted to 8 by addition of 25% (w/v) NaOH in water and the product was extracted with chloroform (3 x 50 ml). The organic phase was dried over $MgSO_4$, filtered and the solvent removed under vacuum to yield a white solid. Yield: 503 mg (84 %).

^{1}H NMR (400 MHz, $CDCl_3$): δ_H (ppm): 8.96 (dd, 2H, $^4J_{HH}$ = 1.6 Hz, $^5J_{HH}$ = 0.8 Hz, $H_{3,3'}$), 8.87 (dd, 2H, $^3J_{HH}$ = 5.2 Hz, $H_{6,6'}$), 7.91 (dd, 2H, $H_{5,5'}$), 4.00 (s, 6H, OCH_3).

bromopentacarbonylrhenium(I): [Re(CO)$_5$Br]

A previously developed method[100] was used in this synthesis. Bromine (50 µl, 0.94 mmol, 1.15 eq) was added to a solution of dirhenium decacarbonyl (536 mg, 0.82 mmol, 1 eq) in dichloromethane (20 ml) at 5 ºC protected from light. The solution was stirred at 5 ºC for 30 minutes. The solvent was removed under vacuum and the solid washed with water to yield a white powder. Yield: 482 mg (72 %).

IR (THF): ν_{CO} (cm^{-1}): 2154w (A_1), 2046s (E), 1987m (A_1).

***fac*–(2,2'–bipyridine)bromotricarbonylrhenium(I): [Re(bpy)(CO)$_3$Br] (R1–a)**

A recently described procedure was employed.[101] A solution of [$Re(CO)_5Br$] (594 mg, 1.46 mmol,1 eq) and 2,2'–bipyridine (228 mg, 1.46 mmol, 1 eq) in toluene (60 ml) was refluxed for 1 hour. The initially colorless solution became

yellow and changed to orange. After 30 minutes a yellow solid in suspension was observed. The mixture was allowed to cool and placed in the freezer (–23 ºC) for 1 hour. The solution was filtered, and the yellow powder obtained washed with hexane and vacuum dried. Yield: 694 mg (93 %).

IR (THF): ν_{CO} (cm^{-1}): 2020s (*A*'), 1919s (*A*'), 1895s (*A*'').

^{1}H NMR (400 MHz, $CDCl_3$): δ_H (ppm): 9.10 (ddd, 2H, $^3J_{HH}$ = 5.2 Hz, $^4J_{HH}$ = 1.2 Hz, $^5J_{HH}$ = 0.8 Hz, $H_{6,6'}$), 8.21 (bd, 2H, $H_{3,3'}$), 8.08 (td, 2H, $^3J_{HH}$ = 7.6 Hz, $H_{4,4'}$), 7.55 (ddd, 2H, $H_{5,5'}$).

fac–acetonitrile(2,2'–bipyridine)tricarbonylrhenium(I) hexafluorophosphate: $[Re(bpy)(CO)_3(CH_3CN)][PF_6]$ (R2–a)

A modification of an analogous procedure was employed.[59] **R1–a** (395 mg, 0.77 mmol, 1 eq) and silver hexafluorophosphate (215 mg, 0.85 mmol, 1.1 eq) were dissolved in dry acetonitrile (20 ml) under argon in a round–bottom flask covered to avoid light. The solution was refluxed for 15 hours, allowed to cool and filtered over a glass microfibre filtering paper. The solvent was removed under vacuum, the solid redissolved in acetone that was reevaporated to yield a bright yellow solid (457 mg) that was washed with hexane and diethyl ether. A fraction of the product (104 mg) was recrystallized in CH_2Cl_2:Et_2O. Yield: 92 mg (75%).

IR (THF): ν_{CO} (cm^{-1}): 2037s (A_1), 1932s (*E*).

^{1}H NMR (400 MHz, $CDCl_3$): δ_H (ppm): 8.93 (ddd, 2H, $^3J_{HH}$ = 5.5 Hz, $^4J_{HH}$ = 1.5 Hz, $^5J_{HH}$ = 0.6 Hz, $H_{6,6'}$), 8.48 (bdt, 2H, $^3J_{HH}$ = 8.2 Hz, $H_{3,3'}$), 8.25 (td, 2H, $^3J_{HH}$ = 7.8 Hz, $H_{4,4'}$), 7.65 (ddd, 2H, $^4J_{HH}$ = 1.3 Hz, $H_{5,5'}$), 2.21 (s, 3H, H_3CCN).

(400 MHz, Acetone–d_6): δ_H (ppm): 9.23 (ddd, 2H, $^3J_{HH}$ = 5.5 Hz, $^4J_{HH}$ = 1.4 Hz, $^5J_{HH}$ = 1.0 Hz, $H_{6,6'}$), 8.82 (dt, 2H, $^3J_{HH}$ = 7.9 Hz, $H_{3,3'}$), 8.50 (td, 2H, $^3J_{HH}$ = 7.9 Hz, $H_{4,4'}$), 7.94 (ddd, 2H, $^4J_{HH}$ = 1.2 Hz, $H_{5,5'}$), 2.35 (s, 3H, H_3CCN).

$^{31}P\{^{1}H\}$ NMR (161.9 MHz, Acetone–d_6): δ_P (ppm): –143.6 (septet, $^{1}J_{PF}$ = 708 Hz).

^{19}F NMR (376.4 MHz, Acetone–d_6): δ_F (ppm): –72.56 (d).

fac–(2,2'–bipyridine)tricarbonyl(3–picoline)rhenium(I) hexafluorophosphate: *fac*–[Re(bpy)(CO)$_3$(3–Pic)][PF$_6$] (R3–a)

A modification of a similar reaction was employed.[41] In an argon–filled system protected from light, **R1–a** (100 mg, 0.197 mmol, 1 eq) and silver hexafluorophosphate (55 mg, 0.217 mmol, 1.1 eq) were dissolved in dry THF. Then, 3–picoline (0.5 ml) was added and the solution was refluxed for 1 hour. The solution was allowed to cool, filtered over Celite and the solvent removed under vacuum. The mayor excess of picoline was removed by addition and decantation of hexane (3 x 40 ml) to yield a yellow powder (103 mg). X–ray quality crystals were obtained by recrystallization of a fraction of the product (60 mg) in acetone:hexane. Yield: 51 mg (67 %).

IR (THF): ν_{CO} (cm^{-1}): 2032s (*A*'), 1928s (*A*'), 1923s (*A*'').

^{1}H NMR (400 MHz, Acetone–d_6): δ_H (ppm): 9.50 (ddd, 2H, $^{3}J_{HH}$ = 4.4 Hz, $^{4}J_{HH}$ = 1.2 Hz, $^{5}J_{HH}$ = 0.8 Hz, bpy–H$_{6,6'}$), 8.73 (bd, 2H, $^{3}J_{HH}$ = 8.2 Hz, bpy–H$_{3,3'}$), 8.47 (td, 2H, $^{3}J_{HH}$ = 6.0 Hz, bpy–H$_{4,4'}$), 8.44 (m, 1H, pic–H$_2$), 8.32 (bd, 1H, $^{3}J_{HH}$ = 4.4 Hz, pic–H$_6$), 8.01 (ddd, 2H, $^{4}J_{HH}$ = 1.2 Hz, bpy–H$_{5,5'}$), 7.83 (bd, 1H, $^{3}J_{HH}$ = 6.4 Hz, pic–H$_4$), 7.25 (dd, 1H, pic–H$_5$), 2.23 (s, 3H, pic–CH$_3$).

$^{31}P\{^{1}H\}$ NMR (161.9 MHz, Acetone–d_6): δ_P (ppm): –143.6 (septet, $^{1}J_{PF}$ = 703 Hz).

^{19}F NMR (376.4 MHz, Acetone–d_6): δ_F (ppm): –72.50 (d).

fac–(2,2'–bipyridine)tricarbonyl(triethylphosphite)rhenium(I) hexafluorophosphate: *fac*–[Re(bpy)(CO)$_3${P(OEt)$_3$}][PF$_6$] (R4–a)

An analogous procedure to the one employed for the picoline derivative **R3–a** resulted only in partial conversion, so an alternative one employing the acetonitrile intermediate (**R2–a**) was used in this case.[59] The precursor **R2–a**

(164 mg, 0.27 mmol) was dissolved in dry THF (17 ml), triethylphosphite (0.5 ml) was added and the solution refluxed in the dark under argon for 24 hours. The reaction was allowed to cool and the solvent removed under vacuum after adding acetone several times. To remove most of the free phosphite, the solid obtained was washed with hexane and diethyl ether three times and dried, yielding a bright yellow solid (194 mg). A fraction of the product (97 mg) was purified by column chromatography employing Et_2O → 3:1 Et_2O:CH_2Cl_2 → CH_2Cl_2 as eluent. Yield: 67 mg (67%). Crystals suitable for X–ray diffraction were obtained by recrystallization in CH_2Cl_2:Et_2O.

IR (THF): ν_{CO} (cm^{-1}): 2042s (*A*'), 1958s (*A*'), 1926s (*A*'').

^{1}H NMR (400 MHz, $CDCl_3$): δ_H (ppm): 8.89 (bd, 2H, $^3J_{HH}$ = 5.6 Hz, $H_{6,6'}$), 8.74 (bd, 2H, $^3J_{HH}$ = 8.1 Hz, $H_{3,3'}$), 8.32 (bt, 2H, $^3J_{HH}$ = 7.9 Hz, $H_{4,4'}$), 7.62 (ddd, 2H, $^4J_{HH}$ = 1.3 Hz, $H_{5,5'}$), 3.81 (quintet, 6H, $^3J_{PH}$ = $^3J_{HH}$ = 7.1 Hz, CH_2), 1.06 (t, 9H, CH_3).

^{31}P{^{1}H} NMR (161.9 MHz, $CDCl_3$): δ_P (ppm): 108.1 (s, $P(OEt)_3$), –143.6 (septet, $^1J_{PF}$ = 712 Hz, PF_6).

^{19}F NMR (376.4 MHz, $CDCl_3$): δ_F (ppm): –72.95 (d, $^1J_{FP}$ = 712 Hz).

fac–[4,4'–bis(methoxycarbonyl)–2,2'–bipyridine]bromotricarbonyl rhenium(I): *fac*–[Re(BMCbpy)(CO)$_3$Br] (R1–b)

The same procedure employed for the unsubstituted bipyridine complex **R1–a** was used in this case.[101] A solution of $[Re(CO)_5Br]$ (298 mg, 0.734 mmol, 1 eq) and 4,4'–bis(methoxycarbonyl)–2,2'–bipyridine (197 mg, 0.734 mmol, 1 eq) in toluene was refluxed for an hour. The solution became orange and the product precipitated as an orange powder. The reaction was allowed to cool and placed in the freezer (–23 ºC) for two hours. The product was filtered, washed with hexane and vacuum dried, to yield an orange powder. Yield: 445 mg (97 %).

IR (THF): ν_{CO} (cm^{-1}): 2022s (*A*'), 1925m (*A*'), 1901m (*A*''), 1740w (ester).

^{1}H NMR (400 MHz, $CDCl_3$): δ_H (ppm): 9.23 (d, 2H, $^{3}J_{HH}$ = 5.6 Hz, $H_{6,6'}$), 8.85 (bs, 2H, $H_{3,3'}$), 8.08 (dd, 2H, $^{4}J_{HH}$ = 1.6 Hz, $H_{5,5'}$), 4.10 (s, 6H, OCH_3).

^{13}C{^{1}H} NMR (100.6 MHz, $CDCl_3$): δ_C (ppm): 196.3 ($CO_{ct-a,b}$), 187.9 (CO_{cc}), 163.5 (CO_{ester}), 156.3 ($C_{2,2'}$), 154.3 ($C_{6,6'}$), 140.1 ($C_{4,4'}$), 126.8 ($C_{5,5'}$), 123.2 ($C_{3,3'}$), 54.0 (CH_3).

HR–EI–MS: For $C_{17}H_{12}N_2O_7{}^{79}Br^{185}Re$, observed mass 619.9464, calculated 619.9358, difference 10.6 mDa.

Elemental Analysis: Calculated for $C_{17}H_{12}N_2O_7BrRe$, C, 32.81; H, 1.94; N, 4.50, found C, 32.39; H, 1.86; N, 4.28.

fac–acetonitrile[4,4'–bis(methoxycarbonyl)–2,2'–bipyridine]tricarbonyl rhenium(I) hexafluorophosphate: [Re(BMCbpy)(CO)$_3$(CH$_3$CN)][PF$_6$] (R2–b)

The same procedure as for **Re2–a** was employed. **R1–b** (280 mg, 0.44 mmol, 1 eq) and silver hexafluorophosphate (125 mg, 0.49 mmol, 1.1 eq) were placed inside an argon–filled system protected from light and dry acetonitrile (20 ml) was added. The solution was refluxed for 15 hours. The reaction was allowed to cool and filtered over a glass microfibre filtering paper. The solvent was removed under vacuum, the solid redissolved in acetone and the solvent removed again to yield a bright yellow solid that was washed with hexane and diethyl ether. Yield: 314 mg (98 %). X–ray quality crystals were obtained by recrystallization in CH_2Cl_2:Et_2O.

IR (THF): ν_{CO} (cm^{-1}): 2038s (A_1), 1936s (E), 1739w (ester).

^{1}H NMR (400 MHz, $CDCl_3$): δ_H (ppm): 9.09 (dd, 2H, $^{3}J_{HH}$ = 5.7 Hz, $^{5}J_{HH}$ = 0.6 Hz, $H_{6,6'}$), 8.98 (bd, 2H, $H_{3,3'}$), 8.20 (dd, 2H, $^{4}J_{HH}$ = 1.6 Hz, $H_{5,5'}$), 4.11 (s, 6H, OCH_3), 2.24 (s, 3H, H_3CCN).

(500 MHz, Acetone–d_6): δ_H (ppm): 9.46 (bd, 2H, $^{3}J_{HH}$ = 5.7 Hz, $H_{6,6'}$), 9.42 (bs, 2H, $H_{3,3'}$), 8.34 (dd, 2H, $^{4}J_{HH}$ = 1.3 Hz, $H_{5,5'}$), 4.07 (s, 6H, OCH_3), 2.30 (s, 6H, H_3CCN).

$^{13}C\{^{1}H\}$ NMR (125.6 MHz, Acetone–d_6): δ_C (ppm): 194.2 ($CO_{ct-a,b}$), 190.5 (CO_{cc}), 164.3 (CO_{ester}), 157.9 ($C_{2,2'}$), 156.2 ($C_{6,6'}$), 142.6 ($C_{4,4'}$), 128.5 ($C_{5,5'}$), 125.1 ($C_{3,3'}$), 124.1 (H_3CCN), 54.0 (OCH_3), 3.2 (H_3CCN).

$^{31}P\{^{1}H\}$ NMR (161.9 MHz, DMSO–d_6): δ_P (ppm): –143.6 (septet, $^{1}J_{PF}$ = 703 Hz).

^{19}F NMR (376.4 MHz, DMSO–d_6): δ_F (ppm): –70.05 (d, $^{1}J_{FP}$ = 703 Hz).

HR–ESI–MS: For $C_{19}H_{15}N_3O_7{}^{185}Re$, observed mass 582.0435, calculated 582.0439, difference 0.4 mDa.

Elemental Analysis: Calculated for $C_{19}H_{15}F_6N_3O_7PRe$, C, 31.32; H, 2.08; N, 5.77, found C, 31.46; H, 2.09; N, 5.29.

fac–[4,4'–bis(methoxycarbonyl)–2,2'–bipyridine]tricarbonyl(3–picoline) rhenium(I) hexafluorophosphate: [Re(BMCbpy)(CO)$_3$(3–Pic)][PF$_6$] (R3–b)

The preparation of this picoline complex was carried out from the acetonitrile precursor, as previously described for the phosphite complex **R4–a**. To a solution of **R2–b** (128 mg, 0.18 mmol) in dry THF (20 ml) in a covered flask, 3–picoline (0.5 ml) was added and the mixture was refluxed under argon for 24 hours. The reaction was cooled down to room temperature and the solvent removed to give and orange oil. A bright orange powder was obtained by evaporating the solvent after adding 1:1 acetone:ethanol to the crude. The solid obtained was washed with hexane to remove the excess of free picoline and dried under vacuum. (131 mg). A fraction of the product (68 mg) was recrystallized in acetone:Et_2O. Yield: 51 mg (71%).

IR (THF): ν_{CO} (cm^{-1}): 2034s (A_1), 1927s (E), 1741w (ester).

^{1}H NMR (400 MHz, Acetone–d_6): δ_H (ppm): 9.74 (dd, 2H, $^{3}J_{HH}$ = 5.7 Hz, $^{5}J_{HH}$ = 0.7 Hz, bpy–$H_{6,6'}$), 9.23 (dd, 2H, $^{4}J_{HH}$ = 1.7 Hz, bpy–$H_{3,3'}$), 8.47 (m, 1H, pic–H_2), 8.40 (dd, 2H, bpy–$H_{5,5'}$), 8.33 (bd, 1H, $^{3}J_{HH}$ = 5.7 Hz, pic–H_6), 7.82 (bd, 1H, $^{3}J_{HH}$ = 7.9 Hz, pic–H_4), 7.33 (dd, 1H, pic–H_5), 4.04 (s, 6H, OCH_3), 2.21 (s, 3H, pic–CH_3).

$^{13}C\{^{1}H\}$ NMR (125.7 MHz, Acetone–d_6): δ_C (ppm): 196.1 ($CO_{ct-a,b}$), 191.7 (CO_{cc}), 164.2 (CO_{ester}), 157.7 (bpy–$C_{2,2'}$), 156.3 (bpy–$C_{6,6'}$), 153.1 (pic–C_2), 150.1 (pic–C_6), 142.6 (bpy–$C_{4,4'}$), 141.6 (pic–C_4), 138.5 (pic–C_3), 129.1 (bpy–$C_{5,5'}$), 127.3 (pic–C_5), 125.4 (bpy–$C_{3,3'}$), 54.0 (OCH_3), 18.1 (pic–CH_3).

$^{31}P\{^{1}H\}$ NMR (161.9 MHz, Acetone–d_6): δ_P (ppm): –143.6 (septet, $^{1}J_{PF}$ =708 Hz).

^{19}F NMR (376.4 MHz, Acetone–d_6): δ_F (ppm): –72.54 (d, $^{1}J_{FP}$ = 708 Hz).

HR–ESI–MS: For $C_{23}H_{19}N_3O_7{}^{185}Re$, observed mass 634.0745, calculated 634.0752, difference 0.7 mDa.

Elemental Analysis: Calculated for $C_{23}H_{19}F_6N_3O_7PRe$, C, 35.39; H, 2.45; N, 5.38, found C, 35.02; H, 2.33; N, 5.10.

fac–[4,4'–bis(methoxycarbonyl)–2,2'–bipyridine]tricarbonyl (triethylphosphite)rhenium(I) hexafluorophosphate: $[Re(BMCbpy)(CO)_3\{P(OEt)_3\}][PF_6]$ (R4–b)

The same procedure followed to prepare **R4–a** and **Re3–b** was employed. In a foil–covered and sealed flask, triethylphosphite (0.5 ml) was added to a solution of **R2–b** (124 mg, 0.17 mmol) in dry THF (20 ml) and the solution was refluxed under argon for 24 hours. After allowing the reaction to cool down to room temperature, an orange solid was obtained after evaporating the THF and acetone added afterwards. In order to remove the excess of phosphite, the solid was washed with hexane, yielding an orange powder (129 mg). A fraction of the product (75 mg) was purified by column chromatography employing CH_2Cl_2 → AcOEt as mobile phase. Yield: 56 mg (65%).

IR (THF): ν_{CO} (cm^{-1}): 2044s (*A*'), 1963s (*A*'), 1931s (*A*''), 1740m (ester).

^{1}H NMR (500 MHz, Acetone–d_6): δ_H (ppm): 9.47 (bd, 2H, $^{3}J_{HH}$ = 5.7 Hz, $H_{6,6'}$), 9.35 (bd, 2H, $^{4}J_{HH}$ = 1.6 Hz, $H_{3,3'}$), 8.32 (dd, 2H, $H_{5,5'}$), 4.07 (s, 6H, OCH_3), 3.97 (quintet, 6H, $^{3}J_{PH} = {}^{3}J_{HH}$ = 7.1 Hz, CH_2), 1.06 (t, 9H, CH_3).

$^{13}C\{^{1}H\}$ NMR (125.7 MHz, Acetone–d_6): δ_C (ppm): 194.1 (d, $^{2}J_{PC(cis)}$ = 11.8 Hz, $CO_{ct–a,b}$), 188.3 (d, $^{2}J_{PC(trans)}$ = 95.7 Hz, CO_{cc}), 164.3 (CO_{ester}), 158.0 ($C_{2,2'}$), 156.5 ($C_{6,6'}$), 142.1 ($C_{4,4'}$), 128.2 ($C_{5,5'}$), 125.0 ($C_{3,3'}$), 63.8 (d, $^{2}J_{PC}$ = 7.4 Hz, OCH_2), 54.0 (OCH_3), 16.1 (d, $^{3}J_{PC}$ = 5.4 Hz, CH_3).

$^{31}P\{^{1}H\}$ NMR (161.9 MHz, Acetone–d_6): δ_P (ppm): 107.2 (s, $P(OEt)_3$), –143.7 (septet, $^{1}J_{PF}$ = 707 Hz, PF_6).

^{19}F NMR (376.4 MHz, Acetone–d_6): δ_F (ppm): –72.57 (d, $^{1}J_{FP}$ = 707 Hz).

HR–ESI–MS: For $C_{23}H_{27}N_2O_{10}P^{185}Re$, observed mass 707.0935, calculated 707.0933, difference 0.2 mDa.

Elemental Analysis: Calculated for $C_{23}H_{27}F_6N_2O_{10}P_2Re \cdot H_2O$, C, 31.69; H, 3.35; N, 3.21, found C, 31.20; H, 3.03; N, 3.15.

fac–[4,4'–bis(methoxycarbonyl)–2,2'–bipyridine](difluorophosphate–1κ*O*) tricarbonylrhenium(I): *fac*–[Re(BMCbpy)$(CO)_3(OPOF_2)$][PF_6] (R5)

The neutral compound **R5** was prepared accidentally in an unsuccessful attempt to make **R3–b** from **R1–b** following a reported procedure for a similar reaction.[102] In a round–bottomed flask covered with foil, **R1–b** (100 mg, 0.160 mmol, 1 eq) and $AgPF_6$ (55 mg, 0.217 mmol, 1.35 eq) were dissolved in CH_2Cl_2 (15 ml) and stirred at room temperature for 12 hours. Then, 3–picoline (97 μl, 0.217 mmol, 1.35 eq) was added and the mixture was stirred at room temperature for another 48 hours. After that time, the micture was filtered over celite and the solvent removed under vacuum to yield an orange solid. X–ray quality crystals were obtained crystallizing the product inCH_2Cl_2:Et_2O at –23 ºC.

IR (THF): ν_{CO} (cm^{-1}): 2030s (*A*'), 1930s (*A*'), 1910s (*A*''), 1741m (ester).

^{1}H NMR (400 MHz, $CDCl_3$): δ_H (ppm): 9.23 (dd, 2H, $^{3}J_{HH}$ = 5.6 Hz, $^{5}J_{HH}$ = 0.6 Hz, $H_{6,6'}$), 8.86 (dd, 2H, $^{4}J_{HH}$ = 1.5 Hz, $H_{3,3'}$), 8.16 (dd, 2H, $H_{5,5'}$), 4.11 (s, 6H, OCH_3).

$^{31}P\{^{1}H\}$ NMR (161.9 MHz, $CDCl_3$): δ_P (ppm): –15.29 (t, $^{1}J_{PF}$ = 970 Hz).

^{19}F NMR (376.4 MHz, $CDCl_3$): δ_F (ppm): –83.06 (d, $^{1}J_{FP}$ = 970 Hz).

Appendices

Appendix I. NMR and IR spectra

Nuclear magnetic resonance and infrared spectra not shown in Chapter 2 are included in this section.

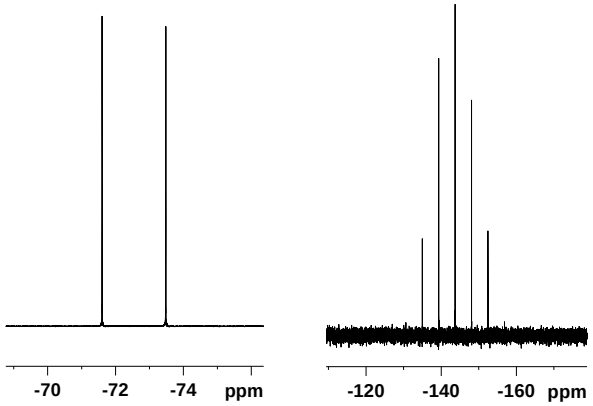

^{19}F (376.4 MHz, left) and ^{31}P (161.9 MHz, right) NMR spectra of [Re(bpy)(CO)$_3$(CH$_3$CN)][PF$_6$] (R2–b) in acetone–d_6 at 298 K

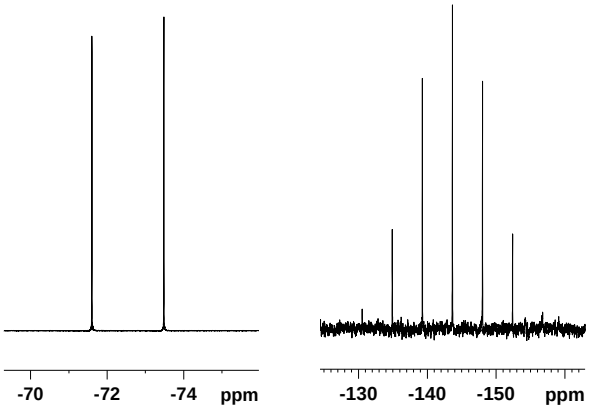

^{19}F (376.4 MHz, left) and ^{31}P (161.9 MHz, right) NMR spectra of [Re(BMCbpy)(CO)$_3$(3–Pic)][PF$_6$] (R3–b) in acetone–d_6 at 298 K

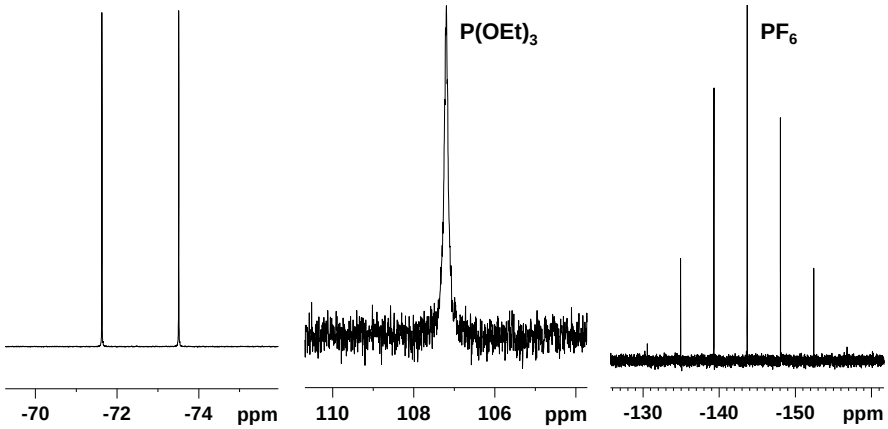

^{19}F (376.4 MHz, left) and ^{31}P (161.9 MHz, center and right) NMR spectra of [Re(BMCbpy)(CO)$_3${P(OEt)$_3$}][PF$_6$] (R4–b) in acetone–d_6 at 298 K

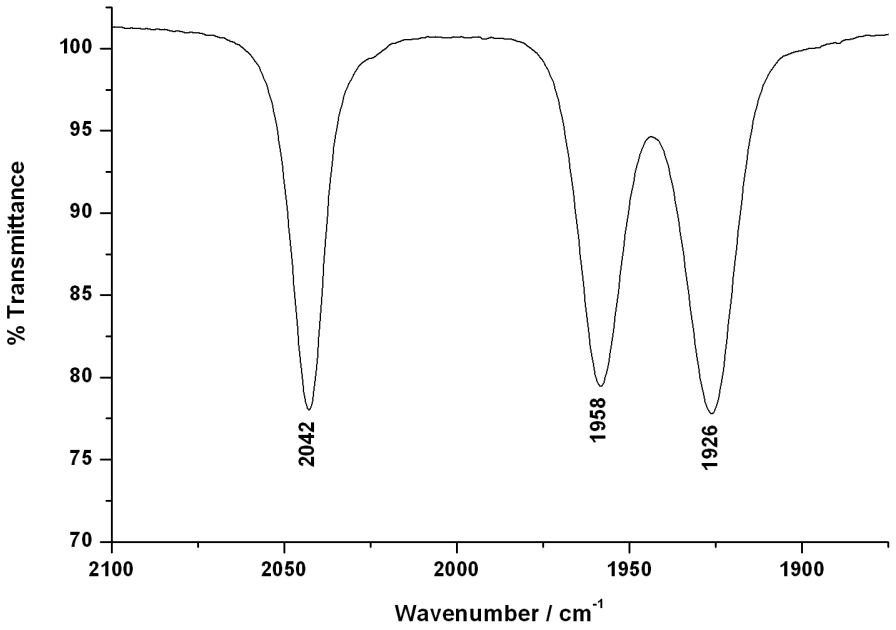

IR spectrum of [Re(bpy)(CO)$_3${P(OEt)$_3$}][PF$_6$] (R4–a) in THF

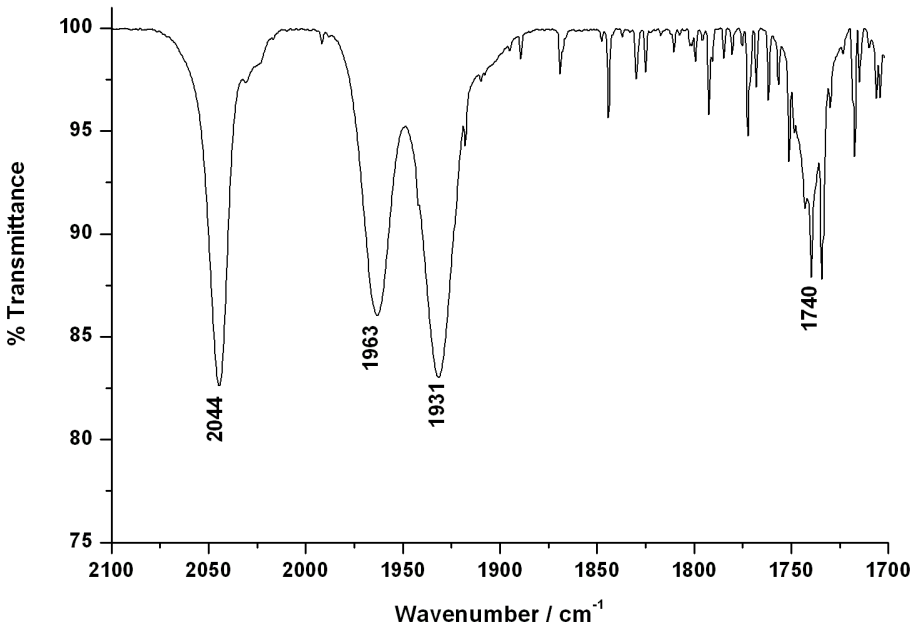

IR spectrum of $[Re(BMCbpy)(CO)_3\{P(OEt)_3\}][PF_6]$ (R4–b) in THF

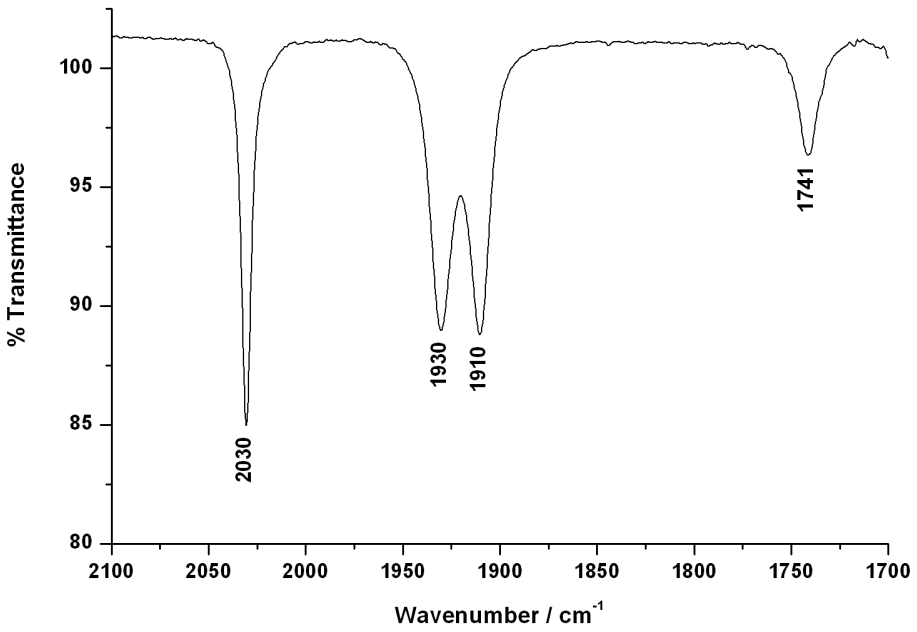

IR spectrum of $[Re(BMCbpy)(CO)_3(OPOF_2)][PF_6]$ (R5) in THF

Appendix II. X–ray crystallography data

Compound	**R3–a**	**R2–b**	**R5**
Formula	$C_{19}H_{15}F_6N_3O_3PRe$	$C_{19}H_{15}F_6N_3O_7PRe$	$C_{17}H_{12}F_6N_2O_9PRe$
M	664.51	728.51	643.46
a / Å	13.1006(4)	10.3451(5)	12.9895(5)
b / Å	11.27050(13)	14.1259(5)	12.1469(2)
c / Å	14.57937(17)	16.5788(9)	14.2301(11)
α / deg	90	90	90
β / deg	98.5041(14)	101.453(6)	113.667(7)
γ / deg	90	90	90
V / $Å^3$	2128.98(7)	1982.84(4)	2056.44(18)
T / K	110(2)	110(2)	110(2)
Space group	$P2_1/c$	$P2_1/c$	$P2_1/c$
Crystal system	monoclinic	monoclinic	monoclinic
Z	4	4	4
RefIns measd	20436	9564	23575
RedIns indep	6851	4781	8049
R_{int}	0.0267	0.0226	0.0364
Final R [I > 2σ(I)]	R_1 = 0.0200	R_1 = 0.0263	R_1 = 0.0289
	wR_2 = 0.0405	wR_2 = 0.0578	wR_2 = 0.0647
GooF on F^2	1.039	1.041	1.055

Appendix III. Cyclic voltammograms

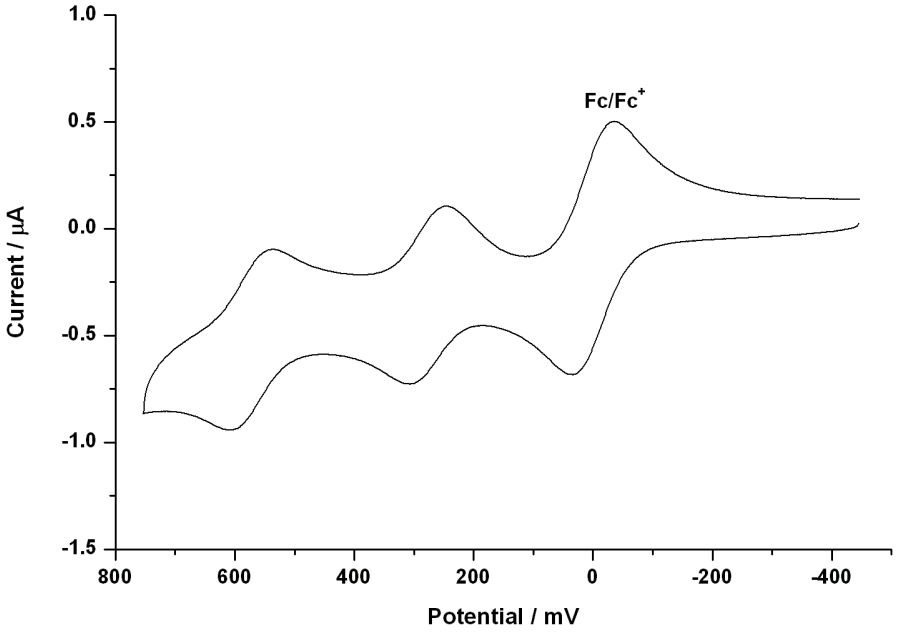

Cyclic voltammogram of ZnTMPP (P4). CH_2Cl_2 2.5 mM Re complex, 0.1 M $TBAPF_6$, 0.8 mM Fc, scan rate 50 mV/s

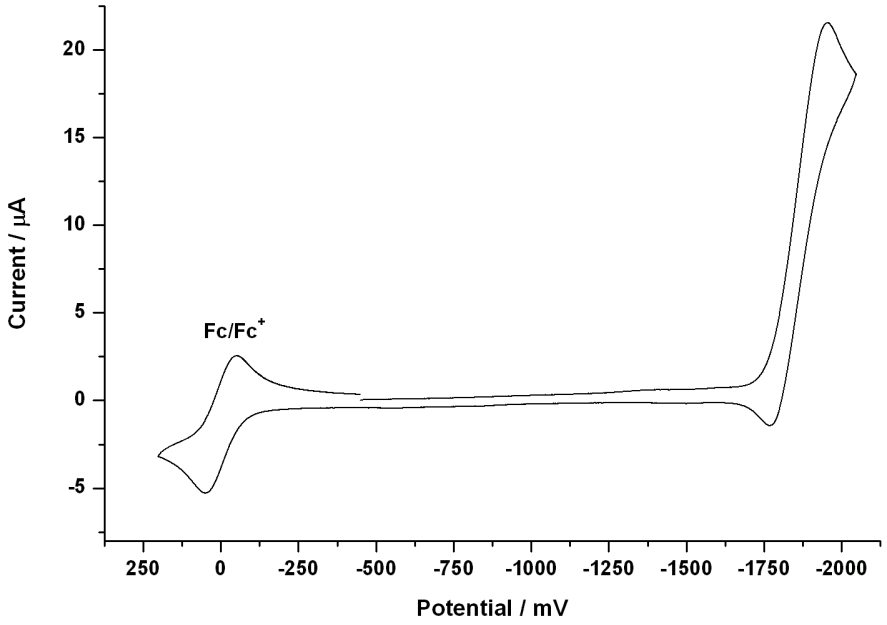

Cyclic voltammogram of $[Re(bpy)(CO)_3Br]$ (R1–a). CH_2Cl_2 2.5 mM Re complex, 0.1 M $TBAPF_6$, 0.8 mM Fc, scan rate 50 mV/s

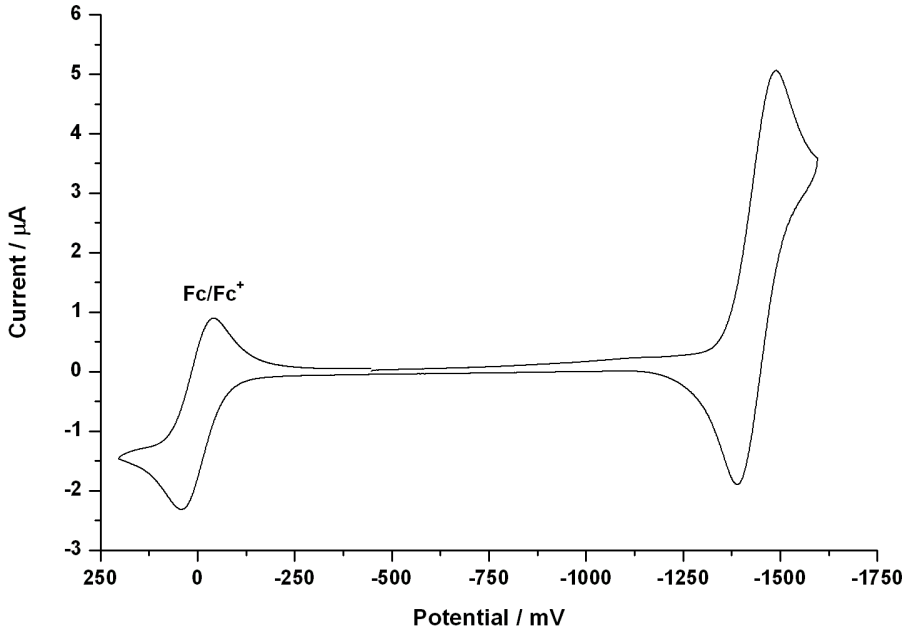

Cyclic voltammogram of [Re(BMCbpy)(CO)$_3$Br] (R1–b). CH_2Cl_2 2.5 mM Re complex, 0.1 M $TBAPF_6$, 0.8 mM Fc, scan rate 50 mV/s

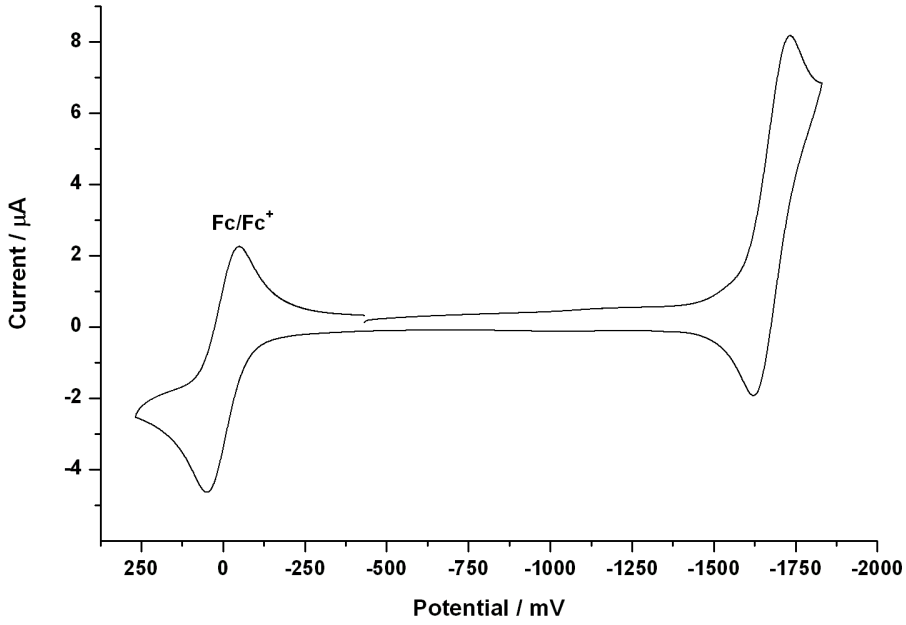

Cyclic voltammogram of [Re(bpy)(CO)$_3${P(OEt)$_3$}][PF_6] (R4–a). CH_2Cl_2 2.5 mM Re complex, 0.1 M $TBAPF_6$, 0.8 mM Fc, scan rate 50 mV/s

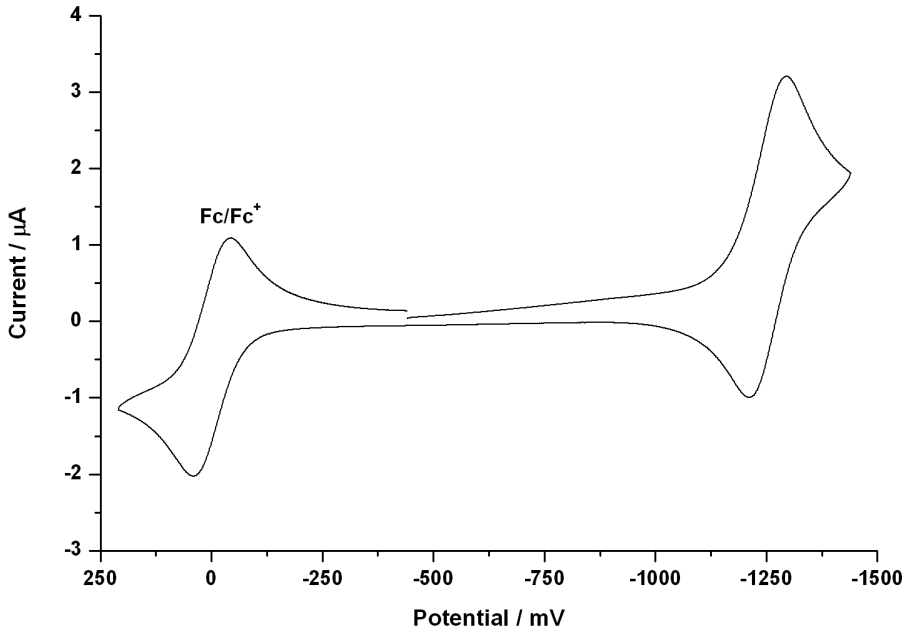

Cyclic voltammogram of $[Re(bpy)(CO)_3\{P(OEt)_3\}][PF_6]$ (R4–b). CH_2Cl_2 2.5 mM Re complex, 0.1 M $TBAPF_6$, 0.8 mM Fc, scan rate 50 mV/s

Appendix IV. UV–Visible absorption and emission spectra of metalloporphyrins

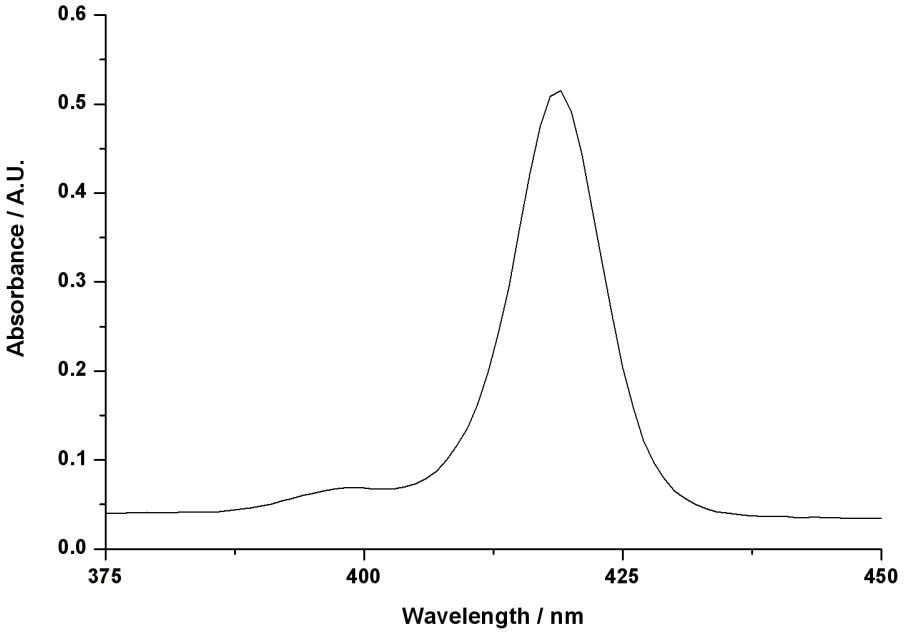

Section of the visible absorption spectrum of ZnTPP (P1) in CH_2Cl_2, 0.5 μM

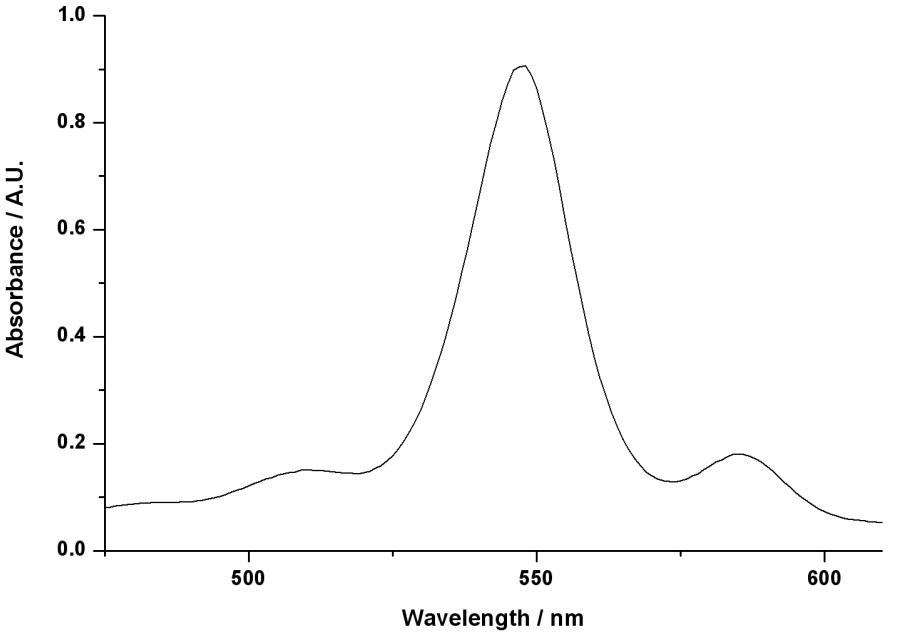

Section of the visible absorption spectrum of ZnTPP (P1) in CH_2Cl_2, 25 μM

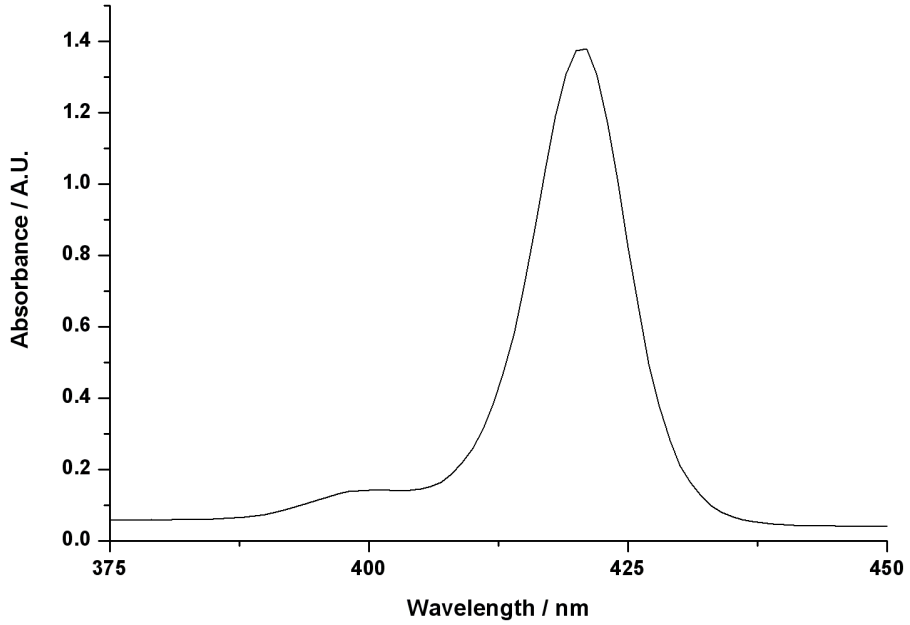

Section of the visible absorption spectrum of ZnTTP (P2) in CH_2Cl_2, 2.5 μM

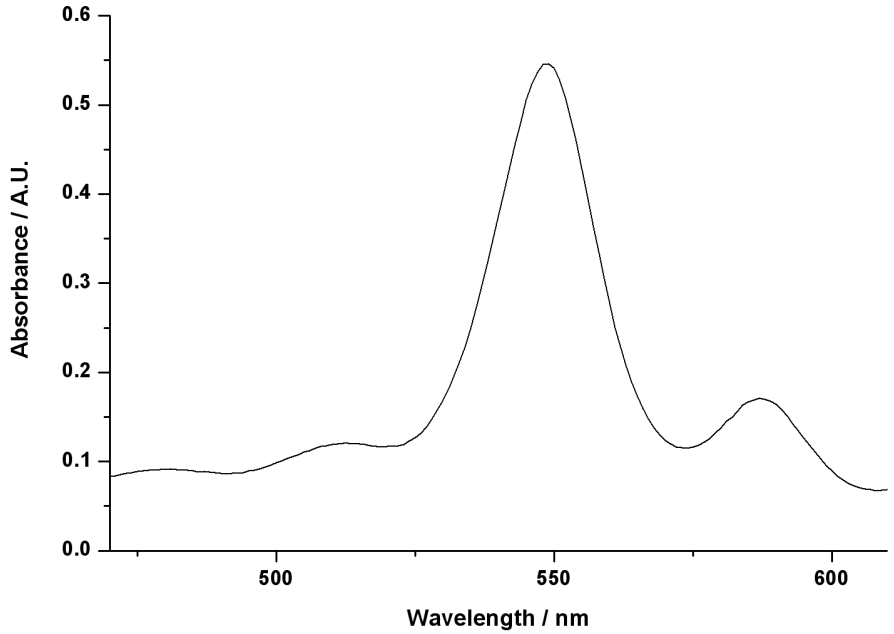

Section of the visible absorption spectrum of ZnTTP (P2) in CH_2Cl_2, 25 μM

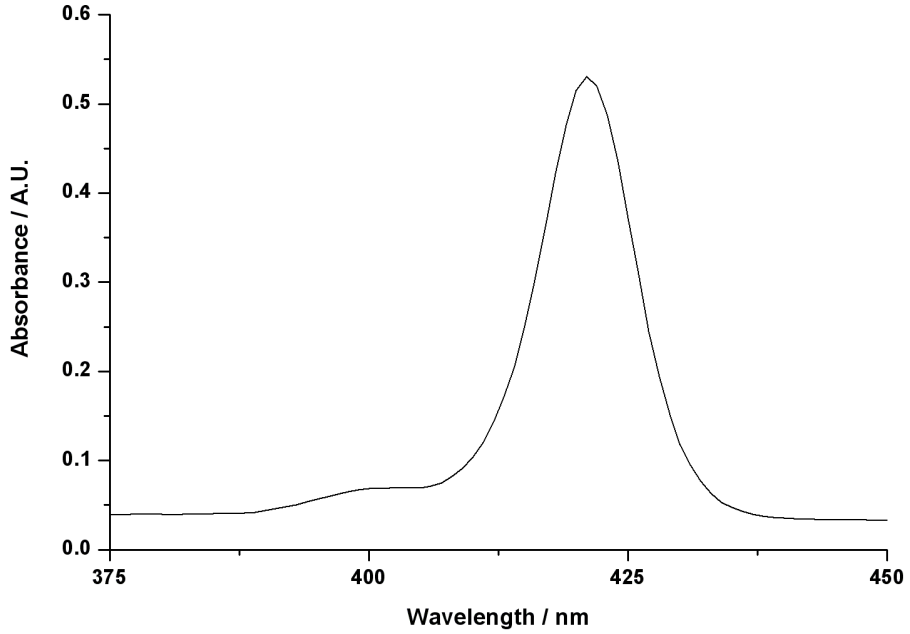

Section of the visible absorption spectrum of ZnTTBPP (P3) in CH_2Cl_2, 0.5 μM

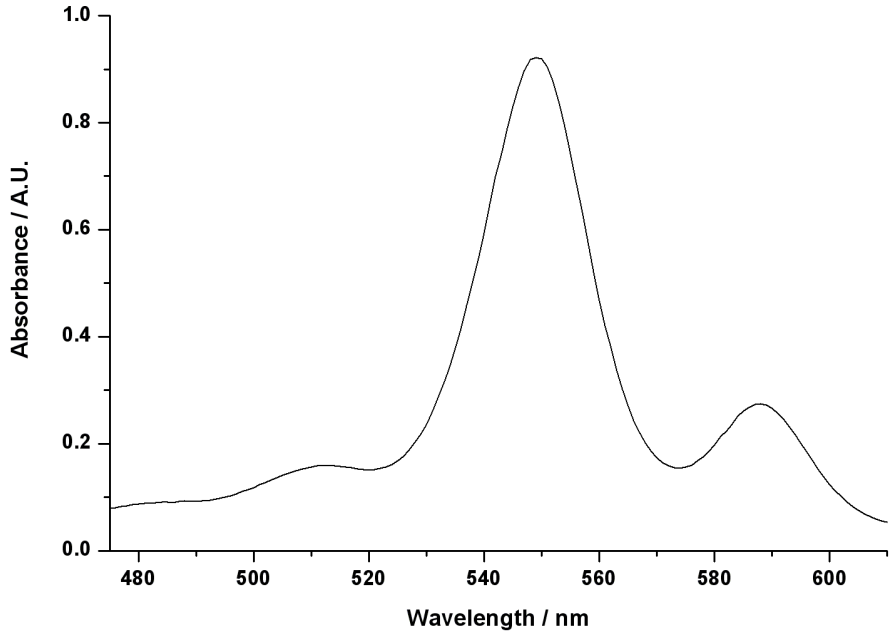

Section of the visible absorption spectrum of ZnTTBPP (P3) in CH_2Cl_2, 2.5 μM

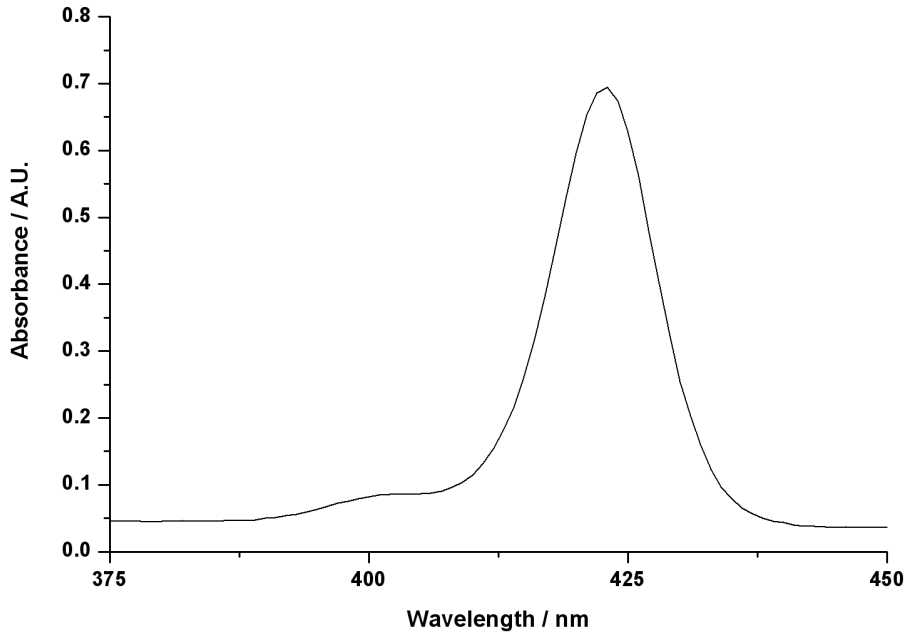

Section of the visible absorption spectrum of ZnTMPP (P4) in CH_2Cl_2, 2.5 μM

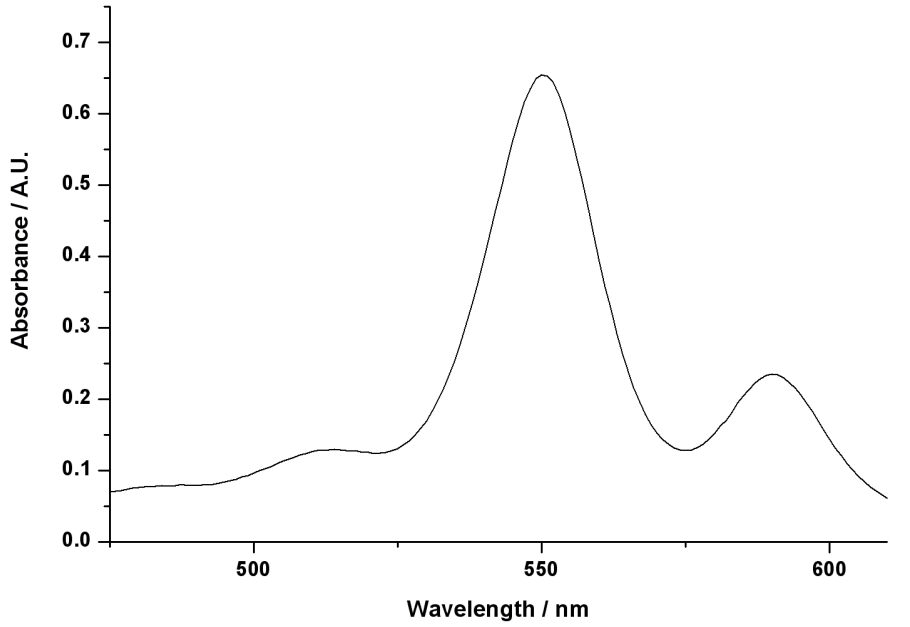

Section of the visible absorption spectrum of ZnTMPP (P4) in CH_2Cl_2, 50 μM

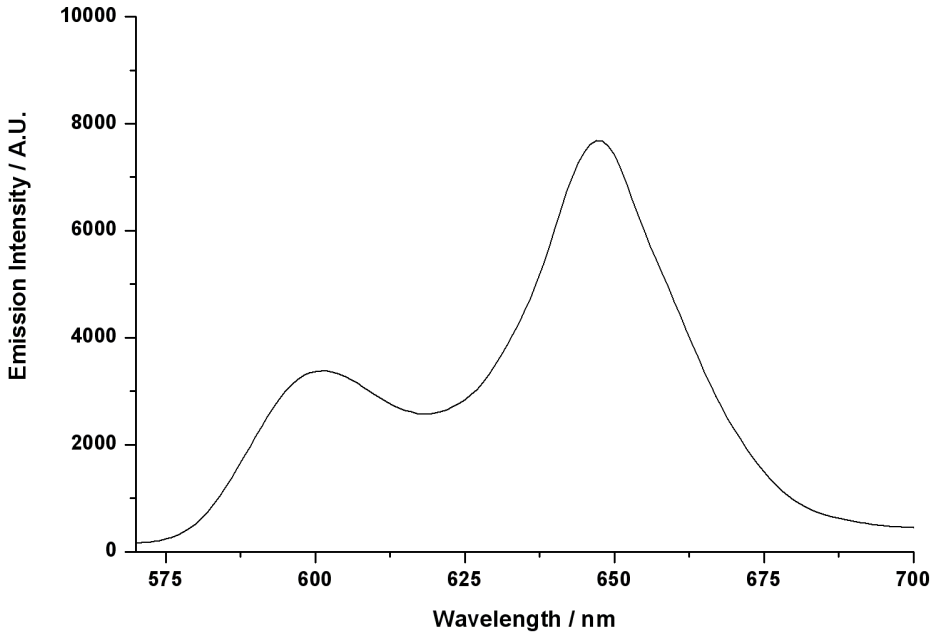

Emission spectra of ZnTPP (P1) in CH_2Cl_2 at room temperature, 25 μM. Excitation wavelentgh 548 nm

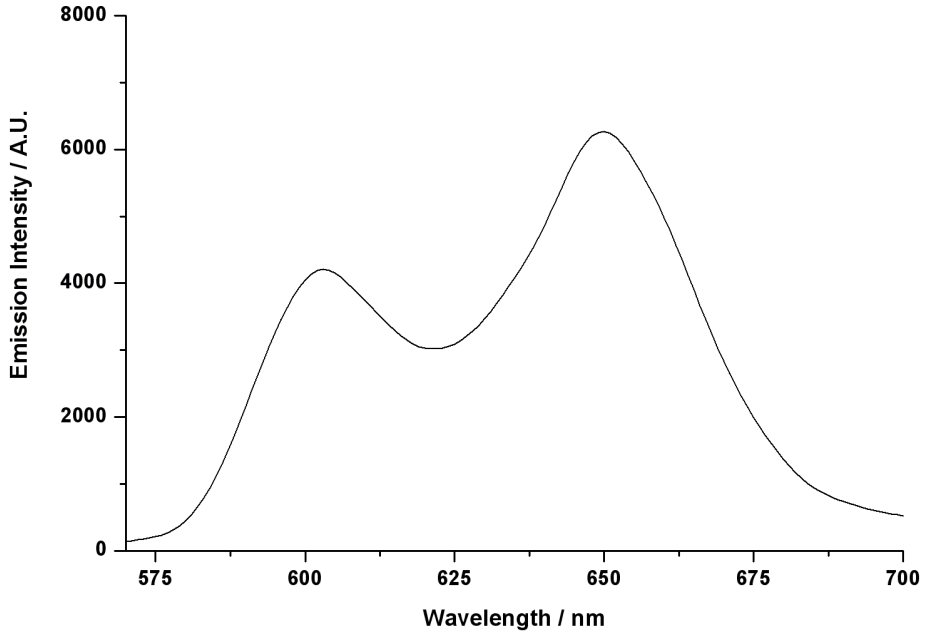

Emission spectra of ZnTTP (P2) in CH_2Cl_2 at room temperature, 25 μM. Excitation wavelentgh 549 nm

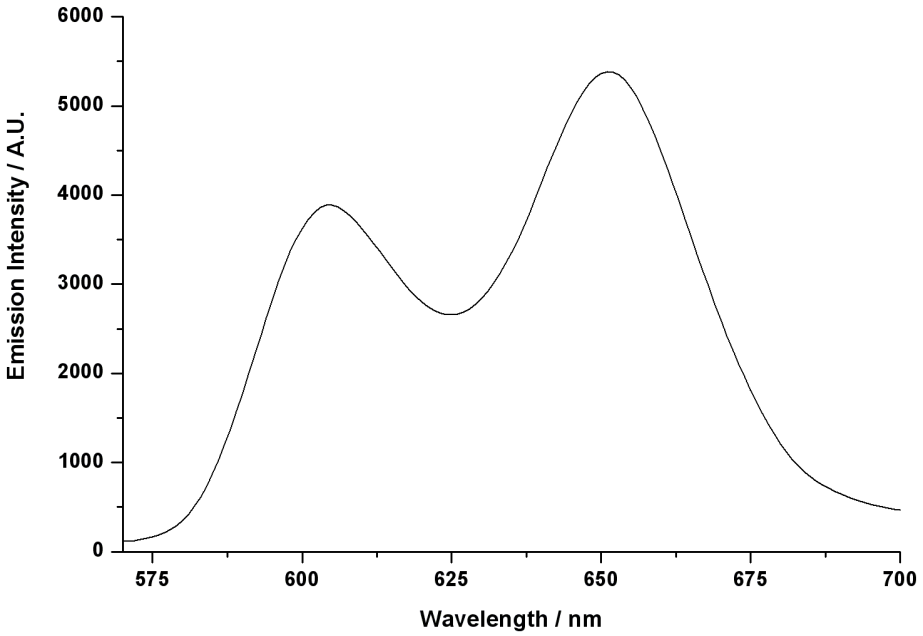

Emission spectra of ZnTTBPP (P3) in CH_2Cl_2 at room temperature, 25 μM. Excitation wavelentgh 549 nm

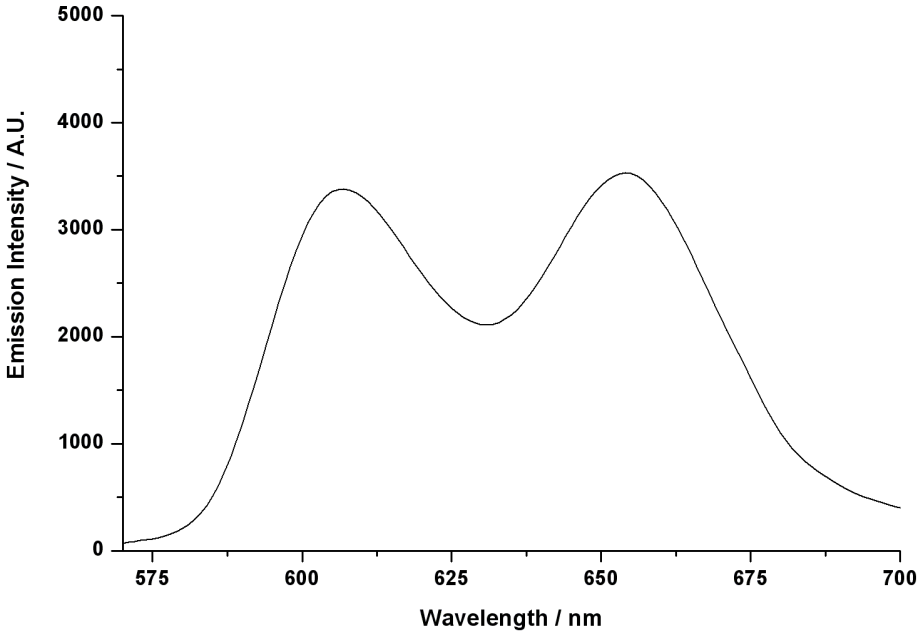

Emission spectra of ZnTMPP (P4) in CH_2Cl_2 at room temperature, 25 μM. Excitation wavelentgh 550 nm

Appendix V. CO formation comparisons

Comparative plots for common porphyrin or rhenium complexes are illustrated in this section. Color scheme of Chapter 5 is employed (see Table 5.2 on page 89)

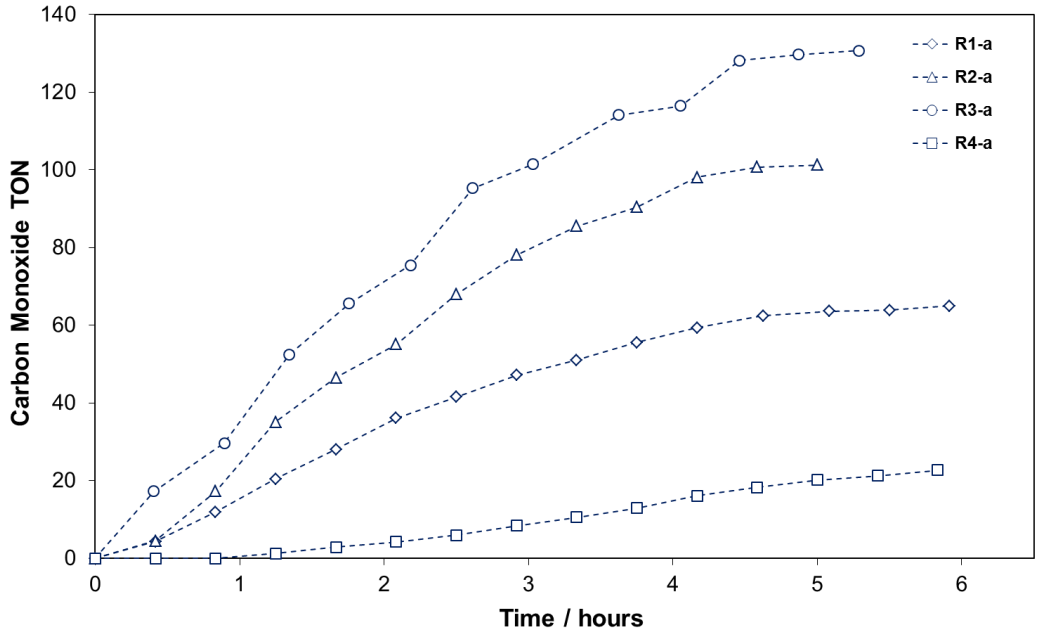

CO formation of the different mixtures with ZnTPP (P1)

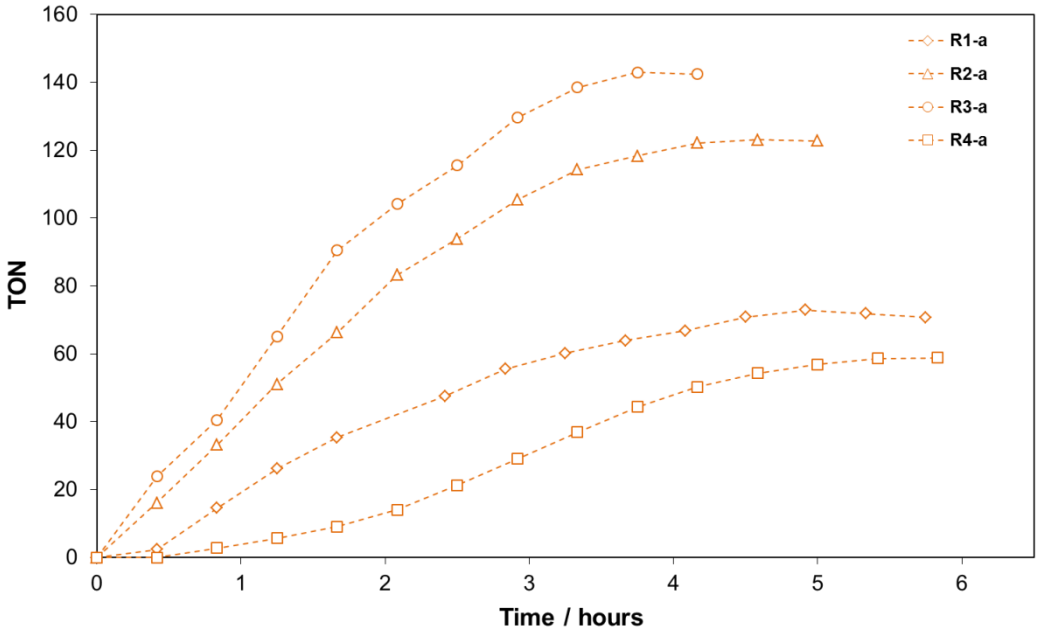

CO formation of the different mixtures with ZnTTP (P2)

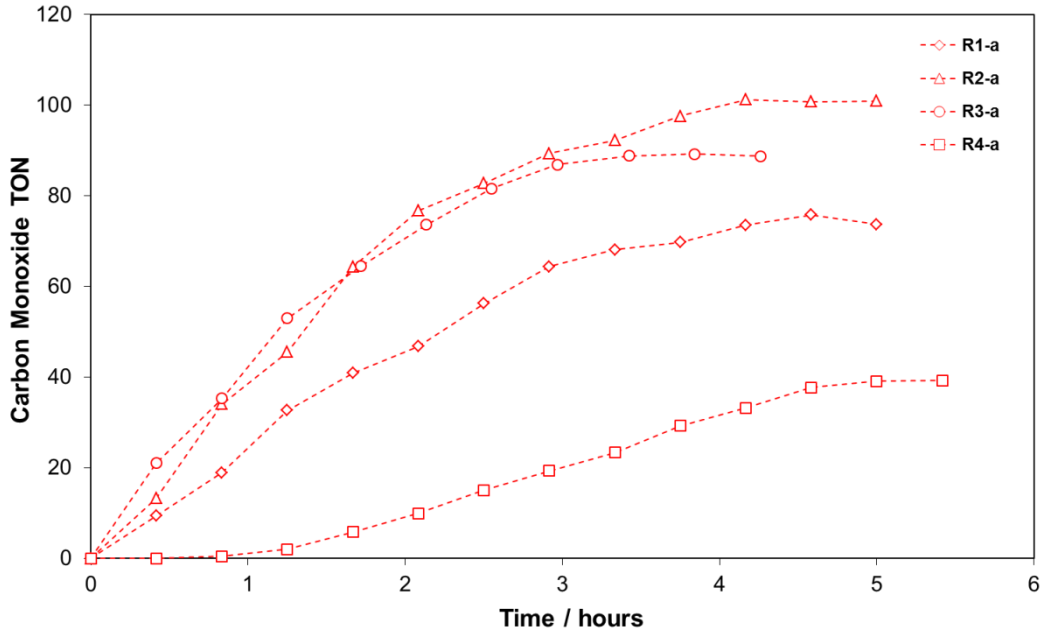

CO formation of the different mixtures with ZnTTBPP (P3)

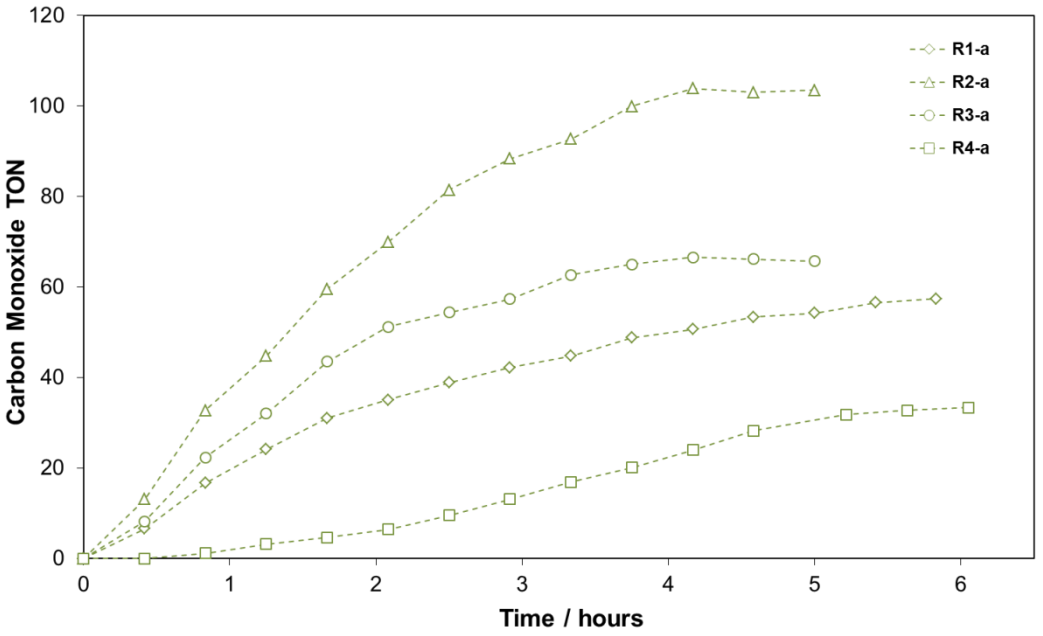

CO formation of the different mixtures with ZnTMPP (P4)

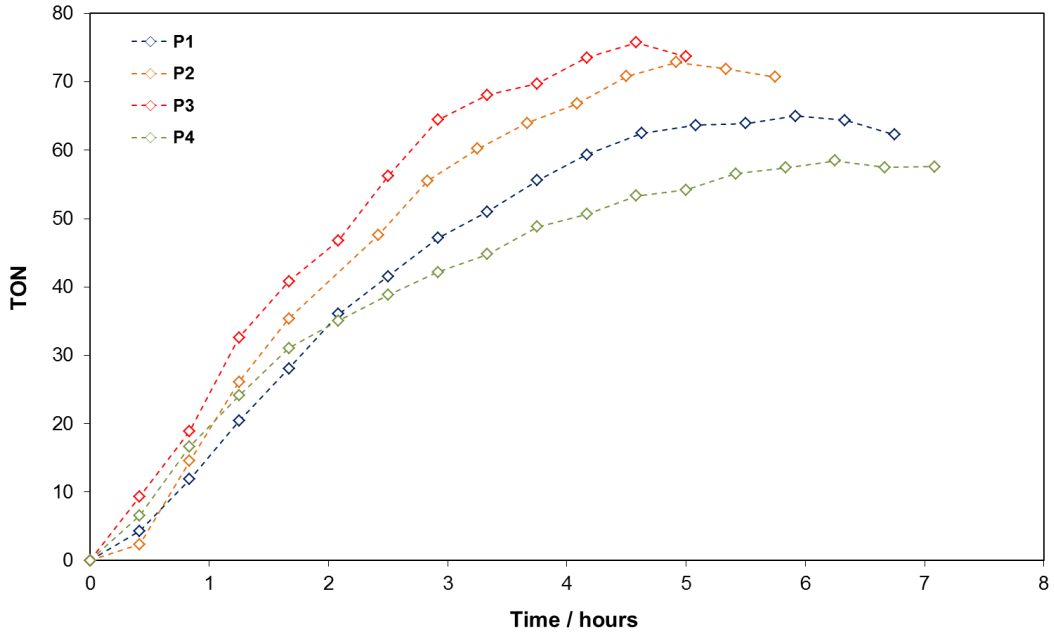

CO formation of the different mixtures with [Re(bpy)(CO)$_3$Br] (R1–a)

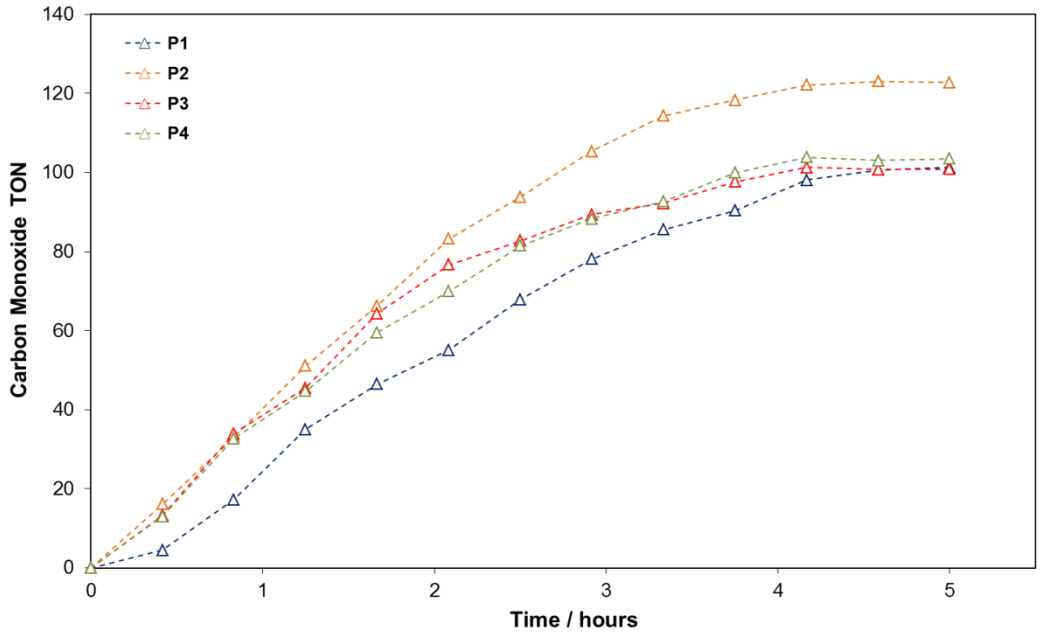

CO formation of the different mixtures with [Re(bpy)(CO)$_3$(CH$_3$CN)] (R2–a)

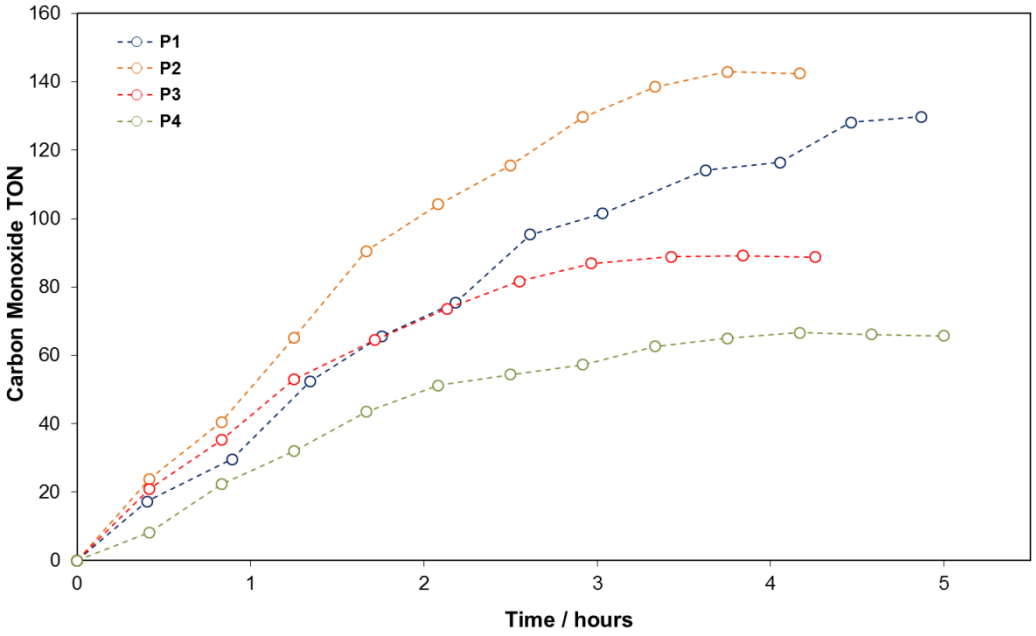

CO formation of the different mixtures with [Re(bpy)(CO)$_3$(3–Pic)] (R3–a)

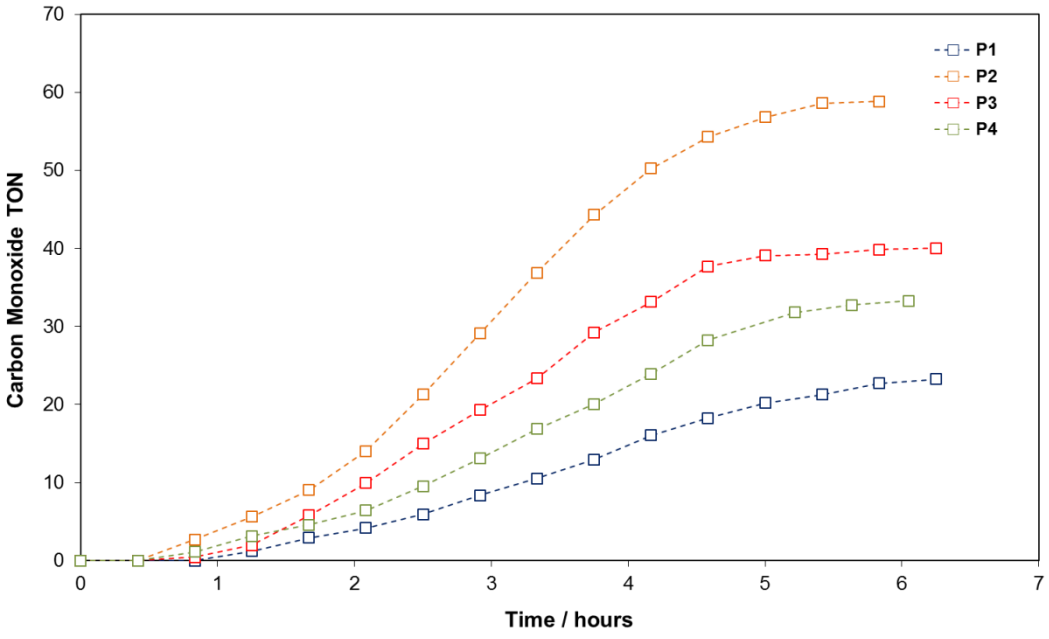

CO formation of the different mixtures with [Re(bpy)(CO)$_3${P(OEt)$_3$}] (R4–a)

Appendix VI. Absorbance variation profiles

Absorbance variation of porphyrin Q(0,1) and Q(0,0) bands and chlorin absorption around 620 nm are shown Values normalized against Q(1,0).

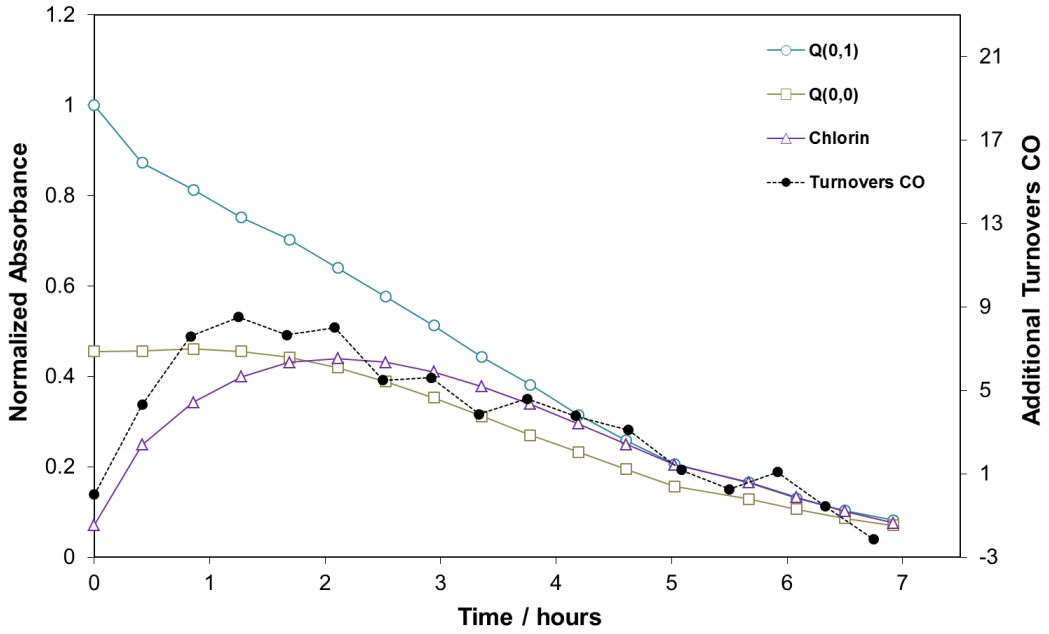

Chlorin and porphyrin Q bands absorbance profiles against irradiation time of ZnTPP: [Re(bpy)(CO)$_3$Br] (P1:R1–a). CO formation of each period is overlaid

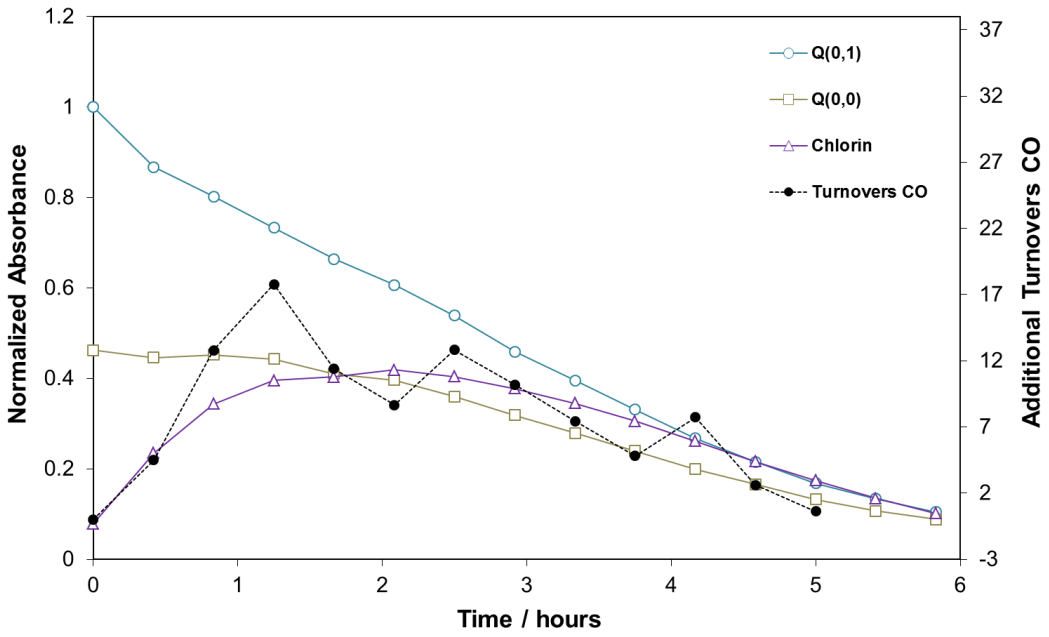

Chlorin and porphyrin Q bands absorbance profiles against irradiation time of ZnTPP: [Re(bpy)(CO)$_3$(CH$_3$CN)][PF$_6$] (P1:R2–a). CO formation of each irradiation period is overlaid

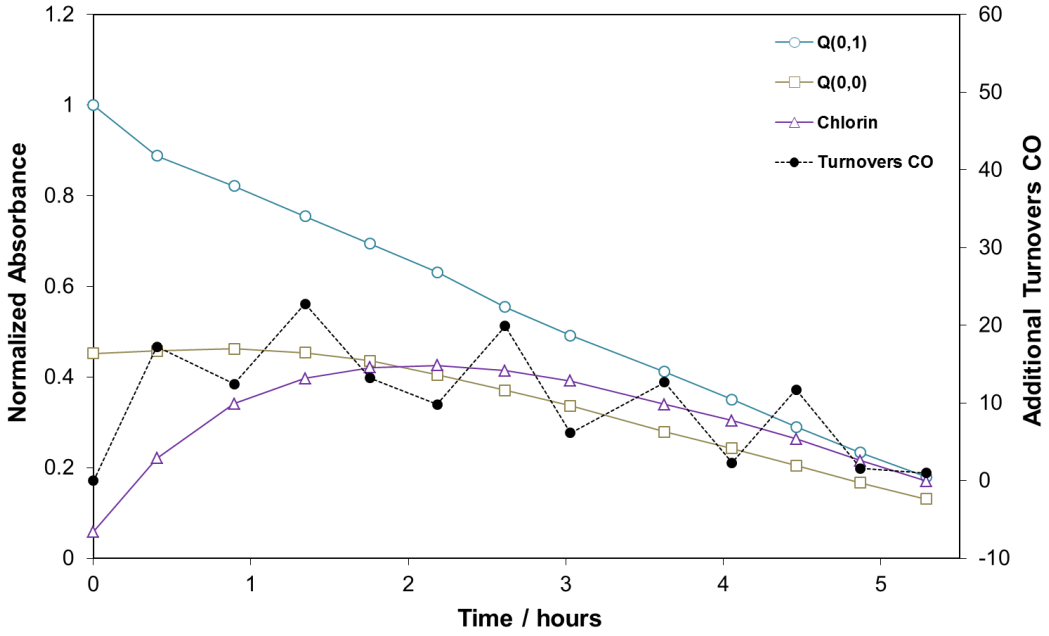

Chlorin and porphyrin Q bands absorbance profiles against irradiation time of ZnTPP: [Re(bpy)(CO)$_3$(3–Pic)][PF$_6$] (P1:R3–a). CO formation of each irradiation period is overlaid

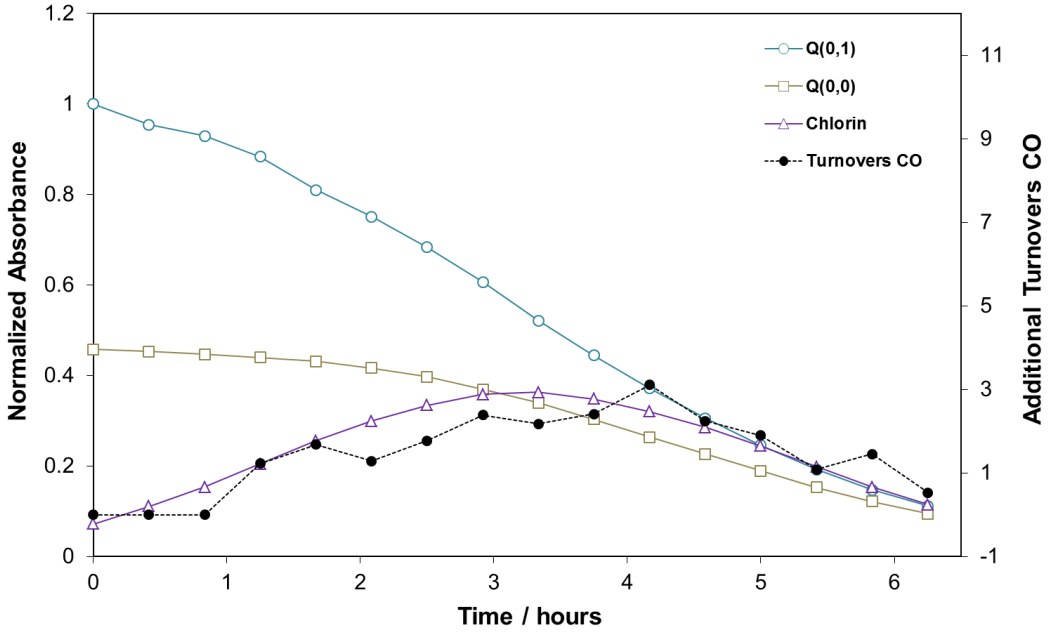

Chlorin and porphyrin Q bands absorbance profiles against irradiation time of ZnTPP: [Re(bpy)(CO)$_3${P(OEt)$_3$}][PF$_6$] (P1:R4–a). CO formation of each irradiation period is overlaid

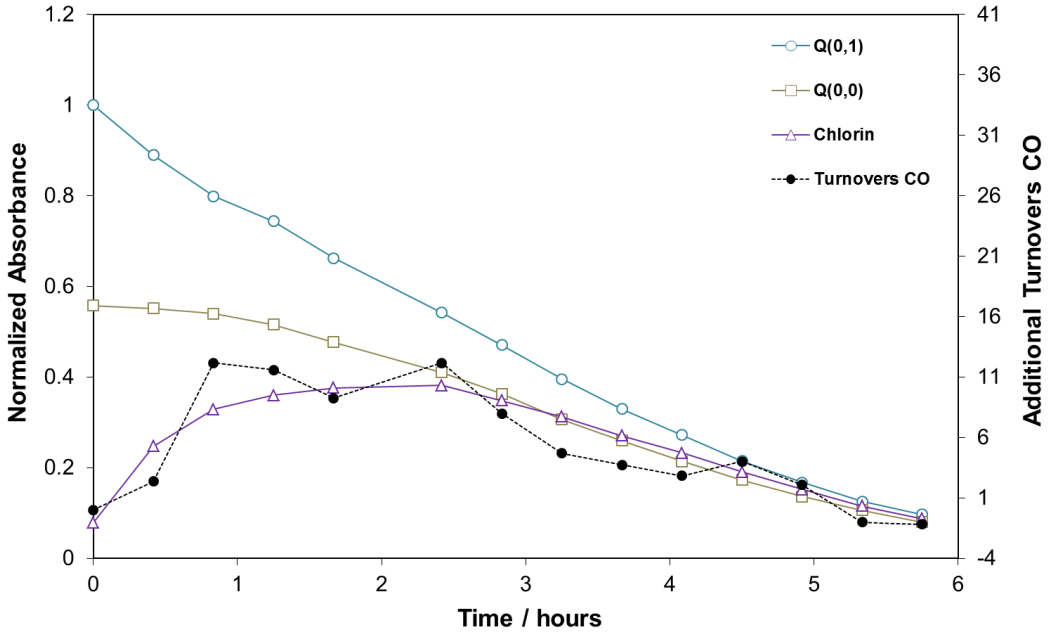

Chlorin and porphyrin Q bands absorbance profiles against irradiation time of ZnTTP: [Re(bpy)(CO)$_3$Br] (P2:R1–a). CO formation of each irradiation period is overlaid

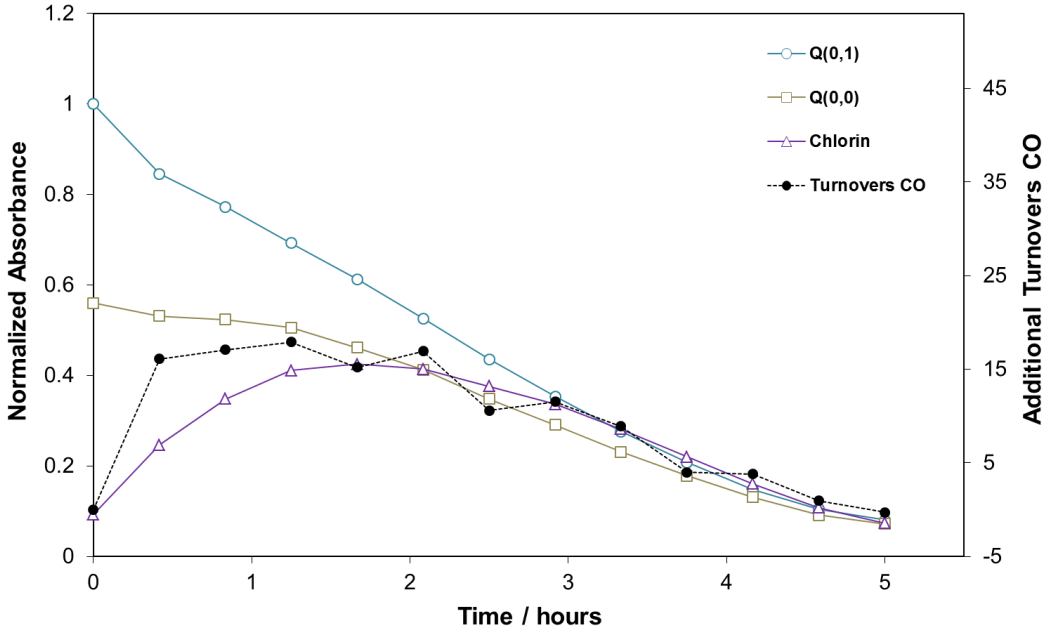

Chlorin and porphyrin Q bands absorbance profiles against irradiation time of ZnTTP: [Re(bpy)(CO)$_3$(CH$_3$CN)][PF$_6$] (P2:R2–a). CO formation of each irradiation period is overlaid

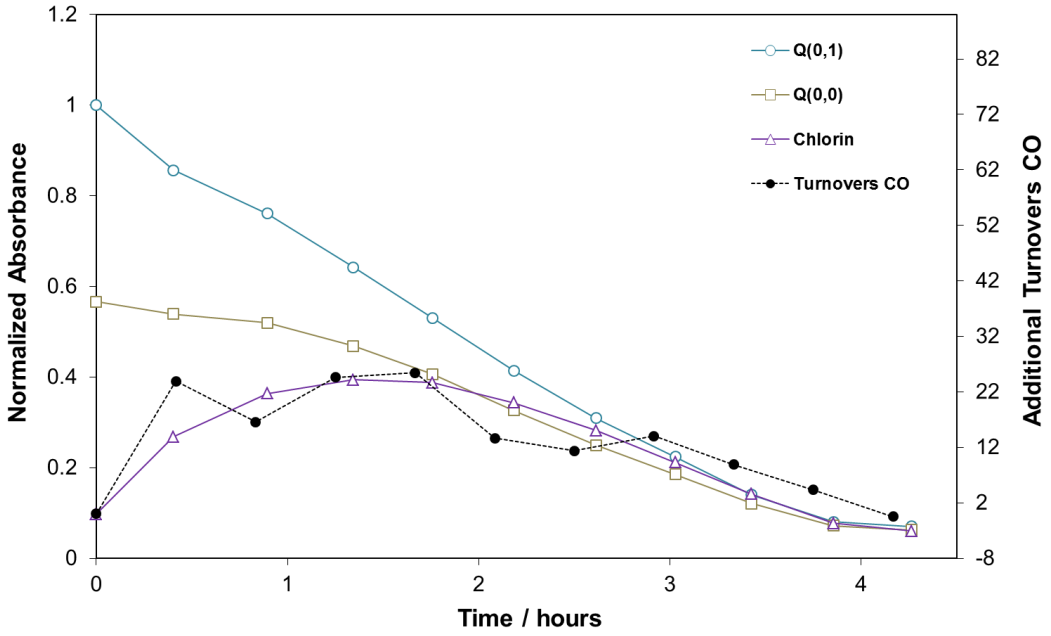

Chlorin and porphyrin Q bands absorbance profiles against irradiation time of ZnTTP: [Re(bpy)(CO)$_3$(3–Pic)][PF$_6$] (P2:R3–a). CO formation of each irradiation period is overlaid

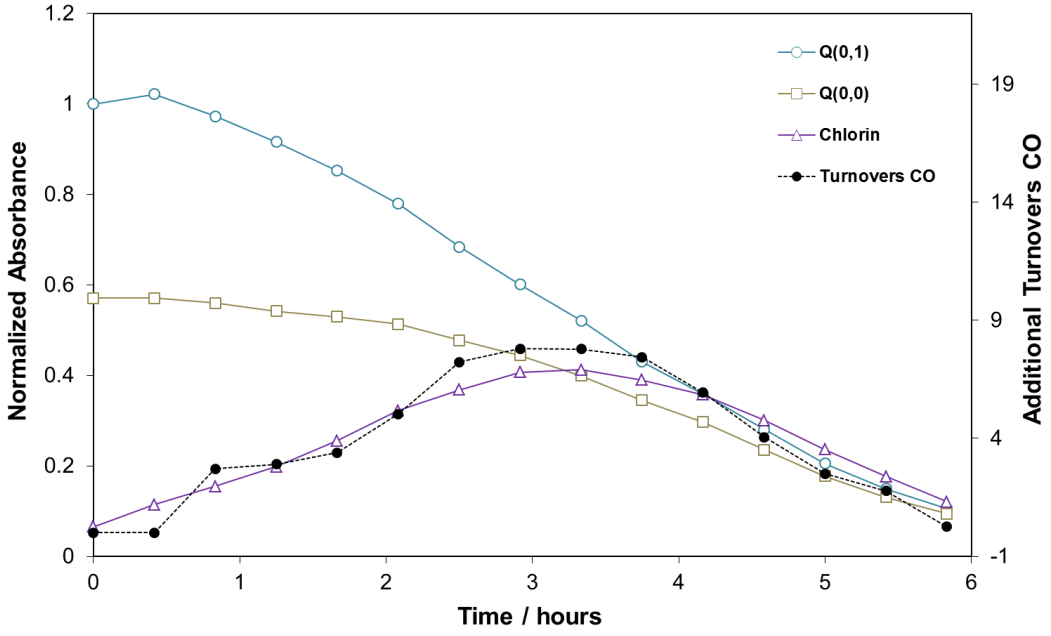

Chlorin and porphyrin Q bands absorbance profiles against irradiation time of ZnTTP: [Re(bpy)(CO)$_3${P(OEt)$_3$}][PF$_6$] (P2:R4–a). CO formation of each irradiation period is overlaid

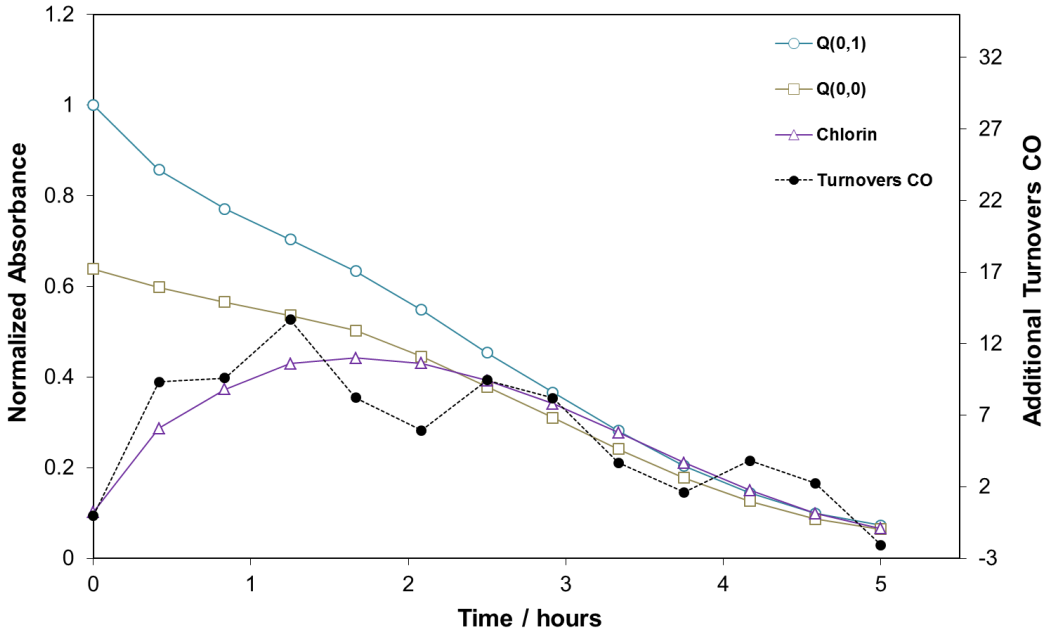

Chlorin and porphyrin Q bands absorbance profiles against irradiation time of ZnTTBPP: [Re(bpy)(CO)$_3$Br] (P3:R1–a). CO formation of each irradiation period is overlaid

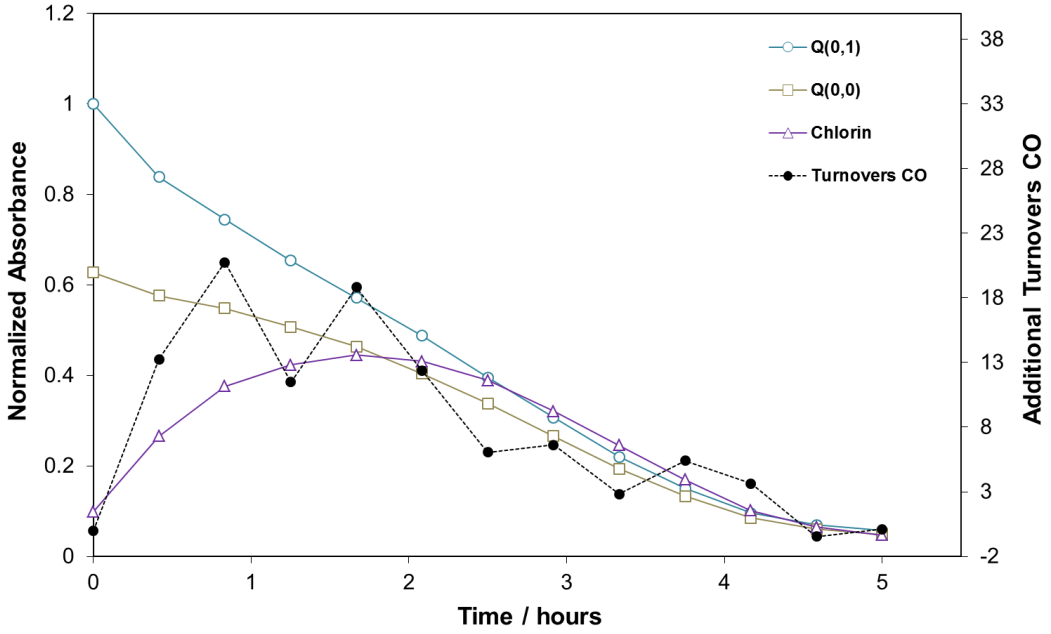

Chlorin and porphyrin Q bands absorbance profiles against irradiation time of ZnTTBPP: [Re(bpy)(CO)$_3$(CH$_3$CN)][PF$_6$] (P3:R2–a). CO formation of each irradiation period is overlaid

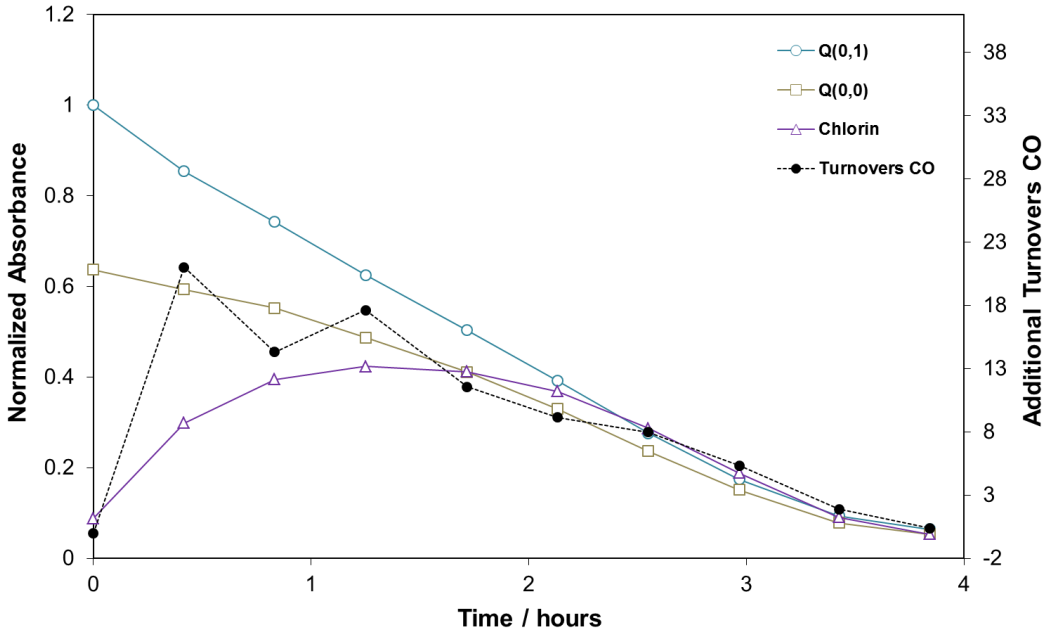

Chlorin and porphyrin Q bands absorbance profiles against irradiation time of ZnTTBPP: [Re(bpy)(CO)$_3$(3–Pic)][PF$_6$] (P3:R3–a). CO formation of each irradiation period is overlaid

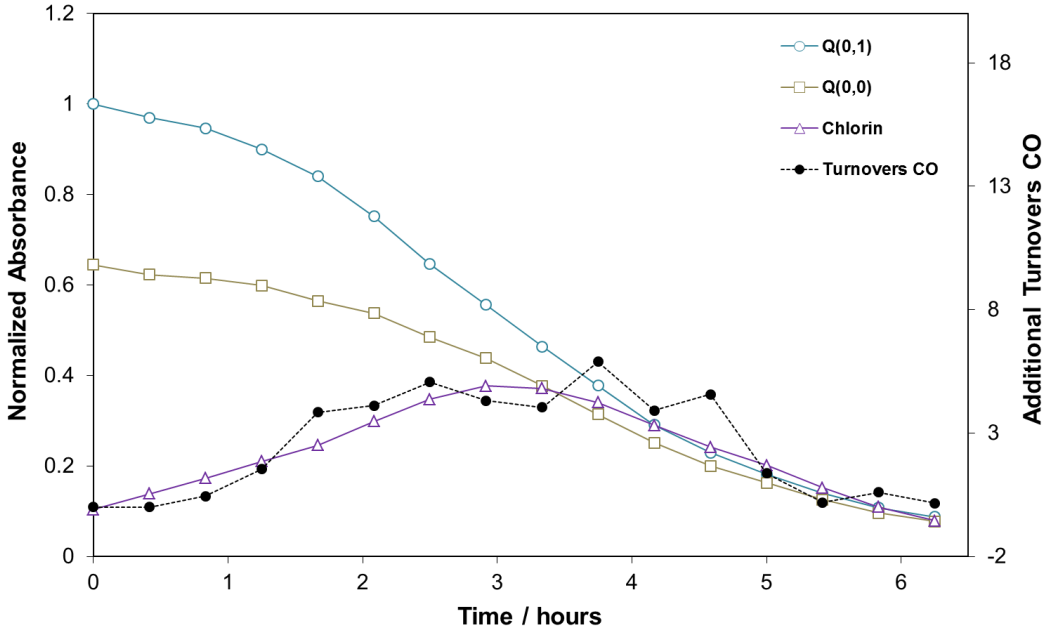

Chlorin and porphyrin Q bands absorbance profiles against irradiation time of ZnTTBPP: [Re(bpy)(CO)$_3${P(OEt)$_3$}][PF$_6$] (P3:R4–a). CO formation of each irradiation period is overlaid

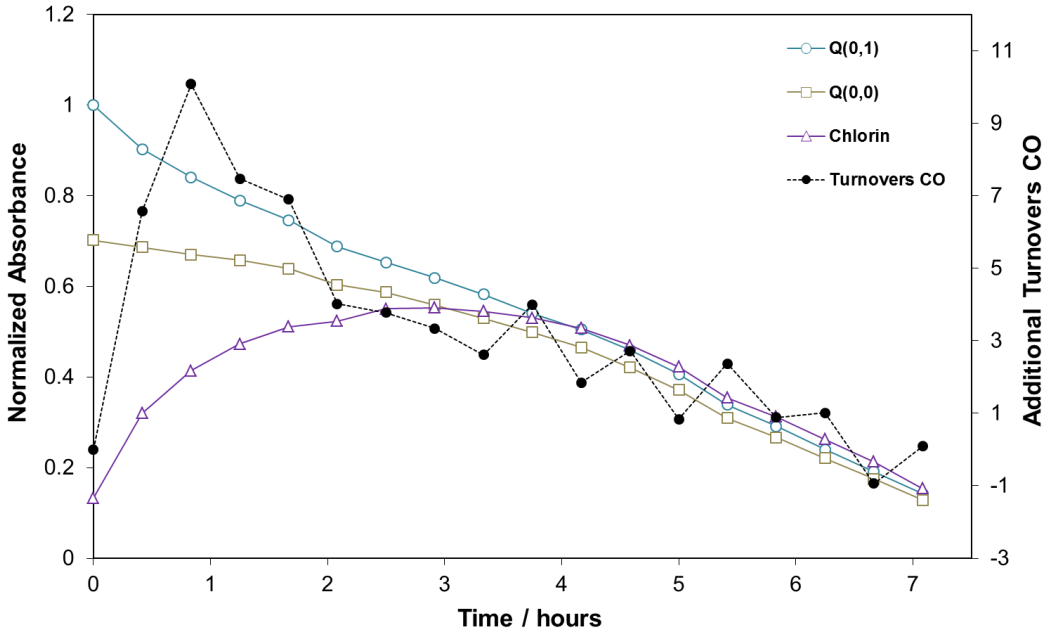

Chlorin and porphyrin Q bands absorbance profiles against irradiation time of ZnTMPP: [Re(bpy)(CO)$_3$Br] (P4:R1–a). CO formation of each irradiation period is overlaid

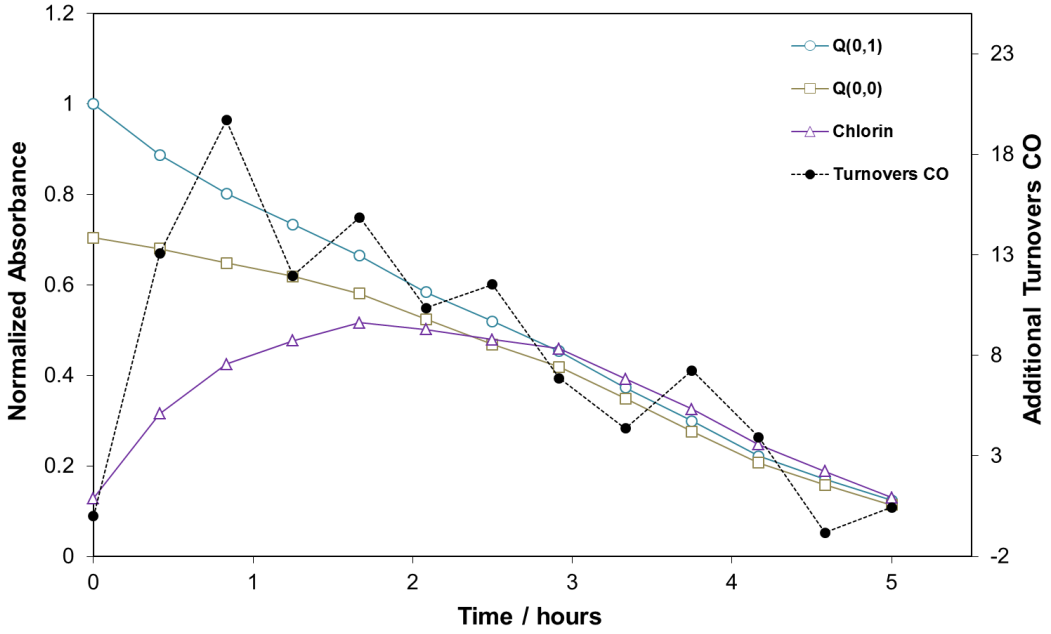

Chlorin and porphyrin Q bands absorbance profiles against irradiation time of ZnTMPP: [Re(bpy)(CO)$_3$(CH$_3$CN)][PF$_6$] (P4:R2–a). CO formation of each irradiation period is overlaid

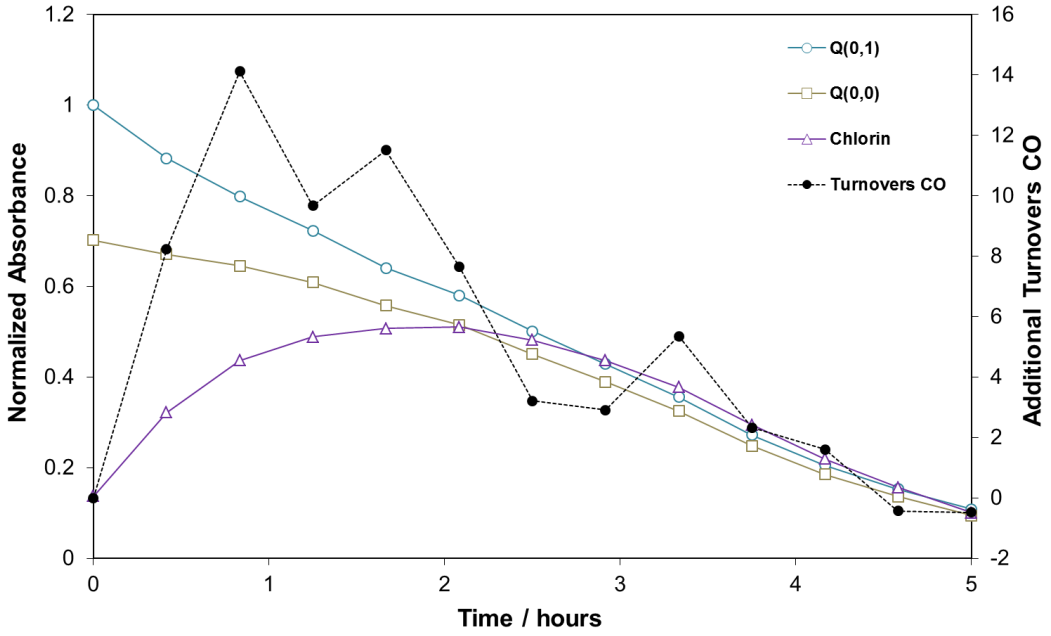

Chlorin and porphyrin Q bands absorbance profiles against irradiation time of ZnTMPP: [Re(bpy)(CO)$_3$(3–Pic)][PF$_6$] (P4:R3–a). CO formation of each irradiation period is overlaid

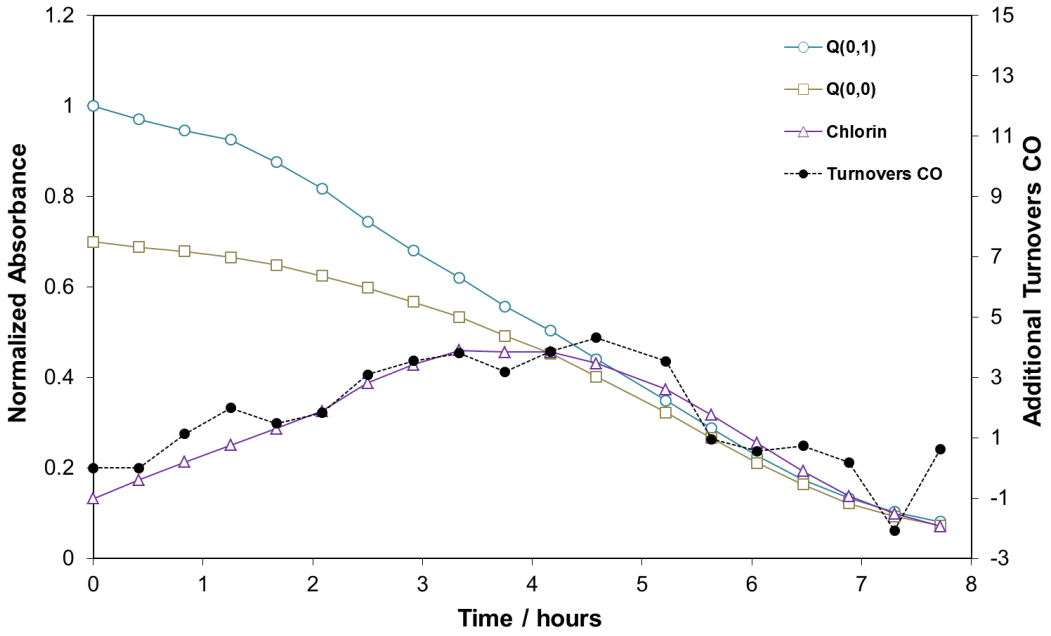

Chlorin and porphyrin Q bands absorbance profiles against irradiation time of ZnTMPP: [Re(bpy)(CO)$_3${P(OEt)$_3$}][PF$_6$] (P4:R4–a). CO formation of each irradiation period is overlaid

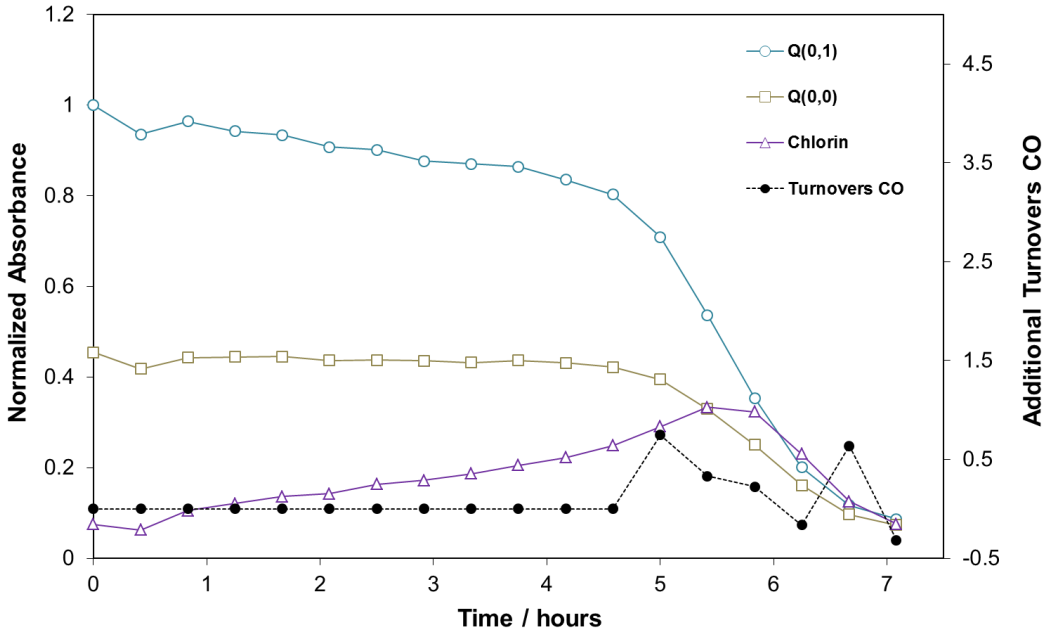

Chlorin and porphyrin Q bands absorbance profiles against irradiation time of ZnTPP: [Re(BMCbpy)(CO)$_3$Br] (P1:R1–b). CO formation of each irradiation period is overlaid

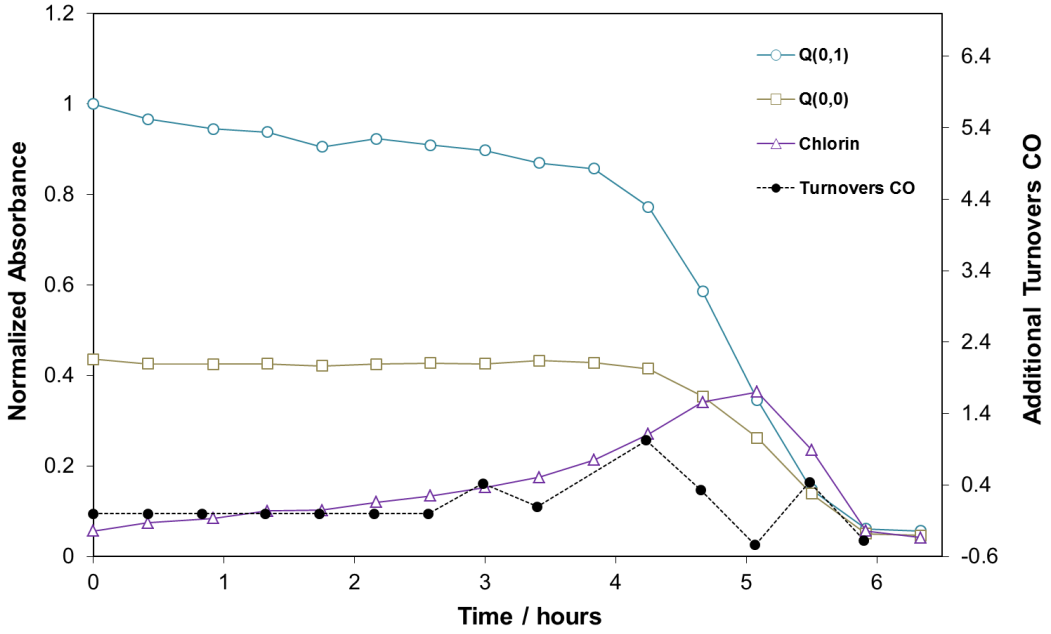

Chlorin and porphyrin Q bands absorbance profiles against irradiation time of ZnTPP: [Re(BMCbpy)(CO)$_3$(CH$_3$CN)][PF$_6$] (P1:R2–b). CO formation of each irradiation period is overlaid

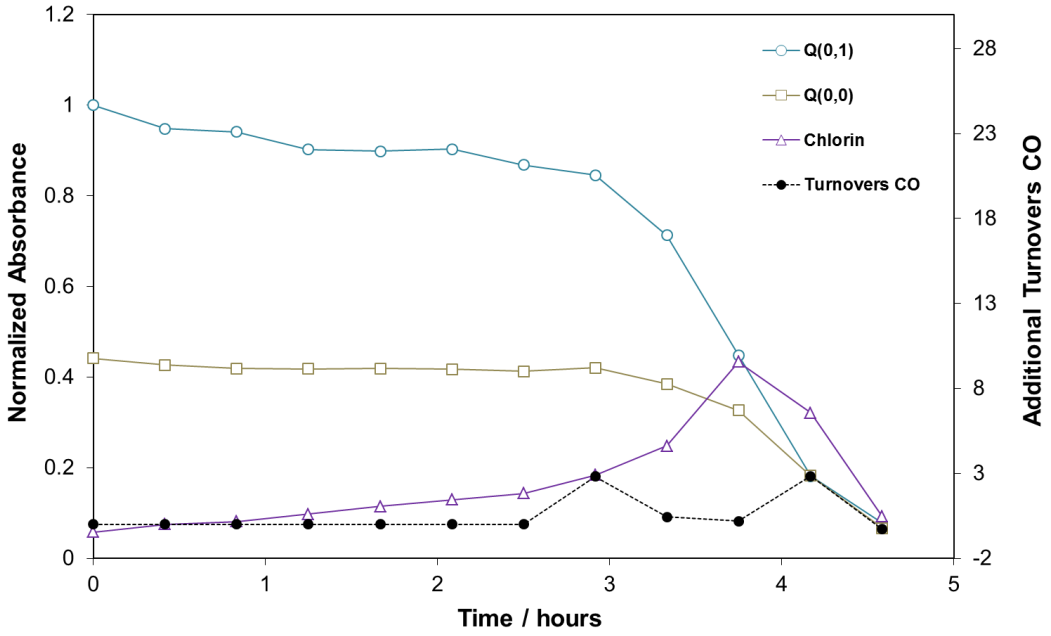

Chlorin and porphyrin Q bands absorbance profiles against irradiation time of ZnTPP: [Re(BMCbpy)(CO)$_3$(3–Pic)][PF$_6$] (P1:R3–b). CO formation of each irradiation period is overlaid

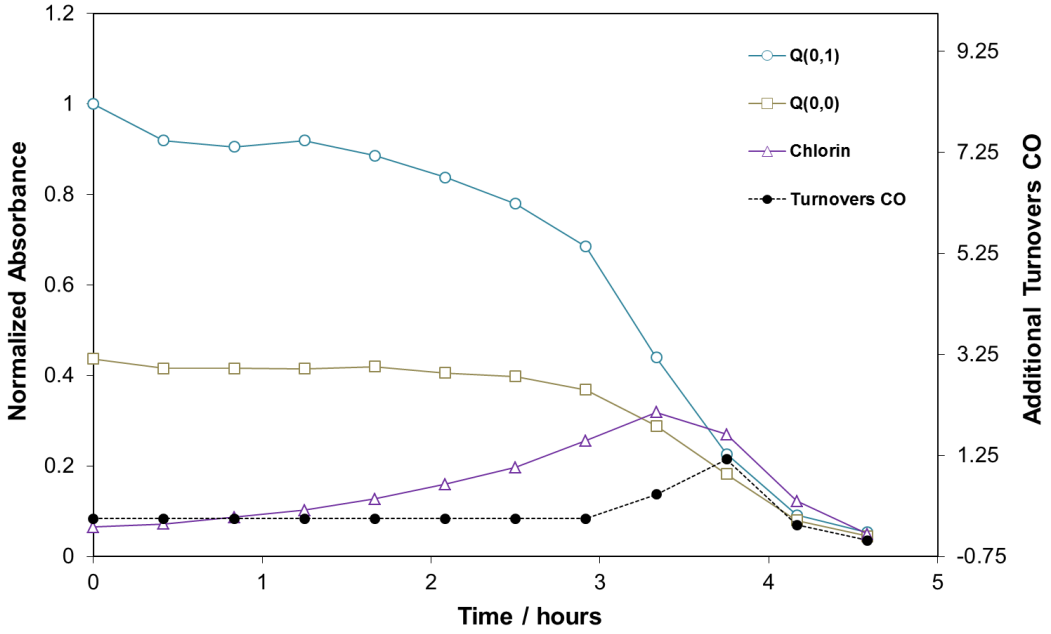

Chlorin and porphyrin Q bands absorbance profiles against irradiation time of ZnTPP: [Re(BMCbpy)(CO)$_3${P(OEt)$_3$}][PF$_6$] (P1:R4–b). CO formation of each irradiation period is overlaid

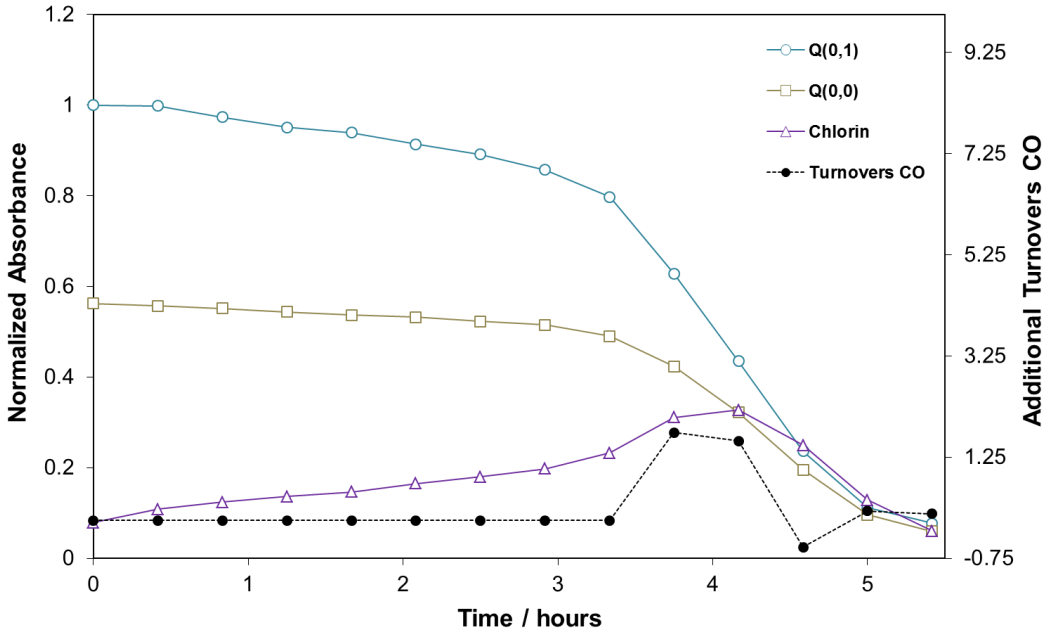

Chlorin and porphyrin Q bands absorbance profiles against irradiation time of ZnTTP: [Re(BMCbpy)(CO)$_3$Br] (P2:R1–b). CO formation of each irradiation period is overlaid

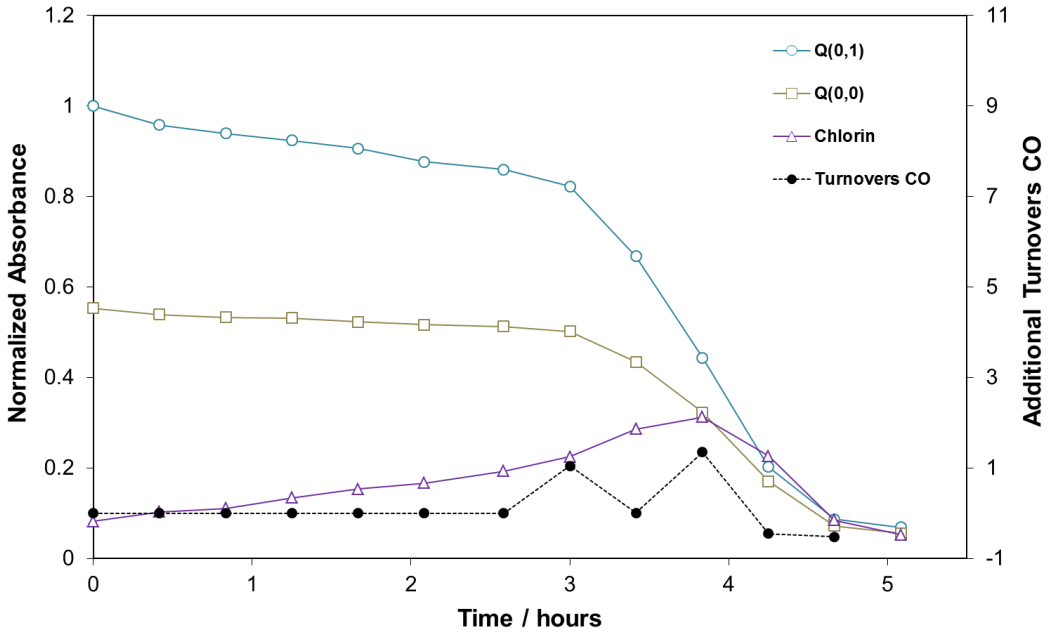

Chlorin and porphyrin Q bands absorbance profiles against irradiation time of ZnTTP: [Re(BMCbpy)(CO)$_3$(CH$_3$CN)][PF$_6$] (P2:R2–b). CO formation of each irradiation period is overlaid

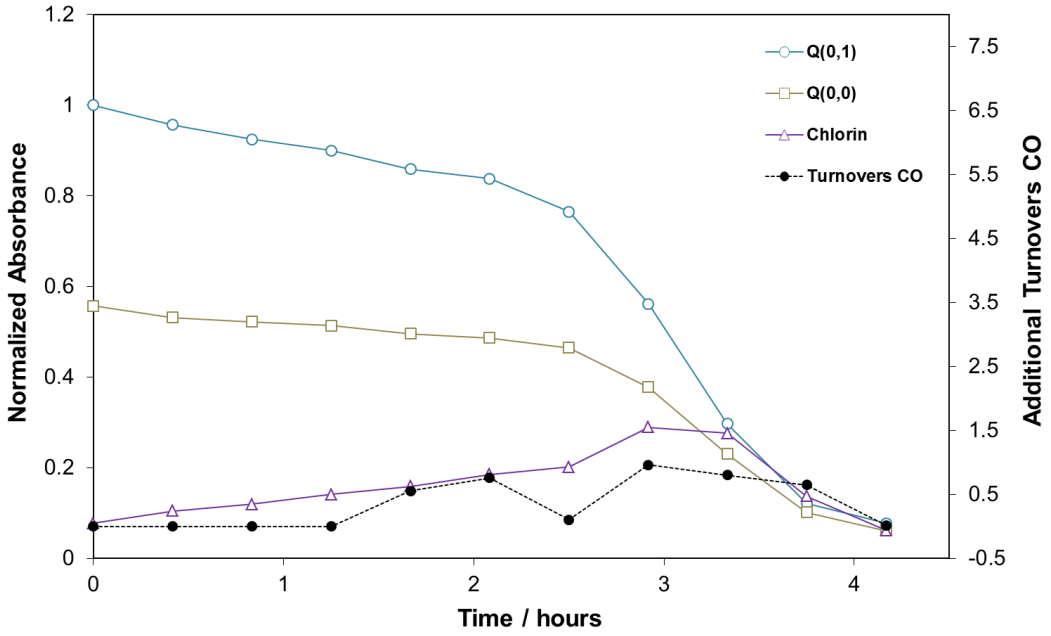

Chlorin and porphyrin Q bands absorbance profiles against irradiation time of ZnTTP: [Re(BMCbpy)(CO)$_3$(3–Pic)][PF$_6$] (P2:R3–b). CO formation of each irradiation period is overlaid

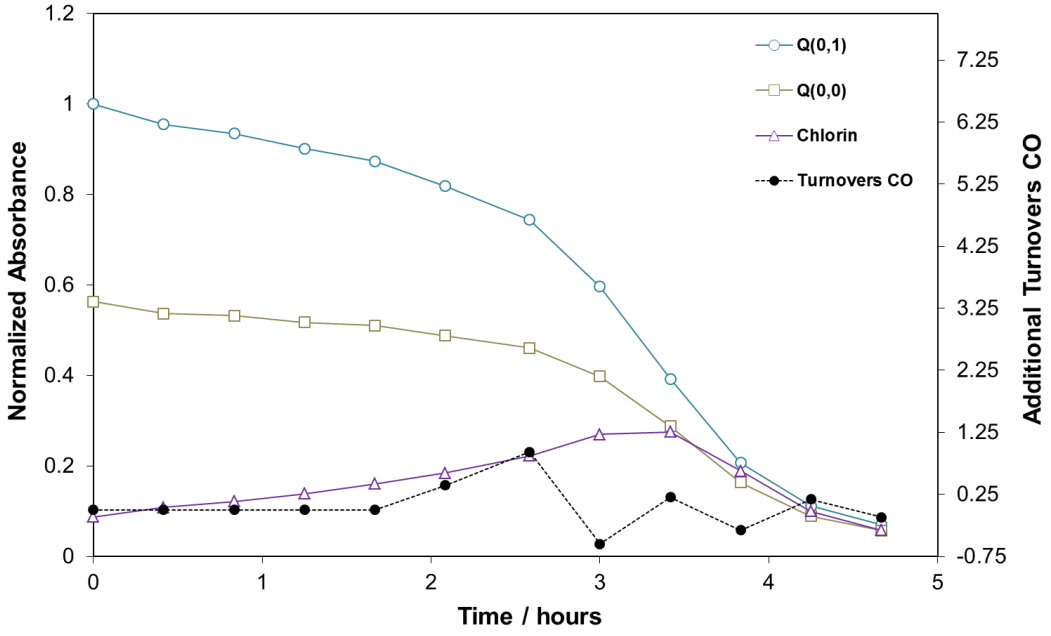

Chlorin and porphyrin Q bands absorbance profiles against irradiation time of ZnTTP: [Re(BMCbpy)(CO)$_3${P(OEt)$_3$}][PF$_6$] (P2:R4–b). CO formation of each irradiation period is overlaid

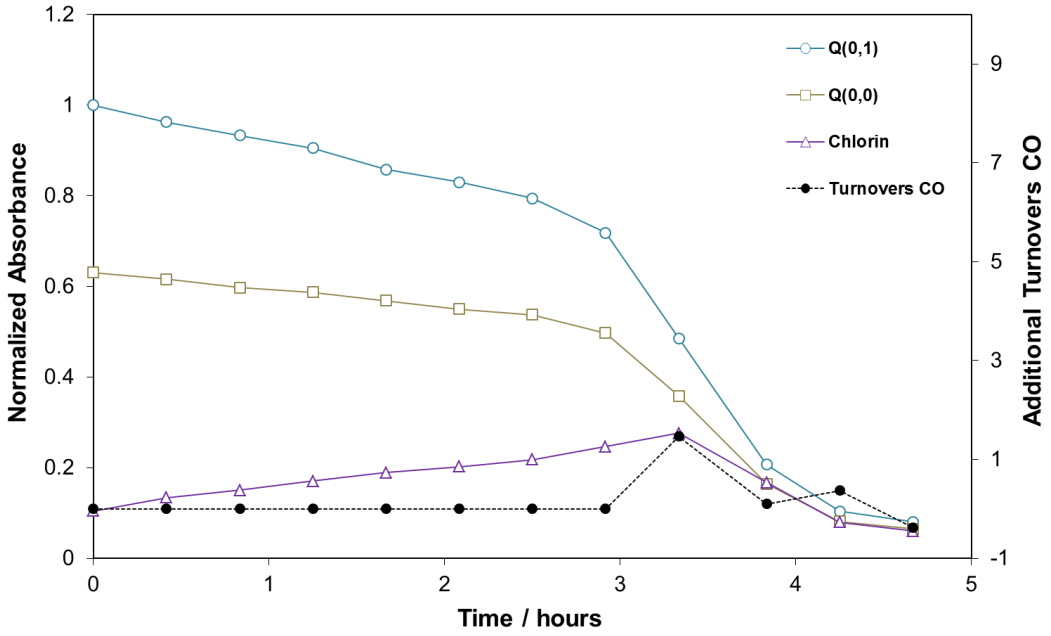

Chlorin and porphyrin Q bands absorbance profiles against irradiation time of ZnTTBPP: [Re(BMCbpy)(CO)$_3$(CH$_3$CN)][PF$_6$] (P3:R2–b). CO formation of each irradiation period is overlaid

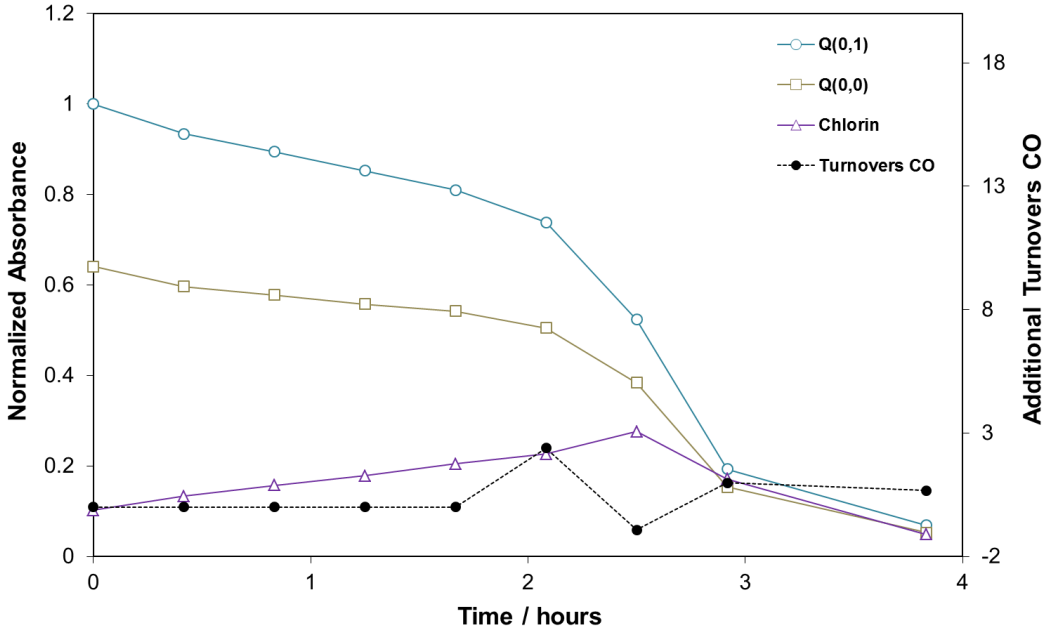

Chlorin and porphyrin Q bands absorbance profiles against irradiation time of ZnTTBPP: [Re(BMCbpy)(CO)$_3$(3–Pic)][PF$_6$] (P3:R3–b). CO formation of each irradiation period is overlaid

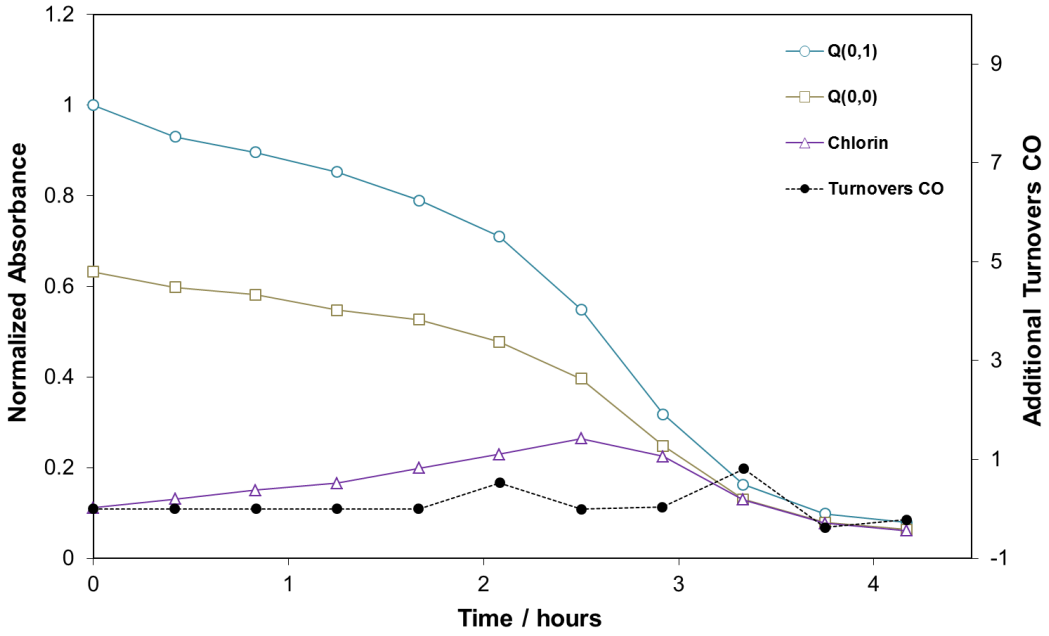

Chlorin and porphyrin Q bands absorbance profiles against irradiation time of ZnTTBPP: [Re(BMCbpy)(CO)$_3${P(OEt)$_3$}][PF$_6$] (P3:R4–b). CO formation of each irradiation period is overlaid

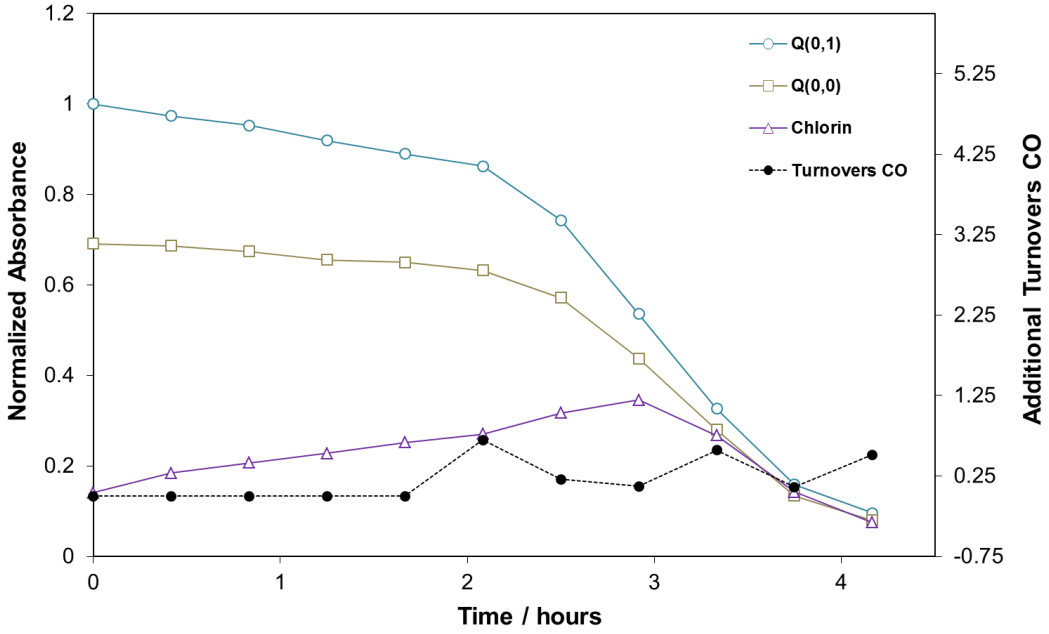

Chlorin and porphyrin Q bands absorbance profiles against irradiation time of ZnTMPP: [Re(BMCbpy)(CO)$_3$(CH$_3$CN)][PF$_6$] (P4:R2–b). CO formation of each irradiation period is overlaid

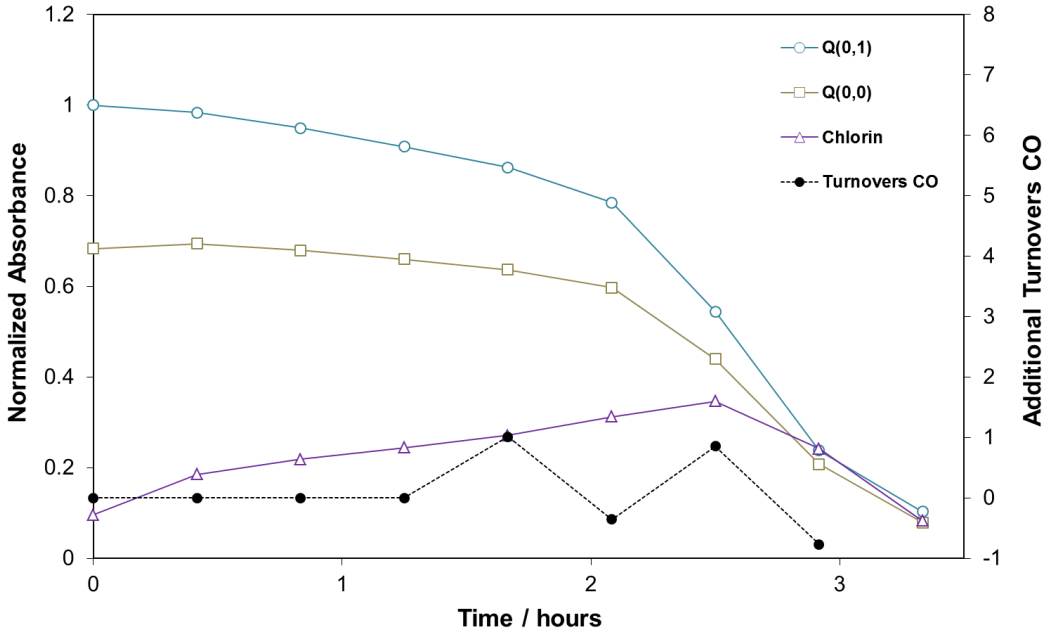

Chlorin and porphyrin Q bands absorbance profiles against irradiation time of ZnTMPP: [Re(BMCbpy)(CO)$_3$(3–Pic)][PF$_6$] (P4:R3–b). CO formation of each irradiation period is overlaid

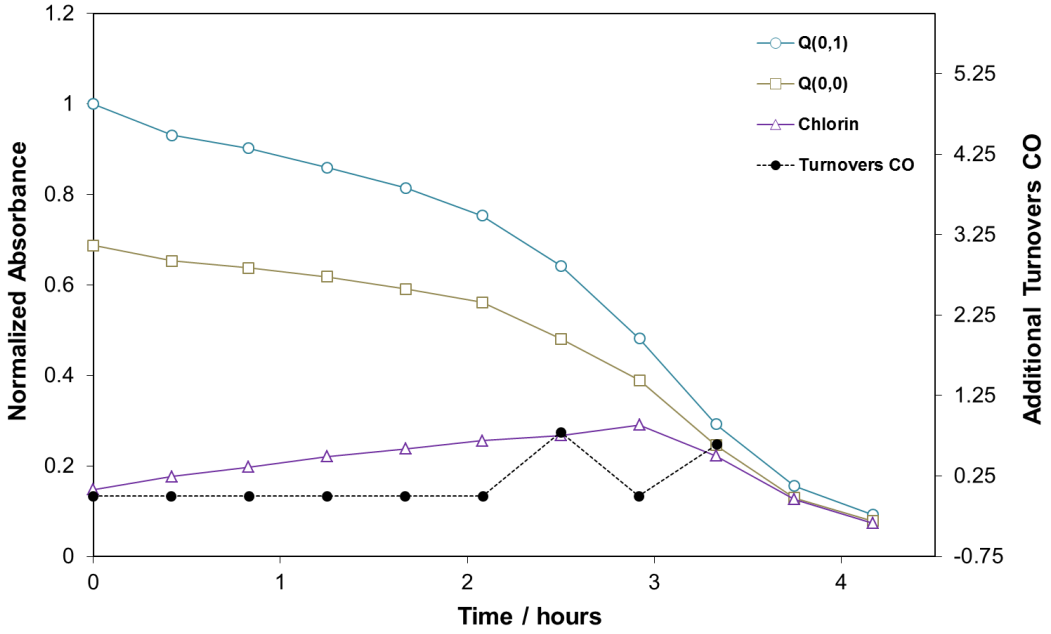

Chlorin and porphyrin Q bands absorbance profiles against irradiation time of ZnTMPP: [Re(BMCbpy)(CO)$_3${P(OEt)$_3$}][PF$_6$] (P4:R4–b). CO formation of each irradiation period is overlaid

Appendix VII. CO formation profiles

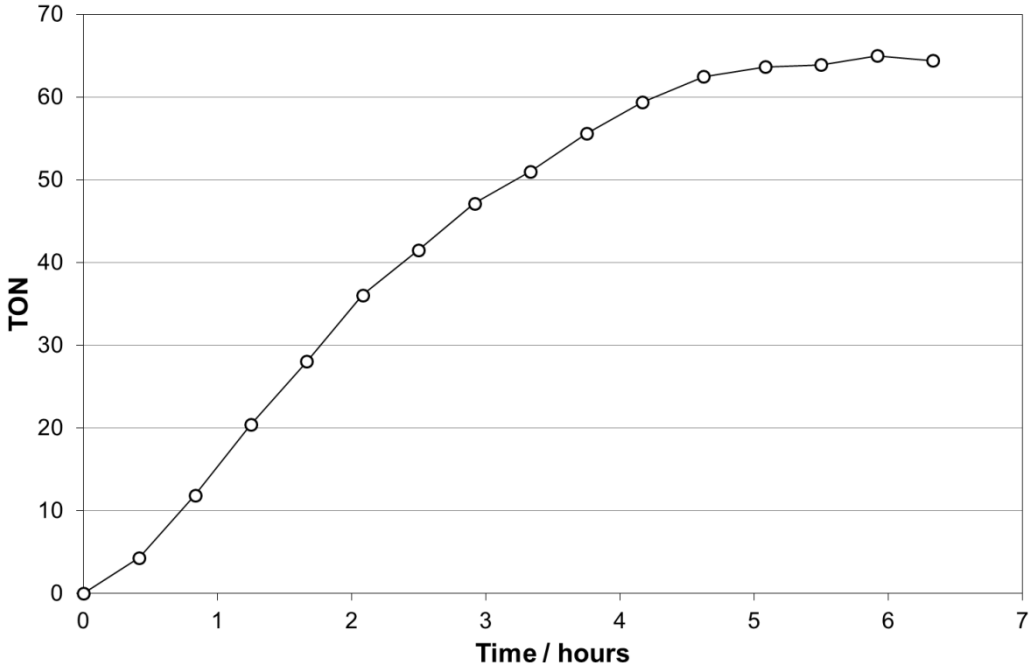

CO formation against irradiation time of ZnTPP: [Re(bpy)(CO)$_3$Br] (P1:R1–a)

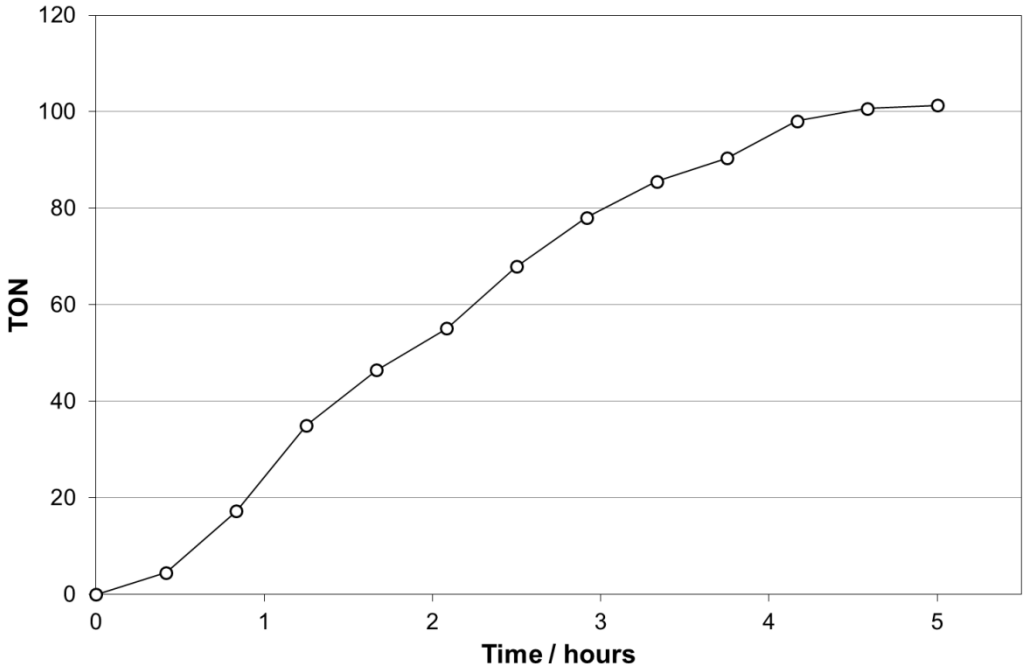

CO formation against irradiation time of ZnTPP: [Re(bpy)(CO)$_3$(CH$_3$CN)][PF$_6$] (P1:R2–a)

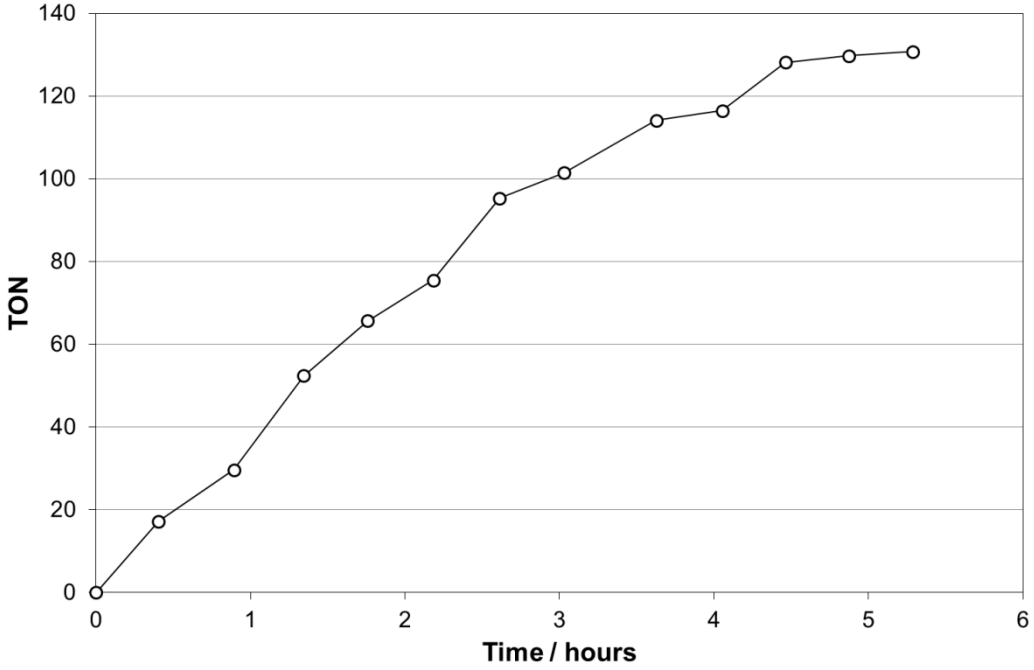

CO formation against irradiation time of ZnTPP: [Re(bpy)(CO)$_3$(3–Pic)][PF$_6$] (P1:R3–a)

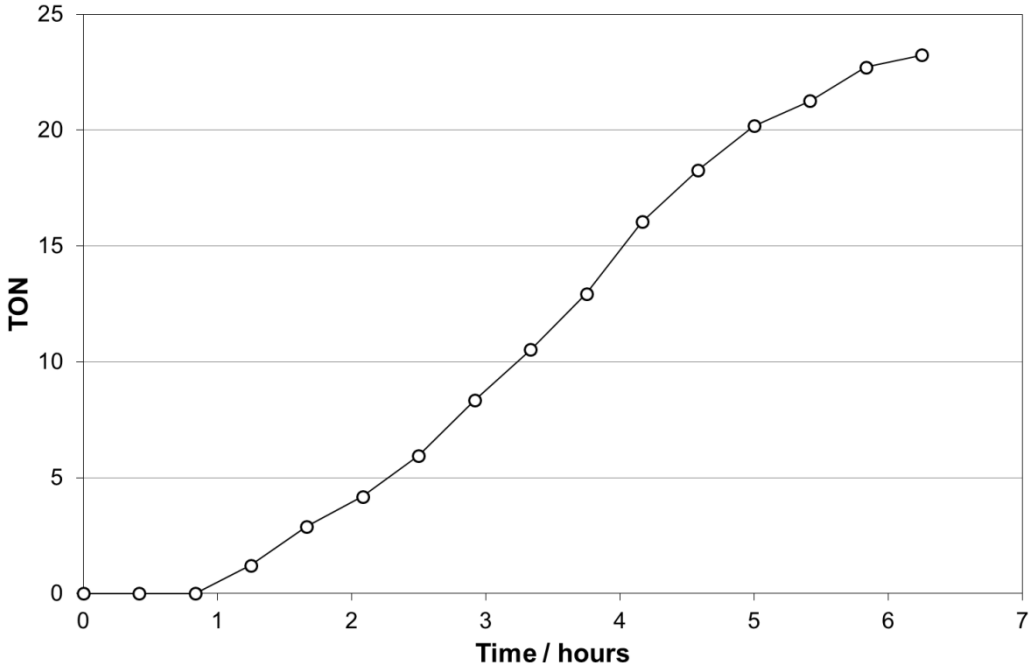

CO formation against irradiation time of ZnTPP: [Re(bpy)(CO)$_3${P(OEt)$_3$}][PF$_6$] (P1:R4–a)

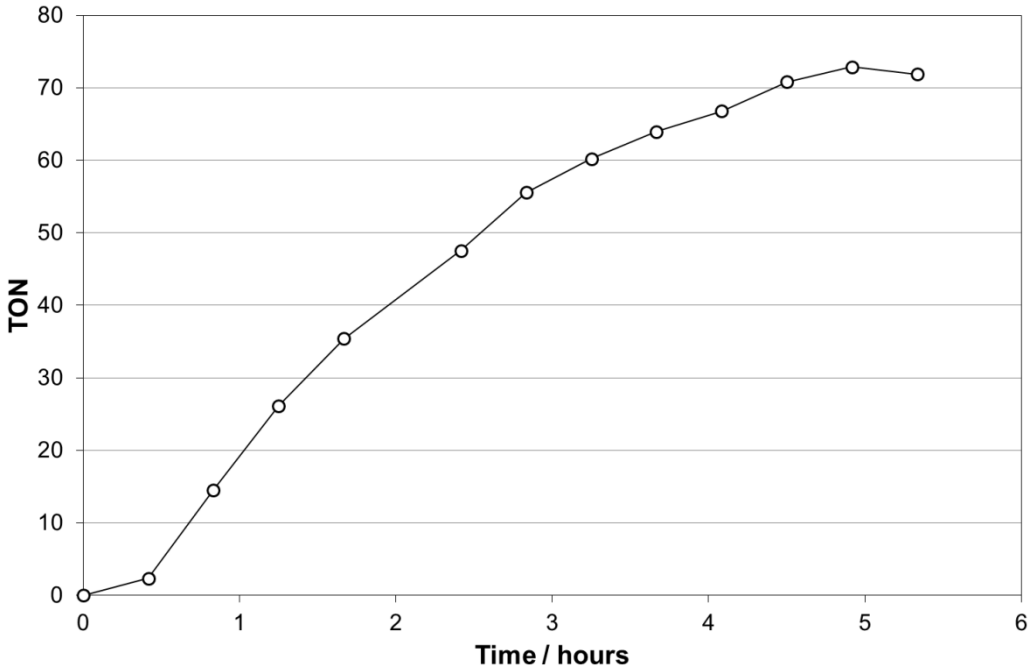

CO formation against irradiation time of ZnTTP: [Re(bpy)(CO)3Br] (P2:R1–a)

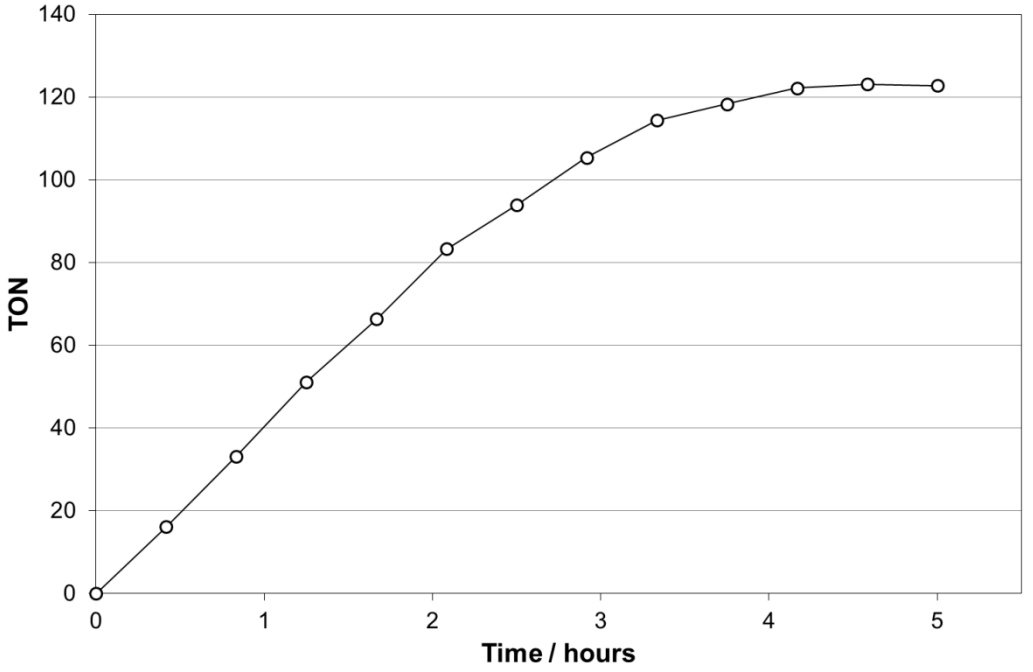

CO formation against irradiation time of ZnTTP: [Re(bpy)$(CO)_3(CH_3CN)][PF_6]$ (P2:R2–a)

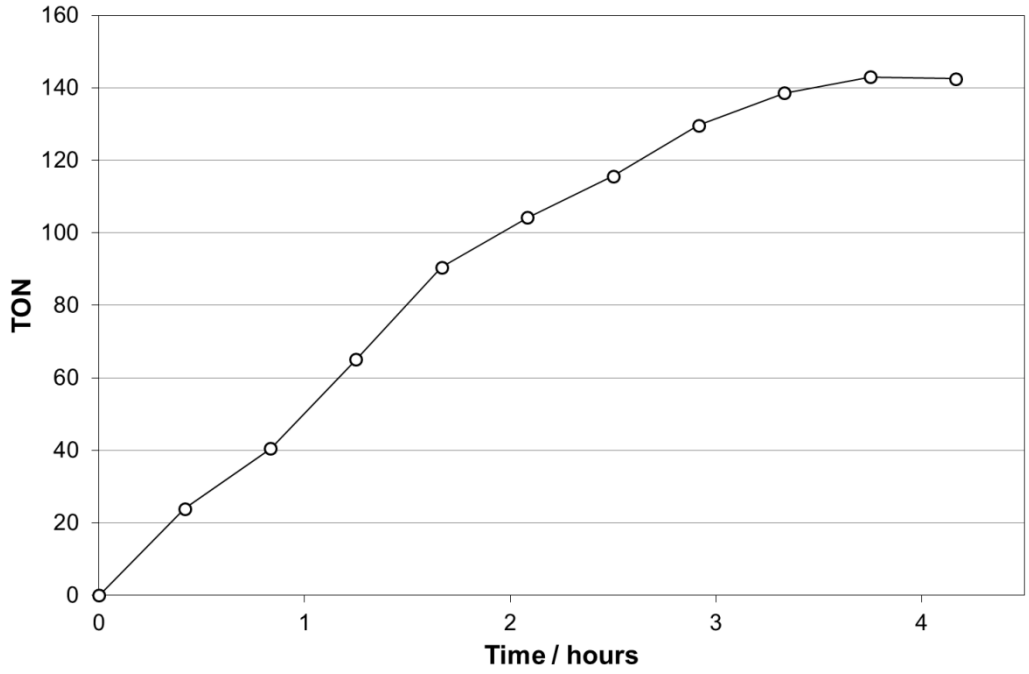

CO formation against irradiation time of ZnTTP: [Re(bpy)(CO)$_3$(3–Pic)][PF$_6$] (P2:R3–a)

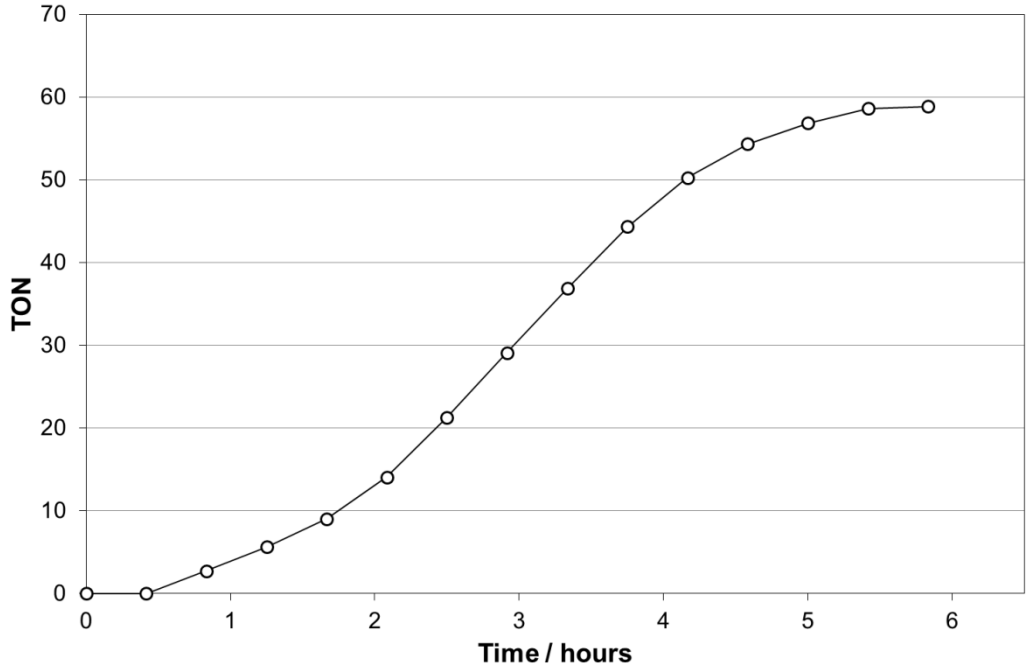

CO formation against irradiation time of ZnTTP: [Re(bpy)(CO)$_3${P(OEt)$_3$}][PF$_6$] (P2:R4–a)

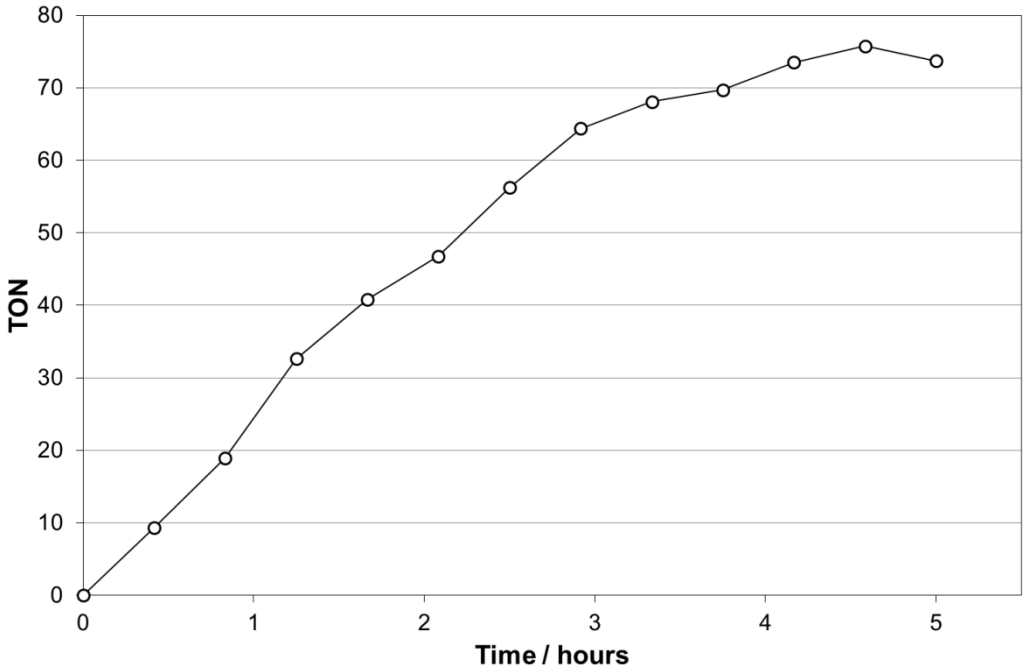

CO formation against irradiation time of ZnTTBPP: [Re(bpy)(CO)$_3$Br] (P3:R1–a)

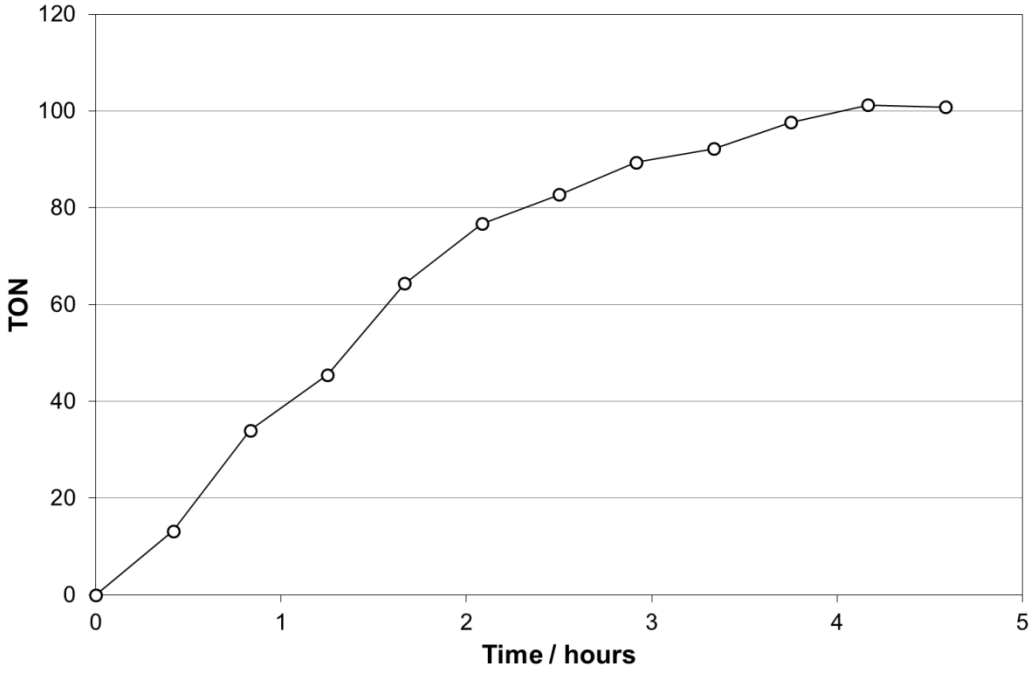

CO formation against irradiation time of ZnTTBPP: [Re(bpy)(CO)$_3$(CH$_3$CN)][PF$_6$] (P3:R2–a)

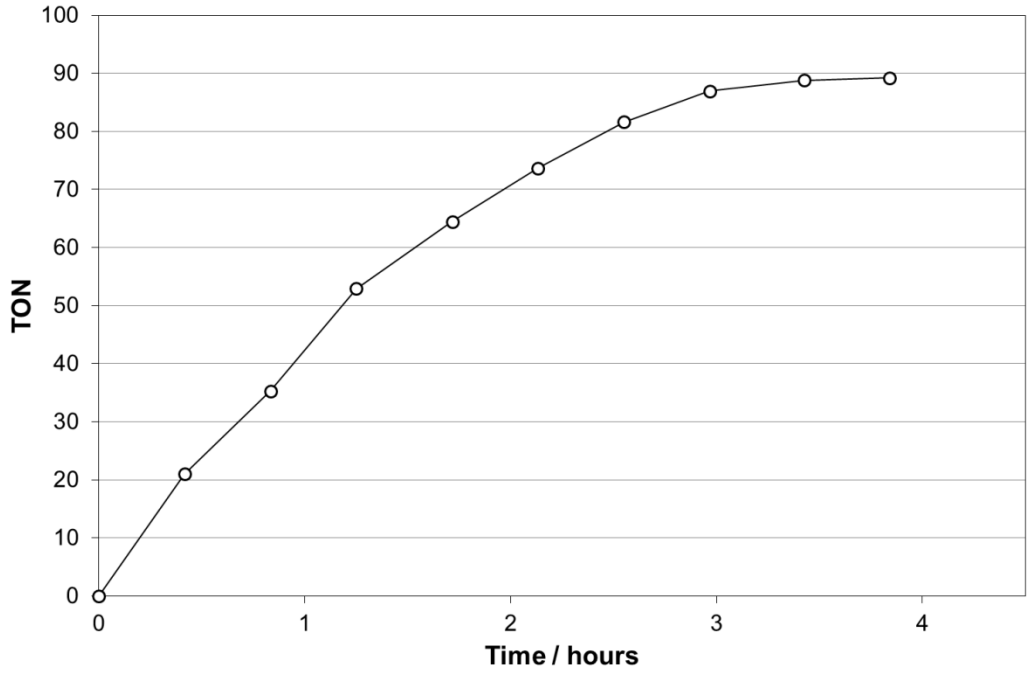

CO formation against irradiation time of ZnTTBPP: [Re(bpy)(CO)$_3$(3–Pic)][PF$_6$] (P3:R3–a)

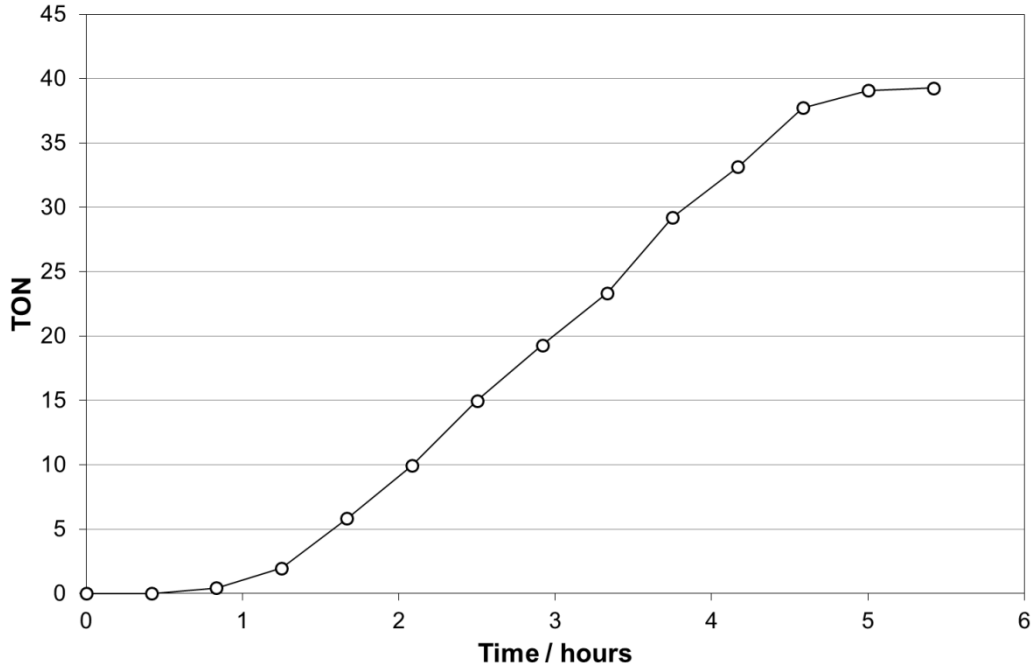

CO formation against irradiation time of ZnTTBPP: [Re(bpy)(CO)$_3${P(OEt)$_3$}][PF$_6$] (P3:R4–a)

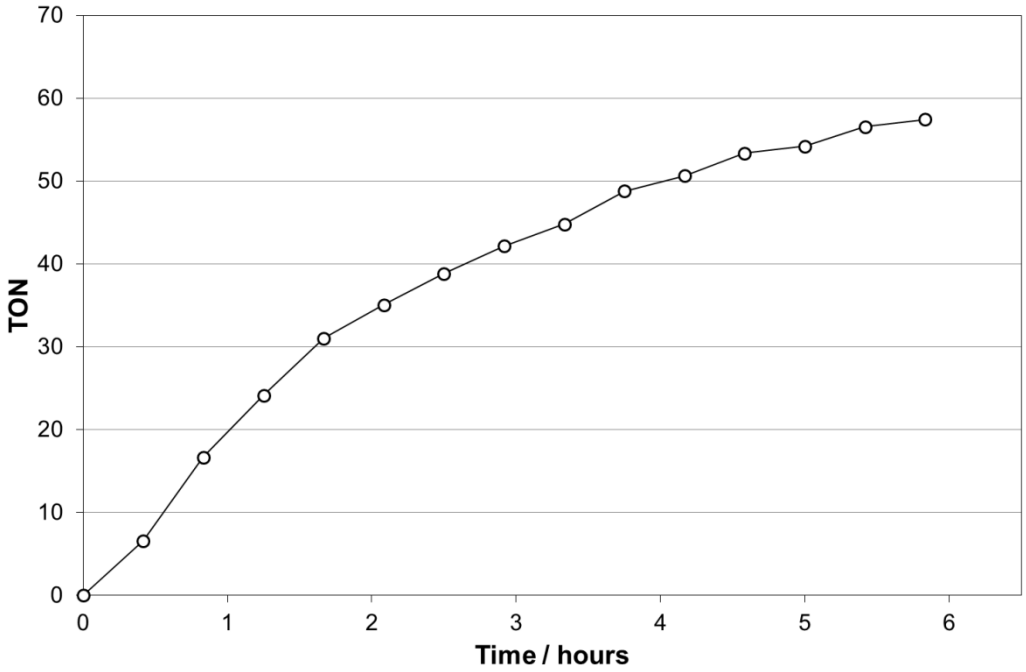

CO formation against irradiation time of ZnTMPP: [Re(bpy)(CO)$_3$Br] (P4:R1–a)

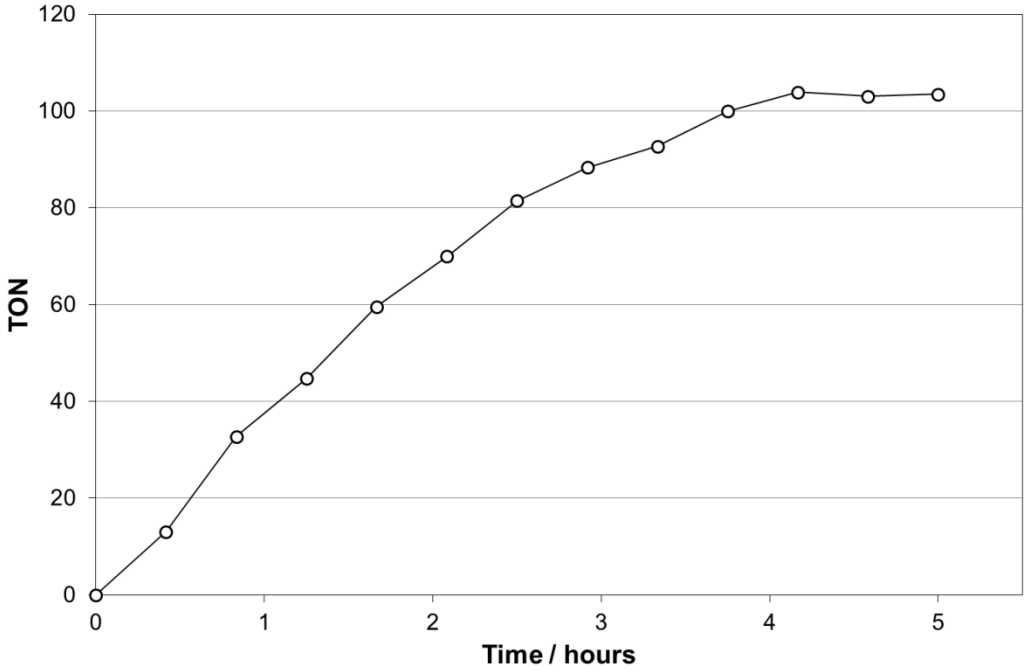

CO formation against irradiation time of ZnTMPP: [Re(bpy)(CO)$_3$(CH$_3$CN)][PF$_6$] (P4:R2–a)

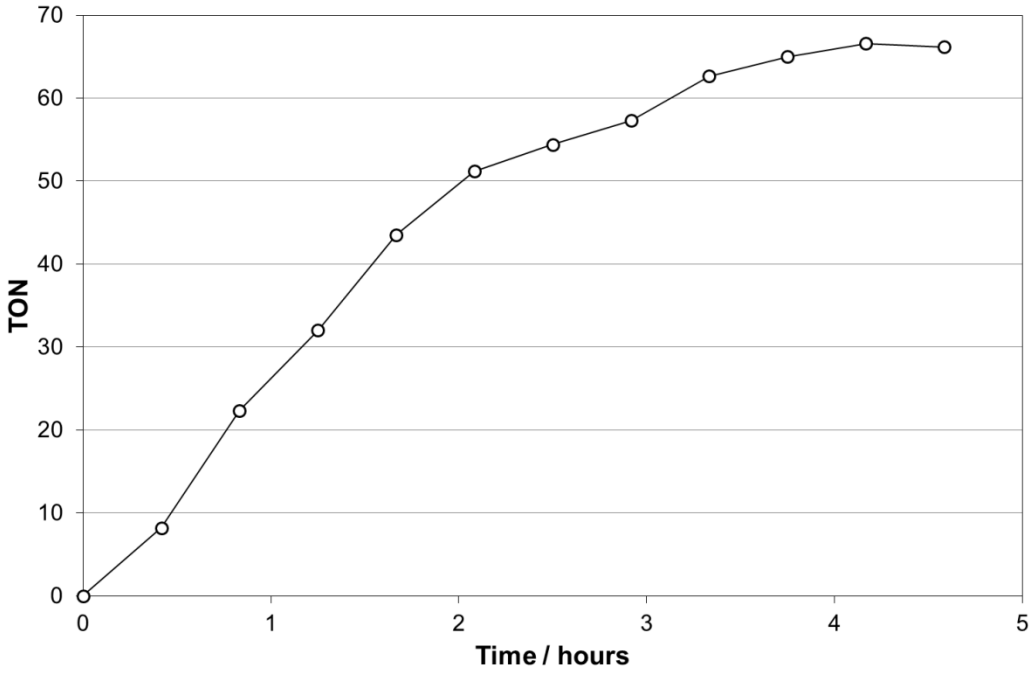

CO formation against irradiation time of ZnTMPP: [Re(bpy)(CO)$_3$(3–Pic)][PF$_6$] (P4:R3–a)

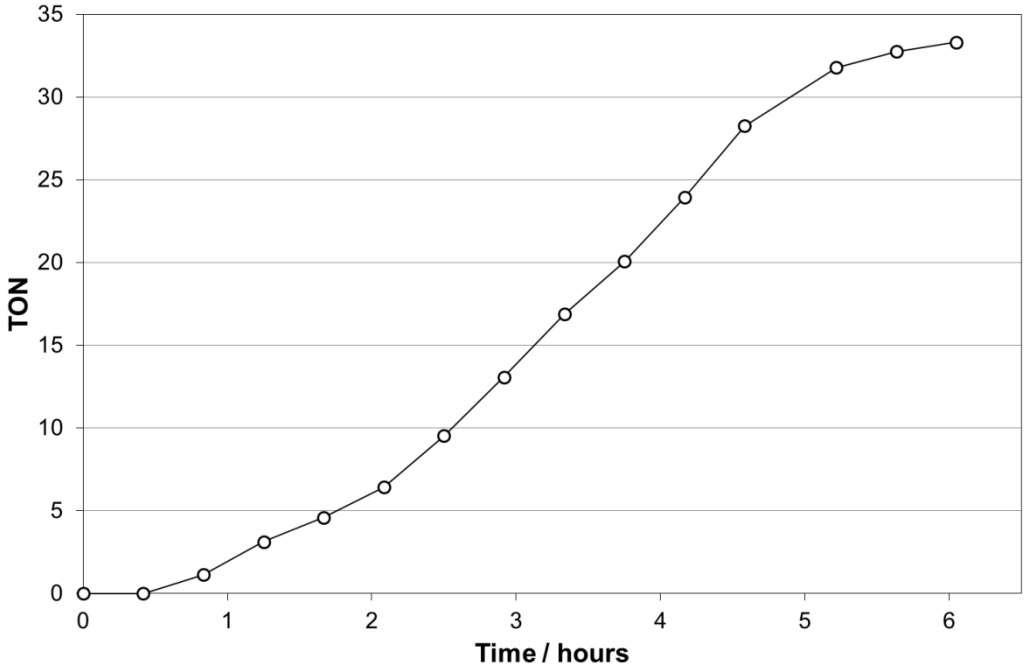

CO formation against irradiation time of ZnTMPP: [Re(bpy)(CO)$_3${P(OEt)$_3$}][PF$_6$] (P4:R4–a)

Definitions and Abbreviations

Ac	Acetyl ($CH_3C(O)$—)
BMCbpy	4,4'–bis(methoxycarbonyl)–2,2'–bipyridine
bpy	2,2'–bipyridine
C_{cc}	Carbon atom of the carbonyl ligand in *cis* position with both bipyridine nitrogen atoms
C_{ct}	Carbon atom of the carbonyl ligands in *cis–trans* positions respecto to the two bipyridine nitrogen atoms
CODH	Carbon monoxide dehydrogenase
Cyclam	1,4,8,11–tetraazacyclotetradecane
DFT	Density functional theory
ΔG_0	Difference in Gibbs free energy between reactant and product energy surfaces minima. General electron transfer driving force
ΔG_{PET}	Photoinduced electron transfer driving force
DMF	*N*,*N*–dimethylformamide
E_{00}	Difference in energy between the fundamental vibrational states of the ground and first excited electronic states
E_a	Activation energy
EDTA	Ethylenediaminetetraacetic acid
E_{ox}	Halfwave potential of the first oxidation process of a porphyrin
E_{red}	Halfwave potential of the first reduction process of a rhenium complex
$^{1st}E_{1/2}$	Halfwave potential of a generic first oxidation or reduction process
$^{2nd}E_{1/2}$	Halfwave potential of a generic second oxidation or reduction process
Et	Ethyl (CH_3CH_2—)
FB	Free base (porphyrin)
Fc / Fc^+	Ferrocene / ferrocenium redox couple
GC	Gas chromatography

HMD	5,7,7,12,14,14–hexamethy1–1,4,8,11–tetraazacyclotetradeca–4,11–diene
HOMO	Highest occupied molecular orbital
HR–EI–MS	High resolution electron ionization mass spectrometry
HSQC	Heteronuclear single quantum coherence / correlation spectroscopy
ID	Inner diameter
IR	Infrared spectroscopy
LUMO	Lowest unoccupied molecular orbital
Me	Methyl (CH_3—)
^{3}MLCT	Triplet metal–to–ligand charge transfer electronic state
MOFs	Metal–organic frameworks
NADH	Reduced form of the nicotinamide adenine dinucleotide
NADPH	Reduced form of the nicotinamide adenine dinucleotide phosphate
NHE	Normal hydrogen electrode
NMR	Nuclear magnetic resonance
OD	Outer diameter
OER	One electron reduced (species)
ORTEP	Oak Ridge thermal ellipsoid plot
P^0 / P^+	First oxidation step (of a porphyrin)
P^+ / P^{2+}	Second oxidation step (of a porphyrin)
PET	Photoinduced electron transfer
3–Pic	3–Picoline
$TBAPF_6$	Tetrabutylammoinum hexafluorophosphate
TCD	Thermal conductivity detector
TEA	Triethylamine
TEOA	Triethanolamine (tris(2–hydroxyethyl)amine)
THF	Tetrahydrofuran

TLC Thin layer chromatography

TMPP *meso*–tetrakis(*p*–methoxyphenyl)porphyrin

TOF Turnover frequency. Number of molecules of product formed per molecule of catalyst and time unit

TON Turnover number. Number of molecules of product formed per molecule of catalyst

TON_{max} Maximum amount of product formed by one catalytic system

TPP *meso*–tetraphenylporphyrin

TRIR Time–resolved infrared spectroscopy

TTBPP *meso*–tetrakis(*p*–*tert*–butylphenyl)porphyrin

t_{TON} Time to reach TON_{max}

TTP *meso*–tetratolylporphyrin

UV Ultraviolet (radiation)

References

1. Aresta, M., Dibenedetto, A., *Dalton Trans.* **2007**, 2975–2992.
2. Roy, S. C., Varghese, O. K., Paulose, M., Grimes, C. A., *ACS Nano* **2010**, *4*, 1259–1278.
3. West, N. M., Miller, A. J. M., Labinger, J. A., Bercaw, J. E., *Coord. Chem. Rev.* **2011**, *255*, 881–898.
4. Wender, I., *Fuel Process. Technol.* **1996**, *48*, 189–297.
5. Fujita, E., *Coord. Chem. Rev.* **1999**, *185–6*, 373–384.
6. Morris, A. J., Meyer, G. J., Fujita, E., *Acc. Chem. Res.* **2012**, *42*, 1983–1994.
7. Lehn, J. M., Ziessel, R., *Proc. Natl. Acad. Sci. U.S.A.* **1982**, *79*, 701–704.
8. Hawecker, J., Lehn, J. M., Ziessel, R., *Helv. Chim. Acta* **1986**, *69*, 1990–2012.
9. Takeda, H., Ishitani, O., *Coord. Chem. Rev.* **2010**, *254*, 346–354.
10. Takeda, H., Koike, K., Morimoto, T., Inumaru, H., Ishitani, O., in *Advances in Inorganic Chemistry, Vol 63: Inorganic Photochemistry, Vol. 63* (Ed.: R. S. G. VanEldik), **2011**, pp. 137–186.
11. Hori, H., Johnson, F. P. A., Koike, K., Takeuchi, K., Ibusuki, T., Ishitani, O., *J. Chem. Soc., Dalton Trans.* **1997**, 1019–1023.
12. Takeda, H., Koike, K., Inoue, H., Ishitani, O., *J. Am. Chem. Soc.* **2008**, *130*, 2023–2031.
13. Hori, H., Johnson, F. P. A., Koike, K., Ishitani, O., Ibusuki, T., *J. Photochem. Photobiol., A* **1996**, *96*, 171–174.
14. Koike, K., Hori, H., Ishizuka, M., Westwell, J. R., Takeuchi, K., Ibusuki, T., Enjouji, K., Konno, H., Sakamoto, K., Ishitani, O., *Organometallics* **1997**, *16*, 5724–5729.
15. Ishitani, O., George, M. W., Ibusuki, T., Johnson, F. P. A., Koike, K., Nozaki, K., Pac, C., Turner, J. J., Westwell, J. R., *Inorg. Chem.* **1994**, *33*, 4712–4717.
16. Tsubaki, H., Sugawara, A., Takeda, H., Gholamkhass, B., Koike, K., Ishitani, O., *Res. Chem. Intermed.* **2007**, *33*, 37–48.
17. Sung–Suh, H. M., Kim, D. S., Lee, C. W., Park, S. E., *Appl. Organomet. Chem.* **2000**, *14*, 826–830.
18. Hwang, J. S., Kim, D. S., Lee, C. W., Park, S. E., *Korean J. Chem. Eng.* **2001**, *18*, 919–923.
19. Ettedgui, J., Diskin–Posner, Y., Weiner, L., Neumann, R., *J. Am. Chem. Soc.* **2011**, *133*, 188–190.
20. Wang, C., Xie, Z., deKrafft, K. E., Lin, W., *J. Am. Chem. Soc.* **2011**, *133*, 13445–13454.
21. Yadav, R. K., Baeg, J.–O., Oh, G. H., Park, N.–J., Kong, K.–J., Kim, J., Hwang, D. W., Biswas, S. K., *J. Am. Chem. Soc.* **2012**, *134*, 11455–11461.
22. Benson, E. E., Kubiak, C. P., Sathrum, A. J., Smieja, J. M., *Chem. Soc. Rev.* **2009**, *38*, 89–99.
23. Sato, S., Arai, T., Morikawa, T., Uemura, K., Suzuki, T. M., Tanaka, H., Kajino, T., *J. Am. Chem. Soc.* **2011**, *133*, 15240–15243.
24. Windle, C. D., Perutz, R. N., *Coord. Chem. Rev.* **2012**, 10.1016/j.ccr.2012.1003.1010.
25. Hayashi, Y., Kita, S., Brunschwig, B. S., Fujita, E., *J. Am. Chem. Soc.* **2003**, *125*, 11976–11987.
26. Agarwal, J., Fujita, E., Schaefer, H. F., Muckerman, J. T., *J. Am. Chem. Soc.* **2012**, *134*, 5180–5186.
27. Bian, Z.–Y., Chi, S.–M., Li, L., Fu, W., *Dalton Trans.* **2010**, *39*, 7884–7887.
28. Gholamkhass, B., Mametsuka, H., Koike, K., Tanabe, T., Furue, M., Ishitani, O., *Inorg. Chem.* **2005**, *44*, 2326–2336.

29. Koike, K., Naito, S., Sato, S., Tamaki, Y., Ishitani, O., *J. Photochem. Photobiol., A* **2009**, *207*, 109–114.
30. Sato, S., Koike, K., Inoue, H., Ishitani, O., *Photochem. Photobiol. Sci.* **2007**, *6*, 454–461.
31. Hawecker, J., Lehn, J. M., Ziessel, R., *J. Chem. Soc., Chem. Commun.* **1983**, 536–538.
32. Ziessel, R., Hawecker, J., Lehn, J. M., *Helv. Chim. Acta* **1986**, *69*, 1065–1084.
33. Grant, J. L., Goswami, K., Spreer, L. O., Otvos, J. W., Calvin, M., *J. Chem. Soc., Dalton Trans.* **1987**, 2105–2109.
34. Willner, I., Maidan, R., Mandler, D., Durr, H., Dorr, G., Zengerle, K., *J. Am. Chem. Soc.* **1987**, *109*, 6080–6086.
35. Mandler, D., Willner, I., *J. Chem. Soc., Perkin Trans. 2* **1988**, 997–1003.
36. Yokoi, N., Miura, Y., Huang, C.–Y., Takatani, N., Inaba, H., Koshiyama, T., Kanamaru, S., Arisaka, F., Watanabe, Y., Kitagawa, S., Ueno, T., *Chem. Commun.* **2011**, *47*, 2074–2076.
37. Woolerton, T. W., Sheard, S., Reisner, E., Pierce, E., Ragsdale, S. W., Armstrong, F. A., *J. Am. Chem. Soc.* **2010**, *132*, 2132–2133.
38. Woolerton, T. W., Sheard, S., Pierce, E., Ragsdale, S. W., Armstrong, F. A., *Energy Environ. Sci.* **2011**, *4*, 2393–2399.
39. Aspley, C. J., Lindsay Smith, J. R., Perutz, R. N., Pursche, D., *J. Chem. Soc., Dalton Trans.* **2002**, 170–180.
40. Aspley, C. J., Lindsay Smith, J. R., Perutz, R. N., *J. Chem. Soc., Dalton Trans.* **1999**, 2269–2271.
41. Gabrielsson, A., Hartl, F., Zhang, H., Lindsay Smith, J. R., Towrie, M., Vlcek, A., Perutz, R. N., *J. Am. Chem. Soc.* **2006**, *128*, 4253–4266.
42. Gabrielsson, A., Hartl, F., Lindsay Smith, J. R., Perutz, R. N., *Chem. Commun.* **2002**, 950–951.
43. Gabrielsson, A., Lindsay Smith, J. R., Perutz, R. N., *Dalton Trans.* **2008**, 4259–4269.
44. Kiyosawa, K., Shiraishi, N., Shimada, T., Masui, D., Tachibana, H., Takagi, S., Ishitani, O., Tryk, D. A., Inoue, H., *J. Phys. Chem. C* **2009**, *113*, 11667–11673.
45. Schneider, J., Vuong, K. Q., Calladine, J. A., Sun, X.–Z., Whitwood, A. C., George, M. W., Perutz, R. N., *Inorg. Chem.* **2011**, *50*, 11877–11889.
46. Windle, C. D., Campian, M. V., Duhme–Klair, A.–K., Gibson, E. A., Perutz, R. N., Schneider, J., *Chem. Commun.* **2012**, *48*, 8189–8191.
47. Marcus, R. A., *Angew. Chem. Int. Ed. Engl.* **1993**, *32*, 1111–1121.
48. Marcus, R. A., *Annu. Rev. Phys. Chem.* **1964**, *15*, 155–196.
49. Marcus, R. A., *J. Chem. Phys.* **1956**, *24*, 966–978.
50. Adler, A. D., Longo, F. R., Finarell, J. D., J., G., Assour, J., Korsakof, L., *J. Org. Chem.* **1967**, *32*, 476.
51. He, C., He, Q., Deng, C., Shi, L., Zhu, D., Fu, Y., Cao, H., Cheng, J., *Chem. Commun.* **2010**, *46*, 7536–7538.
52. George, R. G., Padmanabhan, M., *Polyhedron* **2003**, *22*, 3145–3154.
53. Fernandez–Galan, R., Manzano, B. R., Otero, A., Lanfranchi, M., Pellinghelli, M. A., *Inorg. Chem.* **1994**, *33*, 2309–2312.
54. Fulmer, G. R., Miller, A. J. M., Sherden, N. H., Gottlieb, H. E., Nudelman, A., Stoltz, B. M., Bercaw, J. E., Goldberg, K. I., *Organometallics* **2010**, *29*, 2176–2179.
55. Becker, E. D., Bradley, R. B., *J. Chem. Phys.* **1959**, *31*, 1413–1414.
56. Castellano, S., Günther, H., Ebersole, S., *J. Phys. Chem.* **1965**, *69*, 4166–4176.
57. Osborne, A. G., *Monatsh. Chem.* **1988**, *119*, 1385–1395.
58. Koike, K., Okoshi, N., Hori, H., Takeuchi, K., Ishitani, O., Tsubaki, H., Clark, I. P., George, M. W., Johnson, F. P. A., Turner, J. J., *J. Am. Chem. Soc.* **2002**, *124*, 11448–11455.

59. Hori, H., Koike, K., Ishizuka, M., Takeuchi, K., Ibusuki, T., Ishitani, O., *J. Organomet. Chem.* **1997**, *530*, 169–176.
60. Werrett, M. V., Chartrand, D., Gale, J. D., Hanan, G. S., MacLellan, J. G., Massi, M., Muzzioli, S., Raiteri, P., Skelton, B. W., Silberstein, M., Stagni, S., *Inorg. Chem.* **2011**, *50*, 1229–1241.
61. Sazonov, P. K., Artamkina, G. A., Khrustalev, V. N., Antipin, M. Y., Beletskaya, I. P., *J. Organomet. Chem.* **2003**, *681*, 59–69.
62. Horn, E., Snow, M. R., *Aust. J. Chem.* **1980**, *33*, 2369–2376.
63. Woller, E. K., DiMagno, S. G., *J. Org. Chem.* **1997**, *62*, 1588–1593.
64. Gritzner, G., *Pure Appl. Chem.* **1990**, *62*, 1839–1858.
65. Tsierkezos, N. G., *J. Solution Chem.* **2007**, *36*, 289–302.
66. Abeed, F. A., Alallaf, T. A. K., Sulaiman, S. T., *Analyst* **1988**, *113*, 333–336.
67. Bond, A. M., McLennan, E. A., Stojanovic, R. S., Thomas, F. G., *Anal. Chem.* **1987**, *59*, 2853–2860.
68. Bao, D., Millare, B., Xia, W., Steyer, B. G., Gerasimenko, A. A., Ferreira, A., Contreras, A., Vullev, V. I., *J. Phys. Chem. A* **2009**, *113*, 1259–1267.
69. Pavlishchuk, V. V., Addison, A. W., *Inorg. Chim. Acta* **2000**, *298*, 97–102.
70. Kadish, K. M., Kevin, M. S., Guilard, R., in *The porphyrin handbook, Vol. 9*, Academic Press, **2000**.
71. Armaroli, N., Diederich, F., Echegoyen, L., Habicher, T., Flamigni, L., Marconi, G., Nierengarten, J. F., *New J. Chem.* **1999**, *23*, 77–83.
72. Binstead, R. A., Crossley, M. J., Hush, N. S., *Inorg. Chem.* **1991**, *30*, 1259–1264.
73. Hariprasad, G., Dahal, S., Maiya, B. G., *J. Chem. Soc., Dalton Trans.* **1996**, 3429–3436.
74. Hodge, J. A., Hill, M. G., Gray, H. B., *Inorg. Chem.* **1995**, *34*, 809–812.
75. Buchler, J. W., Elsasser, K., Kihnbotulinski, M., Scharbert, B., *Angew. Chem. Int. Ed. Engl.* **1986**, *25*, 286–287.
76. Panda, D. K., Goodson, F. S., Ray, S., Lowell, R., Saha, S., *Chem. Commun.* **2012**, *48*, 8775–8777.
77. Wolberg, A., *Isr. J. Chem.* **1974**, *12*, 1031.
78. Schmidt, S. P., Schuster, G. B., *J. Am. Chem. Soc.* **1980**, *102*, 7100–7103.
79. Johnson, F. P. A., George, M. W., Hartl, F., Turner, J. J., *Organometallics* **1996**, *15*, 3374–3387.
80. Paolucci, F., Marcaccio, M., Paradisi, C., Roffia, S., Bignozzi, C. A., Amatore, C., *The Journal of Physical Chemistry B* **1998**, *102*, 4759–4769.
81. Benson, E. E., Kubiak, C. P., *Chem. Commun.* **2012**, *48*, 7374–7376.
82. Breikss, A. I., Abruna, H. D., *J. Electroanal. Chem.* **1986**, *201*, 347–358.
83. Shaw, J. R., Schmehl, R. H., *J. Am. Chem. Soc.* **1991**, *113*, 389–394.
84. Worl, L. A., Duesing, R., Chen, P. Y., Dellaciana, L., Meyer, T. J., *J. Chem. Soc., Dalton Trans.* **1991**, 849–858.
85. Pelleteret, D., Fletcher, N. C., *Eur. J. Inorg. Chem.* **2008**, 3597–3605.
86. Sullivan, B. P., Bolinger, C. M., Conrad, D., Vining, W. J., Meyer, T. J., *J. Chem. Soc., Chem. Commun.* **1985**, 1414–1415.
87. Gouterman, M., *J. Mol. Spectrosc.* **1961**, *6*, 138–163.
88. Gouterman, M., Wagnière, G. H., Snyder, L. C., *J. Mol. Spectrosc.* **1963**, *11*, 108–127.
89. Keegan, J. D., Bunnenberg, E., Djerassi, C., *Spectrochim. Acta, Part A: Molecular Spectroscopy* **1984**, *40*, 287–297.
90. Prashanth Kumar, P., Maiya, B. G., *New J. Chem.* **2003**, *27*, 619–625.
91. Chizhova, N. V., Mamardashvili, N. Z., *Russ. J. Inorg. Chem.* **2011**, *56*, 484–488.
92. Choi, M. T. M., Choi, C.–F., Ng, D. K. P., *Tetrahedron* **2004**, *60*, 6889–6894.
93. Muzart, J., *Tetrahedron* **2009**, *65*, 8313–8323.
94. Casanova, M., Zangrando, E., Iengo, E., Alessio, E., Indelli, M. T., Scandola, F., Orlandi, M., *Inorg. Chem.* **2008**, *47*, 10407–10418.

95. Zhang, P., Wang, M., Li, C., Li, X., Dong, J., Sun, L., *Chem. Commun.* **2010**, *46*, 8806–8808.
96. Perrin, D. D., Amarego, W. L. F., *Purification of Laboratory Chemicals*, 3rd ed., Butterworth–Heinemann, Oxford, United Kingdom, **1988**.
97. Dolomanov, O. V., Bourhis, L. J., Gildea, R. J., Howard, J. A. K., Puschmann, H., *J. Appl. Crystallogr.* **2009**, *42*, 339–341.
98. Sheldrick, G. M., *Acta Crystallogr., Sect. A: Found. Crystallogr.* **2008**, *A64*, 112–122.
99. Miyoshi, D., Karimata, H., Wang, Z.–M., Koumoto, K., Sugimoto, N., *J. Am. Chem. Soc.* **2007**, *129*, 5919–5925.
100. Kutal, C., Weber, M. A., Ferraudi, G., Geiger, D., *Organometallics* **1985**, *4*, 2161–2166.
101. Smieja, J. M., Kubiak, C. P., *Inorg. Chem.* **2010**, *49*, 9283–9289.
102. Uppal, B. S., Booth, R. K., Ali, N., Lockwood, C., Rice, C. R., Elliott, P. I. P., *Dalton Trans.* **2011**, *40*, 7610–7616.